Guidance for rendezvous and formation flying in elliptical orbits

Peters, T.V.

DOI
10.4233/uuid:76aad116-9a1b-4f8a-a289-4727ea10e709

Publication date
2024

Document Version
Final published version

Citation (APA)
Peters, T. V. (2024). *Guidance for rendezvous and formation flying in elliptical orbits*. [Dissertation (TU Delft), Delft University of Technology]. https://doi.org/10.4233/uuid:76aad116-9a1b-4f8a-a289-4727ea10e709

Guidance for rendezvous and formation flying in elliptical orbits

Guidance for rendezvous and formation flying in elliptical orbits

Dissertation

for the purpose of obtaining the degree of doctor

at Delft University of Technology

by the authority of the Rector Magnificus, Prof. dr. ir. T.H.J.J. van der Hagen,

chair of the Board for Doctorates

to be defended publicly on

Tuesday 17 September 2024, at 15:00

by

Thomas Vincent PETERS,

Master of Science in Aerospace Engineering,
Delft University of Technology, The Netherlands

born in Emmen, The Netherlands

This dissertation has been approved by the promotors.

Composition of the doctoral committee:

Rector Magnificus,	Chairperson
Prof. dr. ir. P.N.A.M. de Visser,	Delft University of Technology, *promotor*
Ir. R. Noomen,	Delft University of Technology, *copromotor*

Independent members:

Dr. J. Guo,	Delft University of Technology
Prof. dr. ir. P.J.G. Teunissen,	Delft University of Technology
Prof. dr. F. Topputo,	Politecnico di Milano, Italy
Prof. Dr.-Ing. B. Dachwald,	FH Aachen, Germany
Prof. dr. M. MacDonald,	University of Strathclyde, United Kingdom
Prof. dr. L.L.A. Vermeersen,	Delft University of Technology, *reserve member*

Keywords: Rendezvous, Formation Flying, Guidance

Printed by: Ridderprint | **www.ridderprint.nl**

Front: Oscar D. Peters

ISBN 978-94-6384-613-4

An electronic version of this dissertation is available at:

http://repository.tudelft.nl/

That is the exploration that awaits you.
Not mapping stars and studying nebula, but charting the unknown possibilities of existence.
– Q (John de Lancie)

in “All good things…”, *Star Trek: The Next Generation*
Ronald D. Moore & Brannon Braga

Contents

List of figures

List of tables

Acknowledgements

I would like to express my deepest appreciation to my professor and my academic mentor at Delft University. This work would not have been possible without their support and feedback. I am also deeply grateful to the (former) head of the GNC section at GMV, for allowing me to write the articles about the work performed at GMV that form the basis for this thesis. Thanks should also go to the European Space Agency for providing the funding required to perform the design projects in the field of rendezvous and formation flying.

Special thanks to my colleagues at GMV for providing many opportunities for interesting discussions and for providing valuable insights into the problems I encountered.

I would like to thank my husband, my friends, and my family to whom I have said “only two more years” far too often. Without their support I would not have been able to persist.

Summary

Although the first automated rendezvous in space took place in the late 1960s and rendezvous and formation flying in low-Earth orbit have become established technologies, it remains an active field of research. Miniaturization of components and entire spacecraft has enabled the development of CubeSat formation flying and rendezvous missions. At the same time, the number of missions in general has increased, leading to a growing population of space debris.

The dynamics of rendezvous of spacecraft in circular orbits is a problem that is well-understood and that is regularly taught in orbital mechanics majors, as are the techniques of linearization and the applications of the state transition matrix. The design of strategies for rendezvous and formation flying often makes use of standard building blocks in the form of specific manoeuvres and trajectories. Typical rendezvous manoeuvres include the Hohmann transfer and the radial hop, a manoeuvre that can change the along-track separation but that does not change the semi-major axis. Typical rendezvous and formation flying trajectories include drift orbits, safe orbits and hold points on V-bar. In this study, the Hohmann transfer, the radial hop and the useful relative trajectories were generalized to elliptical orbits, and this has enabled the application of the insights gained from circular orbit rendezvous and formation flying to elliptical orbits. The cotangential transfer manoeuvre has been developed as a generalization of the Hohmann transfer, preserving the tangentiality of the impulses. The transfer time becomes a function of the initial and final conditions. The development of the cotangential transfer has led to the identification of new constants of motion that describe the behaviour of the z-coordinate in the tangential or flight-path reference frame. In this reference frame the x-axis points in the direction of the orbital velocity of the target, the y-axis points in the direction opposite to the angular momentum vector and the z-axis completes the right-handed reference frame. The z-coordinate in the tangential frame shows a simple oscillation with a fixed displacement from the origin and multiplied by a scaling factor, and the y-coordinate shows a simple oscillation around the origin also multiplied by a scaling factor. This observation has led to a straightforward generalization of the eccentricity/inclination vector separation strategy to elliptical orbits. To create a safe orbit, the phase angle between the oscillations in the y and z-directions must have a value larger than a certain margin and the vertical displacement must be such that the trajectory winds around the origin, ensuring passive safety. Zero drift is obtained by setting the semi-major axis equal to that of the target. In addition, safe orbits with an alignment of the relative positions of the chaser and the target along a specified direction at a specific true anomaly of the target orbit

have been developed. These safe orbits can be used to align the chaser and the target with a specific direction such as, for example, the Sun direction. An example of a rendezvous trajectory featuring the Hohmann transfer, and the aligned safe orbit has been elaborated.

The radial hop transfer has been generalized to non-drifting transfers between eccentric orbits. The non-drifting transfer algorithm can be incorporated in a generalization to eccentric orbits of a close-range circular orbit rendezvous strategy featuring non-drifting radial hops. Two different generalizations are possible based on the assumptions that are made when generalizing the notion of hold points to elliptical orbits: the transfer can either target a point in the local vertical, local horizontal (LVLH) frame, or a trajectory defined in terms of relative orbital elements. From the perspective of propellant consumption, it is convenient to define hold points as drift-free natural motion trajectories based on differences in either the relative mean anomaly or the relative argument of perigee. On the other hand, from the perspective of obtaining a fixed relative geometry (for example, a point on the line of sight to the target in the LVLH-frame) it may be more convenient to transfer between two points defined explicitly as Cartesian relative state vectors in the LVLH-frame.

It has been determined that tangential and perpendicular in-plane impulses can both directly change three out of the four relative orbital elements that govern the in-plane relative motion. The tangential impulse directly modifies the relative semi-major axis and the components of the relative eccentricity vector. The evolution of the relative mean anomaly is indirectly affected because the relative semi-major axis directly relates to the rate of change of the relative mean anomaly. The perpendicular impulse directly modifies the components of the relative eccentricity vector and the relative mean anomaly. In both cases, the way in which the relative eccentricity vector changes depends on the position along the reference orbit. The fact that the same phenomenon occurs in circular orbits indicates that this is the most natural generalization of the Hohmann transfer and the radial hop transfer to elliptical orbits.

The insights gained from the theoretical developments have been applied to the mission analysis for Proba-3, a formation flying mission in a highly elliptical orbit. Proba-3 will perform Solar coronagraphy and formation manoeuvring demonstrations in a six-hour region around apogee. The two spacecraft are in free flight during the passage through perigee. The spacecraft perform a two-impulse transfer, where the first manoeuvre serves to break the formation at the end of an apogee pass, and the second manoeuvre serves to re-establish the formation at the start of the next apogee pass. The design of the formation deployment has been based on the concept of the safe orbit to manage observability and ground contact constraints. The ΔV required for formation keeping and all nominal manoeuvres has been analysed.

In addition, design and analysis of the off-nominal operations of Proba-3 has been performed. It was demonstrated that safe trajectories exist for Proba-3 and that the mission can be performed safely even if failures occur. The contingency operations make use of the concept of the safe orbit and the collision avoidance manoeuvre. The manoeuvres and the trajectory to enter into safe orbit and the trajectory after application of a collision avoidance manoeuvre have been analysed, and it was found that these manoeuvres are feasible, and the resulting trajectories are safe. It was determined that all manoeuvres can be performed under control of the ground segment and that control can successfully be handed back to the spacecraft after the ground segment has commanded a transfer to nominal conditions.

This thesis has demonstrated that the knowledge of and insight in circular orbit rendezvous can be leveraged to understand elliptical orbit rendezvous by generalizing the building blocks of rendezvous strategies, namely the manoeuvres and trajectories. This allows design strategies for rendezvous and formation flying in circular orbits to be applied to elliptical orbits as well. The theoretical advances have been employed in a practical setting to design the relative trajectories for the Proba-3 mission, paving the way for the development of a guidance function to be implemented in the on-board software of the Proba-3 spacecraft.

Samenvatting

Hoewel de eerste geautomatiseerde rendezvous in de ruimte al plaatsvond in de late jaren zestig van de vorige eeuw, en rendezvous en formatievlucht in lage aardbanen inmiddels een gevestigde techniek zijn geworden, blijft het een actief onderzoeksveld. Miniaturisatie van onderdelen en complete satellieten heeft formatievlucht en rendezvous van CubeSats mogelijk gemaakt. Tegelijkertijd is het aantal ruimtemissies toegenomen, hetgeen heeft geleid tot een groeiende hoeveelheid ruimteafval.

De dynamica van rendezvous in cirkelbanen is een bekend probleem dat vaak wordt onderwezen in colleges over baanmechanica, net als de wiskundige techniek om een dynamisch probleem te lineariseren, en de toepassingen van de zogenaamde “state transition matrix”. Bij het ontwerpen van strategieën voor rendezvous en formatievlucht wordt veelvuldig gebruik gemaakt van standaard bouwstenen in de vorm van specifieke manoeuvres en overgangsbanen. Typische voorbeelden van rendezvousmanoeuvres zijn de Hohmann overgangsbaan en de zogenaamde “radial hop”, dat wil zeggen, een manoeuvre die zorgt voor een verandering van de afstand tussen de satellieten in de bewegingsrichting, maar die de halve-lange as van de overgangsbaan gelijk houdt aan de halve-lange as van de referentiebaan. Typische banen voor rendezvous en formatievlucht zijn driftbanen (banen waarin de afstand tussen de satellieten in de bewegingsrichting verandert doordat de halve-lange as verschillend is), botsingsvrije banen (banen waarin de inclinatievector en de eccentriciteitsvector verschillend zijn om botsingen te voorkomen) en rustpunten langs de snelheidsvector van de referentiebaan. In deze these zijn de Hohmann overgangsbaan, de “radial hop” en de bruikbare overgangsbanen die normaliter gebruikt worden bij circulaire banen veralgemeniseerd om ze ook van toepassing te maken op rendezvous in elliptische banen. Door vergelijkbare bouwstenen te gebruiken, kunnen de inzichten in het ontwerpen van strategieën voor rendevous en formatievlucht in cirkelbanen worden toegepast in elliptische banen.

De cotangentiële overgangsbaan is ontwikkeld als een veralgemenisering van de Hohmann overgangsbaan, waarbij de tangentialiteit van de impulsieve manoeuvres met de referentiebaan is behouden. Door deze randvoorwaarde in acht te nemen wordt de tijd die doorgebracht wordt in de overgangsbaan een functie van de begin- en eindcondities. De ontwikkeling van de cotangentiële overgangsbaan heeft geleid tot nieuwe baanconstanten die het gedrag van de z-coördinaat in het baan-tangentiële assenstelsel op een eenvoudige manier beschrijven. In dit assenstelsel wijst de x-as in de richting van de vliegsnelheid in de referentiebaan, de y-as in de richting tegenovergesteld aan de normaalvector van het baanvlak, en de z-as voltooit het rechtshandige assenstelsel. De z-coördinaat in het tangentiële assenstelsel vertoont

een eenvoudige harmonische oscillatie met een gemiddelde verplaatsing, die wordt vermenigvuldigd met een schaalfactor die afhangt van de ware anomalie. De y-coördinaat vertoont ook een eenvoudige harmonische oscillatie vermenigvuldigd met een (andere) schaalfactor. Op deze manier kan de strategie om door de inclinatie- en eccentriciteitsvectoren te veranderen botsingsvrije banen te creëren, op een eenvoudige manier veralgemeniseerd worden van cirkelvormige naar elliptische banen. Om een botsingsvrije baan te realiseren moet de fasehoek tussen de harmonische oscillaties in de y- en z-richtingen groter zijn dan een bepaalde waarde, en moet de verplaatsing van het middelpunt van de oscillatie in de z-richting zo gekozen worden dat de relatieve baan in het yz-vlak met een zekere marge om de oorsprong van het assenstelsel draait. In een dergelijke baan kan drift in de bewegingsrichting voorkomen worden door de halve-lange as gelijk te stellen aan de halve-lange as van de referentiebaan. Er is ook een methode ontwikkeld om deze botsingsvrije banen op een specifiek punt in de referentiebaan door een specifiek punt in een relatief assenstelsel (dat wil zeggen, lokaal verticaal, lokaal horizontaal (LVLH) of tangentiëel) te laten bewegen. Op deze manier kunnen de twee satellieten op een specifiek punt in de referentiebaan in een bepaalde richting (bijvoorbeeld de richting naar de Zon) worden uitgelijnd. In de these wordt een voorbeeld uitgewerkt van een rendezvousvlucht die gebruik maakt van Hohmann overgangsbanen en een uitgelijnde botsingsvrije baan.

De "radial hop" is veralgemeniseerd tot een drift-vrije overgangsbaan tussen eccentrische banen. Het algoritme voor de berekening van de drift-vrije overgangsbanen kan gebruikt worden om een strategie voor een rendezvousvlucht op kleine afstand met "radial hops" tussen circulaire banen te veralgemeniseren naar elliptische banen. Er zijn twee manieren om dit aan te pakken, afhankelijk van de manier waarop tussentijdse banen (de zogenaamde "hold points") worden veralgemeniseerd naar elliptische banen. De eindconditie van de overgangsbaan kan ofwel een specifiek punt in het LVLH-assenstelsel zijn, of een tussenbaan die wordt gedefinieerd door middel van relatieve baanelementen. Vanuit het gezichtspunt van stuwstofverbruik is het praktisch om de tussenbaan te definiëren als een drift-vrije natuurlijke baan met kleine verschillen in de gemiddelde anomalie of de perigeumhoek ten opzichte van de referentiebaan. Aan de andere kant kan het soms nodig zijn dat de ene satelliet op een specifieke positie ten opzichte van de andere satelliet aankomt (bijvoorbeeld op een punt op de gezichtslijn van een sensor). In dat geval is het nodig om een overgangsbaan te definiëren tussen twee posities die worden gegeven als Cartesiaanse coördinaten in het LVLH-assenstelsel.

Impulsieve manoeuvres in de tangentiële en de loodrechte richtingen kunnen elk drie van de vier baanelementen beïnvloeden die de relatieve beweging in het baanvlak bepalen. De tangentiële impuls verandert de halve-lange as en de twee componenten van de eccentriciteitsvector. Het gedrag van de gemiddelde anomalie wordt indirect beïnvloed doordat een verandering in de halve-lange as ook de gemiddelde hoeksnelheid in de baan verandert. De loodrechte impuls verandert de componenten van de eccentriciteitsvector en de gemiddelde anomalie. In beide gevallen wordt de verandering van de componenten van de eccentriciteitsvector mede bepaald door de positie in de referentiebaan. Aangezien hetzelfde gebeurt in circulaire referentiebanen, toont het aan dat het de meest natuurlijke veralgemenisering van de Hohmann overgangsbaan en de "radial hop" is naar problemen met elliptische banen.

De inzichten die zijn opgedaan bij de ontwikkeling van de theorie zijn toegepast op de missieanalyse van Proba-3, waarbij twee satellieten in formatie vliegen in een elliptische referentiebaan. Het hoofddoel van de missie is om de Zon te bestuderen met een coronograaf, waarbij de ene satelliet de Zon in het beeld van een camera op de andere satelliet precies afdekt. Een ander doel is het uittesten van manoeuvres in een vaste formatie, waarmee bijvoorbeeld de afstand tussen de satellieten kan worden verkleind, of de formatie naar een andere kijkrichting kan worden gedraaid. Voor beide doelen moeten de satellieten zeer nauwkeurig ten opzichte van elkaar worden gepositioneerd (en blijven) door continue regeling met behulp van stuwraketten, en dit is alleen mogelijk in een periode van zes uur rond het apogeum. De satellieten vliegen in de rest van de baan in vrije val, zo ook bij het passeren van het perigeum. De overgangsbaan wordt gecontroleerd door middel van twee snelheidsimpulsen. De eerste impuls brengt de formatie in de juiste overgangsbaan om op het gewenste punt aan te komen (dat wil zeggen, op een specifieke afstand en op één lijn met de Zon). De tweede impuls zorgt ervoor dat de relatieve snelheid tot een kleine waarde wordt teruggebracht en de vaste formatie weer kan worden aangenomen voordat de volgende apogeumpassage begint. De satellieten worden gezamenlijk gelanceerd, en aan het begin van de missie moeten de satellieten eerst gescheiden worden, om daarna een rendezvousvlucht uit te voeren. Het ontwerp van deze rendezvousvlucht is gebaseerd op het concept van de botsingsvrije baan, en houdt rekening met de mogelijkheden om waarnemingen te doen en met de contacttijden met het grondstation. De vereiste hoeveelheid ΔV is berekend voor het behouden van de formatie en alle nominale manoeuvres.

Daarnaast zijn ook de niet-nominale activiteiten van Proba-3 ontworpen en geanalyseerd. Niet-nominale activiteiten worden uitgevoerd als er een probleem optreedt. Botsingsvrije banen zijn gedefiniëerd voor Proba-3, en het is vastgesteld dat de missie veilig kan worden uitgevoerd, ook wanneer er een fout optreedt. De manoeuvres die worden uitgevoerd na het optreden van een onvoorziene fout zijn gebaseerd op botsingsvrije banen en ontwijkingsmanoeuvres. De manoeuvres en de overgangsbanen die nodig zijn om de botsingsvrije baan te bereiken, en de baan die wordt gevolgd na een ontwijkingsmanoeuvre zijn geanalyseerd, en deze zijn haalbaar en kunnen veilig worden uitgevoerd. De manoeuvres om terug te keren naar de nominale baan en activiteiten kunnen onder controle van het grondsegment worden uitgevoerd, en daarna kunnen de boordcomputers van de satellieten de controle weer overnemen.

In deze dissertatie is het aangetoond dat de kennis van en het inzicht in rendezvous in cirkelbanen kan worden ingezet om een beter begrip van rendezvous in ellipsvormige banen te verkrijgen door de bouwstenen van rendezvousstrategieën (manoeuvres en overgangsbanen) te veralgemeniseren. Op deze manier kunnen ontwerpstrategieën die nu al toegepast worden op rendezvous tussen twee satellieten in cirkelbanen, óók worden toegepast op rendezvous tussen twee satellieten in elliptische banen. De verkregen theoretische inzichten zijn in de praktijk toegepast op het ontwerp van de relatieve banen die de Proba-3 missie zal gebruiken, en om de weg te bereiden voor het ontwerp van de guidance algoritmen die in de on-board computer van Proba-3 zullen worden geïnstalleerd.

1
Introduction

The process of rendezvous refers to a sequence of manoeuvres and controlled relative trajectories that aim to bring a spacecraft in close vicinity of another spacecraft [1]. The active spacecraft is referred to as the chaser, while the passive spacecraft is referred to as the target [2]. Rendezvous considered as a mission phase occurs after launch and phasing, and before proximity operations, including berthing and/or docking [1]. The objective of phasing is to reduce the phase angle between the chaser and the target spacecraft. During phasing the chaser is brought into approximately the same orbital plane as the target with approximately the same eccentricity and argument of perigee, while the difference in semi-major axis is chosen such that the phase angle between the chaser and the target decreases, typically to a distance of the order of 100 km. In some cases, notably technology demonstrator missions, the chaser and the target are launched together, and no phasing is required, since they remain in close vicinity while in orbit [3]. Proximity operations refer to all operations during which the chaser operates in close vicinity to the target [4,5], typically up to 100 m. During rendezvous, the chaser trajectory is controlled by means of impulsive manoeuvres that last a small fraction of its orbital period. In between these manoeuvres the chaser is in free drift. During proximity operations the chaser trajectory can be controlled by means of impulsive manoeuvres, or it can be continuously controlled using the thrusters. In the latter case the chaser is in forced motion, and the thrusters compensate for any relative accelerations to maintain the desired reference trajectory.

Formation flying [6] refers to techniques to maintain a desired separation, relative position and/or relative orientation between two or more spacecraft. Within the discipline of formation flying the terminology used is different from the terminology of rendezvous. In formation flying the passive spacecraft is sometimes referred to as the leader or master, and the active spacecraft as the follower or slave. The leader/follower distinction refers to which spacecraft performs the manoeuvres [6], while the master/slave distinction refers to which spacecraft acts as the coordinator in the formation control [7]. The master spacecraft computes and distributes the reference state for one or more slave spacecraft. Of course, other approaches are possible: to save propellant, spacecraft could switch roles. It is also possible to define a “virtual centre” or a reference point around which the nominal states of all spacecraft in the formation are defined [8].

Different architectures and network topologies are possible, and this is an active field of research, especially for larger formations [9]. Another important concept is that of the virtual structure [10]. In a virtual structure two or more spacecraft function as a single rigid body, for example, to precisely align a lens located on one spacecraft with a detector on another spacecraft. The required precision for formation flying depends on the mission application. Virtual structure missions as a rule have high relative position and attitude accuracy requirements, whereas other missions only require precise knowledge of the relative position and velocity (e.g., GRACE [11] requires precise knowledge of the relative position for precise attitude alignment to perform satellite-to-satellite tracking).

Rendezvous and formation flying are techniques for operating multiple spacecraft within a single mission that require a precise coordination between spacecraft. Other configurations that feature multiple spacecraft operating together are constellations and satellite swarms. Constellations and satellite swarms tend to have a low level of coordination between the different spacecraft. Spacecraft in constellations are separated by large distances and are controlled individually. A typical example is the Walker constellation [12], with satellites distributed over several orbital planes with the same inclination. A satellite swarm consists of many spacecraft with a low level of coordinated control [13]. Spacecraft in satellite swarms can be separated at small, medium, or large distances. However, constellations and satellite swarms are beyond the scope of this thesis.

This introductory chapter provides examples of applications of rendezvous and formation flying. The state of the art is reviewed, both in terms of past, present, and future missions, and in terms of the research that these missions have stimulated. The relative motion around spacecraft in circular orbits is discussed, including useful impulsive manoeuvring strategies and trajectory types. The Proba-3 mission for formation flying in a highly elliptical orbit (HEO) is introduced, discussing the mission objectives, the mission architecture, and the gaps in existing theoretical knowledge that need to be addressed in the development of the Guidance, Navigation and Control (GNC) system. This naturally leads to the research motivation and the research questions addressed in this dissertation. The introductory chapter closes with an outline of the thesis and its scope.

1.1 Applications

The applications of rendezvous and formation flying are diverse and span a range of technological and scientific fields. Rendezvous and formation flying are key technologies for missions requiring the coordinated operation of more than one spacecraft in proximity. The technological applications of rendezvous and formation flying include, amongst others [1]:

- Exchange of crew
- Refuelling and resupply
- Transfer of planetary samples
- Re-joining of a lander
- Repositioning of spacecraft
- Retrieval of spacecraft
- On-orbit servicing
- On-orbit construction
- Active Debris Removal
- Fractionated spacecraft

Scientific and operational applications of formation flying leverage the capability to create larger apertures, longer focal lengths and baselines for scientific instruments than would be possible in an individual spacecraft. Based on a survey in appendix F, technologies and scientific objectives for formation flying missions that are operational or have been proposed include:

- Synthetic Aperture Radar (SAR)
- SAR interferometry
- Gravity field recovery
- Coordinated observation, 3D mapping and triangulation
- Study of space plasmas, the magnetosphere, and the electrodynamics environment
- Planet finding
- Gravity wave detection

The examples above show that formation flying and rendezvous are an indispensable operational element for many mission applications, enabling mission architectures and performances that would otherwise be impossible. These exciting applications drive the state of the art of hardware (improving and miniaturizing sensors and actuators) and the state of the art of control systems (including improved theories for relative motion and manoeuvring schemes).

1.2 State of the art

The state of the art of rendezvous and formation flying sees the development of formations of smaller satellites, and more sophisticated GNC algorithms allowing a greater degree of on-board autonomy. This section reviews the state of the art of missions featuring semi-automated, automated, and autonomous rendezvous and formation flying. Appendix F provides a table of all the missions that have been surveyed, including key characteristics of these missions. A quantitative analysis of the missions is performed in section 1.2.1 followed by a qualitative analysis in section 1.2.2. It has been observed that the development of new missions often leads to a corresponding development of new GNC algorithms, including new theories of relative motion and manoeuvre computation algorithms. These developments will be discussed further in section 1.2.3. More extensive reviews of small satellite formation flying missions have been performed in the past [14–16]. The review performed here aims to identify broad trends for formation flying, and to emphasize that most current and planned formation flying missions take place in low-Earth orbit (LEO). The work presented in this thesis intends to generalize the rendezvous and formation flying guidance algorithms to (highly) elliptical orbits, and to demonstrate that rendezvous and formation flying missions are possible in this non-standard orbital environment.

1.2.1 Quantitative analysis of rendezvous and formation flying missions

The space missions surveyed in appendix F can be analysed in terms of the size of the spacecraft, the orbital environment, mission objectives and the type of relative formation that is used. The size classes are grouped according to Table 1.1. Most large missions associated with crewed spaceflight (such as the Space Shuttle, Soyuz, H-II Transfer Vehicle (HTV) etc. [2]) have been excluded, apart from the Automated Transfer Vehicle (ATV) [17]. The ATV is included because of the importance of its heritage of GNC algorithms and trajectory design [18,19]. The ATV rendezvous trajectory forms an important inspiration for the work performed in this thesis.

Table 1.1: Satellite size classes [16].

Class	Size range / kg
Large	≥ 1000
Medium	500 – 1000
Small	< 500
Mini	100 – 500
Micro	10 – 100
Nano	1 – 10
Pico	0.1 – 1
Femto	< 0.1

The list of missions provided in appendix F is analysed. Current trends in the size classes of missions are identified. Trends in the evolution of mission size can help to identify which size classes have a particular interest in the development of rendezvous and formation flying technologies. The distribution of operational orbits is examined to establish whether rendezvous and formation flying missions are constrained to specific orbits. The field of application of the missions is studied to determine which applications benefit from formation flying and rendezvous, and to determine whether there are any trends in the evolution of application areas. Finally, the type of relative formation is identified to establish the type of relative trajectories that are most important in rendezvous and formation flying and that may help guide the development of relative trajectories for elliptical orbits in this thesis.

Figure 1.1 shows the evolution of the number of missions (including mission studies and cancelled missions) that perform semi-automated, automated, and autonomous rendezvous and/or formation flying. There is a clear increase in the rate at which new missions are being launched starting around 2009. This increase is especially noticeable in the nanosatellite category, which of course includes the numerous new CubeSat missions. This is a clear indication that rendezvous and formation flying are viewed as an enabling technology for realising more ambitious mission objectives. Note that the horizontal axis representing the planned launch date is not linear; the first entries advance one year at a time, and the last entries (from 2022 onwards) advance in steps of 3, 5 and 20 years.

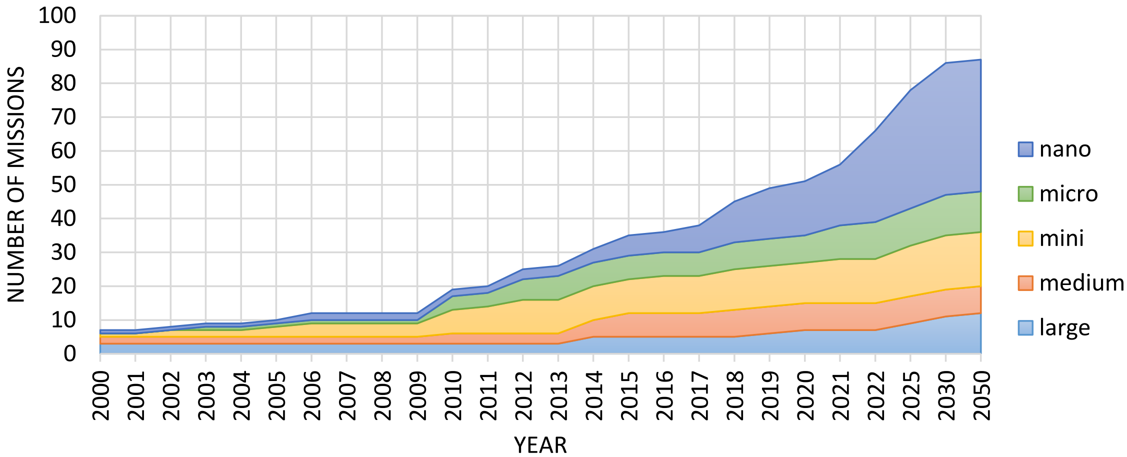

Figure 1.1: Missions (including studies) involving rendezvous and/or formation flying by launch date.

Figure 1.2 shows the trend towards smaller spacecraft even more clearly. The relative proportion of minisatellites and microsatellites shows an increase between 2005 and 2016, and nanosatellite missions are starting to dominate from 2016 onwards.

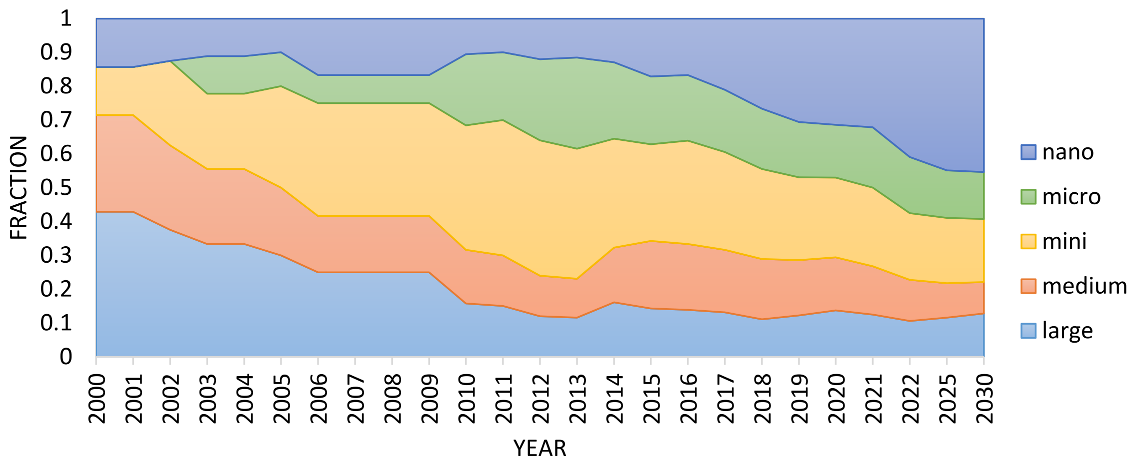

Figure 1.2: Evolution of rendezvous and/or formation flying spacecraft size as a fraction of total.

Figure 1.3 shows the formation flying and rendezvous missions by orbital environment. Figure 1.3 shows that over three quarters (77%) of all missions take place in LEO, with GEO, L2 and HEO taking fractions of around 5% each. LLO has only been used for a single mission, representing 1% of the total.

Most rendezvous and formation flying missions currently take place in LEO, with some exceptions that require a specific orbital environment (figure 1.3). LEO is cheap and easy to reach, with ride-sharing options available for smaller satellites [20–22]. Earth observation missions including SAR, SAR interferometry and gravity field mapping take place in LEO [11,23,24]. Current formation flying and rendezvous technology demonstrator missions also mostly take place in LEO [15].

Orbits around the Earth-Sun Lagrange point L2 are often considered for large formation flying telescopes. Advantages of this location are the quiet perturbation environment (both from a radio-spectrum and from a dynamics perspective), the absence of eclipses leading to a more uniform thermal environment, and the ease of communication [25]; the L2 point allows uninterrupted and unobstructed observations.

HEOs are often considered as a cheaper alternative than the Lagrange point orbits, even though such HEOs present some limitations [26]. HEO has the advantages that the launch and orbit transfer costs are low, Global Positioning System (GPS) measurements are available in the region around perigee, and the apogee region is a low-perturbation environment in which science experiments can be performed. The disadvantages with respect to the Lagrange point orbits are that communication is more difficult, eclipses can be present (especially during eclipse seasons), the thermal environment is not uniform over the orbit (as the formation moves closer and further away from Earth) and science operations must be suspended during the passage through perigee. HEOs are also well-suited for investigating the interaction of the solar wind with the magnetosphere, as studied by the Magnetospheric Multiscale Mission (MMS) [27] and Cluster [28–30] missions.

The geostationary orbit (GEO) is important for a wide variety of applications including telecommunications and Earth observation (e.g., weather satellites) because objects in GEO appear stationary with respect to the surface of Earth. This allows continuous communication and/or observation. Two important developments have taken place in GEO that are relevant to formation flying and rendezvous. The first development is the collocation of satellites in the same orbital slot to optimize the use of the limited amount of space available in GEO [9,31]. The second development is the first application of On-Orbit Servicing (specifically, life extension) of a geostationary telecommunications satellite by docking to it and providing orbit and attitude control services after the client satellite has depleted its propellant tanks [32].

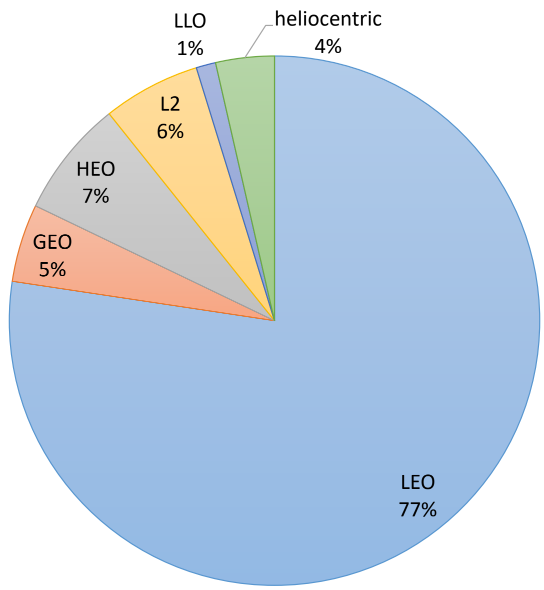

Figure 1.3: Rendezvous and formation flying missions by orbit type.

Finally, low-lunar orbit (LLO) and heliocentric orbits are important for achieving specific mission objectives, for example to investigate the lunar gravity field [33], to investigate the Sun [34] or to perform fundamental research [35].

Figure 1.4 shows a breakdown of the missions by mission objective. The great majority of the missions taking place in LEO are Earth observation, technology demonstration missions or a combination of the two. Over half of the missions (55%) are technology demonstrators, and CubeSat missions represent about 63% of such missions. The next big portion is formed by Earth observation missions, which include the afternoon train [23] and morning constellation [36], GRACE [37] and TanDEM-X [24]. Astronomy and astrophysics cover about 12% of the missions, including large telescopes such as Darwin [38], the Terrestrial Planet Finder (TPF) [39], the Large Interferometer For

1

Exoplanets (LIFE) [40], the InfraRed Space Interferometer (IRASSI) [41], the X-ray Evolving Universe Spectroscopy (XEUS) [42] and Simbol-X [43]. The rest of the mission objectives cover comparatively smaller fields.

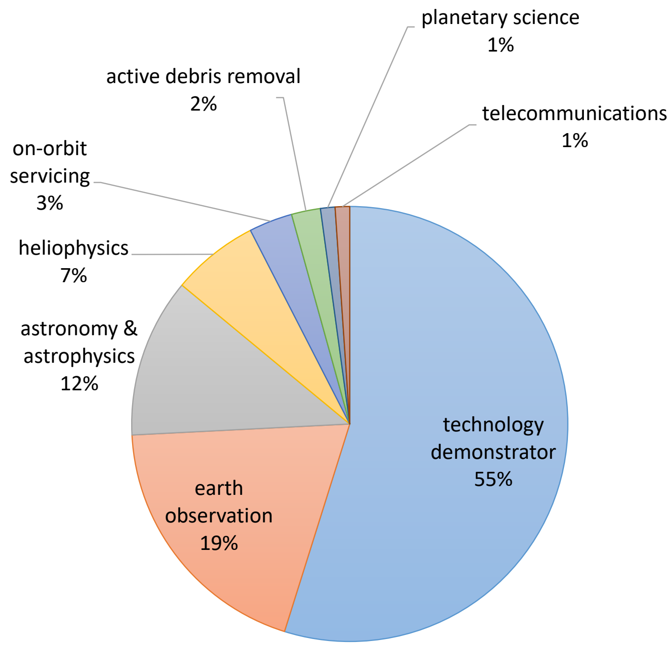

Figure 1.4: Rendezvous and formation flying missions by mission objective.

Figure 1.5 shows trends in the fields of application of rendezvous and formation flying missions. Technology demonstrator missions continue to comprise the major part of missions. This indicates that rendezvous and formation flying remains an active field of research. Formation flying appears to have become an established technology for Earth observation missions (in particular, gravity field recovery). Note also that in recent years On-Orbit Servicing and Active Debris Removal missions have been studied and executed.

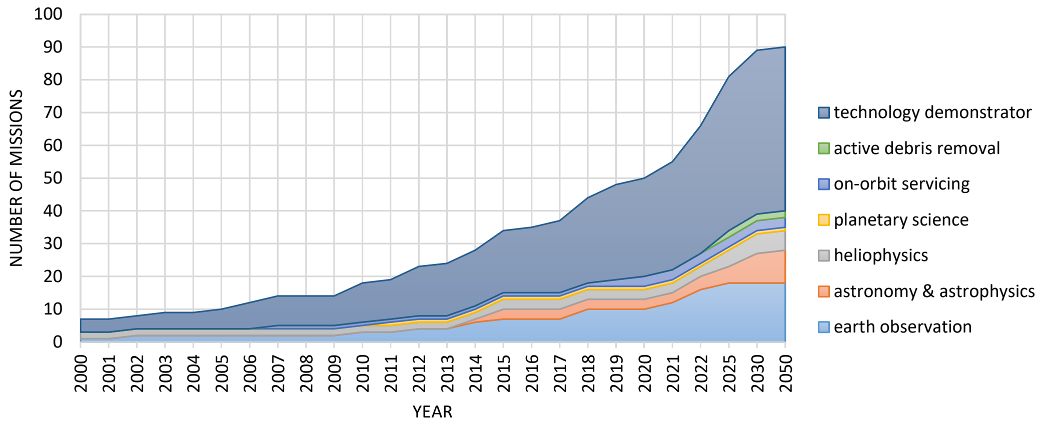

Figure 1.5: Trends in the mission objectives of rendezvous and formation flying missions.

Another important trend is the increase in the relative proportion of small satellite technology demonstration missions. To emphasize this point, figure 1.6 shows the number of small satellite technology demonstration missions that feature rendezvous and formation flying. In recent years, the number of rendezvous and formation flying technology demonstrator missions with CubeSats has increased dramatically. This illustrates the interest in developing this technology for CubeSats, and it appears that it is particularly useful for small satellites. The benefits of formation flying (in terms of increased baselines, focal length and/or aperture) can compensate for the small size of the platform.

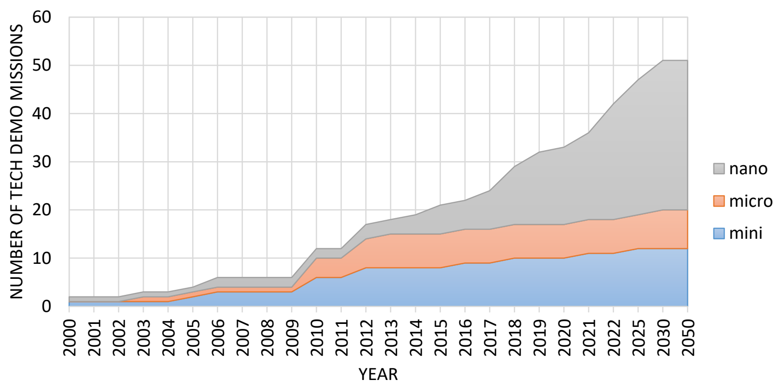

Figure 1.6: Evolution of the number of small satellite technology demonstrator missions.

Figure 1.7 breaks down the missions according to the type of relative motion. The design of the relative motion is driven by the mission needs; for example, safety, observation geometry and propellant cost to maintain the formation. Eccentricity / inclination vector separation [44], along-track separation [11] and rendezvous trajectories [1] each take up about 20% of the missions. Eccentricity / inclination vector separation [44] is a strategy where the chaser and the target orbits are separated by small differences in the eccentricity and inclination vectors, and that exhibits excellent passive trajectory safety because the chaser winds around the velocity vector of the target orbit (called the V-bar) but never intersects it (see also section 1.3).

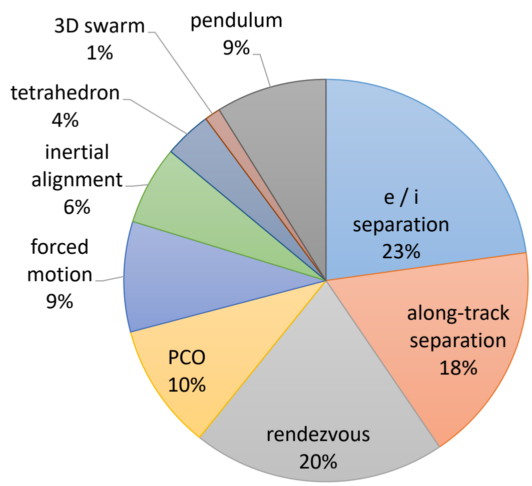

Figure 1.7: Rendezvous and formation flying missions by relative motion type.

Along-track separation means that the chaser is located on the target orbit separated by a difference in mean anomaly. This ensures that the chaser spacecraft flies over approximately the same area with a time offset with respect to the target, and this allows simultaneous or near-simultaneous observation of the same features on ground by both the chaser and the target spacecraft. The along-track separation strategy does not exhibit the passive safety features of the eccentricity / inclination vector separation. The rendezvous category is comprehensive, in the sense that a wide variety of different rendezvous trajectories has been proposed and tried out. Typically, the rendezvous sequence features elements of along-track drift, along-track hold points on V-bar and forced motion [18]. Radial hop manoeuvres and safe orbits based on eccentricity / inclination vector separation are occasionally used [45,46]. The projected circular orbit (PCO) [6] or halo [9] is related to the eccentricity / inclination vector separation, with the difference that the chaser winds around the radius vector of the target orbit (called the R-bar) instead of the V-bar. This improves the downward viewing geometry but removes the passive safety feature of the eccentricity / inclination vector separation.

The pendulum formation [47] uses an out-of-plane separation (that is, a small difference in inclination and/or right ascension of the ascending node) to create a baseline perpendicular to the reference orbital plane. This allows observing the same point on Earth from multiple viewing directions. The pendulum formation is usually combined with an along-track separation to avoid collisions. Forced motion profiles are used during the final stages of rendezvous [1], but they also form part of maintenance strategies for pointing a formation along a specific direction [48]. Forced motion trajectories require constant operation of the thrusters, which makes them costly to perform, certainly over long(er) time intervals. This means that such formations are usually small, are maintained for a brief period (such as during rendezvous) and/or in an orbital environment where the perturbations (and therefore the propellant cost) are low. Maintaining a formation in an inertial direction is a specific application of a forced motion trajectory that is used for astronomical observations. For example, the occulter spacecraft and the coronagraph spacecraft of the Proba-3 mission align with the Sun direction to observe the Solar corona [48]. This formation is maintained during the apogee arc only because the perturbations (here mainly gravity gradient and solar radiation pressure) are sufficiently low to be compensated effectively by means of cold-gas thrusters. The tetrahedron formation has been used by missions such as Cluster and MMS to perform three-dimensional observations of the magnetosphere and its interaction with the Solar wind.

1.2.2 Qualitative analysis of rendezvous and formation flying missions

In addition to this quantitative analysis, several qualitative observations can be made as well. Several institutions and organizations have been very successful in developing their capabilities for formation flying and rendezvous of CubeSats. Typically, they have used an incremental approach, developed more complex missions, and built on the lessons learned from previous missions. Very successful in CubeSat formation flying are the Deutsches Zentrum für Luft- und Raumfahrt (DLR) with BIROS/AVANTI [49], the Zentrum für Telematik with Netsat [50] and the Telematic International Mission / Telematics Earth Observation Mission (TIM/TOM) [51], the University of Toronto with CanX4/5 [52], the Aerospace Corporation with the Aerocube series [53], Hawkeye 360 with the Hawk CubeSats [54], Tyvak with NanoACE and the Cubesat Proximity Operations Demonstration (CPOD) [55], and Stanford University, which is involved as GNC specialist for many small missions [56–59]. Tyvak's NanoACE and CPOD missions are especially impressive, having managed to integrate a 6-degrees-of-freedom (6-DOF) propulsion system, sensors and docking system into a 3-unit CubeSat form factor.

CubeSat mission developers are most interested in developing formation flying capabilities to execute more ambitious missions. In this sense the "NewSpace" approach appears to drive a greater willingness to demonstrate the more challenging and riskier technologies required for formation flying, and CubeSats appear to be especially well suited for such technologies. Multiple CubeSats collaborate towards the same mission goal to provide high-quality data that are out of reach for a single CubeSat and that in the past could only be provided by larger platforms. In this sense, a formation of CubeSats may turn out to reduce the overall mission risk, because the failure of a single CubeSat in a formation may still allow the formation to continue operating even if at a degraded level of performance. Developments in the established space industry appear to move at a slower pace unless specific mission needs are addressed through autonomous or semi-autonomous formation flying and rendezvous:

- Formation flying satellite missions for gravity field research have reached a high level of maturity. The GRAIL formation flying mission has successfully mapped the gravity field of the Moon. Gravity field recovery typically requires a low level of accuracy of the control (but a high level of accuracy of the knowledge of the relative position) of the formation (the separation distance can vary by as much as 100 km in case of GRACE [11]), and the required manoeuvrability of the spacecraft is low: the spacecraft tend to have only one or a few orbit control thrusters without 6-DOF control capability, and manoeuvres occur infrequently (the time between manoeuvres can be 60 days or more for GRACE).
- Collocation of geostationary telecommunications satellites in the same orbital slot has been performed since the 1980s. In the past these missions would be operated from ground using ground tracking measurements. In recent years there is a drive towards autonomous orbit maintenance of collocated satellites.
- Active Debris Removal and On-Orbit Servicing are two areas that have received considerable institutional attention in recent years. As the amount of space debris continues to grow, space agencies are becoming increasingly interested in developing the capability to remove debris from orbit.
- The Mars Sample Return mission architecture calls for rendezvous operations to be conducted in Mars orbit to transfer surface samples from an ascent vehicle to the Earth return vehicle, which is envisaged to transfer the samples to Earth.

The development of more sophisticated theories of motion and more complex manoeuvring strategies often goes hand in hand with the development and execution of space missions [49,60–63]. This is especially true for the smaller satellite missions, including CubeSats. As mentioned earlier most of these missions are performed in LEO.

The development of increasing formation flying capabilities at universities has led to the creation of the commercial company HawkEye360 that specializes in the detection and localization of radio sources on the surface of Earth. To this aim the company has launched a constellation of sets of three CubeSats flying in formation that are able to triangulate the position of such radio sources [54].

Other institutes have experienced failures in their attempts to deploy formation flying missions. These failures have occurred because the CubeSats did not power up as expected, or because failures occurred after the satellites initially powered up successfully. Two such missions that failed at an early stage, namely CANYVAL-X

[64] and CANYVAL-C [65], were intended to perform Solar coronagraphy like Proba-3. The main difference between the mission concept for Proba-3 and that for the two CANYVAL missions is that the Proba-3 mission will take place in HEO and the CANYVAL missions were intended to take place in LEO.

In the early 2000s space agencies showed high interest in developing large missions that feature formation flying for astronomical purposes. The Darwin mission and the TPF mission were proposed to detect and study terrestrial exoplanets, and XEUS and Simbol-X were proposed to perform X-ray astronomy. Unfortunately, none of these studies have led to a successful mission, and all studies concluded that the required formation flying technology was not sufficiently mature at the time to perform these missions at an acceptable level of risk of failure. The formation flying capabilities that Proba-3 will demonstrate are often mentioned when discussing planet-finding missions such as Darwin [38], LIFE [40] and IRASSI [41]. The original Darwin mission study was concluded in 2007 and no further developments are taking place. The IRASSI mission has recently been proposed using a similar architecture as Darwin, citing the increased technological maturity of formation flying technologies as a main reason for renewed interest in this mission concept [40]. At the time that the X-ray observatory missions XEUS and Simbol-X were studied, it was thought that X-ray interferometry telescopes would require formation flying to create a sufficiently long baseline. Recent technological advances have made it possible to create X-ray interferometers with a baseline of only 1 to 2 meters [66]. Nevertheless, there are several smaller missions that plan to use formation flying as a key enabling technology. The Virtual Telescope for X-ray Observations (VTXO) [67] plans to use a lens spacecraft and a detector spacecraft to perform X-ray observations, and the Space Experiment of IR Interferometric Observation Satellites (SEIRIOS) [68] plans to use infrared interferometry for exoplanet detection and characterization.

Many missions use or are planned to use formation flying and rendezvous, with most of these taking place in LEO. In recent years there has been an increase in smaller CubeSat missions that use formation flying for a variety of purposes and that offer a cost-effective opportunity to perform high-quality observations. The larger telescope missions tend to prefer orbits around the Earth-Sun Lagrange point L2 because it is a low-perturbation orbital environment with little thermal variation, and it allows uninterrupted science operations. The initial proposal for Proba-3 pointed out that HEO is a cheap alternative to L2 orbits, and CubeSat missions could potentially make use of such HEOs to reach mission objectives similar to that of the larger space telescopes. The current work opens the way for CubeSat formations in HEOs.

1.2.3 Rendezvous and formation flying GNC

As stated in section 1.2.2, the development of new GNC algorithms is often driven by the development of missions that require formation flying and/or rendezvous.

1

Rendezvous and formation flying GNC is reviewed more in detail in sections 2.1 and 3.1, but this section points out some of the current trends and recent developments. Current trends can broadly be grouped into the following categories:

- Development of more sophisticated theories of relative motion
- Development of novel relative navigation algorithms
- Development of novel guidance and control strategies
    - Optimization of manoeuvre strategies including scheduling constraints
    - Renewed interest in impulsive manoeuvre strategies with few impulses

Development of relative motion theories

The development of more sophisticated theories of relative motion has been an active field of research for decades. Carter surveyed available relative motion theories in 1998 [69], including a reference to Stern, who solved the equations of relative motion in 1963 [70]. Alfriend evaluated state-of-the-art theories in 2005 [71], assessing the performance of the state transition matrix of Gim and Alfriend [72]. This state transition matrix is based on Brouwer's theory for orbits perturbed by the flattening of Earth (the so-called J_2 effect) [73,74], and it remains one of the most accurate linear theories. Reference [6] contains a description of many different types of the state transition matrix and includes a full description of the Gim-Alfriend theory. This theory provides a linearization of the transformation from the Cartesian state to relative osculating elements, a linearization of the transformation from osculating to mean orbital elements, and a linearization of the state transition matrix for mean orbital elements. Sullivan performed a review of available relative motion theories in 2017 [75], and notes that while the Gim-Alfriend theory is highly accurate, it is also one of the most computationally expensive. This review also reveals several interesting trends. Researchers at DLR [61,76–78] and at Stanford University [63] abandoned the Cartesian local-vertical, local horizontal (LVLH) state vector in favour of a state vector expressed in terms of relative orbital elements. Perturbations are more easily included and recent theories include both the flattening of Earth and differential drag [60,63]. The usage of relative orbital elements avoids the transformation from the Cartesian LVLH state to relative orbital elements and the linearization errors associated with this transformation. This transformation is much more sensitive to linearization errors than the transition matrix for relative orbital elements [77]. Modern theories often perform non-linear transformations from mean to osculating orbital elements, and from orbital elements to inertial states, retaining a linear model only for the relative mean orbital elements [75]. Of great relevance to missions like Proba-3 is the relative motion theory by Chihabi and Ulrich [79,80], which is valid for HEOs and includes gravity field harmonics up to degree 5, third-body perturbations and atmospheric drag.

The theoretical work presented in the first part of this thesis focuses more on the peculiarities of the geometry of relative motion and attempts to find an elementary representation of trajectories. In the future, this representation can be combined with perturbation models to yield more accurate results and still retain the simplicity of the representation. Furthermore, the Proba-3 mission performs station-keeping during apogee, and an impulsive transfer through perigee that takes around half an orbital period. This transfer is affected by errors in the manoeuvre application due to thruster errors. The combination of the short propagation times and thruster errors make the use of high-accuracy relative motion theories less relevant for Proba-3.

Development of relative navigation techniques

Novel navigation techniques are focused on relative GPS (rGPS) and optical navigation. GPS receivers and camera sensors are reliable, cheap, small and have a low mass. This makes them well-suited for cooperative formation flying and rendezvous, and especially for small, low-cost missions. rGPS has become the de-facto standard for formation flying [81]. rGPS is only available in orbits around Earth, and preferably with at least the perigee altitude below the GPS constellation. In the Proba-3 mission concept rGPS measurements availability is only expected in the region around perigee. Camera sensors are useful for formation flying and rendezvous missions, and they are especially relevant for small missions and for cases with uncooperative targets such as Active Debris Removal missions. Camera sensors can operate at a wide variety of distances, but they are limited by eclipse and other observation constraints (for example, no Earth in background). Novel relative navigation algorithms rely on sophisticated theories of relative motion to overcome constraints on observability such as eclipse [61,78]. To resolve the full state these theories rely on combining camera sensor measurements with known manoeuvre sizes [82,83], on known camera offsets with respect to the centre of mass of the satellite [84], or on precise modelling of the dynamics and the (nonlinear) observation geometry [85]. Formations that include more than two spacecraft can exploit simultaneous observations of multiple satellites to determine the geometry of the formation [86–88].

Development of manoeuvring strategies

Interesting recent developments in the field of manoeuvring strategies focus on optimization of manoeuvres, considering scheduling constraints and time-varying cost functions. Roscoe *et al.* [89] divide the trajectory in a large set of intervals and uses a quadratic cost function in a solution that resembles a multiple-burn linear quadratic regulator (LQR). This can be compared to the analytical minimum-square norm solution for continuous thrust by Sengupta and Vadali [90] and Cho and Park [91,92]. Roscoe then proceeds to select the intervals where the manoeuvres that have the largest magnitude occur, and further optimizes the manoeuvre locations using primer vector theory [93–100]. Anderson and Schaub [101] use an N-impulse approach that controls five out of six relative orbital elements. The manoeuvre locations are fixed and the MATLAB built-in optimizer fmincon is used to find the optimum solution. Gaias, d'Amico and Ardaens [102] and Gaias and d'Amico [103] describe optimal manoeuvring strategies that feature a manoeuvre planner that can take into account constraints on observability, thruster configuration and attitude, passive safety and others. Notably, these guidance and control strategies use a combination of a high-fidelity model for long-term trajectory planning and lower-fidelity models for short-term manoeuvre planning. The high-fidelity model is used to define free-drift trajectory segments, and the lower-fidelity model determines the manoeuvres required to transfer from one trajectory segment to the next. This ensures that the lower-fidelity model is only used for short propagation times during which perturbations have a shorter amount of time to act. Koenig and d'Amico [104] build on the idea of including constraints by allowing the cost function to vary over time, but take a completely different approach to the trajectory optimization based on reachable set theory. Reachable set theory was developed in the late 1960s [105–108] and applied to impulsive optimal control, but apparently not used afterwards until the publication of [104] and [109]. Although on-board optimization of manoeuvres is possible, it tends to be computationally costly and generally requires iterative methods, such that convergence needs to be addressed. For example, Koenig and d'Amico [104] state that their algorithm provides valid solutions for each iteration. On-board applications usually rely on more conservative, less sophisticated guidance schemes, see for example [55]. Roscoe [55] uses simple manoeuvres and trajectory elements to build up the overall concept of operations for CPOD. The work performed in this dissertation is more in line with this type of approach, where robust, simple algorithms are used to compute the manoeuvres on board. References [110,111,52] describe the on-board algorithms for the CanX-4/5 mission, including flight results. The algorithms are simple and robust and feature a small number of manoeuvres. More generally there is an interest in finding simple closed-form expressions for lower bounds on the ΔV required and in finding manoeuvring solutions with a low number of impulses (two, three or four) [103,112,113]. The current theoretical work fits in well with these approaches, and the practical work is compatible with the observed need for simple and robust manoeuvring strategies for on-board usage in flight software.

1.3 Relative motion around circular orbits

Relative motion around objects in circular orbits can most easily be understood in terms of relative orbital elements [114]. The relative orbital elements correspond to eigenmodes of the linearized dynamics matrix and their associated eigenvectors. Figure 1.8 graphically shows the natural motions associated with the modes of the relative motion. It identifies the semi-major axis / mean longitude mode, the eccentricity vector mode, and the inclination vector mode. Initial conditions for each mode are indicated by black circles. Appendix A.4 provides a detailed description of the initial conditions shown in the figure.

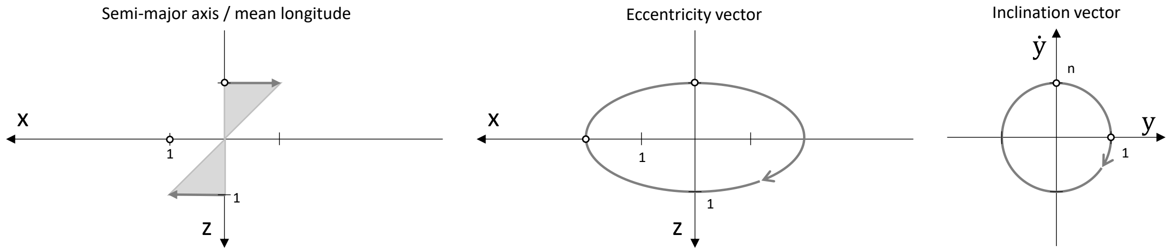

Figure 1.8: In-plane and out-of-plane natural dynamics modes.

The semi-major axis / mean longitude modes cause along-track drift if the relative semi-major axis is non-zero, and an along-track displacement if the relative mean longitude is non-zero. The eccentricity vector modes cause a 2 x 1 elliptical motion in the plane of the reference orbit. There are two eccentricity vector modes separated 90° in phase angle. The two modes correspond to two linearly independent solutions that are indicated in the figure. One solution starts at a position on the positive x-axis with a velocity in the negative z-direction, and the other starts at the negative z-axis with a velocity in the negative x-direction. The two linearly independent solutions corresponding to the inclination vector modes cause an out-of-plane oscillation. The first solution starts with a positive non-zero position and zero velocity and the second solution starts with zero position and non-zero velocity.

All relative motion solutions can be composed from these solutions by scaling and summing. One particularly useful set of solutions combines the eccentricity and the inclination vector modes. Simultaneous excitation of the eccentricity and inclination vector modes leads to the projected circular orbit and to the eccentricity / inclination separation.

Figure 1.9 shows the projected circular orbit. A drift-free projected circular orbit trajectory is shown in bold, and a trajectory with a relative semi-major axis of 1 m is shown in a dashed line. An inspection of the projection on the xy-plane shows that the projection onto this plane is a circle. An observer directly below the formation would see the chaser circling around the target. The projection onto the xz-plane shows the 2 x 1 ellipse around the origin that is typical for a small difference in the eccentricity vector. Finally, the projection onto the yz-plane shows that the chaser trajectory passes through the origin, and the orbital plane crossings (y-coordinate equal to zero) occur when the z-coordinate is equal to zero. Small differences in the semi-major axis (which may for example be caused by orbit insertion errors) can cause the centre of the relative trajectory to drift away from the origin. This can cause the intersection points to move arbitrarily close to the origin, leading to collision. As a result, the projected circular orbit is not passively safe.

1

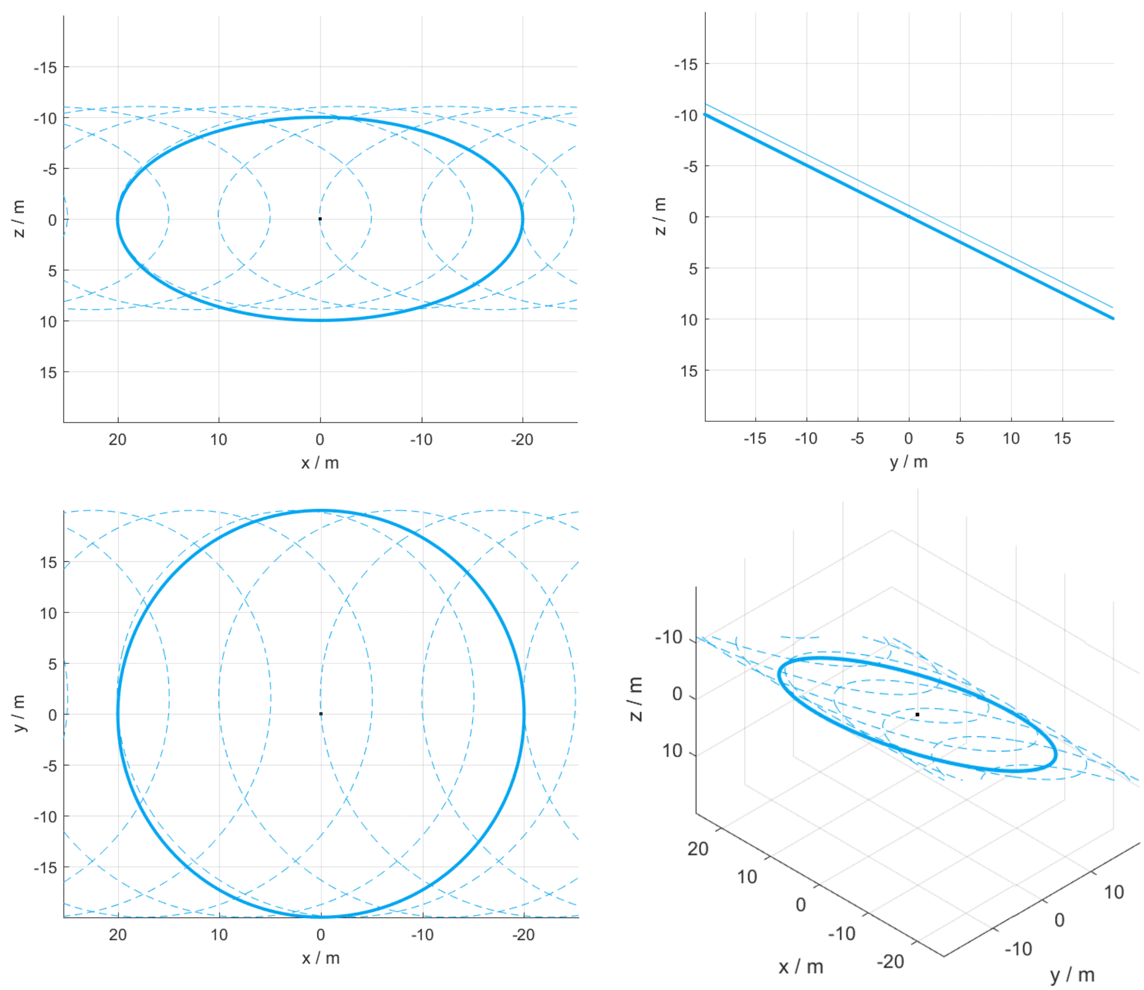

Figure 1.9: The projected circular orbit.

Figure 1.10 shows the eccentricity/inclination vector separation. A drift-free eccentricity/inclination vector separation trajectory is shown in bold, and a trajectory with a relative semi-major axis of 1 m is shown in a dashed line. The amplitude of the out-of-plane oscillation is half as large as that of the projected circular orbit. The projection onto the xz-plane again shows the 2 x 1 ellipse around the origin. The chaser passes through the origin in the projection onto the xy-plane. An observer directly below the formation would see the chaser pass directly in front or behind the target. The projection onto the yz-plane shows a circular trajectory around the origin. The crossings of the orbital plane (the xz-plane) occur when the chaser has the maximum vertical separation distance, and the crossings with the horizontal plane (the xy-plane) occur when the chaser has the maximum out-of-plane distance. This means that the trajectory can never cross the origin, even if along-track drift due to a small difference in semi-major axis is present.

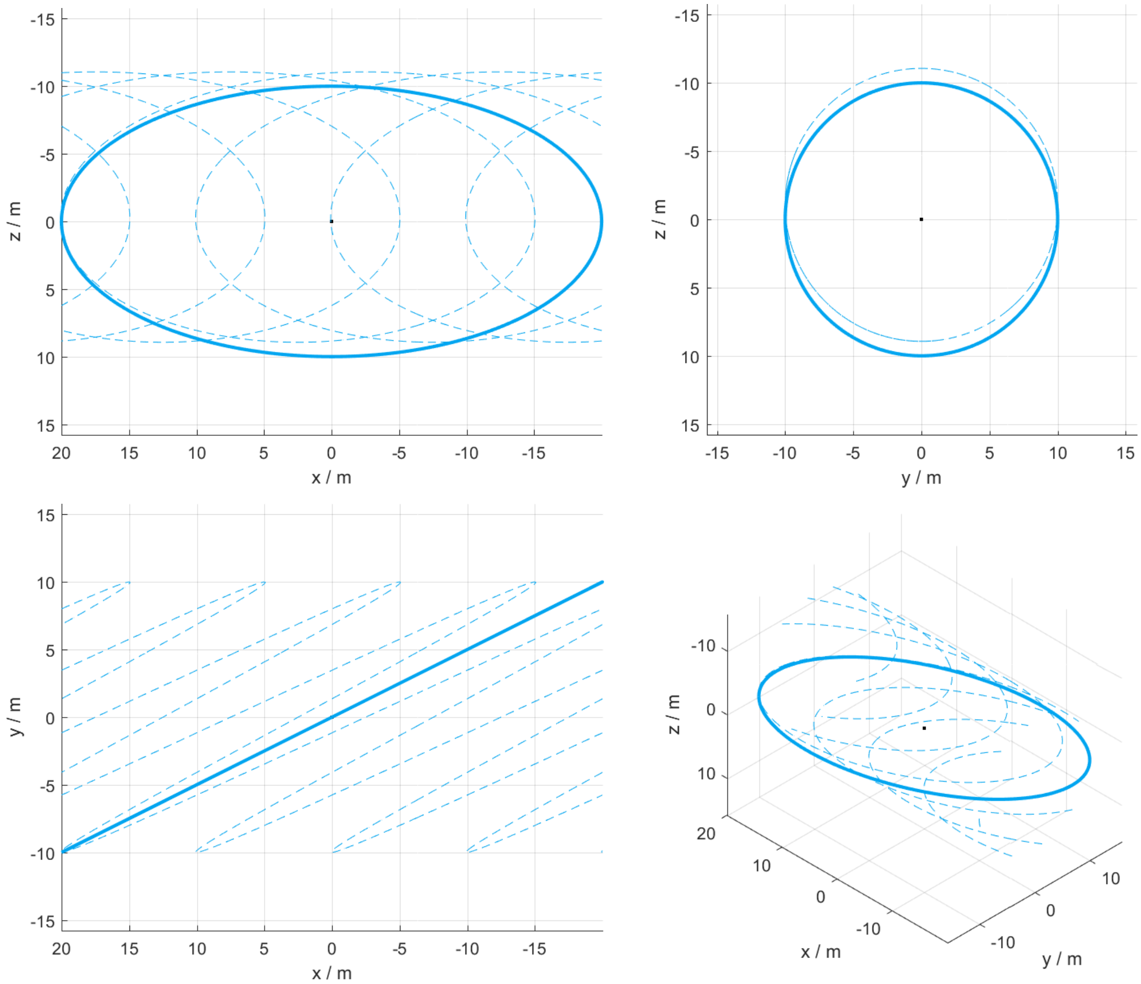

Figure 1.10: Eccentricity/inclination vector separation.

The previous paragraphs dealt with natural motions, without any impulsive manoeuvres. Figure 1.11 shows the effects of a tangential and a radial impulsive manoeuvre performed at the origin. (The out-of-plane motion can be controlled independently of the in-plane motion, for example by performing a manoeuvre at the orbit plane crossing to stop the out-of-plane motion.) The axes of the figure are scaled to unit distance, and the ΔV's contain the orbital rate n as a common factor. Tangential manoeuvres excite the semi-major axis mode and the eccentricity vector mode. A tangential manoeuvre with a magnitude of $n/4$ leads to an along-track displacement of $6\pi/4$ (scaled by the unit of distance) after completing one orbital revolution. The mean longitude mode is affected indirectly through the coupling factor between the relative semi-major axis and the relative mean longitude, and this coupling leads to along-track drift. Radial manoeuvres excite the mean longitude mode and the eccentricity vector mode, while the relative semi-major axis remains unchanged, and this ensures that the trajectory remains drift-free. A radial manoeuvre with a magnitude of n leads to an along-track displacement of 4. The relative motion

1

associated with small impulses is described by Gauss' variational equations [44,115,116].

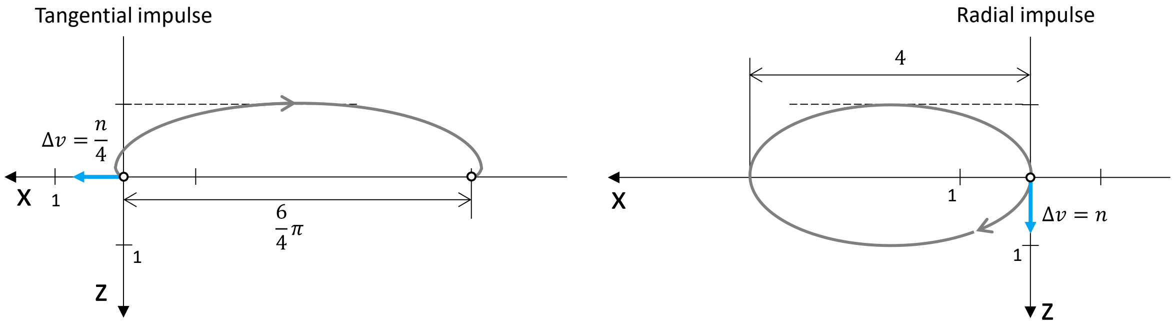

Figure 1.11: The effects of a tangential impulse and a radial impulse.

Figure 1.12 shows two distinct manoeuvre concepts that are often used in circular orbit rendezvous. The left-hand side shows the Hohmann transfer, a manoeuvre that is used to change the altitude between two circular orbits. The right-hand side shows a radial hop transfer, a manoeuvre that is used to modify the along-track separation without changing the relative semi-major axis.

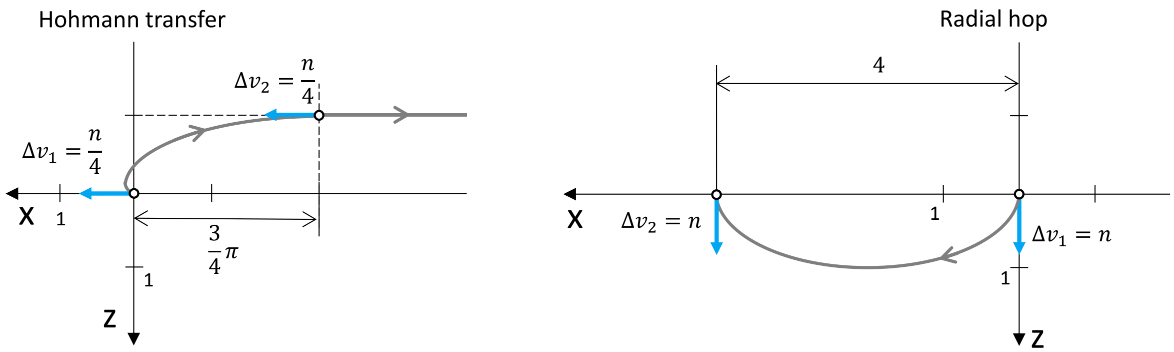

Figure 1.12: Typical rendezvous manoeuvres.

Both manoeuvres are used in the rendezvous strategy of ATV, which uses a Hohmann transfer from a phasing orbit to a point on V-bar behind the target, followed by a radial hop to a terminal approach point close to the International Space Station.

Appendix A provides a more detailed review of relative motion dynamics, including a derivation of the variational equations and their solution. The objective of this thesis is to leverage the understanding of the relatively straightforward relative dynamics around circular orbits to develop an equal understanding of the more complicated relative dynamics around spacecraft in elliptical orbits.

1.4 Proba-3

Proba-3 is a technology demonstrator mission developed within the General Support Technology Program of the European Space Agency (ESA). The primary mission objective is to demonstrate the precise formation flying technologies that are required for space science. This includes the demonstration of formation maintenance, formation breaking and formation re-acquisition, precise station-keeping along a fixed direction, and the demonstration of formation flying manoeuvres such as resizing, retargeting and combined manoeuvres. Proba-3 will also demonstrate high-accuracy formation flying sensors in orbit. The secondary mission objective is to perform coronagraphy as a distributed coronagraph system.

Proba-3 consists of two three-axis stabilized spacecraft: the Coronagraph Spacecraft (CSC) and the Occulter Spacecraft (OSC). The spacecraft will perform close formation flying in HEO. Figure 1.13 shows the CSC and the OSC flying in formation.

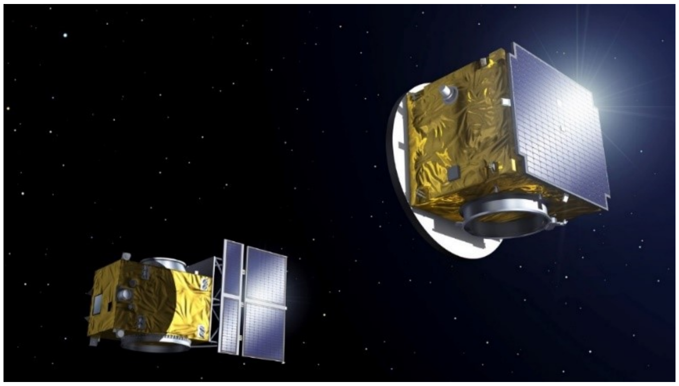

Figure 1.13: An artist's impression of the Proba-3 mission. The CSC is on the left and the OSC is on the right ©ESA [117].

Phase A of Proba-3 started in October 2006. As of 2022, Airbus Defence and Space has manufactured the Proba-3 platforms, including the propulsion system, harness, and thermal control system. At the time of writing the platforms are at the QinetiQ facility in Kruibeke, where the avionics and electronics will be integrated [118]. The launch of Proba-3 is planned for 2024. In the words of Agnes Mestreau-Garreau (Proba-3 project manager, ESA):

'Achieving precise formation flying will open up a whole new era. [...] For science and Earth observation, larger apertures, longer focal lengths, and baselines far beyond what can be achieved with a single spacecraft can be met with precision formation flying. In-orbit servicing and deorbiting becomes feasible, as does the automated rendezvous and docking needed for the ambitious Mars Sample Return mission, retrieving a sample Martian regolith (dust) to bring back to Earth. [...] Proba 3 will provide the technology required for missions several times more expensive and that would otherwise be unaffordable [119].'

1.5 Research motivation and research questions

The first automated rendezvous took place on October 30th, 1967, when Cosmos 186 performed a rendezvous and docked to Cosmos 188 [120]. Since then, many automated rendezvous and formation flying missions have been performed, and most of these have taken place in LEO. Missions taking place in elliptical orbits have used ground-based computation of manoeuvre commands and have not attempted to study relative trajectories in elliptical orbits as a generalization of relative trajectories in circular orbits [27–29]. Automated (or even autonomous) formation flying and rendezvous in elliptical orbits offer new possibilities for missions. Elliptical orbits can be a deliberate design choice for a formation flying or rendezvous mission, leveraging the quiet orbital environment of the apogee region to form a virtual structure telescope [26], sampling different regions of a planetary magnetic field [27–29], or potentially lowering the overall mission ΔV by performing rendezvous in an elliptical parking orbit [121]. Elliptical orbits can also be a contingency option, for example for the Mars Sample Return mission rendezvous. Rendezvous may need to take place in an elliptical orbit if the ascent vehicle does not successfully place the sample canister into the desired circular orbit [122]. A recent study has shown that upper stages remain in GTO as space debris [123,124] unless measures are taken to ensure more rapid re-entry. Rendezvous techniques for performing Active Debris Removal in GTO could be a welcome addition to the options available for debris mitigation.

The development of rendezvous and formation flying technologies for elliptical orbits can therefore be seen as both a method of risk mitigation (considering elliptical orbits as a non-nominal situation) or as an opportunity for performing new types of missions (exploiting the characteristics of elliptical orbits to enable new types of missions and new research). Rendezvous and formation flying in elliptical orbits are not necessarily more difficult than rendezvous and formation flying in circular orbits, but do present unique challenges. The linearized relative dynamics equations are more complicated, and it is not immediately obvious how the lessons learned in circular orbit rendezvous and formation flying can be applied to elliptical orbits. These issues need to be addressed in the development of new GNC algorithms and in mission design. The objective of this thesis is to enable rendezvous and formation flying in elliptical orbits by leveraging as much as possible the insights obtained from circular orbit rendezvous.

The Proba-3 mission is planned to perform formation flying in HEO, and a full understanding of the relative dynamics is crucial for the development of the on-board control system. The first step in this development process is to perform mission analysis of the formation flying aspects of this mission. The formation flying mission analysis provides strategies for the different mission phases, defines operational timelines, and characterizes the ΔV required for all operations. The theory developed in the first two chapters is applied to the Proba-3 mission, but is more broadly applicable, for example to Active Debris Removal and to constellation servicing. The following research questions are formulated to address the issues raised above.

1 – Can Hohmann transfers, drifting orbits and safe orbits be generalized to transfers between elliptical orbits?

In the linearized setting the Hohmann transfer to change altitude is optimal in the sense that it requires minimum ΔV. The Hohmann transfer consists of two impulsive manoeuvres of equal magnitude spaced half an orbital period apart. Another characteristic of the Hohmann transfer is that both impulsive ΔV's are parallel to the velocity vector of the reference orbit. This leads to two beneficial attributes. Transfers from a drifting orbit above or below the reference orbit to the reference orbit only have a single intersection point with the reference orbit. A transfer that occurs at a large distance away from the target can keep a camera sensor pointing in the direction of the velocity vector of the reference orbit while the manoeuvres are performed if the manoeuvring thrusters are located on the opposite face of the chaser spacecraft with respect to the camera sensor, and this direction will roughly correspond to the direction to the target spacecraft.

Co-elliptic drift orbits are orbits that cause along-track drift with respect to the target spacecraft, but whose relative altitude with respect to the target does not change. In circular orbits this corresponds to a difference in orbital radius, and the chaser spacecraft moves in straight-line trajectories with respect to the target. Another popular family of trajectories combines the in-plane oscillation associated with the relative eccentricity vector with the out-of-plane oscillation associated with the relative inclination vector [44,125]. On one extreme is the projected circular orbit (also referred to as halo orbit) in which the chaser appears to orbit the target when viewed from directly below the formation. This occurs when the relative eccentricity vector and the relative inclination vector are parallel. On the other extreme is the pure eccentricity / inclination vector separation, in which the chaser appears to orbit the target when viewed along the orbital velocity vector of the target. This occurs when the relative eccentricity vector and the relative inclination vector are perpendicular. Other formations that are occasionally used are the cartwheel formation, combining a small difference in the eccentricity vector with an arbitrary along-track separation, and the pendulum formation, combining a small difference in the inclination vector with an arbitrary non-zero along-track separation.

Chapter 2 generalizes the Hohmann transfer, the co-elliptic drift orbit, and the safe orbit to eccentric orbit rendezvous. The desirable characteristics of the manoeuvre and the trajectory types carry over to elliptical orbits. To illustrate how the benefits of tangential impulses translate to eccentric orbits, figure 1.14 shows a general transfer between two eccentric orbits that has impulses tangential to the departure and the

1

arrival orbits. The figure shows that the transfer orbit is tangent to the departure orbit at the departure point, and tangent to the arrival orbit at the arrival point. This means that the transfer orbit has a single point in common with the departure orbit and a single point in common with the arrival orbit, and this characteristic is beneficial to the safety of the transfer.

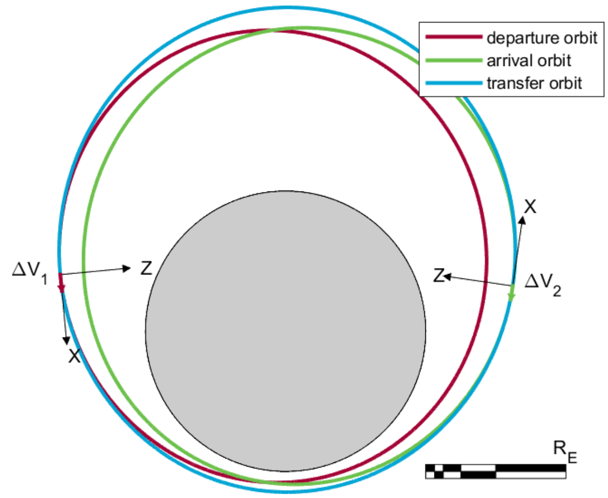

Figure 1.14: General orbit transfer with tangential impulses.

2 – Can radial hop manoeuvres and V-bar hold points be generalized to transfers between elliptical orbits?

A radial hop transfer is another example of a simple bi-impulsive manoeuvre. This manoeuvre consists of two radial impulses spaced half an orbital period apart, and it changes the along-track distance of the chaser with respect to the target while leaving the relative semi-major axis unaltered. A major advantage of this manoeuvre therefore lies in the fact that if the second impulse is not executed, the chaser returns to its original position one full revolution later.

Hold points on V-bar are stationary points that provide an along-track separation between the chaser and the target, and that (at least in theory) require no ΔV to maintain. These points are often used as station-keeping points for rendezvous, or as nominal position for formation-flying missions.

Chapter 3 generalizes the radial hop transfer in two different ways. A non-drifting transfer is described between two (Cartesian) points defined in the LVLH-frame and another between two states defined in terms of relative orbital elements. Hold points on V-bar are generalized to relative trajectories that are defined by a difference in mean anomaly, argument of perigee, or a combination of the two.

3 – How can the nominal operations be designed for the Proba-3 formation flying in a highly eccentric orbit?

The nominal operations for Proba-3 consist of the operations to be performed during each orbit, and the deployment of the formation at the start of the mission. The nominal scenario for one orbit covers activities at the apogee pass and the perigee pass. During the apogee pass, Proba-3 performs science operations and engineering experiments. During the perigee pass, the spacecraft are in free flight until the formation is re-acquired at the start of the next apogee pass. The Proba-3 spacecraft are equipped with several sensor systems, each with different accuracies and fields of view. At the end of the perigee pass, the spacecraft must re-acquire the required relative geometry that ensures that the spacecraft are within the field of view of the relative sensors. A strategy for the typical, nominal operational orbit needs to be defined that allows to break formation at the end of the apogee arc, and to re-acquire the formation at the start of the next apogee arc.

Both the gravity gradient and the accelerations associated with the rotation of the LVLH-frame are higher around perigee than they are around apogee. Consequently, the dynamics of the formation are changing faster around perigee than around apogee. Both effects have an impact on the propulsion system requirements. In the Proba-3 mission, this issue is solved by including a high-thrust propulsion system on one spacecraft, and a low-thrust propulsion system on the other. The ΔV required for both propulsion systems needs to be determined.

As the formation spends a large amount of time in the region around perigee in free drift, the effect of Solar radiation pressure and drag on the relative trajectory in this region may be non-negligible. In the apogee region the relative motion is continuously controlled as the spacecraft form a virtual structure. During this time, the Solar radiation pressure perturbation must be compensated for using the low-thrust propulsion system.

Before the nominal operations can begin, the spacecraft are separated from the launch vehicle and commissioned individually. After the commissioning is complete, the spacecraft need to perform a sequence of manoeuvres to reduce the inter-satellite distance and enter the nominal orbit sequence. A strategy needs to be defined for this sequence of manoeuvres that considers the safety, duration and the ΔV required.

4 – How can the off-nominal operations be designed for the Proba-3 formation flying in a highly eccentric orbit?

In any realistic design for a space mission the possibility of failures must be considered. Formation flying missions present a greater challenge than missions featuring a single spacecraft, because of the additional elements required (sensors, actuators, inter-satellite link) and because the proximity operations carry the additional risk of collisions between the spacecraft that comprise the formation.

The Proba-3 mission needs to maintain an inertial formation in the region around apogee, and break and re-acquire formation in the region around perigee during every orbit. This means that every orbit, one or both spacecraft in the formation perform impulsive and forced motion manoeuvres, acquire the correct formation geometry such that measurements can be taken by relative sensors with different levels of accuracy and differently sized fields of view in complex sequences of operations. Although the nominal operations are designed in such a way as to minimize failures, it is mandatory to protect the formation against the impact of failures if one were to occur.

Strategies need to be defined to bring the formation into a safe state if a failure does occur. These strategies need to ensure that the relative trajectory remains collision-free for a given amount of time. During this time, relative measurements are not available and relative control of the formation is not possible.

In circular orbits trajectory protection is often obtained by ensuring that the relative trajectories are passively safe or by actively protecting the trajectory. Active trajectory protection involves monitoring the trajectory and triggering a collision avoidance manoeuvre (CAM) if the trajectory exits certain predefined bounds. Proba-3 envisages two different types of protection for off-nominal situations: entry into a safe orbit and a CAM. In chapter 2 the eccentricity / inclination vector separation strategy for passive trajectory protection is generalized to elliptical orbits. The entry into safe orbit and the medium-term stability of the safe orbit need to be analysed to ensure that the relative trajectory remains safe both during the transfer and during an extended stay in the safe orbit.

If a collision is imminent, then a CAM is performed that leads to an immediate departure and that ensures the two spacecraft do not return to proximity one orbit later. A strategy needs to be defined for the CAM and this strategy needs to be analysed to determine the safety and the associated ΔV cost[1].

1.6 Outline and scope

The focus of this thesis is on the design and development of manoeuvres and trajectories for formation flying in elliptical orbits, and to perform the mission analysis for the Proba-3 mission using these tools and techniques. The tools and techniques that are developed in this thesis are of course applicable beyond the Proba-3 mission,

[1] The algorithm for the collision avoidance manoeuvre presented in chapter 5 contains an error. The corrected algorithm is provided in appendix E, along with a discussion of the reason for the error to occur.

as they apply to more general rendezvous and formation flying missions. The algorithms developed in this thesis can be used to study rendezvous in the context of Active Debris Removal missions, the Mars sample return mission and on-orbit construction missions. Beyond the rendezvous and formation flying applications, the algorithms developed here can be utilized for general orbit control around an elliptical reference orbit. This means that the algorithms can be used for orbit control (for example for Molniya type orbits) or for calculating trajectory correction manoeuvres for interplanetary trajectories.

The thesis is organized as follows. Chapter 2 presents the linear cotangential transfer as a generalization of the Hohmann transfer and an analysis of safe orbits for elliptical orbits. The cotangential manoeuvre is useful for long- and medium-range rendezvous to alter the relative drift rate of the chaser spacecraft. The safe orbit can be used to provide passive safety to formations. Chapter 3 describes the non-drifting transfer as a generalization of the radial hop transfer (see section 1.3 for a description of these manoeuvres for circular orbits). Chapter 4 presents the mission analysis for the nominal operations of Proba-3, and chapter 5 presents the mission analysis for the non-nominal or contingency operations of Proba-3. Chapter 6 provides conclusions to the thesis, answering the research questions posed above, and revisiting the Proba-3 mission. The afterword in chapter 7 contains some observations on the mission design process, and a short overview of the status of the Proba-3 guidance algorithms. Appendices provide additional details of algorithms used in the trajectory analysis and a tabulated survey of formation flying and rendezvous missions.

Chapters 2 and 3 have been published earlier in the AIAA Journal of Guidance, Control and Dynamics, chapter 4 has been published in Acta Astronautica, and chapter 5 has been published in the International Journal of Space Science and Engineering. Minor editorial changes have been made to these articles to harmonize the style, and the spelling convention has been changed to British English.

2

Linear Cotangential Transfers and Safe Orbits for Elliptic Orbit Rendezvous[2]

This article presents the theory for linear cotangential transfers and safe orbits for elliptic orbit rendezvous. Expressions for the transfer angle and the required ΔV's are derived. Singularities in the algorithm can occur if the two orbits intersect. Alternative manoeuvres for such singular cases are developed. The linear cotangential transfer algorithm is compared to the non-linear cotangential transfer and the algorithm is found to be very similar. The development of the linear cotangential transfer leads to a new set of relative orbital elements that are well suited for defining safe trajectories. The characteristics of safe trajectories are discussed, and a linear safety checking algorithm is developed. Finally, the combination of the cotangential transfers and safe orbits is used to define safe rendezvous trajectories for elliptical orbit rendezvous.

2.1 Introduction

Rendezvous and formation flying mission studies in recent years have been characterized by a greater drive towards on-board autonomy, and a desire to extend rendezvous capabilities to non-cooperative targets such as space debris. There is also an increasing interest in performing rendezvous and formation flying in elliptic orbits.

---

[2] This chapter was previously published in AIAA Journal of Guidance, Control, and Dynamics, doi: 10.2514/1.G005152. The spelling was changed to British spelling. Minor typos have been corrected.

These developments would extend the range of possible rendezvous missions from controlled, circular orbits with a cooperative target to uncontrolled, eccentric orbits with an uncooperative target.

Safe rendezvous trajectories are of great importance to mid-range rendezvous scenarios that feature limited navigation capabilities, limited ground contact opportunities, a high drive for on-board autonomy or a combination of these three. The mid-range rendezvous phase starts when the chaser switches from absolute navigation to relative navigation based on a camera sensor. The linear relative navigation problem based on angles-only navigation during the long-range phase is not fully observable unless manoeuvres are performed [82] or individual features on the target can be distinguished [126]. To aid the angles-only navigation in achieving fast convergence, the relative trajectory of the chaser needs to include some variation in relative altitude with respect to the target. Some relative drift between the chaser and the target also improves performance of the navigation [127], as does the inclusion of the J_2 perturbation into the linear model [127] or the use of a non-linear approach [85,128]. The Gauss [129] or Laplace method and a differential correction algorithm [130] could be used to initialize the filter, but ground tracking data can also be used to initialize the relative navigation filter [85]. The accuracy that can be achieved by means of ground tracking is lower than the accuracy that can be achieved by means of relative camera sensors [131,132]. Passively safe, collision-free trajectories can facilitate the transition between ground-based tracking and relative navigation. Safe trajectories may also be required during the initial formation deployment and acquisition, or to return from non-nominal situations. For example, formation deployment based on eccentricity / inclination vector separation is proposed for the Proba-3 mission [133], a precision formation flying mission in HEO with eccentricity 0.81. In the case of Proba-3, the relative sensors are only available at a relatively close range, such that the formation deployment and acquisition need to be performed using manoeuvres uploaded by ground command. The trajectory needs to remain safe for a longer period, because no on-board autonomy is present during this phase, and ground commands are expected to be available only once per day.

In a circular reference orbit scenario the Hohmann transfer and eccentricity / inclination vector separation [44] are considered important building blocks for constructing a guidance profile or reference trajectory for the mid-range rendezvous. The linear Hohmann transfer in circular orbit rendezvous is a transfer manoeuvre to an orbit with a different altitude for which the first and the second ΔV are equal in magnitude and direction [134]. A recent article describes how the eccentricity / inclination separation was used to define the trajectories for an un-cooperative rendezvous [135]. Both elements can be generalized for use in eccentric orbits, but there is some freedom in the choice of parameters or conditions that are kept invariant when the eccentricity is non-zero. The cotangential transfer is a generalization of the

Hohmann transfer in circular orbit rendezvous. The condition that is kept invariant is the tangency at the initial and terminal points. The generalization of eccentricity / inclination vector separation leads to families of collision-free relative trajectories when the eccentricity is larger than zero.

The non-linear cotangential transfer algorithm was developed in the early 1960's [136], but recently a new derivation of the algorithm has been presented [137]. The cotangential transfer is a type of transfer that is extremely useful for safe impulsive rendezvous. The cotangential transfer is near-optimal for transfers between elliptical orbits [138]. The transfer orbit has only a single intersection point with the terminal orbit, which enhances the safety of the transfer. Finally, the direction of the ΔV is tangential to the reference orbital velocity vector, which means that the spacecraft attitude can remain stationary in the tangential or flight-path reference frame, pointing in the general direction of the target. The ΔV for the cotangential transfer exceeds the ΔV of the optimal transfer by only 1% if the eccentricity is less than 0.2 [139]. A more extensive comparison shows that the cotangential transfer performs well over a wide range of true anomalies, if the orbits do not intersect [140]. If the orbits do intersect, singularities appear in the algorithm [141]. An iterative algorithm for linear, cotangential transfers between J_2 perturbed relative orbits is presented in [142]. An analytical algorithm for the linear cotangential transfer has been concisely described in [143] in the context of the development of a linear rendezvous guidance system. Another description of linear cotangential transfers is provided in [144], but the solution for the transfer angle is not provided.

The problem of optimal formation reconfiguration has been addressed in several recent papers [103,112,113]. Gaias and D'Amico [103] provide manoeuvring schemes for circular orbits and identifies the cotangential transfer case that is currently studied as the tangent-tangent bi-impulsive manoeuvre with zero or non-zero difference in semi-major axis. If the relative semi-major axis is zero, the solution is identified as requiring numerical solution of the transfer angle, and if the relative semi-major axis is non-zero, the solution is identified as requiring numerical solution of both the location of the first manoeuvre and the transfer angle. Gaias and D'Amico [103] also provide lower bounds for the ΔV for formation reconfigurations in circular orbits. Chernick and D'Amico [112,113] extend the analysis of the lower bounds for the ΔV for formation reconfigurations in eccentric orbits and provide manoeuvring schemes based on reachable set theory. Lower bounds for the ΔV and a three-impulse manoeuvre scheme are provided by Chernick and D'Amico [112]. Gaias and D'Amico [103] and Chernick and D'Amico [112] point out that bi-impulsive manoeuvring schemes generally must be solved numerically, and cannot achieve the absolute ΔV minimum because they lack extra degrees of freedom to allow optimization of the ΔV. Closed-form expressions for bi-impulsive manoeuvres have been used in flight demonstrations in near circular orbits. These closed-form bi-impulsive manoeuvre solutions can only establish three desired ROE after execution [112]. In the relative motion problem the out-of-plane coordinate is decoupled from the in-plane motion and can be controlled separately. Chernick and D'Amico [112,113] provide a manoeuvring scheme for the out-of-plane motion.

Linear relative motion theories can be derived either by solving the linearized equations of relative motion [145], or by finding the matrices of partial derivatives of the orbital elements to the Cartesian state [146,147]. The equivalence of both approaches can be demonstrated [148]. For circular orbit rendezvous the equations that describe the relative motion are known as the Clohessy-Wiltshire or Hill-Clohessy-Wiltshire equations [149]. These equations can be recast in terms of relative orbital elements [114]. Relative motion theories that include perturbations can be obtained relatively easily from (semi-)analytical satellite theories. The state transition matrix is often generated for use in differential correction orbit determination schemes [146,150]. Gim and Alfriend derived a relative motion theory that includes J_2 from Brouwer's theory [72]. An overview of different state transition matrices is provided by Alfriend et al [151]. Recent work provides a number of methods for including J_2 and drag for short-term and long-term propagation [60,63,152,153]. Note that theories that include J_2 and drag apply to central bodies that possess an equatorial bulge and an atmosphere, such as Earth. The perturbation due to J_2 is of the order of J_2, times the mean orbital rate, times the propagation time, or $\mathcal{O}(10^{-3})$ for transfer durations of about half an orbit in LEO. Relative drag can have a major impact on the long-term evolution of relative trajectories, and it depends on multiple factors such as the ambient density, orbital velocity, and the ratio of the ballistic coefficients of the chaser and the target. In this article it is assumed that the ballistic coefficients of the chaser and the target are comparable in magnitude, and that relative drag is negligible. Perturbations are excluded in this analysis of guidance algorithms, because manoeuvres are expected to occur frequently during the rendezvous, and thrust errors can be as large as a few percent of the nominal ΔV [154]. Thrust errors can have out-of-plane components, and for this reason safe trajectories such as the eccentricity / inclination vector separation are designed to consider margins for these and other perturbations. Guidance algorithms based on unperturbed relative motion can still be used even if the perturbations are not negligible or the propagation time is long. In such cases guidance strategies that divide the guidance problem into long-term evolution and short-term manoeuvring can be applied in a scheme referred to as precompensation [112]. In this scheme the long-term evolution model (which includes J_2, drag and other perturbations) is used to plan a sequence of changes in the relative orbital elements. These changes in the relative orbital elements are realized by means of impulsive ΔV's that are planned for a short time interval of up to a few revolutions during which the effect of the perturbations is negligible, and the impulsive ΔV's are calculated using the unperturbed relative motion model.

This article presents a novel set of algorithms for cotangential transfer manoeuvres and trajectories that can be used for rendezvous problems in eccentric orbits. An important driver in the development of the algorithms presented in this article has been to try to link the theory of elliptic rendezvous to elementary treatments of circular orbit rendezvous, such that rendezvous in elliptic orbits can be seen as a straightforward extension of circular orbit rendezvous. Many elementary discussions are available for circular orbit rendezvous and most aspects of these treatments can directly be applied to elliptic orbits when suitable assumptions are made. In this paper the relative dynamics are described using linearized relative motion around an unperturbed, eccentric Keplerian orbit to ensure that the connection with manoeuvres developed for linearized relative motion around an unperturbed, circular Keplerian orbit (the Clohessy Wiltshire equations) is as clear as possible. A previous article detailed the development of an analytical algorithm for non-drifting transfers that can be compared to the radial hop trajectory in circular orbit rendezvous [155]. The present article discusses the cotangential transfer and eccentricity / inclination vector separation [44] (also referred to as the projected circular orbit [151]) as the basic building blocks of a rendezvous strategy for elliptic orbit rendezvous. These two concepts seem unrelated at first sight, but a deep connection exists between the two upon closer investigation. This connection is exploited to develop a set of related algorithms that taken together can be used to design a rendezvous strategy. The cotangential transfer manoeuvre presented in this article is a closed-form bi-impulsive in-plane transfer solution that can establish the desired relative semi-major axis, eccentricity, and argument of perigee. The solution presented in this paper provides the transfer angle if the location of the first manoeuvre is given and is valid for eccentric orbits. Intersecting initial and final trajectories can cause singularities in the linear cotangential manoeuvre computation algorithm, and the singularities occur at the intersection points. Seen in another way, the study of the singularities in the linear cotangential manoeuvre algorithm reveals a connection with trajectory safety features. Specifically, a linear trajectory crossing algorithm can be derived from the cotangential transfer algorithm [122]. The present article shows that the trajectory crossing algorithm can be used not only to reveal the singularities in the cotangential transfer, but also to establish short-term in-plane trajectory safety and to generalize the eccentricity / inclination vector separation to eccentric orbits. The development of the cotangential transfer algorithm leads to a new set of relative orbital elements (ROE) that can be used to define these families of relative trajectories that generalize the eccentricity / inclination vector separation. Appendix B in section 2.9 provides the relationship between the ROE defined in this paper and other sets of ROE [145,147].

This paper is the result of an investigation into the operational aspects of the cotangential transfer algorithm. Section 2.2 provides a brief description of the linearized motion model. Section 2.3 provides the full derivation and a comprehensive analysis of the linear cotangential transfer algorithm, to examine singularities in the algorithm and to develop manoeuvres for the singular case. Section 2.4 defines families of relative trajectories that generalize the eccentricity / inclination vector separation strategy based on relative orbital elements (ROE) that follow naturally from the derivation of the cotangential transfer and to examine the safety of these families of trajectories. Section 2.5 develops a rendezvous strategy based on the cotangential transfer and the eccentricity / inclination vector separation generalized to eccentric orbits. The novel contribution of this investigation is a set of algorithms for cotangential manoeuvre computation, safe orbit definition and rendezvous trajectory design that generalize circular orbit rendezvous design concepts and as such simplify the design of elliptic orbit rendezvous trajectories.

2.2 Linearized Relative Motion Model

The orbit of the target spacecraft is taken as the reference orbit. The reference orbit is assumed to be an unperturbed elliptical Keplerian orbit for the purpose of developing the manoeuvring scheme. Figure 2.1 shows the local vertical, local horizontal (LVLH) and the tangential or flightpath (TAN) reference frames. The Cartesian state vector is defined as $\mathbf{x} = [x \quad y \quad z \quad \dot{x} \quad \dot{y} \quad \dot{z}]^T$. A subscript is used to indicate whether the relative state is in the LVLH frame or in the TAN frame. Because the principal focus of this analysis is aimed at non-equatorial, eccentric orbits (far away from the singularities at e = 0 and i = 0), the familiar Keplerian orbital elements are used to define the vector of ROE as $\boldsymbol{\delta\alpha} = [\delta a \quad \delta e \quad \delta i \quad \delta\Omega \quad \delta\omega \quad \delta M]^{\mathrm{T}}$.

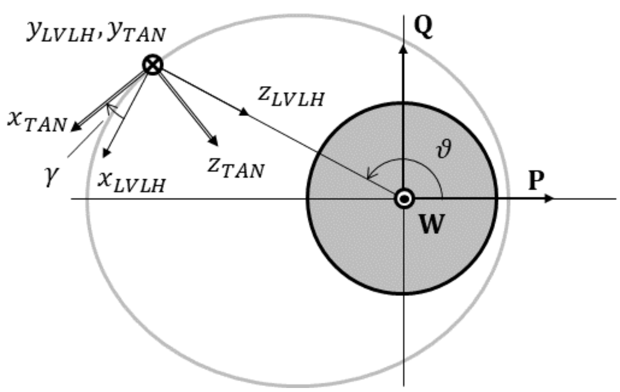

Figure 2.1: LVLH and TAN frames with respect to the perifocal frame.

The derivation of the state transition matrix in terms of the Keplerian elements is provided by Montenbruck and Gill [146] for relative motion in the inertial frame and by Schaub and Junkins [147] for relative motion in the LVLH frame and is not repeated here. The details of the transformation and the mapping matrices for the TAN frame coordinates are given in Appendix A in section 2.8. In a linearized setting the cotangential transfer is based on two impulses parallel to the velocity vector of the reference orbit. The general expression for a two-pulse manoeuvre is given by Gaias and D'Amico [103] and Chernick and D'Amico [112]:

$$\begin{aligned}\boldsymbol{\delta\alpha}^+(t_2) = \boldsymbol{\Phi}_\alpha(t_2,t_1)\{&\boldsymbol{\delta\alpha}^-(t_1) + \boldsymbol{\Gamma}_{LVLH}(t_1)\mathbf{R}_\gamma(t_1)\boldsymbol{\Delta}\mathbf{V}_{TAN.1}\}\\ &+ \boldsymbol{\Gamma}_{LVLH}(t_2)\mathbf{R}_\gamma(t_2)\boldsymbol{\Delta}\mathbf{V}_{TAN,2}\end{aligned} \tag{2.1}$$

The superscripts "+" and "-" indicate the state vector immediately before and immediately after the application of a ΔV. The matrix $\boldsymbol{\Gamma}$ is the control-input matrix or Gauss' variational equations in matrix form. The rotation matrix $\mathbf{R}_\gamma$ indicates a rotation around the y-axis by flight-path angle γ, see also Appendix A in section 2.8.

2.3 Linear Cotangential Transfer

2.3.1 Cotangential Transfer Problem Solution

The first step in developing the linear cotangential transfer algorithm is to write Eq. (2.1) explicitly in terms of the cotangential impulses and the ROE. Battin [156] provides expressions for Gauss' variational equations for the Keplerian elements and for components of the ΔV along the velocity vector and perpendicular to it. The perpendicular component of the ΔV is dropped and only the column of the matrix is used which relates the parallel component of the ΔV to changes in the ROE.

$$\begin{aligned}\begin{bmatrix}\delta a_2^+\\ \delta e_2^+\\ \delta\omega_2^+\\ \delta M_2^+\end{bmatrix} = \begin{bmatrix}1 & 0 & 0 & 0\\ 0 & 1 & 0 & 0\\ 0 & 0 & 1 & 0\\ -\frac{3}{2}a^{-1}n(t_2-t_1) & 0 & 0 & 1\end{bmatrix}&\left(\begin{bmatrix}\delta a_1^-\\ \delta e_2^-\\ \delta\omega_1^-\\ \delta M_1^-\end{bmatrix} + \frac{2}{eV_1}\begin{bmatrix}a\eta^{-2}e\theta_1^2\\ (\rho_1-\eta^2)\\ \sin\vartheta_1\\ -\rho_1^{-1}(\rho_1+e^2)\eta\sin\vartheta_1\end{bmatrix}\Delta V_{\parallel,1}\right)\\ +\frac{2}{eV_2}&\begin{bmatrix}a\eta^{-2}e\theta_2^2\\ (\rho_2-\eta^2)\\ \sin\vartheta_2\\ -\rho_2^{-1}(\rho_2+e^2)\eta\sin\vartheta_2\end{bmatrix}\Delta V_{\parallel,2}\end{aligned} \tag{2.2}$$

where η is equal to $\sqrt{1-e^2}$, $\rho = 1 + e\cos\vartheta$, $\theta = \sqrt{2\rho-\eta^2}$, and n is the orbital rate. The expression for the local orbital velocity appearing in the matrix in equation (2.2) can be derived from the vis-viva law [129]:

$$V = an\eta^{-1}\theta \tag{2.3}$$

The scaling functions ρ and θ, which govern the behaviour of the orbital radius and the orbital velocity, respectively, form part of many expressions that are derived in this article. The equations for the relative semi-major axis, eccentricity and argument of perigee are required for the solution of the transfer angle, while the equation for the relative mean anomaly is required to find the along-track motion during the transfer. The first three equations can be simplified to:

$$\begin{aligned}
a^{-1}\Delta a &= a^{-1}(\delta a_2^+ - \delta a_1^-) = \eta^{-2}\theta_1^2 \Delta V_{\parallel,1}^* + \eta^{-2}\theta_2^2 \Delta V_{\parallel,2}^* \\
e\Delta e &= e(\delta e_2^+ - \delta e_1^-) = (\rho_1 - \eta^2)\Delta V_{\parallel,1}^* + (\rho_2 - \eta^2)\Delta V_{\parallel,2}^* \\
e\Delta\omega &= e(\delta\omega_2^+ - \delta\omega_1^-) = \sin\vartheta_1\, \Delta V_{\parallel,1}^* + \sin\vartheta_2\, \Delta V_{\parallel,2}^*
\end{aligned} \tag{2.4}$$

2

The velocity impulses have been normalized according to $\Delta V^* = 2V^{-1}\Delta V$. The solution strategy is as follows. First, the transfer angle is found as a function of the initial true anomaly and the differences in relative semi-major axis, eccentricity, and argument of perigee. Second, the velocity impulses are found. Finally, the equation for the relative mean anomaly is used to determine the along-track distance after the manoeuvre. To solve Eq. (2.4) the system is rewritten as:

$$\begin{aligned}
&a^{-1}\Delta a - 2\eta^{-2}e\Delta e = \Delta V_{/\!/,1}^* + \Delta V_{/\!/,2}^* \\
&e(a^{-1}\Delta a - 2\eta^{-2}e\Delta e) - \Delta e = -\cos\vartheta_1\, \Delta V_{/\!/,1}^* - \cos\vartheta_2\, \Delta V_{/\!/,2}^* \\
&e\Delta\omega = \sin\vartheta_1\, \Delta V_{/\!/,1}^* + \sin\vartheta_2\, \Delta V_{/\!/,2}^*
\end{aligned} \tag{2.5}$$

The left-hand sides of these equations are functions of the ROE only, and not of the true anomaly. This means that these elements are ROE in their own right. To define the new set, Eq. (2.5) is multiplied by the semi-latus rectum. The left-hand-side of the first of Eq. (2.5) can now be compared to the variation of the semi-latus rectum $\delta p = \eta^2\delta a - 2ae\delta e$ [147]. The new relative orbital elements replacing the relative semi-major axis, eccentricity, and argument of perigee (and their inverse relations) are defined as follows:

$$\begin{aligned}
&C_1 = \delta p = \eta^2\delta a - 2ae\delta e \quad && \delta a = \eta^{-4}\big((1+e^2)C_1 - 2eC_2\big) \\
&C_2 = e\delta p - p\delta e && \delta e = p^{-1}(eC_1 - C_2) \\
&C_3 = -ep(\delta\omega + \cos i\, \delta\Omega) && \delta\omega = -e^{-1}p^{-1}C_3
\end{aligned} \tag{2.6}$$

The term $\cos i\, \delta\Omega$ has been added to the definition of C_3 to decouple the in-plane and out-of-plane motion, see Appendix B in section 2.9. For in-plane transfers such as the cotangential transfer, there is no change in the right ascension of the ascending node Ω such that $\Delta C_3 = ep\Delta\omega$ for in-plane transfers.

Eq. (2.5) can be rewritten using angle sum identities for ϑ_2 to yield a set of equations in terms of the initial true anomaly, the transfer angle φ and the scaled velocity impulses. The transfer angle φ is the difference between the initial true anomaly and the final true anomaly.

$$\begin{aligned}
\Delta C_1 &= p\big(\Delta V_{\parallel,1}^* + \Delta V_{\parallel,2}^*\big) \\
\Delta C_2 &= p\big(-\cos\vartheta_1\, \Delta V_{\parallel,1}^* - \cos\vartheta_1 \cos\varphi\, \Delta V_{\parallel,2}^* - \sin\vartheta_1 \sin\varphi\, \Delta V_{\parallel,2}^*\big) \\
\Delta C_3 &= p\big(-\sin\vartheta_1\, \Delta V_{\parallel,1}^* - \sin\vartheta_1 \cos\varphi\, \Delta V_{\parallel,2}^* - \cos\vartheta_1 \sin\varphi\, \Delta V_{\parallel,2}^*\big)
\end{aligned} \tag{2.7}$$

After elementary manipulation of these equations the following result is obtained:

$$\begin{aligned} &\Delta C_1 + \cos\vartheta_1\,\Delta C_2 + \sin\vartheta_1\,\Delta C_3 = p\Delta V^*_{/\!/,2}(1-\cos\varphi) \\ &\sin\vartheta_1\,\Delta C_2 - \cos\vartheta_1\,\Delta C_3 = p\Delta V^*_{/\!/,2}\sin\varphi \end{aligned} \tag{2.8}$$

The left-hand sides of this equation are real-valued trigonometric polynomials of the initial true anomaly with the new ROE as coefficients. The polynomials are labelled P_1 and P_2. P_1 (i.e., a ΔP_1) depends on C_1, C_2 and C_3, while P_2 only depends on C_2 and C_3.

$$\begin{aligned} &P_1 = C_1 + C_2\cos\vartheta_1 + C_3\sin\vartheta_1 \\ &P_2 = C_2\sin\vartheta_1 - C_3\cos\vartheta_1 \end{aligned} \tag{2.9}$$

Eq. (2.8) now becomes:

$$\begin{aligned} &\Delta P_1 = p\Delta V^*_{/\!/,2}(1-\cos\varphi) \\ &\Delta P_2 = p\Delta V^*_{/\!/,2}\sin\varphi \end{aligned} \tag{2.10}$$

The solution for the transfer angle can be found by performing the Weierstrass substitution, and is given by:

$$\varphi = 2\tan^{-1}\left(\frac{\Delta P_1}{\Delta P_2}\right) \tag{2.11}$$

Care should be taken when ΔP_2 is equal to 0 as the argument of the arctangent function becomes infinitely large; in this case the transfer angle is equal to 180°. Next, the velocity impulses are determined. Squaring Eq. (2.10) and summing them leads to the following expression for the second velocity impulse (where it is noted that Eq. (2.10) is used twice to obtain the expression for ΔP_1 and simplify the result):

$$\Delta V^*_{/\!/,2} = \frac{1}{2}\frac{(\Delta P_1)^2 + (\Delta P_2)^2}{p\Delta P_1} \tag{2.12}$$

To find the simplest possible expressions for the ΔV's, note that the sum of the squares of polynomials P_1 and P_2 is equal to:

$$(\Delta P_1)^2 + (\Delta P_2)^2 = (\Delta C_s)^2 + 2\Delta C_1\Delta P_1 \tag{2.13}$$

To simplify expressions the parameter C_s is defined by:

$$(\Delta C_s)^2 = (\Delta C_2)^2 + (\Delta C_3)^2 - (\Delta C_1)^2 \tag{2.14}$$

This means that the second velocity impulse can also be written as:

$$\Delta V^*_{/\!/,2} = \frac{1}{p}\left\{\frac{1}{2}\frac{(\Delta C_s)^2}{\Delta P_1} + \Delta C_1\right\} \tag{2.15}$$

2

Using the first of Eq. (2.7) a simple expression for the normalized velocity impulses can be found:

$$\begin{aligned} \Delta V^*_{/\!/,1} &= -\frac{(\Delta C_s)^2}{2p\Delta P_1} \\ \Delta V^*_{/\!/,2} &= \frac{1}{p}\Delta C_1 - \Delta V^*_{/\!/,1} \end{aligned} \tag{2.16}$$

This completes the derivation of the cotangential transfer algorithm. In this derivation the ROE C_1, C_2, C_3 and C_s have been defined. The ROE C_1, C_2 and C_3 are alternatives to the semi-major axis, eccentricity, and argument of perigee. The constant C_s does not form part of this new set. The set of alternative elements is completed by defining element C4 based on the mean anomaly. Chernick and D'Amico [112] and Riggi and D'Amico [157] refer to this orbital element as the modified relative mean longitude. In the current treatment the modified relative mean longitude is scaled by $a \cdot \eta^{-1}$:

$$C_4 = a(\delta\omega + \cos i\,\delta\Omega + \eta^{-1}\delta M) \tag{2.17}$$

The C set of ROE is non-singular when the eccentricity goes to zero and can be seen as a generalization of the travelling ellipse formulation that is in use in circular orbit rendezvous, see Appendix B in section 2.9. Using this new element, the equation for the relative mean anomaly from Eq. (2.2) can be rewritten as follows:

$$\begin{aligned} \Delta C_4 = -\frac{3}{2}\eta^{-1}n(t_2 + kT)\delta a1 — \frac{3}{2}\eta^{-3}an(t_2 - t_1 + kT)\theta_1^2\Delta V^*_{\parallel,1} \\ - ae\sin\vartheta_1\,\rho_1^{-1}\Delta V^*_{\parallel,1} - ae\sin\vartheta_2\,\rho_2^{-1}\Delta V^*_{\parallel,2}, \hookleftarrow \quad k \in \mathbb{Z} \end{aligned} \tag{2.18}$$

Allowance has been made for a coasting arc in the initial orbit and a longer coasting time in the transfer orbit, where the coasting time in the transfer orbit can be extended by integer multiples of the orbital period. In principle it would be possible to solve this equation for the initial true anomaly. However, like Kepler's equation, this equation does not have a closed-form solution, and a numerical method would need to be used. In section 2.5 an alternative approach is used to ensure that the chaser arrives at the correct along-track distance.

The ΔV required for the linear cotangential manoeuvre can be compared to the ΔV lower bounds provided by Chernick and d'Amico [112]. Chernick and d'Amico [112] show that a lower bound for the ΔV can be established that is based on the ROE that requires the largest ΔV to change, and this ROE change is referred to as the dominant

ROE change. The lower bound for in-plane transfers is given by the largest of the ΔV's required to change the semi-major axis, the modified relative mean longitude and the eccentricity vector.

$$(na\eta)^{-1}\Delta V_{LB} = \max\left(\frac{a^{-1}\|\Delta\delta a\|}{2(1+e)}, \frac{\|\Delta\delta\lambda_e\|}{3(1+e)\Delta M}, \frac{\|\Delta\delta\mathbf{e}\|}{\sqrt{3e^4-7e^2+4}}\right) \tag{2.19}$$

In equation(2.19), $a\eta\delta\lambda_e = C_4$ and the relative eccentricity vector is given by [147]:

$$\delta\mathbf{e} = \begin{bmatrix}\delta q_1\\ \delta q_2\end{bmatrix} = \begin{bmatrix}\cos\omega & -e\sin\omega\\ \sin\omega & e\cos\omega\end{bmatrix}\begin{bmatrix}\delta e\\ \delta\omega\end{bmatrix} \tag{2.20}$$

The ΔV required for the linear cotangential manoeuvre can be solved for the special case of co-apsidal transfers to compare expressions for the case of dominant $\|\Delta\delta a\|$ and dominant $\|\Delta\delta\mathbf{e}\|$. The cotangential manoeuvre (like the Hohmann transfer in circular orbit rendezvous) is not designed for solving changes in the modified relative mean longitude, and the case of dominant $\|\Delta\delta\lambda_e\|$ is not considered for comparison here. The total ΔV for the general linear cotangential transfer is given by:

$$\Delta V_{tot} = \Delta V_{\parallel,1} + \Delta V_{\parallel,2} = \frac{1}{2}an\eta^{-1}\left\{\theta_1\left\|\frac{(\Delta C_s)^2}{2p\Delta P_1}\right\| + \theta_2\left\|\frac{1}{p}\Delta C_1 + \frac{(\Delta C_s)^2}{2p\Delta P_1}\right\|\right\} \tag{2.21}$$

If the change in the relative argument of perigee is equal to zero, and the transfer is started at apogee or at perigee, then the transfer angle is 180° and the ΔV can be rewritten in terms of changes in the relative semi-major axis and relative eccentricity.

$$\Delta V_{tot} = \begin{cases}\frac{1}{2}n\{\eta\Delta\delta a - ae\eta^{-1}\Delta\delta e\}, & \frac{-(1-e)\eta^2}{2-2e-\eta^2} < \frac{a\Delta\delta e}{\Delta\delta a} < \frac{(1+e)\eta^2}{2+2e-\eta^2}\\ \frac{1}{2}na\eta^{-1}\Delta\delta e, & \frac{a\Delta\delta e}{\Delta\delta a} \le \frac{-(1-e)\eta^2}{2-2e-\eta^2} \vee \frac{a\Delta\delta e}{\Delta\delta a} \ge \frac{(1+e)\eta^2}{2+2e-\eta^2}\end{cases} \tag{2.22}$$

The nature of the total ΔV changes depending on whether the initial and final orbit intersect or not. The limit cases can be derived from the control input matrix (explicitly given in equation (2.2)), determining the ratio of the change in semi-major axis and the change in eccentricity that can be achieved by means of a single impulse. Intersecting initial and final orbits are further discussed in section 2.3.3.

If the cotangential manoeuvre only changes the semi-major axis, then the total ΔV is related to the lower bound as:

$$\frac{\Delta V_{tot}}{\Delta V_{LB}} = \frac{\frac{1}{2} n\eta\Delta\delta a}{\frac{n\eta}{2(1+e)}\Delta\delta a} = 1 + e \tag{2.23}$$

Equation (2.23) shows that the ΔV is higher than the lower bound by a factor equal to the eccentricity. The lower bound is obtained by examining the effect of a single, tangential manoeuvre performed at perigee. Such a manoeuvre achieves the maximum change in semi-major axis, but it also changes the eccentricity. This is a strong indication that the ΔV lower bound for dominant $\|\Delta\delta a\|$ is unlikely to be achievable.

On the other hand, if the cotangential manoeuvre changes the eccentricity and the change in eccentricity is larger than the limits identified in (2.22), then the total ΔV is related to the lower bound as:

$$\frac{\Delta V_{tot}}{\Delta V_{LB}} = \frac{\frac{1}{2} na\eta^{-1}\Delta\delta e}{\frac{na\eta\Delta\delta e}{\sqrt{3e^4 - 7e^2 + 4}}} = \frac{1}{2}\eta^{-2}\sqrt{3e^4 - 7e^2 + 4} \tag{2.24}$$

Equation (2.24) shows that the total ΔV is less than 4.1% above the lower bound if the eccentricity of the reference orbit is smaller than 0.5, and less than 11.4% above the lower bound if the eccentricity of the reference orbit is smaller than 0.7.

2.3.2 Geometrical Representation of the Transfer

The cotangential transfer can be represented geometrically in terms of the C set of ROE and the normalized velocity impulses in a diagram. This diagram is a phase portrait of the scaled z-coordinate in the TAN frame and facilitates the identification of key points and relevant angles in the transfer problem. The geometrical representation provides a direct connection between the key ROE C_1, C_2 and C_3, and the behaviour of the z-coordinate in the tangential frame. It ensures that the phase angles of the transfer trajectory can be identified by inspection, and it allows for a straightforward identification of the singularities in the algorithm as crossing points with the reference trajectory. The tangency condition at the end of the trajectory can be verified in the diagram in Figure 2.2 as the transfer ends at zero altitude (z = 0) with zero vertical velocity (z' = 0). The diagram therefore captures all important geometrical features of coplanar elliptic trajectories with respect to a reference orbit.

First note that the z-coordinate in the TAN frame can be expressed as (see Appendix B in section 2.9):

$$\rho\theta z_{TAN} = -(C_1 + C_2\cos\vartheta + C_3\sin\vartheta) = -P_1 \tag{2.25}$$

The z-coordinate depends on the same polynomial P_1 that was identified in the solution of the cotangential transfer angle, equation (2.9). The z-coordinate is scaled by ρ and by θ as follows:

$$\hat{z}_{TAN} = \rho\theta z_{TAN} = \frac{V\eta^3}{nr} z_{TAN} \tag{2.26}$$

In other words, the scaling depends both on the local orbital velocity and on the local orbital radius. The rate of change of the scaled coordinate with respect to the true anomaly is given by:

$$\hat{z}'_{TAN} = \frac{d}{d\vartheta}\hat{z}_{TAN} = -\frac{d}{d\vartheta}P_1 = P_2 \tag{2.27}$$

The behaviour of the scaled z-coordinate is affected by tangential velocity impulses, and it has been shown in equation (2.25) that a simple relation exists between the scaled z-coordinate and the C set of ROE. The effect of the normalized tangential and radial velocity impulses on the C set of ROE is derived from Eq. (2.1) and (2.6) (see also Appendix B in section 2.9):

$$\frac{\partial \mathbf{C}}{\partial \mathbf{V}^*_{TAN}} = p \begin{bmatrix} 1 & e\sin\vartheta\,\rho^{-1} \\ -\cos\vartheta & \frac{1}{2}(1+e^2)\sin\vartheta\,\rho^{-1} \\ -\sin\vartheta & -\frac{1}{2}\{2e + (1+e^2)\cos\vartheta\}\rho^{-1} \\ -e\sin\vartheta\,\rho^{-1}\eta^{-2} & \eta^{-2} \end{bmatrix} \tag{2.28}$$

The effect of a normalized tangential velocity impulse on the elements C_1, C_2 and C_3 is expressed in terms of simple trigonometric functions. To complete the diagram, define the parameter C_m and the phase angle α as follows:

$$\begin{aligned} C_m &= \sqrt{(C_2)^2 + (C_3)^2} \\ \alpha &= \tan^{-1}(C_3, C_2) \end{aligned} \tag{2.29}$$

The geometry of the cotangential transfer can now be summarized in a diagram. Figure 2.2 shows the geometry of a generic cotangential transfer.

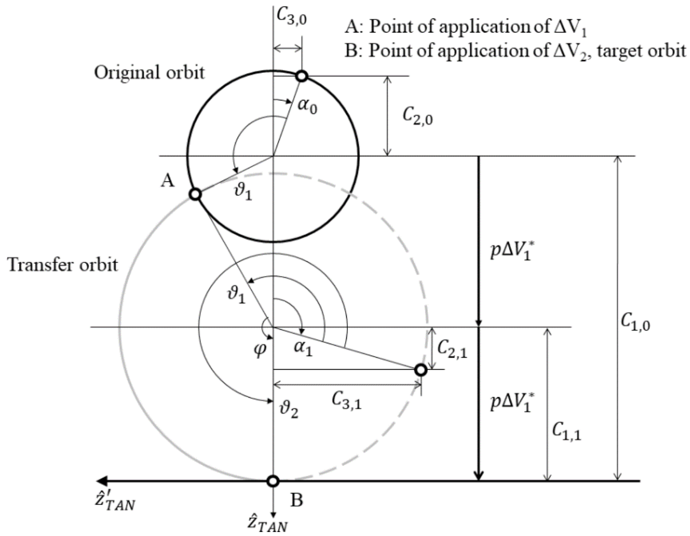

Figure 2.2: Cotangential transfer diagram.

The transfer starts in the relative orbit represented by the circle at the top, parameterized by the three ROE $C_{1,0}$, $C_{2,0}$ and $C_{3,0}$. The scaled z-coordinate traces out a circle in the phase portrait diagram, with a phase angle α determined by the relative magnitudes of the ROE C_2 and C_3. A tangential velocity impulse changes the altitude of the circle of the scaled z-coordinate and the ROE C_2 and C_3 change in such a way as to match the derivative of the scaled z-coordinate at the point of application. The z-coordinate now traces out a circular arc equal to the transfer angle φ to reach the target orbit. The transfer arc is indicated by the set of ROE $C_{1,1}$, $C_{2,1}$ and $C_{3,1}$. The second tangential velocity impulse ends the transfer at the origin. The scaled z-coordinate in the TAN frame with respect to an elliptic reference orbit behaves in a manner similar to the z-coordinate in the LVLH frame with respect to a circular orbit. The scaled z-coordinate in the TAN frame follows a simple harmonic oscillation around a fixed mean altitude and it is independent of the modified relative mean longitude. All these aspects are the same as the behaviour of the z-coordinate in the LVLH frame in circular orbit rendezvous.

2.3.3 Singularities in the Algorithm and Alternative Manoeuvres

The cotangential algorithm contains singularities for certain sets of initial and final conditions. Inspection of the cotangential transfer diagram for the singular cases shows that singularities in the cotangential transfer algorithm occur when the initial orbit intersects the final orbit. Figure 2.3 shows this situation in the cotangential transfer diagram. The shaded region in Figure 2.3 represents the portion of the trajectory below the reference orbit, with the intersections occurring at S_1 and S_2. This diagram allows determining of the location of the singularities, namely, the true anomalies of the intersection points. Intersections occur when the scaled z-coordinate can become zero. By inspection of Figure 2.3 and equation (2.25) the intersection criterion is deduced, namely that the absolute value of ΔC_1 needs to be smaller than ΔC_m. The true anomalies of the intersections can be found by finding the zeros of equation (2.25).

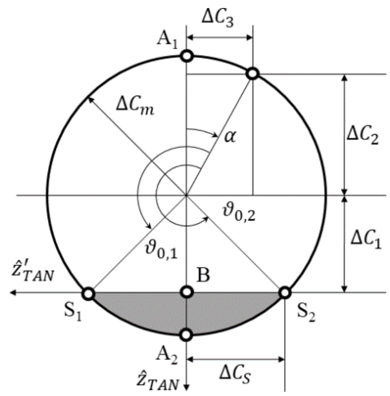

Figure 2.3: Location of singularities in the cotangential transfer algorithm.

The geometrical relations of Figure 2.3 can be analysed to help find the solution for the true anomalies of the intersections:

$$
\begin{aligned}
\sin\vartheta_{0,1} &= -\frac{\Delta C_2 \Delta C_s + \Delta C_1 \Delta C_3}{(\Delta C_m)^2}, \quad & \cos\vartheta_{0,1} &= \frac{\Delta C_3 \Delta C_s - \Delta C_1 \Delta C_2}{(\Delta C_m)^2} \\
\sin\vartheta_{0,2} &= \frac{\Delta C_2 \Delta C_s - \Delta C_1 \Delta C_3}{(\Delta C_m)^2}, \quad & \cos\vartheta_{0,2} &= -\frac{\Delta C_3 \Delta C_s + \Delta C_1 \Delta C_2}{(\Delta C_m)^2}
\end{aligned}
\tag{2.30}
$$

The behaviour of the cotangential transfer algorithm near the singularity can be understood graphically by comparing Figure 2.2 and Figure 2.3, approaching the singularity from below or above. In both cases, the algorithm fits a circle of infinite radius through the point S and point B, and as the centre of the circle of the transfer orbit moves further away from the target orbit the ΔV increases. When approaching the singularity from above the transfer angle approaches zero as the true anomaly approaches the true anomaly of the intersection. When approaching the singularity from below the transfer angle approaches 2π as the true anomaly approaches the true anomaly of the intersection. If the orbits intersect the first and the second ΔV are in opposite directions, while if the orbits do not intersect (as depicted in Figure 2.2) both ΔV's are in the same direction. The first condition of equation (2.7) still applies, which states that for linearized dynamics the sum of the normalized ΔV's needs to be equal to the change in semi-latus rectum. If the ΔV's have opposite sign, then they can become unbounded, while if the ΔV's have the same sign, then the first condition of equation (2.7) provides an upper limit to the size of each of the ΔV's. Clearly, the singularity in the algorithm needs to be avoided to limit the ΔV. Three alternatives to the cotangential transfer are explored when the initial and final orbit intersect.

The first option is to perform the transfer from points that are as far removed from the singularity as possible, starting either above (1) or below (2) the target orbit. In Figure 2.3 these points are labelled A_1 and A_2. The ΔV's have opposite sign even if the transfer starts as far from the singularity as possible. The transfer angle φ is equal to 180°. The transfer for case 1 is developed below. The transfer for case 2 can be developed in an analogous manner. Equation (2.16) shows that the ΔV depends on the polynomial P_1. At point A the polynomial P_1 becomes:

$$\Delta P_{1,\alpha} = \Delta C_1 + \Delta C_2 \cos\alpha + \Delta C_3 \sin\alpha = \Delta C_1 + \Delta C_m \tag{2.31}$$

This expression is inserted into equation (2.16) to obtain the normalized ΔV's:

$$\begin{aligned} \Delta V^*_{\parallel,1,\alpha} &= \frac{1}{2} p^{-1}(\Delta C_1 - \Delta C_m) \\ \Delta V^*_{\parallel,2,\alpha} &= \frac{1}{2} p^{-1}(\Delta C_1 + \Delta C_m) \end{aligned} \tag{2.32}$$

The second option is to use a single manoeuvre performed at the crossing point. The ΔV needs to satisfy the following equation:

$$\begin{bmatrix} \Delta C_1 \\ \Delta C_2 \\ \Delta C_3 \end{bmatrix} + p \begin{bmatrix} 1 & e \sin\vartheta\, \rho^{-1} \\ -\cos\vartheta & \frac{1}{2}(1+e^2)\sin\vartheta\, \rho^{-1} \\ -\sin\vartheta & -\frac{1}{2}\{2e + (1+e^2)\cos\vartheta\}\rho^{-1} \end{bmatrix} \begin{bmatrix} \Delta V^*_{\parallel} \\ \Delta V^*_{\perp} \end{bmatrix} = \begin{bmatrix} 0 \\ 0 \\ 0 \end{bmatrix} \tag{2.33}$$

This equation can be solved by inserting the true anomaly of one of the two crossing points from equation (2.30), and solving the overdetermined system. Alternatively, it can be observed that the tangential component of the ΔV needs to nullify the difference in semi-major axis; only the tangential component of the ΔV can change the semi-major axis. The tangential ΔV is found to be equal to:

$$\Delta V^*_{/\!/} = \frac{\eta^2}{\theta^2}\left(\frac{\delta a^+ - \delta a^-}{a}\right) \tag{2.34}$$

The ΔV is rewritten in terms of the C set of ROE:

$$p\Delta V^*_{/\!/} = \frac{\eta^2}{\theta^2}\left(\frac{(1+e^2)\Delta C_1 - 2e\Delta C_2}{\eta^2}\right) = \frac{(1+e^2)\Delta C_1 - 2e\Delta C_2}{\theta^2} \tag{2.35}$$

The radial ΔV can be found by inserting the tangential ΔV into the first line of equation (2.33) and solving for the radial component. (Of course, line two and three lead to the same result.)

$$p\Delta V_{\perp}^{*} = \frac{\rho\left(\Delta C_1 - p\Delta V_{/\!/}^{*}\right)}{e\sin\vartheta} = \frac{2\rho}{\theta^2}\frac{\cos\vartheta\Delta C_1 - \Delta C_2}{\sin\vartheta} \tag{2.36}$$

The true anomaly of the first intersection from equation (2.30) is inserted to find the radial ΔV at this point:

$$\frac{\cos\vartheta_{0,1}\,\Delta C_1 - \Delta C_2}{\sin\vartheta_{0,1}} = -\frac{(\Delta C_2\Delta C_s + \Delta C_1\Delta C_3)\Delta C_s}{\Delta C_2\Delta C_s + \Delta C_1\Delta C_3} = -\Delta C_s \tag{2.37}$$

The radial component of the ΔV at the first intersection is equal to:

$$p\Delta V_{\perp}^{*} = -\frac{2\rho_{0,1}}{\theta_{0,1}^2}\Delta C_s \tag{2.38}$$

At the second crossing the radial component switches sign; the tangential component of the ΔV is the same as for the first crossing. This manoeuvre is performed at the intersection point, which achieves the desired change in relative orbital elements with a single impulse. This means that transfer is optimal under the assumption that a single ΔV is used.

For the third alternative there is only a single point of intersection (so $\Delta C_m = \Delta C_1$). The tangential ΔV to be applied at the intersection point can be found by means of equation (2.35). The intersection occurs at ϑ = π + α, so, using the definition of α from equation (2.29) and the fact that $C_m = \Delta C_1$, equation (2.35) can be rewritten as:

$$\Delta V_{/\!/}^{*} = \frac{1}{p}\Delta C_1 \tag{2.39}$$

This means that a tangential impulse at the single point of intersection that is aimed to remove the semi-major axis is basically the same as the second manoeuvre of the cotangential transfer, and therefore also corrects the relative eccentricity and argument of perigee.

$$\cos\vartheta = -\operatorname{sgn}(\Delta C_1)\frac{\Delta C_2}{\Delta C_s}, \qquad \sin\vartheta = -\operatorname{sgn}(\Delta C_1)\frac{\Delta C_3}{\Delta C_s} \tag{2.40}$$

The formulation for the crossing manoeuvre cannot be simplified as readily for specific cases as the cotangential manoeuvre. The crossing manoeuvre can achieve the desired set of ROE in a single impulse, but the same change can be achieved more efficiently in a multi-impulse scheme. To show this, consider the following example comparing the ΔV for the cotangential transfer and the crossing manoeuvre to the lower bound. Assume the target spacecraft is orbiting in a reference orbit around Earth with a semi-major axis of 20000 km and an eccentricity of 0.2. The chaser performs the following change in relative orbital elements:

$$\Delta\boldsymbol{\delta\alpha} = [\Delta\delta a \quad \Delta\delta e \quad \Delta\delta\omega] = [200\,m \quad 1\cdot 10^{-5} \quad 0°] \tag{2.41}$$

Equation (2.22) states that if the change in relative eccentricity is larger than $8 \cdot 10^{-6}$, then the initial and final relative orbits intersect, and the change in relative eccentricity dominates. For this transfer the change in parameter C_1 is -208 m, the change in parameter C_2 is -233.6 m, and the change in C_3 is zero. Equation (2.19) is used to find the lower bound for the ΔV as 22.7 mm/s, and equation (2.22) is used to find the ΔV for the cotangential transfer from perigee to apogee as 22.8 mm/s, or 0.5% above the lower bound. Using equation (2.30) the two crossings are found to be symmetric with respect to apogee and occur at a true anomaly of 48.7° and 311.3°. According to equations (2.35) and (2.38) the ΔV to be applied at the crossing has a magnitude of 35.6 mm/s, or 56.9% above the lower bound. This example illustrates that the cotangential manoeuvre, performed far away from the singularities at the crossing points, is generally more efficient in terms of ΔV than the crossing manoeuvre if the cotangential manoeuvre is performed far away from the intersection points.

2.3.4 Comparison with Non-Linear Cotangential Transfer Solution

The non-linear coplanar cotangential transfer problem can be stated as follows: Given the semi-major axes, eccentricities, and arguments of perigee of the initial and final orbits and the true anomaly at which the transfer starts, find the transfer angle of the transfer orbit. The orbital parameters of the transfer orbit and the transfer time can then easily be calculated. This derivation follows Zhang [137,158], with some modifications. The derivation starts from the following relationship between the terminal radii, flight-path angles and the transfer angle given in [159] (p. 240).

$$r_2 \tan\gamma_1 + r_1 \tan\gamma_2 = (r_2 - r_1)\cot\frac{1}{2}\varphi \tag{2.42}$$

The first step to solve equation (2.42) is to multiply by $\rho_1\rho_2$ and by $\tan\frac{1}{2}\varphi$ to remove the devisors:

$$(p_1 e_2 \sin\vartheta_2 + p_2 e_1 \sin\vartheta_1)\tan\frac{1}{2}\varphi = p_2\rho_1 - p_1\rho_2 \tag{2.43}$$

Unlike [137], the departure point or initial true anomaly is considered as given, such that the unknowns in equation (2.43) are the transfer angle and the true anomaly of the arrival point. The transfer angle is defined as the difference in true latitude, that is, $\varphi = \omega_2 - \omega_1 + \vartheta_2 - \vartheta_1$. The transfer angle is used to eliminate the true anomaly of the arrival point:

$$\{p_1 e_2 \sin(\vartheta_1 - \Delta\omega + \varphi) + p_2 e_1 \sin\vartheta_1\} \tan\frac{1}{2}\varphi \\ = p_2(1 + e_1\cos\vartheta_1) - p_1\{1 + e_2\cos(\vartheta_1 - \Delta\omega + \varphi)\} \tag{2.44}$$

Then angle sum and difference operations on the sine and cosine terms of the compound angle can be performed, followed by the Weierstrass substitution on the sine and cosine terms of the transfer angle φ. Simplification leads to the following expression for the transfer angle:

$$\tan\frac{\varphi}{2} = \frac{p_2 - p_1 + (p_2 e_1 - p_1 e_2 \cos\Delta\omega)\cos\vartheta_1 - p_1 e_2 \sin\Delta\omega \sin\vartheta_1}{(p_2 e_1 - p_1 e_2\cos\Delta\omega)\sin\vartheta_1 + p_1 e_2 \sin\Delta\omega\cos\vartheta_1} \tag{2.45}$$

In equation (2.45) the following expressions for the ROE C_1, C_2 and C_3 can be identified that are the non-linear counterpart to the definition in equation (2.6):

$$\begin{aligned} \Delta C_{1,nl} &= \Delta p = p_2 - p_1 \\ \Delta C_{2,nl} &= p_1 e_1(1 - \cos\Delta\omega) + e_1\Delta p - p_1 \Delta e \cos\Delta\omega = p_2 \mathrm{e}_1 - p_1 e_2 \cos\Delta\omega \\ \Delta C_{3,nl} &= -p_1(e_1 \sin\Delta\omega + \Delta e \sin\Delta\omega) = -p_1 e_2 \sin\Delta\omega \end{aligned} \tag{2.46}$$

Equation (2.45) can now be written in the same form as equation (2.11), the only difference being that non-linear analogues of the parameters C_1, C_2 and C_3 are used:

$$\varphi = 2\tan^{-1}\left(\frac{\Delta P_{1,nl}}{\Delta P_{2,nl}}\right) \tag{2.47}$$

The singularities in the algorithm are the same as those given by equation (2.30). To show this, the condition for intersection is examined. The intersection can be found by letting the radius of the initial orbit be equal to radius of the second orbit and solving for the true anomaly of the initial orbit.

$$\frac{p_1}{1 + e_1\cos(l - \omega_1)} = \frac{p_2}{1 + e_2\cos(l - \omega_2)} \tag{2.48}$$

The true longitude l is equal to $\vartheta_1 + \omega_1$, so the following equation can be found from equation (2.48):

$$p_1 + p_1 e_2 \cos(\vartheta_1 - \Delta\omega) = p_2 + p_2 e_1 \cos\vartheta_1 \tag{2.49}$$

Using the cosine difference formula and collecting terms in the sine and cosine of the true anomaly of the first orbit leads to the following expression:

$$p_2 - p_1 + (p_2 e_1 - p_1 e_2 \cos\Delta\omega)\cos\vartheta_1 - p_1 e_2 \sin\Delta\omega \sin\vartheta_1 \\ = \Delta C_{1,nl} + \Delta C_{2,nl}\cos\vartheta_1 + \Delta C_{3,nl}\sin\vartheta_1 = 0 \tag{2.50}$$

This is indeed the non-linear equivalent of setting equation (2.25) to zero.

The determination of the non-linear ROE C_1, C_2 and C_3 shows that this set of ROE is defined with respect to a certain reference orbit, unlike the set of Kepler elements. These ROE show up in the determination of whether orbits intersect and the determination of the required tangential ΔV's to transfer between orbits. In the linear case, the new ROE can also be used as alternatives to the classical ROE to simplify the description of the relative motion in the TAN frame. The fact that there is a close correspondence between the linear and the non-linear cotangential transfer means that the orbit intersection checks and the identification of the correct initial true anomaly for the cotangential transfer between intersecting orbits from section 2.3.3 can be used in the case of non-linear transfers as well. This approach was followed in [160] to create a non-linear guidance function for the long-range rendezvous phase of an MSR type mission.

2.4 Trajectory Safety and Safe Orbits

Trajectory safety is an important design consideration, especially in the presence of trajectory uncertainty. Along-track uncertainty tends to be much larger than the uncertainty in the radial and cross-track directions, because small errors in the estimation of the semi-major axis lead to uncertainty in mean anomaly that grows with time due to the coupling between these elements [44]. The eccentricity / inclination vector separation strategy was developed to exploit this fact; eccentricity vector separation leads to a separation in the radial direction and inclination vector separation leads to a separation in the cross-track direction. If the angle between the relative eccentricity vector and the relative inclination vector (or, alternatively, the phase angle between the radial and cross-track oscillations) is selected properly, then the trajectory remains collision-free even in the presence of trajectory uncertainty.

2.4.1 Eccentric Safe Orbits from Generalized Inclination / Eccentricity Vector Separation

Eccentricity / inclination vector separation is a strategy used in circular reference orbits to define trajectories that are safe from collisions. The resulting trajectory is referred to as eccentricity / inclination vector separation, projected circular orbit or safe orbit if the in-plane and out-of-plane oscillations have the same amplitude. In this document the name "safe orbit" will be used. The eccentricity / inclination vector separation strategy is used for collocating geostationary communications satellites [161] and has recently been used in several formation flying missions in LEO [125,162,163].The reason this type of trajectory is safe is that the projection on the y-z plane of the LVLH frame can be shaped such that the chaser never comes close to the origin. If the amplitudes of the in-plane and out-of-plane oscillations are equal, the projection on the y-z plane is a circle. The centre of the circle always lies on the z-axis, but it can have a certain non-zero altitude with respect to the origin. If the altitude is not equal to zero, then the trajectory experiences along-track drift.

The concept of the safe orbit is generalized to eccentric reference orbits. Trajectories are discussed in a general setting first and a phase angle is included to shift from safe to other types of trajectories such as the halo formation [161]. The specific case of non-drifting safe orbits is treated. Finally, a method is derived to generate safe orbits that pass through a specified point at a specified true anomaly of the reference orbit. Specific geometric conditions at particular points along the orbit are of interest, for example, for satisfying geometric constraints such as ground station visibility, illumination conditions or alignment with astronomical objects. Target observation by means of visual cameras could for example be performed from a safe orbit if the Sun-target-chaser geometry is favourable.

Jiang et al [164] show that drift-free relative trajectories in the LVLH frame lie on a quadric surface in three-dimensional space, and that the quadric surface can be a one-sheet hyperboloid, an elliptic cone or an elliptic cylinder. The idea of embedding the rather complicated relative trajectory into a simpler geometric shape is very interesting. Instead of examining a single trajectory, the whole family of trajectories that lie on the surface can be examined at once. The geometric shape of the surface is simpler, so the analysis to determine whether the shape satisfies certain constraints (such as the trajectory being free from collisions) becomes simpler. If the entire shape satisfies the constraint, then the analysis can stop after this first step. If it does not, then the more complex geometry of the individual trajectory can be analysed to determine whether that specific trajectory at least satisfies the constraint. The approach of Jiang et al [164] cannot be applied directly to generate general safe trajectories because Jiang et al [164] do not include the semi-major axis difference (and therefore trajectory drift) into the analysis. The analysis is performed in the LVLH frame, and the LVLH z-coordinate is dependent on the relative mean anomaly which makes the LVLH z-coordinate dependent on the along-track drift if the relative semi-major axis is non-zero. In other words, if along-track drift is present, then the principal assumption in Jiang et al [164] is violated and the simple geometrical relations identified by Jiang et al no longer apply. Dang et al in [165,166] base their analysis on the work of Jiang et al [164] and provide analytical bounds on the inter-satellite distance, but their approach does not retain the simplicity of the geometrical bounds provided by Jiang et al [164]. In this section geometrical relations are sought that are similar to those found by Jiang et al [164] and that enable fast analysis of families of trajectories. The TAN frame is used instead of the LVLH frame, and simple geometrical relations are defined between the elements C and families of trajectories in the TAN frame. This allows for a straightforward definition of safe orbits that generalize the concept of eccentricity / inclination vector separation, and for simple and fast checks of the trajectory safety. The focus lies on the perpendicular and out-of-plane coordinates, and safe orbits are defined in such a way that the larger uncertainty in the along-track direction does not influence the overall safety of the trajectory, similar to the approach in [44] for circular orbit rendezvous.

In section 2.3.2 it has been observed that the z-coordinate in the TAN frame is independent of the modified relative mean longitude and that the behaviour of the scaled z-coordinate is a simple trigonometric function. In the following sections the idea to identify simple geometries for trajectory families is applied to identify safe trajectories in the TAN frame. Because the z-coordinate in the TAN frame is independent of the modified relative mean longitude, only the projection on the y-z plane needs to be examined to determine whether the possibility of a collision exists or not. This means that the number of dimensions that need to be analysed in the first step of the analysis is reduced from 3 to 2. Both the y-coordinate and the z-coordinate in the TAN frame are fairly simple trigonometric functions of the true anomaly, and no secular terms are present. The collision analysis becomes correspondingly simpler.

2.4.2 General Trajectories and Safe Orbits

The out-of-plane motion is parameterized in terms of the elements C_5 and C_6, which relate to the relative orbital elements δi and $\delta\Omega$ as follows:

$$\begin{aligned} C_5 &= -p(\cos\omega\,\delta i + \sin i \sin\omega\,\delta\Omega) \\ C_6 &= p(\sin\omega\,\delta i - \sin i \cos\omega\,\delta\Omega) \end{aligned} \tag{2.51}$$

To fully decouple the in-plane and out-of-plane motion the in-plane element C_3 is redefined as $C_3 = -ep(\delta\omega + \cos i\,\delta\Omega)$. The out-of-plane coordinate in the TAN frame can be expressed as a function of C_5 and C_6:

$$\hat{y}_{TAN} = \rho y_{TAN} = C_5 \sin\vartheta - C_6 \cos\vartheta \tag{2.52}$$

In equation (2.52) $\hat{y}_{TAN}$ is the out-of-plane coordinate scaled by ρ. Next equation (2.25) is reparametrized using equation (2.29) and equation (2.52) is re-parameterized using the following definitions:

$$C_5 = \lambda C_m \cos\beta\,, \qquad C_6 = \lambda C_m \sin\beta \tag{2.53}$$

The parameter λ is the ratio of the amplitude of the out-of-plane oscillation with respect to the amplitude of the in-plane oscillation and β is the true anomaly at which the chaser crosses the orbital plane of the target in ascending direction (i.e., the relative ascending node). Note that the oscillation in the out-of-plane direction can also be inverted by changing the sign of the elements C_5 and C_6. The scaled motion in the y-z plane of the TAN frame can now be written in the following form:

$$\begin{aligned} \hat{y}_{TAN} &= \lambda C_m \sin(\vartheta - \beta) = \lambda C_m \sin(\tau - \tau_0) \\ \hat{z}_{TAN} &= -\{C_1 + C_m \cos(\vartheta - \alpha)\} = -\{C_1 + C_m \cos\tau\} \end{aligned} \tag{2.54}$$

In equation (2.54) $\tau = \vartheta - \alpha$ and $\tau_0 = \beta - \alpha$. For non-zero C_m and λ the scaled coordinates in the y-z plane traces a line if τ_0 is equal to ½π, a circle if τ_0 is equal to 0 and $\lambda = 1$ and an ellipse otherwise. The case of τ_0 equal to 0 is of interest for generalizing the safe orbit to an eccentric reference orbit. Of course, different generalizations of the projected circular orbit are now possible that all approach a circular projection when the eccentricity goes to zero, due to the presence of the amplitude ratio λ. That is to say, one could assign whichever function of the eccentricity to the parameter λ, as long as it approaches to 1 when the eccentricity goes to zero. If no restrictions are placed on the amplitude ratio, then the parameter λ can be set to any value. Equation (2.54) indicates that if $|C_1| < |C_m \cos\tau_0|$, the trajectories wind around the origin.

One-parameter families of curves can now be identified that depend on the parameter α and that have the same value for the parameters C_1, C_m, λ and τ_0. The parameter α is a phase angle, C_1 is the relative altitude, C_m the dimension or size, λ the ratio of amplitudes of the out-of-plane to the in-plane oscillations and τ_0 the angle between the relative eccentricity and inclination vectors. For the definition of eccentricity / inclination vector separation with a circular reference orbit similar parameters are used. In case of a circular reference orbit the in-plane phase angle α can be varied without altering the shape of the relative trajectory: the projection of the trajectory on the x-z plane of the LVLH frame remains a 2:1 ellipse, and the projection of the trajectory on the y-z plane remains a circle (only if λ is equal to 1, of course). In the case of an elliptic reference orbit the shape of trajectories is more complicated because of the scaling factors acting on the y and z coordinates, and each member of the family of trajectories is scaled differently. On the other hand, the boundary of a family of trajectories as a whole (defined by means of Eq. (2.54) in terms of the parameters C_1, C_m, λ and τ_0) is reasonably simple. The boundary can be obtained by examining the envelope of the family of curves parameterized by τ and the extreme values of the scaling function ρ. The point of the boundary closest to the origin always lies on the ellipse for which ρ is equal to 1 + e, that is to say, the closest approach of the trajectory family as a whole always occurs at perigee, because in this case both the y and z coordinates are scaled by the largest value. The closest approach of the family evaluated at perigee therefore provides a conservative, lower bound estimate of the closest approach of any individual member of that family.

Following this general discussion, the eccentricity / inclination vector separation is examined. Eccentricity / inclination vector separation occurs when τ0 is equal to 0. If τ_0 is equal to 0, then the scaled coordinates behave as follows:

$$\begin{aligned} \hat{y}_{TAN} &= \lambda C_m \sin\tau \\ \hat{z}_{TAN} &= -(C_1 + C_m \cos\tau) \end{aligned} \tag{2.55}$$

This is the parametric equation of an ellipse with centre $(0,-C_1)$, major axis C_m along the z-axis and minor axis $\lambda \cdot C_m$ along the y-axis. Figure 2.4 shows the families of safe orbits that Eq. (2.55) generates. The value of the parameter λ is 1, C_m is equal to 10. On the left of Figure 2.4 $C_1 = 0$ and on the right $C_1 = C_m$. The scaled coordinates (that is, y is scaled by ρ and z is scaled by ρθ) are the same for all members of the trajectory family.

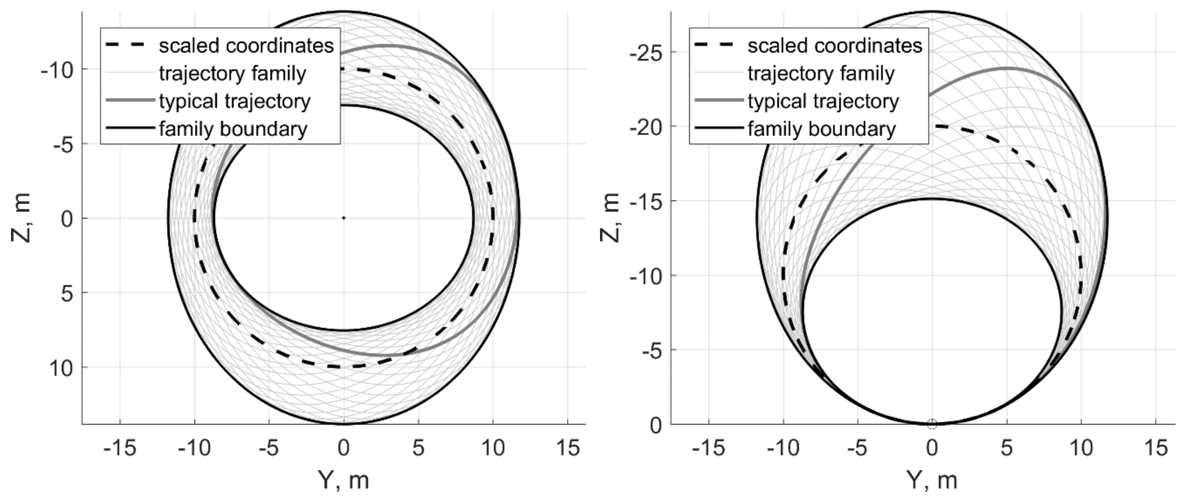

(a) $C_1 = 0$ (b) $C_1 = C_m$

Figure 2.4: Boundaries for safe trajectories.

Figure 2.4 shows that the inner boundary of the family of trajectories around the origin is determined by the inner elliptical boundary that results from $\rho = 1 + e$ if $|C_1| < |C_m|$. This family of trajectories encloses the origin and contains both drifting and non-drifting trajectories. To ensure drift-free trajectories, the difference in semi-major axis must be equal to zero. In terms of the ROE C_1 and C_2 this means:

$$C_1 = \frac{2e}{1+e^2} C_2 = \frac{2e}{1+e^2} C_m \cos\alpha \tag{2.56}$$

The drift-free safe orbit encloses the origin. Finally, for drift-free trajectories centred on the origin $C_4 = 0$.

The safe orbit formulation in this article can be compared to the formulations of the eccentricity / inclination vector separation found in literature. D' Amico and Montenbruck [44] define the eccentricity / inclination vector separation using the eccentricity vector and the inclination vector. In near-circular orbits the eccentricity vector is usually parameterized in terms of small differences in the parameters $q_1 = e\cos\omega$ and $q_2 = e\sin\omega$ [147], and the inclination vector is parameterized in terms of δi and $\delta\Omega\sin i$. The ROE defining the eccentricity and inclination vectors are multiplied by the argument of latitude $u = \vartheta + \omega$. The elements C can be recovered from the elements used by Chernick and D'Amico [112] using:

$$\begin{bmatrix} C_1 \\ C_2 \\ C_3 \\ C_4 \\ C_5 \\ C_6 \end{bmatrix} = p \begin{bmatrix} 1 & 0 & -2\eta^{-2} e\cos\omega & -2\eta^{-2} e\sin\omega & 0 & 0 \\ e & 0 & -\eta^{-2}(1+e^2)\cos\omega & -\eta^{-2}(1+e^2)\sin\omega & 0 & 0 \\ 0 & 0 & \sin\omega & -\cos\omega & 0 & -e\cot i \\ 0 & \eta & 0 & 0 & 0 & 0 \\ 0 & 0 & 0 & 0 & -\cos\omega & -\sin\omega \\ 0 & 0 & 0 & 0 & \sin\omega & -\cos\omega \end{bmatrix} \begin{bmatrix} a^{-1}\delta a \\ \delta\lambda_e \\ \delta q_1 \\ \delta q_2 \\ \delta i \\ \delta\Omega\sin i \end{bmatrix} \tag{2.57}$$

The formulation in terms of elements C conveniently decouples the in-plane and out-of-plane motions. The main difference with the formulation for circular orbits is that the semi-latus rectum is used as the basis for elements C_1 and C_2.

2.4.3 Trajectories with Alignment

This section discusses trajectories that pass through a user-specified position vector in the TAN frame at a specified true anomaly. This can be useful for example for ensuring proper lighting conditions of the target spacecraft. The relative semi-major axis δa, the amplitude ratio λ and the out-of-plane phase angle τ_0 are given as design parameters. The y and z coordinates of the trajectory are given as a function of C_2 and C_3 by equation (2.54). The value of C_1 in the equation for the z-coordinate as a function of C_2 and the relative semi-major axis can be obtained from equation (2.6).

$$C_1 = (1+e^2)^{-1}(\eta^4 \delta a_{des} + 2eC_2) \tag{2.58}$$

The equations for the y- and z-coordinate can then be written as the following system of equations:

$$\begin{bmatrix} y_{TAN} \\ z_{TAN} + \rho^{-1}\theta^{-1}\dfrac{\eta^4}{1+e^2}\delta a_{des} \end{bmatrix} = \rho^{-1}\theta^{-1} \begin{bmatrix} \lambda\theta\sin(\vartheta-\tau_0) & -\lambda\theta\cos(\vartheta-\tau_0) \\ -\left(\dfrac{2e}{1+e^2}+\cos\vartheta\right) & -\sin\vartheta \end{bmatrix} \begin{bmatrix} C_2 \\ C_3 \end{bmatrix} \tag{2.59}$$

The solution for this system of equations is:

$$
\begin{bmatrix} C_2 \\ C_3 \end{bmatrix} = \rho\left\{\cos\tau_0 + \frac{2e}{1+e^2}\cos(\vartheta-\tau_0)\right\}^{-1} \times \begin{bmatrix} \lambda^{-1}\sin\vartheta & -\theta\cos(\vartheta-\tau_0) \\ -\lambda^{-1}\left(\frac{2e}{1+e^2}+\cos\vartheta\right) & -\theta\sin(\vartheta-\tau_0) \end{bmatrix} \begin{bmatrix} y_{TAN} \\ z_{TAN} + \rho^{-1}\theta^{-1}\frac{\eta^4}{1+e^2}\delta a_{des} \end{bmatrix} \tag{2.60}
$$

The constant C_4 is obtained from the x-coordinate in the tangential frame, which is given by (Appendix B, section 2.9):

$$
x_{TAN} = \rho^{-1}\eta^{-2}\theta^{-1}\{e(\theta^2+2)\sin\vartheta\, C_1 - 2(\rho+e^2)\sin\vartheta\, C_2 + 2(e+\cos\vartheta)\rho C_3\} + \theta C_4 \tag{2.61}
$$

The constant C_1 as a function of C_2 and the relative semi-major axis is inserted, and the equation is solved:

$$
C_4 = \theta^{-1}x_{TAN} - \eta^2\theta^{-2}\frac{e\sin\vartheta}{\rho}\left(\frac{2}{1+e^2}\rho+1\right)\delta a_{des} + 2\theta^{-2}\left(\frac{\sin\vartheta}{1+e^2}C_2 - \frac{e+\cos\vartheta}{\eta^2}C_3\right) \tag{2.62}
$$

Finally, the elements C_5 and C_6 are found from:

$$
\begin{aligned} C_5 &= \lambda(C_2\cos\tau_0 - C_3\sin\tau_0) \\ C_6 &= \lambda(C_2\sin\tau_0 + C_3\cos\tau_0) \end{aligned} \tag{2.63}
$$

The procedure to obtain a trajectory that passes through a point (x, y, z) in the TAN frame, with the relative semi-major axis δa, the amplitude ratio λ and the out-of-plane phase angle τ_0 given as design parameters, is as follows. First, equation (2.60) is used to obtain C_2 and C_3. Equation (2.58) is used to obtain C_1 and equation (2.62) is used to obtain C_4. Finally, equation (2.63) is used to obtain the elements C_5 and C_6. The state in the TAN frame can be found using the matrices defined in Appendix B, section 2.9. Alternatively, the C set of ROE can be converted to Keplerian ROE.

Some limitations of this procedure need to be pointed out. The procedure obviously does not work if the amplitude ratio λ is set to zero, because in this case the relative motion occurs in the orbital plane of the reference orbit. Second, if the out-of-plane phase angle τ_0 is smaller than $\sin^{-1}\left(\frac{2e}{1+e^2}\right)$, then the divisor in equation (2.60) can become zero for certain values of the true anomaly, which leads to singular trajectories that may have infinite size.

2.5 Rendezvous Strategy Based on Cotangential Transfers and Safe Orbits

In this section an example of a rendezvous strategy is presented that incorporates the ideas developed in the previous sections. Perturbations are excluded from this analysis. The perturbation-free manoeuvring strategy described here can be incorporated into a guidance function that does consider perturbations using the precompensation technique described by Chernick and D'Amico [112].

The initial conditions for the rendezvous strategy are a drift orbit at a given altitude below the target orbit. The terminal conditions for the strategy are a safe orbit with specific properties, namely, arriving at a specific point at a specific true anomaly. Tangential and out-of-plane manoeuvres are used to reach the terminal conditions. Figure 2.5 shows a diagram of the rendezvous strategy.

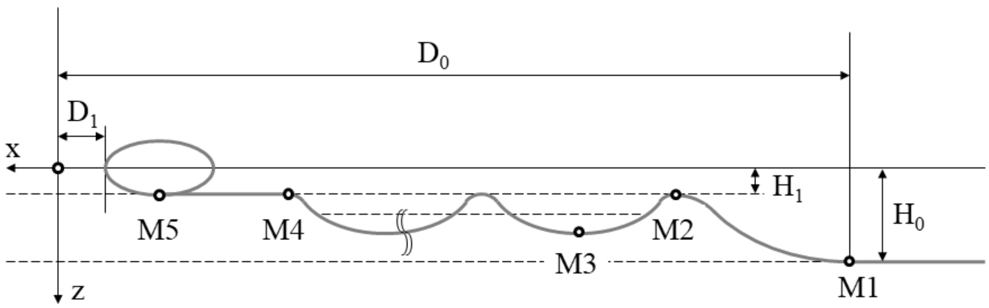

Figure 2.5: Rendezvous strategy.

Before manoeuvre M1 the chaser is a co-elliptic orbit below the target orbit. Manoeuvre M1 is a cotangential transfer that raises the relative apogee to H_1. Between manoeuvres M2 and M4 the chaser is in a drifting orbit with a relative perigee below H1. The drift orbit with altitude variations ensures that the chaser arrives at the proper distance from the target when performing manoeuvre M4. Manoeuvre M3 is an out-of-plane manoeuvre. Manoeuvre M4 inserts the chaser into a co-elliptic orbit. Finally, manoeuvre M5 inserts the chaser into a safe orbit. To complete the definition of this strategy, two additional aspects need to be examined. First, the lowest possible co-elliptic drift orbit that connects to the safe orbit needs to be found. This co-elliptic orbit is tangent to the safe orbit. In addition, the drift rate between M2 and M4 needs to be modulated to ensure proper phasing.

2.5.1 Co-elliptic Orbits Connecting to Safe Orbits

A co-elliptic orbit is defined with respect to a reference orbit. It is coplanar with the reference orbit and has the same argument of perigee. The value of the eccentricity is such that the altitude variation with respect to the reference orbit is as small as possible [167]. The linear co-elliptic orbit is defined in terms of the ROE as follows:

$$\delta e = -ea^{-1}\delta a, \qquad \delta\omega = 0 \tag{2.64}$$

The co-elliptic orbit in terms of the parameters C_1, C_2 and C_3 is found from equation (2.6). The equation for the z coordinate in the co-elliptic orbit can now be found from equations (2.6), (2.25) and (2.64):

$$z_{TAN} = -\rho^{-1}\theta\delta a = -\frac{1}{\cos\gamma}\delta a \tag{2.65}$$

The range of the z-coordinate of the co-elliptic orbit is determined by the flight path angle. At apogee and at perigee, the flight path angle is zero and $z_{TAN} = -\delta a$. The maximum flight path angle occurs at $\vartheta = \cos^{-1}(-e)$, and at this point the z-coordinate reaches its extremum $z_{TAN} = -\eta^{-1}\delta a$. The minimum distance between the co-elliptic orbit and the reference orbit is always greater than δa.

The crossing condition $(\Delta C_1)^2 = (\Delta C_2)^2 + (\Delta C_3)^2$ is used to determine the relative semi-major axis of the co-elliptic orbit connecting to a particular safe orbit. The differences in C_1, C_2 and C_3 are taken between the co-elliptic orbit and the safe orbit. The crossing condition leads to a second-degree polynomial in the relative semi-major axis, meaning that there are two co-elliptic orbits that connect to a particular safe orbit:

$$\begin{aligned}\eta^4\left(\delta a_{coelliptic}\right)^2 + 2\left\{-(1+e^2)C_{1,safe} + 2eC_{2,safe}\right\}\delta a_{coelliptic} + \left(C_{1,safe}\right)^2 \\ - \left(C_{2,safe}\right)^2 - \left(C_{3,safe}\right)^2 = 0\end{aligned} \tag{2.66}$$

For a non-drifting safe orbit there is a positive and a negative root. The true anomaly of the intersection is found from equation (2.30). The value of the parameter C_4 is found by equating the x-coordinate at the connection point using equation (2.61) for both possible values of the semi-major axis.

$$\begin{aligned}\rho_i\eta^2\theta_i^2 C_{4,coelliptic,i} \\ &= e\left(\theta_i^2 + 2\right)\sin\vartheta_i\left\{C_{1,safe} - (1+e^2)\delta a_{coelliptic,i}\right\} \\ &- 2(\rho_i + e^2)\sin\vartheta_i\left\{C_{2,safe} - 2e\delta a_{coelliptic,i}\right\} \\ &+ 2\rho_i(e + \cos\vartheta_i)C_{3,safe} + \rho_i\eta^2\theta_i^2 C_{4,safe}, \qquad i = 1,2\end{aligned} \tag{2.67}$$

2.5.2 Altering the Drift Rate

Altering the drift rate is performed by means of tangential manoeuvres. A two-impulse transfer that lasts one revolution alters the relative mean anomaly without changing any of the other ROE. The first impulse of such a transfer is given by:

$$\Delta V = \frac{an\eta}{6\pi\theta N_{orb}}\Delta M \tag{2.68}$$

In equation (2.68) $\Delta M = \delta M_4 - \delta M_2 - 3\pi N_{orb} a^{-1} \delta a_{coelliptic}$, and the term $3\pi \cdot N_{orb} \cdot a^{-1} \cdot \delta a$ represents the drift in the co-elliptic orbit that would have occurred if no manoeuvres would have been performed. The second impulse has the same magnitude as the first impulse but opposite in sign.

Equation (2.68) can be used to set bounds on the number of orbits spent in the drift orbit and determine whether the strategy is feasible for the given initial conditions. The upper bound is found by assuming that the chaser can directly enter the co-elliptic drift orbit and that no ΔV is required to alter the drift rate.

$$N_{orb,\max} = \left\lfloor \frac{\delta M_2 - \delta M_4}{3\pi a^{-1} \delta a_{coelliptic}} \right\rfloor \tag{2.69}$$

The floor function is used to ensure that an integer number of orbits is spent in the drift orbit. The minimum number of orbits spent in the drift orbit is found by assuming that the ΔV required to initiate the drift is equal in magnitude and opposite in sign to the second ΔV of the cotangential manoeuvre.

$$N_{orb,\min} = \left\lceil \frac{\delta M_2 - \delta M_4}{3\pi a^{-1} \left(\delta a_{coelliptic} - 2\theta n^{-1} \eta^{-1} \Delta V_{CTG,2}\right)} \right\rceil \tag{2.70}$$

The ceiling function is used to ensure that an integer number of orbits is spent in the drift orbit. Note that for the strategy discussed here, $\delta a_{coelliptic} < 0$ and $\Delta V_{CTG,2} > 0$, such that the absolute magnitude of the denominator increases. Equation (2.69) ensures that the chaser does not move above the co-elliptic orbit, while equation (2.70) ensures that the chaser does not move below the original orbit. The condition expressed in equation (2.69) potentially affects the safety of the trajectory, while the condition expressed in equation (2.70) ensures that the total ΔV required for manoeuvres M1, M2 and M4 is equal to the ΔV required for the cotangential manoeuvre. Equation (2.70) ensures that the second impulse of the cotangential manoeuvre is effectively split to correct the along-track distance in the drift orbit. If the condition in equation (2.70) is violated, then the correcting the along-track distance requires additional ΔV.

Equation (2.69) establishes a relationship between the altitude of the initial orbit and the along-track distance and determines whether the rendezvous strategy is feasible given the initial altitude and along-track distance. Equation (2.69) implies that the difference in mean anomaly at manoeuvre M2 and manoeuvre M4 either needs to be equal to zero (in which case M2 and M4 coincide) or greater than or equal to the along-track drift during one orbit to ensure that the chaser can spend at least one orbit in the co-elliptic drift orbit.

2.5.3 Drift-Based Rendezvous Strategy Ending in Safe Orbit

The rendezvous strategy shown in Figure 2.5 can now be created and simulated. The strategy consists of a cotangential manoeuvre, a phasing element, and an insertion into a safe orbit. The target state is a (drift-free) safe orbit with alignment. For this safe orbit the elements C_2 and C_3 are computed using equation (2.60), element C_4 using equation (2.62) and C_1 using equation (2.58). The out-of-plane elements C_5 and C_6 are found from equation (2.63). The first step to define the manoeuvre strategy is to compute a cotangential transfer using equations (2.11), (2.16) and (2.18). The cotangential manoeuvre algorithm provides the true anomaly ϑ_2 at which the second impulse (corresponding to M2 in Figure 2.5) needs to be executed and the along-track position C_4 at the end of the transfer. Next, the intersection point of the safe orbit with a co-elliptic drift orbit is obtained from equation (2.66), picking the root that has the same sign as the initial drift orbit. The true anomaly of the intersection is found from equation (2.30). The result is a co-elliptic orbit with elements C_1, C_2 and C_3 found from equations (2.6) and (2.64) and the along-track element C_4 of the intersection point with the safe orbit given by equation (2.67). The ΔV at the connection point M5 is found by converting the change in C elements to a change in Cartesian state. The difference in the position components are of course equal to zero by definition. The drift orbit is propagated backwards from the true anomaly of the intersection point to the first occurrence of the true anomaly of the second impulse of the cotangential manoeuvre. This ensures that there are an integer number of orbits between manoeuvres M2 and M4. The drift rate between manoeuvres M2 and M4 is corrected using tangential manoeuvres derived from equation (2.68). The number of orbits spent in the drift orbit is constrained by (1) ensuring that the trajectory remains below a co-elliptic orbit of altitude H1 and (2) that the ΔV at M2 is greater than zero. Condition (1) and (2) together ensure that the total ΔV required for manoeuvres M1, M2 and M4 does not exceed the total ΔV for a cotangential manoeuvre between the initial orbit and the co-elliptic orbit. The final manoeuvre to be computed is the out-of-plane manoeuvre M3. The intersection points with the orbital plane can be found by setting equation (2.52) to zero. The ΔV is then equal in magnitude and opposite in sign to the out-of-plane velocity. All manoeuvres are now known.

The strategy is simulated for different values of the eccentricity. Table 2.1 lists the parameters used for simulation of the approach strategy. The selected safe orbit is drift-free with equal amplitude in the y- and z-directions.

Table 2.1: Simulation parameters.

Parameter	Value
Reference orbit	
Gravitational parameter	398600.61 km^3/s^2
Semi-major axis	13394 km
Eccentricity	0 – 0.5
True anomaly	50°
Initial conditions	
Initial C_4 (along-track distance)	-2000 m
Initial co-elliptic orbit altitude H_0	100 m
Safe orbit terminal conditions	
Alignment point	[-80 43.3 -25] m
δa	0 m
Out-of-plane motion ratio λ	1
Phase angle τ_0	0°
True anomaly at alignment	130°

Figure 2.6 shows the rendezvous strategy for several values of the eccentricity. The number of revolutions spent in the drifting orbit has been set to 2 for all cases. At zero eccentricity the trajectory is very similar to the conceptual sketch shown in Figure 2.5. When the eccentricity increases, the trajectory starts to deform more and more with respect to the familiar circular orbit rendezvous trajectory. At the same time, all trajectories successfully intercept the alignment point irrespective of the eccentricity. Figure 2.6 also shows that as the eccentricity increases, the safe orbit expands outwards. The exact evolution of the shape of the safe orbit with eccentricity is strongly dependent on the details of the geometry (e.g. the true anomaly and the position of the alignment point), meaning that the suitability of the trajectory for a reference orbit of a given eccentricity needs to be examined using the procedures outlined in section 2.4.2. The same is also true for the co-elliptic drift orbit that connects to the safe orbit.

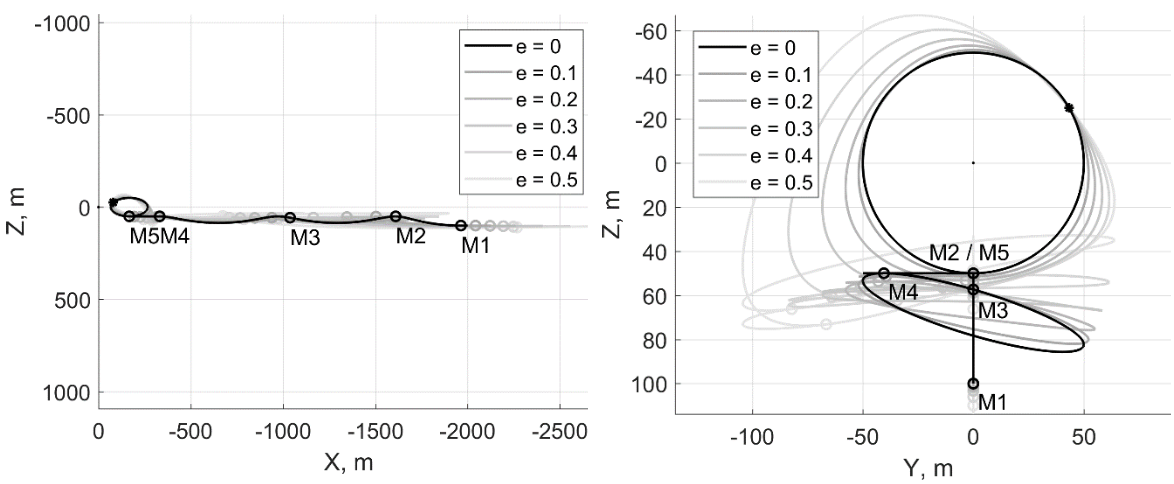

Figure 2.6: Simulated rendezvous trajectory in the tangential frame.

Figure 2.6 shows that at eccentricities of 0.4 and 0.5, the co-elliptic drift orbit that connects to the safe orbit actually enters the circle with radius 50 m centred on the origin in the YZ-projection. This is not necessarily a problem as long as the trajectory does not enter the stay out zone or safety sphere. In this case, if the safety sphere has a radius of 30 m, then the trajectory could still be considered safe. The issue is examined further by examining the calculated parameters of the rendezvous algorithm in Table 2.2.

Table 2.2: Calculated parameters for rendezvous strategy.

	e = 0	e = 0.1	e = 0.2	e = 0.3	e = 0.4	e = 0.5
C_4 at M2, m	-1609,9	-1604,9	-1593,8	-1575,7	-1548,6	-1508,4
C_4 at M4, m	-331,5	-345,7	-364,4	-388,3	-418,8	-460,3
C_4 at M5, m	-166,6	-175,8	-186,9	-199,5	-213,7	-233,2
δa, (equation (2.69)), m	-50,0	-51,2	-53,2	-56,0	-59,8	-65,2
δa, (equation (2.70)), m	-75,0	-75,6	-76,6	-78,0	-79,9	-82,6
$N_{orb,max}$, (equation (2.69))	2	2	2	2	1	1
$N_{orb,min}$, (equation (2.70))	2	2	2	2	2	2

Table 2.2 shows the calculated parameters for the rendezvous strategy for different values of the eccentricity. The first three rows provide the along-track element C_4 for manoeuvres M2, M4 and M5. Rows 4 to 7 evaluate the bounds on the number of orbits spent drifting between M2 and M4 that are provided in equations (2.69) and (2.70). The maximum number of orbits in the drift orbit is equal to 1 for eccentricities of 0.4 and 0.5, while the minimum number of orbits to be spent in the drift orbit is equal to 2. For all other values of the eccentricity, the minimum and the maximum number of orbits in the drift orbit is equal to 2. Condition (2.69) is not fulfilled for eccentricities of 0.4 and 0.5, and as a result the drift orbit between manoeuvre M2 and M4 has its highest point above the co-elliptic drift orbit. In fact, Table 2.2 shows that for eccentricities of 0.4 and 0.5 either condition (2.69) or condition (2.70) needs to be broken. It can be verified that with an initial value of C_4 = 2400 m, the rendezvous can be completed at eccentricities of 0.4 and 0.5 while fulfilling condition (2.69), but that the lower eccentricity cases would need 3 orbits for completing the drift. For the sake of maintaining the number of drift orbits the same across all values of the eccentricity, the non-fulfilment of condition (2.69) is deemed acceptable in this example, because maintaining the number of drift orbits facilitates the visual comparison of the trajectories and also illustrates the consequences of non-fulfilment of these conditions.

The algorithms work for any arbitrary eccentricity; however, Figure 2.6 and Figure 2.7 show that the rendezvous trajectory progressively deviates from the familiar circular rendezvous trajectory as the eccentricity increases. The reason for this is that the scaling factors ρ and θ depend on the eccentricity. Note that the scaling factors also depend on the true anomaly. This causes the geometry of particular rendezvous trajectories to be dependent on the true anomaly of key points of the trajectory such as the alignment point and the starting point. It also means that the geometry of the trajectory is not fully known a priori, especially for HEO rendezvous. From a practical point of view this means that for HEO rendezvous the safety and feasibility of the rendezvous trajectory needs to be analysed during the mission design. During mission design, trajectory design parameters such as the altitude of drift orbits and the dimensions of safe orbits need to be adjusted according to a trajectory safety and feasibility analysis.

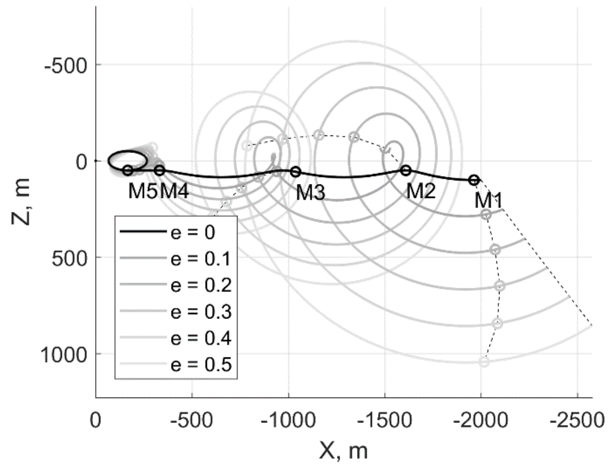

Figure 2.7: Simulated rendezvous trajectory in the LVLH frame.

Figure 2.7 shows the same set of rendezvous trajectories in the LVLH frame. In Figure 2.7 the locus of the locations of the manoeuvres as they evolve with increasing eccentricity is indicated by means of a dotted line. Figure 2.7 shows that it is not obvious how to generate such a trajectory given only Cartesian coordinates in the LVLH frame. Trajectory safety of rendezvous trajectories in elliptic orbit rendezvous cannot be established as easily by inspecting the trajectory in the LVLH frame as it is in the tangential frame of Figure 2.6, because the z-coordinate shows a much greater variation. Of course, the trajectory for zero eccentricity in the LVLH frame corresponds exactly to the trajectory for zero eccentricity in the tangential frame.

Table 2.3 shows the manoeuvre times for the rendezvous strategy expressed as multiples of the orbital period. Table 2.3 shows that the time at which the in-plane manoeuvres M1, M2, M4 and M5 occur remains fairly constant over the different values of the eccentricity. The out-of-plane manoeuvre M3 occurs almost half an hour earlier in the case of e = 0.5 with respect to the circular orbit.

Table 2.3: Manoeuvre times for rendezvous strategy.

	e = 0	e = 0.1	e = 0.2	e = 0.3	e = 0.4	e = 0.5
man. no.	time, h	time, h	time, h	time, h	time, h	time, h
M1	0.167	0.167	0.167	0.167	0.167	0.167
M2	2.309	2.309	2.306	2.301	2.294	2.286
M3	5.952	5.954	5.901	5.800	5.664	5.501
M4	10.880	10.879	10.877	10.872	10.865	10.857
M5	12.380	12.379	12.363	12.335	12.294	12.230

Table 2.4 shows the ΔV required to perform this rendezvous strategy for various values of the eccentricity. Only the magnitude of the ΔV is given. The in-plane manoeuvres M1, M2, M4 and M5 are performed in the direction of the local orbital velocity vector, and the out-of-plane manoeuvre M3 is performed in the out-of-plane direction. The second ΔV of the cotangential manoeuvre is modified to alter the drift rate, and the sum of the ΔV's required for manoeuvres M1, M2 and M4 (the sequence of orbit raising and drift correcting manoeuvres) is equal to the ΔV required for a cotangential manoeuvre from the original orbit to the co-elliptic orbit. The cases for which the eccentricity is 0.4 and 0.5 do not fulfil condition (2.69). As a consequence, additional ΔV is spent to correct the in-plane element C4. The ΔV for the cotangential manoeuvre alone is given in brackets for these cases. The total ΔV required for M1, M2 and M4 can be compared to the ΔV lower bound [112] given by equation (2.19). The dominant change is the change in relative semi-major axis. As in the work of Chernick and D'Amico [112], the out-of-plane manoeuvre M3 is performed at the relative node and therefore optimally changes the out-of-plane motion. Manoeuvre M5 is performed at the intersection of the safe orbit with the co-elliptic orbit by design.

Table 2.4: ΔV required for rendezvous strategy.

	e = 0	e = 0.1	e = 0.2	e = 0.3	e = 0.4	e = 0.5
man. no.	ΔV, mm/s	ΔV, mm/s	ΔV, mm/s	ΔV, mm/s	ΔV, mm/s	ΔV, mm/s
M1	5.09	4.73	4.28	3.77	3.21	2.59
M2	1.46	1.99	3.02	4.73	7.45	11.73
M3	20.36	19.26	19.18	20.04	21.77	24.31
M4	3.63	3.30	2.54	1.09	1.45	5.80
M5	10.18	9.44	8.87	8.59	8.92	10.46
M1+M2+M4	10.18	10.01	9.84	9.60	12.11 (9.21)	20.12 (8.53)
Lower bound	10.18	8.98	7.78	6.58	5.36	4.10
Total	40.73	38.71	37.89	38.23	42.80 (39.90)	54.89 (43.30)

Table 2.4 shows that there is considerable variation in the ΔV associated with each of the manoeuvres depending on the eccentricity of the reference orbit. The order of magnitude of manoeuvres is similar for most manoeuvres apart from the second manoeuvre, which grows from 1.46 mm/s to 11.73 mm/s as the eccentricity grows from 0 to 0.5. The evolution of the ΔV for each of the manoeuvres strongly depends on the local geometry of the trajectory at the time of the manoeuvre, and there is no particular

pattern in the dependency on the eccentricity of the reference orbit. It should be noted that the sequence of manoeuvres generated here is quite artificial; as Figure 2.7 shows the initial conditions have been idealized over the different values of the eccentricity in order to facilitate easy visual comparison of the trajectories and to demonstrate the general applicability of the trajectory and manoeuvre definition strategy. It should be stressed that this selection of the initial conditions is purely for this reason. The strategy is applicable in general for different initial values of the true anomaly and variation in the initial conditions, as long as sufficient along-track distance (as established by equations (2.69) and (2.70)) is available to perform the strategy. More explicitly, for a given safe orbit, the procedure to check the along-track distance is as follows. First, equation (2.11) provides the transfer angle of the cotangential transfer and with that the true anomaly ϑ_2 of manoeuvre M2. Equation (2.18) provides C_4 at the end of the cotangential transfer. Equation (2.30) and (2.67) provide the true anomaly and C_4 at the manoeuvre M5. Back-propagation of the co-elliptic drift orbit from manoeuvre M5 to the first occurrence of ϑ_2 before manoeuvre M5 leads to C_4 of manoeuvre M4. The values of C_4 need to be converted to relative mean anomaly, and equation (2.66) needs to be used to find the relative semi-major axis of the co-elliptic orbit. Now, equation (2.69) can be used to establish whether sufficient along-track distance is available to perform the strategy.

2.6 Conclusion

This paper has created a clear connection between the traditional strategies for rendezvous in circular orbits and corresponding strategies in elliptical orbits. The cotangential transfer for elliptic orbit rendezvous is conceptually similar to the Hohmann transfer in circular orbit rendezvous. In both cases, the ΔV is applied in the direction of the local orbital velocity vector and the z-coordinate or its equivalent in an elliptic reference orbit responds with a change of mean altitude and amplitude of the motion. Some differences do exist. For the linear Hohmann transfer in circular orbit rendezvous, the first and the second ΔV are exactly equal, while in elliptic orbit rendezvous the two ΔV's are generally different in magnitude. The solution of the cotangential transfer leads to a natural definition of a new set of relative orbital elements. The representation of the trajectory in terms of these elements creates a connection to the travelling ellipse formulation in circular orbits, and this concept can aid in the development and analysis of rendezvous strategies. This representation also facilitates the determination of whether two trajectories intersect. Finally, the new set of relative orbital elements can be used to define safe trajectories with and without drift. These safe orbits represent a generalization to non-circular orbits of the safe orbits based on eccentricity / inclination vector separation that are used in circular orbit rendezvous and formation flying.

The combination of the cotangential transfers and safe orbits leads to a useful conceptual approach to defining rendezvous trajectories for elliptical orbits. An analysis of a drift-based rendezvous strategy shows that the same strategy can be applied for both circular and eccentric reference orbits with similar results in terms of manoeuvre application times and ΔV magnitudes. In this sense, classical rendezvous strategies developed for circular orbit rendezvous can be fully generalized following the procedures outlined in this paper.

2.7 Acknowledgement

This work is the result of several years of development, partly performed at GMV with internal funds and partly performed in the frame of different European Space Agency (ESA) funded activities/applications, including HARVD (ESA contract No. 4200019846), iGNC (ESA contract No. 4000103644/11/NL/EK) and AnDROiD (ESA contract 4000110200/14/NL/MV).

2.8 Appendix A: Details of the TAN frame

The transformation matrix $\mathbf{T}_\gamma$ takes a vector from the TAN frame to the LVLH frame, that is to say:

$$\mathbf{x}_{LVLH} = \mathbf{T}_\gamma \mathbf{x}_{TAN} \tag{2.71}$$

The matrix $\mathbf{T}_\gamma$ and its inverse are composed of a rotation matrix and an angular velocity matrix.

$$\mathbf{T}_\gamma = \begin{bmatrix} \mathbf{R}_\gamma & \mathbf{0} \\ -\boldsymbol{\Omega}_\gamma \mathbf{R}_\gamma & \mathbf{R}_\gamma \end{bmatrix}, \qquad \mathbf{T}_\gamma^{-1} = \begin{bmatrix} \mathbf{R}_\gamma^T & \mathbf{0} \\ \mathbf{R}_\gamma^T \boldsymbol{\Omega}_\gamma & \mathbf{R}_\gamma^T \end{bmatrix} \tag{2.72}$$

The rotation matrix for the flight-path angle is given by:

$$\mathbf{R}_\gamma = \begin{bmatrix} \cos\gamma & \sin\gamma \\ -\sin\gamma & \cos\gamma \end{bmatrix} = \theta^{-1} \begin{bmatrix} \rho & e\sin\vartheta \\ -e\sin\vartheta & \rho \end{bmatrix} \tag{2.73}$$

The angular velocity matrix is given by:

$$\boldsymbol{\Omega}_\gamma = \begin{bmatrix} 0 & -\dot{\gamma} \\ \dot{\gamma} & 0 \end{bmatrix} = \eta^{-3} n \rho^2 \theta^{-2} (\rho - \eta^2) \begin{bmatrix} 0 & -1 \\ 1 & 0 \end{bmatrix} \tag{2.74}$$

2.9 Appendix B: Details of element set C

This appendix summarizes the relationships between the C elements, the relative Kepler elements, the Yanamaka-Ankersen integration constants, and the state vector in the tangential frame. Linear transformations between different sets of ROE can be represented as matrices of partial derivatives. The transformation from Kepler elements to C elements is given by the matrix of partials from the C elements to the Kepler orbital elements.

$$\frac{\partial \mathbf{C}}{\partial \mathbf{k}} = p \begin{bmatrix} a^{-1} & -2e\eta^{-2} & 0 & 0 & 0 & 0 \\ ea^{-1} & -(1+e^2)\eta^{-2} & 0 & 0 & 0 & 0 \\ 0 & 0 & 0 & -e\cos i & -e & 0 \\ 0 & 0 & 0 & \eta^{-2}\cos i & \eta^{-2} & \eta^{-3} \\ 0 & 0 & -\cos\omega & -\sin i \sin\omega & 0 & 0 \\ 0 & 0 & \sin\omega & -\sin i \cos\omega & 0 & 0 \end{bmatrix} \tag{2.75}$$

The matrix of partials from the Kepler orbital elements to the C elements is given by:

$$\frac{\partial \mathbf{k}}{\partial \mathbf{C}} = \frac{1}{p} \begin{bmatrix} a\eta^{-2}(1+e^2) & -2ae\eta^{-2} & 0 & 0 & 0 & 0 \\ e & -1 & 0 & 0 & 0 & 0 \\ 0 & 0 & 0 & 0 & -\cos\omega & \sin\omega \\ 0 & 0 & 0 & 0 & -\dfrac{\sin\omega}{\sin i} & -\dfrac{\cos\omega}{\sin i} \\ 0 & 0 & -e^{-1} & 0 & \cot i \sin\omega & \cot i \cos\omega \\ 0 & 0 & e^{-1}\eta & \eta^3 & 0 & 0 \end{bmatrix} \tag{2.76}$$

The elements C can also be related to the Yamanaka-Ankersen set of trajectory integration constants [145]. The order of the integration constants is the same as in the original paper by Yamanaka and Ankersen. The linear transformation matrix from the Yamanaka-Ankersen integration constant to the elements C is given by:

$$\frac{\partial \mathbf{C}}{\partial \mathbf{y}} = \begin{bmatrix} 0 & 0 & -2e & -2 & 0 & 0 \\ 0 & 0 & -(1+e^2) & -2e & 0 & 0 \\ -e & -1 & 0 & 0 & 0 & 0 \\ \eta^{-2} & e\eta^{-2} & 0 & 0 & 0 & 0 \\ 0 & 0 & 0 & 0 & 0 & 1 \\ 0 & 0 & 0 & 0 & -1 & 0 \end{bmatrix} \tag{2.77}$$

The linear transformation matrix from the elements C to the Yamanaka-Ankersen integration constant is given by:

$$\frac{\partial \mathbf{y}}{\partial \mathbf{C}} = \begin{bmatrix} 0 & 0 & e\eta^{-2} & 1 & 0 & 0 \\ 0 & 0 & -\eta^{-2} & -e & 0 & 0 \\ e\eta^{-2} & -\eta^{-2} & 0 & 0 & 0 & 0 \\ -\dfrac{1}{2}(1+e^2)\eta^{-2} & e\eta^{-2} & 0 & 0 & 0 & 0 \\ 0 & 0 & 0 & 0 & 0 & -1 \\ 0 & 0 & 0 & 0 & 1 & 0 \end{bmatrix} \tag{2.78}$$

The Yamanaka-Ankersen equations are non-singular if the eccentricity goes to zero [145]. Equations (2.77) and (2.78) do not contain any divisors of the eccentricity, indicating that the transformation from the C elements and the Yamanaka-Ankersen set of trajectory integration constants is non-singular if the eccentricity goes to zero.

To obtain the linear mapping matrix from the C element vector to the Cartesian state in the TAN frame, the following expression needs to be evaluated:

$$\mathbf{B}_{C,TAN} = \mathbf{T}_{\gamma}^{-1}\mathbf{B}\frac{\partial \mathbf{k}}{\partial \mathbf{C}} \tag{2.79}$$

The elements of the linear mapping matrix from the C element vector to the Cartesian state in the TAN frame can then be found as:

$$\begin{aligned}
&\mathbf{B}_{C,TAN}(1,1) = \rho^{-1}\eta^{-2}\theta^{-1}\{e(\theta^2+2)\sin\vartheta\}, && \mathbf{B}_{C,TAN}(2,1) = -\rho^{-1}\theta^{-1},\\
&\mathbf{B}_{C,TAN}(1,2) = \rho^{-1}\eta^{-2}\theta^{-1}\{-2(\rho+e^2)\sin\vartheta\}, && \mathbf{B}_{C,TAN}(2,2) = -\rho^{-1}\theta^{-1}\cos\vartheta\,,\\
&\mathbf{B}_{C,TAN}(1,3) = \rho^{-1}\eta^{-2}\theta^{-1}\{2(e+cos\,\vartheta)\rho\}, && \mathbf{B}_{C,TAN}(2,3) = -\rho^{-1}\theta^{-1}\sin\vartheta\,,\\
&\mathbf{B}_{C,TAN}(1,4) = \theta, && \mathbf{B}_{C,TAN}(2,4) = 0,\\
&\mathbf{B}_{C,TAN}(3,1) = n\eta^{-5}\theta^{-3}\left\{\frac{1}{2}(1+e^2)\theta^2+\rho^3(\theta^2-2)\right\}, &&\\
&\mathbf{B}_{C,TAN}(3,2) = n\eta^{-5}\theta^{-3}\{(4e^2[e^2+\rho]-2\rho^3)\cos\vartheta+e(1+e^2)\}, &&\\
&\mathbf{B}_{C,TAN}(3,3) = n\eta^{-5}\theta^{-3}\{-2\rho^3\sin\vartheta\}, &&\\
&\mathbf{B}_{C,TAN}(3,4) = n\eta^{-3}\theta^{-1}\{-\rho^2 e\sin\vartheta\}, &&\\
&\mathbf{B}_{C,TAN}(4,1) = n\eta^{-3}\theta^{-3}\{-(\theta^2+\rho)e\sin\vartheta\}, &&\\
&\mathbf{B}_{C,TAN}(4,2) = n\eta^{-3}\theta^{-3}\{(\theta^2+\rho[1-\rho])\sin\vartheta\}, &&\\
&\mathbf{B}_{C,TAN}(4,3) = n\eta^{-3}\theta^{-3}\{(4\eta^2+\rho^2-3[\rho+1])\cos\vartheta-e(2+e^2)\}, &&\\
&\mathbf{B}_{C,TAN}(4,4) = 0 &&
\end{aligned} \tag{2.80}$$

Similarly, the inverse mapping can be found from:

$$\mathbf{B}_{C,TAN}^{-1} = \left(\frac{\partial \mathbf{k}}{\partial \mathbf{C}}\right)^{-1}\mathbf{B}^{-1}\mathbf{T}_{\gamma} \tag{2.81}$$

The elements of the linear mapping matrix from the Cartesian state in the TAN frame to the C element vector can then be found as:

$$
\begin{aligned}
&\mathbf{B}_{C,TAN}^{-1}(1,1) = \theta^{-3}\{2e\rho^2 \sin\vartheta\},\\
&\mathbf{B}_{C,TAN}^{-1}(2,1) = \theta^{-3}\{-2e\rho^2 \sin\vartheta\cos\vartheta\},\\
&\mathbf{B}_{C,TAN}^{-1}(3,1) = \theta^{-3}\{-2e\rho^2 \sin^2\vartheta\},\\
&\mathbf{B}_{C,TAN}^{-1}(4,1) = \eta^{-2}\theta^{-3}\{2\rho^3 - \theta^2\},\\
&\mathbf{B}_{C,TAN}^{-1}(1,2) = \theta^{-3}\{-2(\rho^3 + \theta^2)\},\\
&\mathbf{B}_{C,TAN}^{-1}(2,2) = \theta^{-3}\left\{\begin{matrix}[4\rho^3 + (1+e^2)\rho^2 - 3(1+e^2)\rho - 4(1+e^2)^2 + 5(1+e^2)]\cos\vartheta \\ -e(1+e^2)(2+e^2)\end{matrix}\right\},\\
&\mathbf{B}_{C,TAN}^{-1}(3,2) = \theta^{-3}\{\theta^2 + \rho(\eta^2 + \rho[\theta^2 + 2e\cos\vartheta])\}\sin\vartheta\,,\\
&\mathbf{B}_{C,TAN}^{-1}(4,2) = \eta^{-2}\theta^{-3}\{2e\rho^2 \sin\vartheta\},\\
&\mathbf{B}_{C,TAN}^{-1}(1,3) = n^{-1}\eta^3\theta^{-1}\{2\},\\
&\mathbf{B}_{C,TAN}^{-1}(2,3) = n^{-1}\eta^3\theta^{-1}\{-2\cos\vartheta\},\\
&\mathbf{B}_{C,TAN}^{-1}(3,3) = n^{-1}\eta^3\theta^{-1}\{-2\sin\vartheta\},\\
&\mathbf{B}_{C,TAN}^{-1}(4,3) = n^{-1}\eta\rho^{-1}\theta^{-1}\{-2e\sin\vartheta\},\\
&\mathbf{B}_{C,TAN}^{-1}(1,4) = n^{-1}\eta^3\rho^{-1}\theta^{-1}\{2e\sin\vartheta\},\\
&\mathbf{B}_{C,TAN}^{-1}(2,4) = n^{-1}\eta^3\rho^{-1}\theta^{-1}\{(1+e^2)\sin\vartheta\},\\
&\mathbf{B}_{C,TAN}^{-1}(3,4) = n^{-1}\eta^3\rho^{-1}\theta^{-1}\{-[(1+e^2)\cos\vartheta + 2e]\},\\
&\mathbf{B}_{C,TAN}^{-1}(4,4) = n^{-1}\eta\theta^{-1}\{2\},
\end{aligned}
\tag{2.82}
$$

Neither the linear mapping matrix from the C element vector to the Cartesian state in the TAN frame nor its inverse contains the eccentricity as a divisor. This implies that the C elements do not become singular when the eccentricity goes to zero. In fact, if the eccentricity approaches zero, the expressions in the matrices $\mathbf{B}_{C,TAN}$ and $\mathbf{B}_{C,TAN}^{-1}$ can be compared to the travelling ellipse formulation used in circular orbit rendezvous [168]. If the eccentricity approaches zero, the matrix $\mathbf{B}_{C,TAN}$ becomes:

$$
\lim_{e\downarrow 0} \mathbf{B}_{C,TAN} = \begin{bmatrix} 0 & -2\sin\vartheta & 2\cos\vartheta & 1 \\ -1 & -\cos\vartheta & -\sin\vartheta & 0 \\ -\frac{3}{2}n & -2n\cos\vartheta & -2n\sin\vartheta & 0 \\ 0 & n\sin\vartheta & -n\cos\vartheta & 0 \end{bmatrix}
\tag{2.83}
$$

And the matrix $\mathbf{B}^{-1}_{C,TAN}$:

$$
\lim_{e\downarrow 0} \mathbf{B}_{C,TAN}^{-1} = \begin{bmatrix} 0 & -4 & 2n^{-1} & 0 \\ 0 & 3\cos\vartheta & -2n^{-1}\cos\vartheta & n^{-1}\sin\vartheta \\ 0 & 3\sin\vartheta & -2n^{-1}\sin\vartheta & -n^{-1}\cos\vartheta \\ 1 & 0 & 0 & 2n^{-1} \end{bmatrix}
\tag{2.84}
$$

The parameter C_1 represents the altitude of the centre of the ellipse, the parameter C_4 represents the along-track distance of the centre of the ellipse and the parameters C_2 and C_3 parameterize the 2 x 1 travelling ellipse.

For completeness, the ROE transition matrix for the C elements is given by:

$$\mathbf{\Phi}_C = \frac{\partial \mathbf{C}}{\partial \boldsymbol{\delta\alpha}} \mathbf{\Phi}_\alpha \left(\frac{\partial \mathbf{C}}{\partial \boldsymbol{\delta\alpha}}\right)^{-1} = \begin{bmatrix} 1 & 0 & 0 & 0 \\ 0 & 1 & 0 & 0 \\ 0 & 0 & 1 & 0 \\ -\frac{3}{2}\eta^{-5}(1+e^2)n\,t & -3e\eta^{-5}nt & 0 & 1 \end{bmatrix} \tag{2.85}$$

3

Analytical Solutions to Two-Impulse Non-drifting Transfer Problems for Rendezvous in Elliptical Orbits[3]

This paper develops the analytical solution to the non-drifting transfer problem for rendezvous in elliptical orbits. The transfer algorithm generates a non-drifting, passively safe trajectory between two spacecraft states by finding the appropriate manoeuvres and transfer time. The non-drifting solution is derived first for Cartesian state vectors, which is useful for transferring to a terminal approach point that is defined in terms of such a Cartesian state vector. Next, the transfer problem is solved in terms of differential orbital elements. This second solution lends itself well to perform close-range rendezvous in elliptical orbits.

[3] This chapter was previously published in AIAA Journal of Guidance, Control, and Dynamics, doi: 10.2514/1.61885.

3.1 Introduction

Trajectory safety is of paramount importance during close-range rendezvous and/or formation flying. Passive trajectory protection is a design philosophy that strives to make trajectories safe by ensuring that the trajectory remains collision-free for a specified amount of time, even if the spacecraft becomes unable to apply thrust at some point during the approach. A common method to ensure passive trajectory protection during the close-range rendezvous phases is to require that transfer trajectories be drift-free [154]. This means that if a spacecraft has initiated a transfer trajectory and it is not possible to perform the second manoeuvre, the spacecraft do not drift apart or closer to each other. The spacecraft remains in the transfer trajectory, such that (in the absence of disturbances) it returns to the original point of departure one orbit after the first manoeuvre and to the terminal point after the nominal transfer time plus one orbit [134]. For example, the Automated Transfer Vehicle (ATV) uses a radial impulsive transfer manoeuvre during the close approach phase of rendezvous with the International Space Station (ISS), which indeed guarantees a natural stability in the relative position of the two spacecraft [18]. Up to now, the radial impulsive transfer is the most common non-drifting approach trajectory, the use of which is, however, limited to circular orbits. Di Sotto has provided a numerical algorithm to find general non-drifting transfers in elliptical orbits [169]. The purpose of this document is to describe an analytical solution for the general non-drifting transfer problem between arbitrary relative states during rendezvous in elliptical orbits.

The development of the non-drifting transfer is aimed at rendezvous in elliptical orbits, with a focus on the on-board computation of manoeuvres. At present, most rendezvous missions are carried out in circular LEO, often involving at least one crewed spacecraft, with a push towards greater on-board autonomy [2]. A case can be made for (semi-)autonomous rendezvous in elliptical orbits. Mission scenarios that would require rendezvous include on-orbit inspection & servicing [170], sample return [171], while close formation flying missions use non-drifting trajectories in a similar way to keep the formation safe [44]. A mission for On-Orbit Servicing of geostationary telecommunication satellites has been studied [172], where the objective is to give a life extension by handling the attitude and orbit control tasks of communication satellites whose propellant has been exhausted. On-Orbit Servicing missions could benefit greatly from the capability of performing rendezvous in elliptical orbits, in this case to perform orbital rescue. A failure of the propulsion system of the upper stage of a launch vehicle during the transfer from geostationary transfer orbit (GTO) to GEO may leave a satellite in a fairly eccentric orbit, with Orion 3 as a good example [173]. Such satellites could be rescued by a space tug capable of performing elliptical orbit rendezvous. The potential gains of orbital rescue would be greater than orbital life extension because the satellite-to-be-rescued would be at the beginning of its lifetime instead of at the end. Rendezvous in GTO has been studied before [174], and a mission to perform inspection and servicing in GTO has been proposed [175]. Proba-3, a close formation flying demonstrator mission in HEO, is currently being studied as a preparation for future “virtual structure” space telescopes [176]. HEO provides an acceptably low-perturbation environment for such virtual structures around apocentre, and can be selected as a cost-effective alternative to Lagrange point orbits [26]. The proposed Mars Sample Return (MSR) mission may also benefit from the flexibility provided by elliptical orbit rendezvous and on-board computation of manoeuvres may be required because of the constrained communication link. Elliptic orbit rendezvous capability would provide robustness of the rendezvous mission element to failure in the Planetary Ascent Vehicle (PAV) [122]. If the PAV does not succeed in launching the sample container into the desired circular orbit, and remains in an elliptical orbit, the Earth Return Vehicle (ERV) could perform the rendezvous with the sample container in this orbit. Rendezvous in an elliptical parking orbit could even be included in the nominal mission as a propellant-saving mission element [121]. On-board autonomy is a means to make missions more robust [177], reduce cost [178], and, in the case of MSR, handle communication delays and long periods without communication [179]. It is noted that more on-board computational power is required for increased on-board autonomy [179]. An alternative approach is to develop simple, robust algorithms that can be used in a generalization of the ATV approach strategy to elliptic orbit rendezvous. This has the added advantage that general considerations for the design of the rendezvous strategy can be re-used [180]. Summarizing, the reasons for studying rendezvous in elliptical orbits are greater flexibility and robustness, potential propellant savings, and intrinsic mission needs. The non-drifting transfer fits in as a generalization of passively safe approach strategies already in use for circular orbit rendezvous.

The development of relative motion theories is of major interest to the study of elliptical orbit rendezvous. The equations of motion are relatively easy to solve for circular orbits. These equations are known as the Clohessy-Wiltshire or Hill-Clohessy-Wiltshire equations [149]. Many theories have recently been developed to describe relative motion around elliptical orbits, and a reasonably large portion of these includes perturbations. An overview of relative motion theories is presented in [151]. Perturbed relative motion theories can be obtained relatively easily from (semi-)analytical satellite theories, because the state transition matrix is often generated for use in differential correction orbit determination schemes [146,150]. Such state transition matrices are generally expressed in the inertial frame instead of in the relative orbital frame, and thus require an additional transformation. The transformation matrix between these frames is a composition of the rotation matrix and the angular velocity matrix of the relative reference frame. One of the most frequently cited linear perturbed relative motion theories that include the J_2 perturbation has been derived by Gim and Alfriend [72]. It can be shown that periodic relative trajectories are not possible around elliptical orbits perturbed by J_2, and that near-periodic orbits are only possible around orbits that have a specific inclination [181,182]. However, an examination of the Gim-Alfriend state transition matrix shows that the perturbation is of the order of J_2, times the mean orbital rate, times the propagation time. This works out to a trajectory error of about three parts in a thousand for a typical transfer duration of half an orbital period. For comparison, thrust errors are regularly assumed to be of the order of a few percent [154]. The manoeuvre frequency is generally higher for rendezvous than for formation flying, leading to a shorter propagation time required, and a proportionally greater impact of thruster errors on the trajectory evolution. The J_2 perturbation, which is usually the largest perturbation, is therefore relatively unimportant for the rendezvous problem. For the same reasons (i.e., short propagation times between manoeuvres, and large uncertainties associated with the impulsive manoeuvres), the influence of drag on the trajectory evolution can be neglected as well. The relative dynamics are described using a linearization of the relative motion between two unperturbed Keplerian orbits.

Relative trajectories around an elliptical Keplerian orbit are non-drifting if the difference in semi-major axis between the two orbits is equal to zero. Two main approaches exist to describe the linearized unperturbed relative motion between two spacecraft. The first approach, followed by Yamanaka and Ankersen, uses the Cartesian state vector [145] for solving the linearized equations of relative motion directly, while the second approach uses linear differences in orbital elements [147]. The differences in orbital elements are constants of motion for the relative motion, and they can be found by a transformation of the Cartesian state vector. The problem of finding transfer trajectories can similarly be approached in two different ways. One can use a Cartesian formulation of the problem to find trajectories that link positions specified in Cartesian space, or, alternatively, one can specify a transfer between two sets of (differential) orbital elements. At first glance these two approaches would seem to be the same, except for the formulation of the state vector. However, the difference in formulation of the state vector leads to different applications for the two solutions of the problem. The solution is presented here for both the Cartesian transfer and the differential orbital element transfer.

The requirement that the difference in semi-major axis be zero indicates that the differential orbital elements are the most promising starting point for deriving the non-drifting condition. The in-plane motion is uncoupled from the out-of-plane motion, and the out-of-plane oscillation is periodic in nature, such that the out-of-plane motion does not require additional measures to ensure periodicity of the trajectory. For this reason, the out-of-plane oscillation can be left out of the discussion of obtaining transfers that are periodic. Obviously, the out-of-plane motion does need to be considered when the rendezvous is performed, because all three elements of the position vector need to match the specified terminal conditions. The two-dimensional problem that remains consists of four equations and five unknowns: the transfer time (or angle) and the components of the first and second ΔV. The epoch of the first manoeuvre is assumed to be a given, determined by the rendezvous plan. A commonly used guidance algorithm computes the ΔV required to reach a desired final state departing from a given initial state in a given amount of time by performing a matrix inversion of part of the state transition matrix [183]. Such a transfer is called the two-point transfer or Lambert transfer [134]. The drawback of this approach is that the transfer is almost certainly not periodic. Because the two-point transfer is fully determined, i.e., because it has four equations with four unknowns, it does not allow imposing the condition of periodicity directly. To achieve this, the fixed transfer time needs to be replaced by the non-drifting condition, but in this case a completely different solution strategy must be adopted.

The following strategy is used to arrive at the solution of the non-drifting transfer problem. First, the problem is reduced to three equations and three unknowns; second, the transfer angle is determined, and the required ΔV is computed. The first step in reducing the non-drifting transfer problem should be to find the ΔV component that removes the difference in semi-major axis. This ΔV is tangential to the orbit at the point of application (that is, parallel to the velocity vector of the reference orbit at that point) and can be found easily. As a result, the general non-drifting transfer problem can be reduced to a set of three independent equations. The fourth, dependent, equation simply states that the difference in semi-major axis is zero. It follows that none of the other ΔV's to be applied are allowed to change the semi-major axis difference. This implies that the ΔV's are restricted to the direction perpendicular to the local velocity vector of the reference orbit, and the only undetermined aspect is their magnitude. The problem of the non-drifting transfer can thus be reduced without loss of generality to a problem of three equations and three unknowns: the transfer angle, and the magnitudes of the ΔV's perpendicular to the local velocity vector of the reference orbit. The computation of the transfer angle and the required ΔV's consists of solving a linear algebra problem and a trigonometric polynomial. The linear algebra operations are reasonably straightforward, but the solution of the trigonometric polynomial can be more difficult, especially since the problem in Cartesian formulation involves a cubic equation.

The problem has now been restricted in two ways, firstly by excluding perturbations such as J_2 and drag, and secondly by excluding the out-of-plane motion from the problem. This has important implications for trajectory safety. The approach to trajectory safety followed here is to ensure that trajectories remain collision-free in case no further manoeuvres are applied [154]. This implies that long propagation times are required to evaluate the probability of collision, and in this case the effects of J_2 and drag become important. To mitigate the effects of differential drag on an approach strategy featuring radial hops two approaches are suggested [184]. The approach direction can be chosen such that differential drag acts to drive the chaser away from the chaser. Alternatively, a small tangential component can be added to the first ΔV such that the chaser drifts away from the target. The magnitude would be chosen depending on the ratio of ballistic coefficients of the chaser and the target. Collision risk may also be reduced by adding an out-of-plane oscillation that has the proper phase with respect to the in-plane oscillations. This is the method of inclination / eccentricity vector separation [44]. Trajectories featuring inclination / eccentricity vector separation have been shown to be safe under the J_2 perturbation for 50 orbits [185].

This paper is structured as follows. The next section provides the mathematical description of relative motion in elliptical orbits and provides the mathematical framework for analysing non-drifting transfer manoeuvres in terms of the Cartesian state and in terms of differential orbital elements. The third section provides the solution to the non-drifting transfer problem, the most important aspect of which is the solution of the transfer angle. The problem is solved first for the transfer problem expressed in terms of the Cartesian state. Next the problem is solved in terms of differential orbital elements, and the difference between the solutions is discussed. The fourth section presents a three-step verification of the algorithms. The first step is a comparison between the numerical algorithm developed by Di Sotto and the new solution developed here. The second step is based on a linear propagation of the solution by means of an independently derived linear propagator, namely, the Yamanaka-Ankersen equations. The third step in the verification is to integrate the algorithm into a Keplerian orbit propagator and compare the performance with the results of the linear propagation. The paper ends with conclusions.

3.2 Mathematical Description of the Non-Drifting Transfer Problem

The motion of one spacecraft, the chaser, is described with respect to that of the other spacecraft, the target, which is located at the origin of the local vertical, local horizontal (LVLH) reference frame. The target spacecraft is moving along an unperturbed Keplerian reference orbit, described in terms of the classical Keplerian elements $\boldsymbol{\alpha} = [a \quad e \quad i \quad \Omega \quad \omega \quad M_0]^T$. Figure 3.1 shows the reference orbit and the orientation of the LVLH reference frame with respect to the planet-centred, inertial frame. The y-axis of the LVLH frame is perpendicular to the orbital plane and points in the opposite direction of the angular momentum vector. The z-axis points towards the centre of the planet and the x-axis completes the right-handed reference frame (and is therefore not necessarily aligned with the local velocity vector of the reference orbit) [134]. It should be noted that no conventional notation exists, and that alternative reference frames are possible (see for example [72]). Further, it is often assumed that the coordinate system is cylindrical or spherical, meaning that the x-coordinate or both the x- and y-coordinates are interpreted as angular coordinates. The use of cylindrical or spherical coordinates and the transformation operations required to obtain Cartesian coordinates are independent of the state transition matrix itself, and they do not affect the calculation of manoeuvres. The development of linear algorithms is based only on the state transition matrix, and for this reason, the introduction of cylindrical or spherical coordinates is not required for this development.

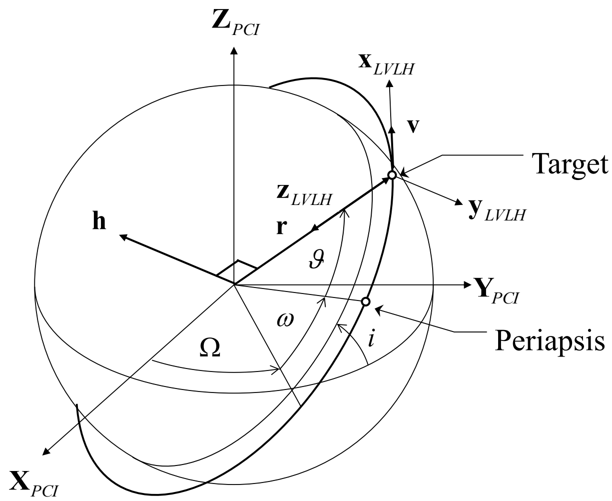

Figure 3.1: LVLH reference frame with respect to the inertial frame.

The relative position and velocity of the chaser spacecraft with respect to the target spacecraft are represented by the Cartesian state vector $\mathbf{x}$. The Cartesian state vector at a certain time 2 can be related to the vector at another time 1 using the state transition matrix $\mathbf{\Phi}$:

$$\mathbf{x}_2 = \mathbf{\Phi}_{1\rightarrow 2}\mathbf{x}_1 \tag{3.1}$$

Several authors suggest a factorization of the state transition matrix into a product of three matrices, one of which is the near-diagonal orbital element transition matrix $\mathbf{\Phi}_{\boldsymbol{\alpha}}$ and the other two produce a change of basis from Cartesian space to differential orbital element space and vice versa [114,147]. So, the Cartesian state vector and the differential orbital elements vector are related through the transformation matrix $\mathbf{B}$, which contains the partial derivatives of the Cartesian state expressed in the LVLH frame to the orbital elements. The partial derivatives are functions of the reference orbital elements.

$$\mathbf{x} = \mathbf{B}\boldsymbol{\delta\alpha} \tag{3.2}$$

where $\boldsymbol{\delta\alpha}$ represents the differential orbital elements vector. The factorization of the state transition matrix is given by:

$$\mathbf{\Phi}_{1\to 2} = \mathbf{B}_2 \mathbf{\Phi}_{\alpha,1\to 2} \mathbf{B}_1^{-1} \tag{3.3}$$

Note that the differential orbital elements need not be the same elements as the orbital elements that define the reference orbit. The differential orbital elements should be regarded as constants of motion for the relative dynamics [114], and any useful set of constants may be selected. The differential orbital elements can be considered as canonical variables for the description of the relative motion in the rendezvous problem [186].

The motion in the in-plane and out-of-plane directions is decoupled, and the state transition matrix is often presented separately for the in-plane and out-of-plane components. However, the use of Keplerian differential orbital elements introduces artificial singularities in the solution at zero eccentricity and zero inclination of the reference orbit, and the motion in the in-plane and out-of-plane directions becomes coupled through the right ascension of the ascending node. The motion in the out-of-plane direction can easily be decoupled by taking the following differential element instead of the argument of pericentre [169]:

$$\delta\psi = \delta\omega + \delta\Omega \cos i \tag{3.4}$$

In the following, it will be tacitly assumed that this change of variables is performed, and the more familiar expression for the argument of perigee is used instead. The solution for the non-drifting transfer only concerns the in-plane motion, because the out-of-plane motion is periodic by itself. Because the out-of-plane motion is uncoupled from the in-plane motion, and because the out-of-plane motion does not require special attention to create periodic trajectories, the state vector contains only the in-plane coordinates. The state vector is organized as follows:

$$\mathbf{x} = [x \quad z \quad \dot{x} \quad \dot{z}]^T \tag{3.5}$$

The in-plane orbital element vector that will be used is the following:

$$\boldsymbol{\delta\alpha} = [\delta a \quad \delta e \quad \delta\omega \quad \eta\delta M]^T \tag{3.6}$$

where η is equal to √(1-e²). The in-plane components of the matrix B are given by:

$$\mathbf{B} = \frac{p}{\rho}\left[\frac{1}{a}\begin{pmatrix} 0 \\ -1 \\ -\frac{3}{2}\dot{\vartheta} \\ \frac{1}{2}\dot{\vartheta}\tan\gamma \end{pmatrix} \quad \eta^{-2}\begin{pmatrix} \{1+\rho\}\sin\vartheta \\ c \\ \{(e\rho + c)/\rho^2 + c\}\dot{\vartheta} \\ s\dot{\vartheta} \end{pmatrix} \quad \begin{pmatrix} 1 \\ 0 \\ \dot{\vartheta}\tan\gamma \\ 0 \end{pmatrix} \quad \eta^{-2}\begin{pmatrix} \rho^2 \\ -es \\ -es\dot{\vartheta} \\ \{\rho-\rho^2\}\dot{\vartheta} \end{pmatrix}\right] \tag{3.7}$$

Besides the semi-latus rectum p, the orbital angular velocity $\dot{\vartheta}$ and the flight path angle γ, the following parameters have been introduced in this equation:

$$\rho = 1 + e\cos\vartheta\,, \qquad s = \rho\sin\vartheta\,, \qquad c = \rho\cos\vartheta \tag{3.8}$$

The matrix B represents the in-plane linear mapping between Cartesian coordinates in the LVLH frame and differential orbital elements [147] adapted to the set of differential orbital elements given in equation (3.6). The linear mapping is valid for small separations compared to the orbital radius of the target. The inverse of the matrix **B** is given by:

$$\mathbf{B}^{-1} = \frac{\rho}{p}\begin{bmatrix} 2a\eta^{-2}(-es & -\{\rho+\rho^2\} & \rho^2\dot{\vartheta}^{-1} & -es\dot{\vartheta}^{-1}) \\ e^{-1}(-\tan\gamma\,\{\rho^2-\eta^2\} & -\{\rho+\rho^2-2\eta^2\} & \{\rho^2-\eta^2\}\dot{\vartheta}^{-1} & -es\dot{\vartheta}^{-1}) \\ e^{-1}\rho^{-1}(e\rho-\{1+\rho\}s\tan\gamma & -\{2+\rho\}s & \{1+\rho\}s\dot{\vartheta}^{-1} & c\rho\dot{\vartheta}^{-1}) \\ e^{-1}\rho^{-1}\left(\{1+\rho\}s\tan\gamma\right. & \left\{2+\rho+\frac{e^2}{\rho}\right\}s & -\{1+\rho\}s\dot{\vartheta}^{-1} & \left.\{2e-c\rho\}\dot{\vartheta}^{-1}\right) \end{bmatrix} \tag{3.9}$$

Lastly, the orbital elements transition matrix is given by:

$$\mathbf{\Phi}_\alpha = \begin{bmatrix} 1 & 0 & 0 & 0 \\ 0 & 1 & 0 & 0 \\ 0 & 0 & 1 & 0 \\ -\frac{3}{2}(\eta a)^{-1}nt & 0 & 0 & 1 \end{bmatrix} \tag{3.10}$$

The orbital elements transition matrix shows that drifting trajectories occur because of a coupling between the difference in semi-major axis and the mean anomaly. This observation immediately shows the usefulness of re-parameterizing the state transition matrix in terms of the orbital elements for analysing the non-drifting transfer problem: if a transfer trajectory can be found that does not have a difference in semi-major axis, then the difference in mean anomaly (and indeed all other elements) will be constant along the trajectory. This leads to a simplification of the problem because the elements transition matrix becomes equal to the identity matrix if the semi-major axis component is dropped.

3.2.1 Cartesian formulation

A general, two-burn transfer can be described in terms of the Cartesian relative state by incorporating two impulsive manoeuvres into the state propagation equation (3.1):

$$\mathbf{x}_2^+ = \mathbf{\Phi}_{1\to 2}(\mathbf{x}_1 + \mathbf{C}_1\mathbf{\Delta V}_1) + \mathbf{C}_2\mathbf{\Delta V}_2 \tag{3.11}$$

The superscripted "-" and "+" indicate the state vector just before and just after the application of the impulsive ΔV, and the matrix **C** relates the 2-by-1 impulsive shot **ΔV** to a change in the 4-by-1 state vector. The 4-by-2 matrix **C** is given by:

$$\mathbf{C} = \begin{bmatrix} \mathbf{0} \\ \mathbf{I} \end{bmatrix} \tag{3.12}$$

The matrix $\mathbf{B}^{-1}$ provides a condition for drift-free trajectories for the Cartesian state vector, by noting that the first row of this matrix relates the state vector to the differential semi-major axis. Setting δa = 0 leads to:

$$esx + (\rho + \rho^2)z - \dot{\vartheta}^{-1}\rho^2\dot{x} + \dot{\vartheta}^{-1}es\dot{z} = 0 \tag{3.13}$$

The procedure outlined in [169] is followed to reduce the dimensions of the Cartesian state transition matrix to 3. Solving for the x-component of the velocity in equation (3.13) allows removing the first column and the third row from the matrix **B**, because the x-component of the velocity becomes dependent on the other three components of the state vector. The reduced matrix **B** is now equal to:

$$\mathbf{B}_{red} = \frac{a}{\rho}\begin{bmatrix} (1+\rho)\sin\vartheta & \eta^2 & \rho^2 \\ c & 0 & -es \\ -s\dot{\vartheta} & 0 & (\rho-\rho^2)\dot{\vartheta} \end{bmatrix} \tag{3.14}$$

The inverse of this matrix is equal to:

$$\mathbf{B}_{red}^{-1} = \frac{1}{\rho a}\begin{bmatrix} 0 & \cos\vartheta & -\dfrac{\sin\vartheta}{\dot{\vartheta}} \\ \dfrac{\rho}{\eta^2} & \dfrac{\sin\vartheta}{e\eta^2} & \dfrac{(1+e^2)\rho - \eta^2}{\dot{\vartheta}e^2\eta^2} \\ 0 & -\dfrac{\sin\vartheta}{e} & -\dfrac{\cos\vartheta}{\dot{\vartheta}e} \end{bmatrix} \tag{3.15}$$

In addition, since the semi-major axis component has been removed, the elements transition matrix is reduced to the identity matrix. Setting the transfer angle φ equal to:

$$\varphi = \vartheta_2 - \vartheta_1 \tag{3.16}$$

The reduced transition matrix can now be found:

$$\mathbf{\Phi}_{red,1\to 2} = \mathbf{B}_{red,2}\mathbf{I}\mathbf{B}_{red,1}^{-1} = \frac{1}{\rho a}\begin{bmatrix} \frac{\rho_1}{\rho_2} & \frac{1+\rho_2}{\rho_2}\sin\varphi & \frac{1+\rho_2}{\dot{\vartheta}_1\rho_2}\left(\frac{1+\rho_1}{1+\rho_2} - \cos\varphi\right) \\ 0 & \cos\varphi & \frac{1}{\dot{\vartheta}_1}\sin\varphi \\ 0 & -\dot{\vartheta}_2\sin\varphi & \frac{\dot{\vartheta}_2}{\dot{\vartheta}_1}\cos\varphi \end{bmatrix} \tag{3.17}$$

This state transition matrix operates on the reduced state vector$\mathbf{x}_{red} = [x \quad z \quad \dot{z}]^T$. Note that the transfer time is no longer explicitly present in the reduced state transition matrix. The state transition matrix for non-drifting trajectories is the product of the matrix $\mathbf{B}_{red}$ and its inverse, evaluated at different epochs. The reduced problem in Cartesian coordinates is given by:

$$\mathbf{x}_{red,2}^{-} = \mathbf{\Phi}_{red,1\to 2}\mathbf{x}_{red,1}^{+} \tag{3.18}$$

Note that $\mathbf{x}_{red,1}^{+} = \mathbf{x}_{red,1}^{-} + \mathbf{C}\mathbf{\Delta V}_{z,1}$ and $\mathbf{x}_{red,2}^{+} = \mathbf{x}_{red,2}^{-} + \mathbf{C}\mathbf{\Delta V}_{z,2}$, with matrix $\mathbf{C}$ appropriately sized. This means that equation (3.18) features the reduced state vector $\mathbf{x}_{red,1}^{+}$ right after the application of ΔV_1 at time 1 and the reduced state vector $\mathbf{x}_{red,2}^{-}$ right before the application of ΔV_2 at time 2. The z-component of the velocity right after the application of ΔV_1 at time 1 and the z-component of the velocity right before the application of ΔV_2 at time 2 are unknowns to be solved for. Figure 3.2 illustrates the known and unknown variables in the non-drifting transfer problem. The initial state vector $[x_1 \quad z_1 \quad \dot{x}_1^{-} \quad \dot{z}_1^{-}]^T$ is given at a known time t_1. The terminal state vector $[x_2 \quad z_2 \quad \dot{x}_2^{+} \quad \dot{z}_2^{+}]^T$ is given at an unknown time t_2. The transfer time (t_2-t_1) and the required impulsive manoeuvres ΔV_1 and ΔV_2 need to be found. The position vector and the z-component of the velocity form part of the state vector in equation(3.18). The x-component of the velocity is implicitly defined by equation (3.13). The transfer time enters into equation (3.18) through the state transition matrix. The problem is solved for the transfer angle φ instead of the transfer time, but the time of the second manoeuvre can easily be recovered by means of Kepler's equation.

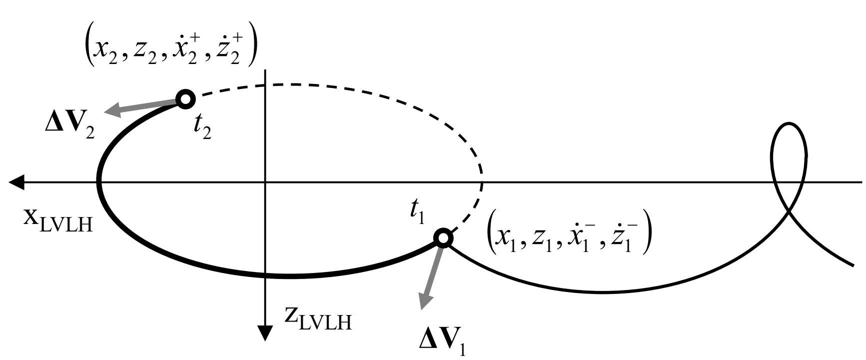

Figure 3.2: Non-drifting transfer problem in Cartesian coordinates.

In practice this algorithm can be used to define a transfer to a certain terminal point from which at a predefined time the chaser starts, for example, a forced motion to the target. The chaser performs station keeping at that terminal point between the time of application of the second ΔV of the transfer and the time at which the forced motion starts. An alternative strategy could be to keep time 2 fixed, such that the forced motion could be scheduled immediately after arriving at the terminal point. Figure 3.2 shows that prior to the manoeuvre at time 1 the chaser is moving along a drifting trajectory. If time 1 is kept free, then the exact point along this trajectory from which the transfer starts must be determined by the calculation of the transfer time. This increases the complexity significantly. Furthermore, because the same scheduling constraints could be met by inserting a time-flexible station-keeping element into the rendezvous scenario, the treatment of this problem is considered beyond the scope of this research.

3.2.2 Differential orbital elements formulation

The two-burn transfer manoeuvre can also be described in terms of differential orbital elements. The starting point is again the basic propagation equation, but this time, it should be the propagation equation for the differential elements. The impulsive manoeuvre needs to be incorporated by introducing a matrix that relates the manoeuvre to changes in the differential orbital elements:

$$\boldsymbol{\delta\alpha}_2^+ = \boldsymbol{\Phi}_{\alpha,1\to2}(\boldsymbol{\delta\alpha}_1^- + \mathbf{K}_1\boldsymbol{\Delta}\mathbf{V}_1) + \mathbf{K}_2\boldsymbol{\Delta}\mathbf{V}_2 \tag{3.19}$$

The matrix $\mathbf{K}$ relates the 2-by-1 impulsive ΔV vector to a change in the 4-by-1 differential orbital elements vector. The ΔV is decomposed in a more convenient frame of reference, with the first component parallel to the velocity vector and the second component perpendicular to the velocity vector.

$$\boldsymbol{\Delta}\mathbf{V} = \begin{bmatrix} \Delta V_{\parallel} \\ \Delta V_{\perp} \end{bmatrix} \tag{3.20}$$

The first reference frame axis is more commonly known as “V-bar”. The matrix $\mathbf{K}$ is related to the inverse of $\mathbf{B}$ by a rotation through the flight path angle around the y-axis:

$$\mathbf{K} = \frac{1}{e^2\rho V}\begin{bmatrix} \dfrac{2ae^2\rho(2\rho-\eta^2)}{\eta^2} & 0 \\ 2e\rho(\rho-\eta^2) & -e^2\eta^2\sin\vartheta \\ 2es & \rho(1+e^2)-\eta^2 \\ -2(\rho+e^2)e\sin\vartheta & -e\eta^2\cos\vartheta \end{bmatrix} \tag{3.21}$$

The description in terms of relative orbital elements directly provides the condition and the required ΔV for drift-free trajectories. Noting that element (1, 2) of the matrix

K is zero, it becomes apparent that the magnitude of the tangential component of the first ΔV should be such that it removes the difference in semi-major axis. The magnitude of the ΔV is:

$$\Delta V_{\parallel} = -\frac{V\eta^2}{2a(2\rho - \eta^2)}\delta a = -\frac{1}{2}\frac{h}{a\rho}\cos\gamma\frac{\delta a}{a} \tag{3.22}$$

The reduced differential orbital elements can be found from equation (3.21), using the tangential ΔV from equation (3.22):

$$\begin{bmatrix}\delta e\\ \delta\omega\\ \delta\tilde{M}\end{bmatrix}_{red} = \begin{bmatrix}\delta e\\ \delta\omega\\ \delta\tilde{M}\end{bmatrix} - \begin{bmatrix}\rho - \eta^2\\ \sin\vartheta\\ -\rho^{-1}(\rho + e^2)\sin\vartheta\end{bmatrix}\frac{r}{ae\rho}\cos^2\gamma\frac{\delta a}{a} \tag{3.23}$$

The problem to be solved in terms of differential orbital elements can now be reduced to three equations:

$$\boldsymbol{\delta\alpha}^{+}_{red,2} = \boldsymbol{\delta\alpha}^{-}_{red,1} + \mathbf{K}_{red,1}\Delta V_{\perp,1} + \mathbf{K}_{red,2}\Delta V_{\perp,2} \tag{3.24}$$

The matrix $\mathbf{K}_{red}$ consists of the second column of matrix **K** of equation (3.21), minus the element corresponding to the semi-major axis. The reduced orbital elements transition matrix is equal to the identity matrix and hence left out, such that the problem can be brought into the following form:

$$\begin{bmatrix}\delta e_2^+\\ \delta\omega_2^+\\ \delta\tilde{M}_2^+\end{bmatrix}_{red} = \begin{bmatrix}\delta e_2^-\\ \delta\omega_2^-\\ \delta\tilde{M}_2^-\end{bmatrix}_{red} + \begin{bmatrix}-e\eta^2\sin\vartheta_1\\ \rho_1(1+e^2)-\eta^2\\ -e\eta^2\cos\vartheta_1\end{bmatrix}\Delta\tilde{V}_{\perp,1} + \begin{bmatrix}-e\eta^2\sin\vartheta_2\\ \rho_2(1+e^2)-\eta^2\\ -e\eta^2\cos\vartheta_2\end{bmatrix}\Delta\tilde{V}_{\perp,2} \tag{3.25}$$

The ΔV has been scaled according to:

$$\Delta\tilde{V}_{\perp} = \frac{1}{e^2\rho V}\Delta V_{\perp} \tag{3.26}$$

Figure 3.3 shows a diagram of the non-drifting transfer problem and summarizes the steps taken up to now. Given the initial differential orbital element vector ($\delta\alpha_1$, δe_1, $\delta\omega_1$, δM_1) at known t_1 and terminal differential orbital element vector (0, δe_2, $\delta\omega_2$, δM_2), find the transfer time (t_2-t_1) and the required impulsive manoeuvres ΔV_1 and ΔV_2. The tangential component of the first manoeuvre can be found from equation (3.22). This leads to a reduced set of non-drifting differential elements, which are found from equation (3.24). The non-drifting components of the second differential orbital element vector and the radial components of the impulsive manoeuvres form part of equation (3.25) explicitly. The transfer time enters this equation implicitly, through the components of the matrix $\mathbf{K}_{red}$, which is evaluated both at θ_1 and at θ_2. Evaluation at θ_2 requires the transfer time. The differential semi-major axis after the transfer is assumed to be zero.

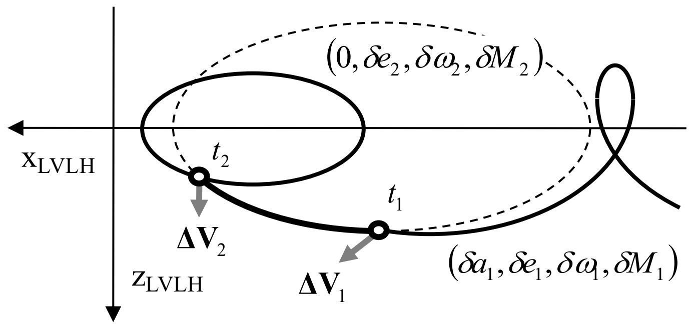

Figure 3.3: Non-drifting transfer problem in terms of differential orbital elements.

An important point to make here is that the two formulations of the problem lead to fundamentally different solutions. While the non-drifting transfer in Cartesian formulation aims for a fixed point in Cartesian space, the differential orbital elements formulation effectively aims for a set of trajectory constants, which means that the Cartesian position at the end point is in fact a function of the unknown transfer time, and this position is not fixed a priori. (Compare the solid ellipse in Figure 3.3 to the fixed end point in Figure 3.2.) The main difference between the two formulations lies in the type of problem to which they are applied. The Cartesian formulation can be used to target a fixed point in Cartesian space from which a forced motion approach to the target can be initiated. This algorithm is useful during the final stage of an impulsive rendezvous, just before switching to a forced motion approach. The differential orbital elements formulation can be used to transfer between trajectories during close range rendezvous. This algorithm can for example be used for transferring to a hold trajectory or to a trajectory with a specified eccentricity / inclination vector separation. In both cases, the differential orbital elements of the terminal trajectory are fixed rather than the Cartesian state of the terminal point.

3.3 Solution of the Non-Drifting Transfer Problem

Having completed the mathematical framework, the solution of the non-drifting transfer problem is now provided. This section solves the problem first in terms of the Cartesian state, and second in terms of the differential orbital elements. Finally, the two solutions are compared.

3.3.1 Solution of the problem in Cartesian formulation

The set of equations (3.18) is not very easy to solve directly. Expanding equation (3.18) by filling in the reduced state transition matrix from equation (3.17) leads to the following result:

$$\begin{aligned} x_2 &= \frac{\rho_1}{\rho_2} x_1 + \frac{1+\rho_2}{\rho_2} \sin\varphi\, z_1 + \frac{1+\rho_2}{\dot{\vartheta}_1 \rho_2}\left(\frac{1+\rho_1}{1+\rho_2} - \cos\varphi\right) \dot{z}_1^+ \\ z_2 &= \cos\varphi\, z_1 + \frac{1}{\dot{\vartheta}_1} \sin\varphi\, \dot{z}_1^+ \end{aligned} \tag{3.27}$$

The equation for the terminal vertical velocity $\dot{z}_2^-$ is not required for finding the transfer angle. In [169] this system of equations is not solved explicitly, but it is stated that $\dot{z}_1^+$ and the transfer angle are the unknown variables. The system of equations is non-linear because the coefficient matrix depends on the unknown transfer time. A numerical solution algorithm could be devised by noting that solving for $\dot{z}_1^+$ requires linear operations only, while solving for the transfer time involves non-linear trigonometric equations. A single, nonlinear equation of the transfer-time can be obtained by solving one of the equations for $\dot{z}_1^+$ and inserting the result into the other equation. A root-finding algorithm can then be employed to find the transfer angle from the resulting transfer time equation. For example, the second equation of (3.27) can be solved for the vertical velocity $\dot{z}_1^+$, which is inserted into the first equation. The only unknown left in this equation is the transfer angle φ.

$$\frac{\rho_1}{\rho_2} x_1 - x_2 + \frac{1+\rho_2}{\rho_2} \sin\varphi\, z_1 + \frac{1+\rho_2}{\rho_2}\left(\frac{1+\rho_1}{1+\rho_2} - \cos\varphi\right)\left(\frac{1}{\sin\varphi} z_2 - \frac{\cos\varphi}{\sin\varphi} z_1\right) = 0 \tag{3.28}$$

The resulting equation may cause problems for the numerical algorithm because it has a singularity when the transfer angle φ is equal to π, due to the inverse sine term. This would be an undesirable characteristic of the transfer angle algorithm; experience from circular orbits rendezvous shows that radial impulsive manoeuvres usually have a transfer angle close to this value [169]. The problem can be solved by multiplying the transfer time equation with the sine of the transfer angle before using the root-finding algorithm, making the function continuous. These simplifications can also be conducted analytically. Multiplying equation (3.28) by $\rho_2 \cdot \sin\varphi$ and simplifying the resulting terms leads to:

$$\rho_1 \sin\varphi\, x_1 - \rho_2 \sin\varphi\, x_2 + (1+\rho_1)(z_2 - \cos\varphi\, z_1) + (1+\rho_2)(-\cos\varphi\, z_2 + z_1) = 0 \tag{3.29}$$

Equation (3.29) can be modified to an equation that depends only on terms that contain the transfer angle explicitly by using angle sum and difference identities on the terms containing ρ_2. This leads to the following trigonometric equation for the transfer angle.

$$q_3 \sin^2\varphi + q_4 \sin\varphi \cos\varphi + q_1 \sin\varphi + q_2 \cos\varphi = q_2 \tag{3.30}$$

The coefficients q_1 to q_4 are:

$$
\begin{aligned}
q_1 &= \rho_1 x_1 - e\sin\vartheta_1\, z_1 - x_2 \\
q_2 &= -2(z_1 + z_2) \\
q_3 &= e(\cos\vartheta_1\, z_2 + \sin\vartheta_1\, x_2) \\
q_4 &= e(\sin\vartheta_1\, z_2 - \cos\vartheta_1\, x_2)
\end{aligned} \tag{3.31}
$$

Equation (3.30) is difficult to solve in its present form. The tangent half-angle identities for the sine and cosine of the transfer angle can be used to transform the trigonometric polynomial into an easier form to solve. The required identities are:

$$\sin\varphi = \frac{2t}{1+t^2} \text{ and } \cos\varphi = \frac{1-t^2}{1+t^2}, \text{ with } t = \tan\left(\frac{1}{2}\varphi\right) \tag{3.32}$$

This operation transforms the trigonometric equation into a cubic polynomial:

$$k_3 t^3 + k_2 t^2 + k_1 t + k_0 = 0 \tag{3.33}$$

The coefficients of this equation are given by:

$$
\begin{aligned}
k_0 &= -(q_4 + q_1) = \rho_1(x_2 - x_1) - e\sin\vartheta_1\,(z_2 - z_1) \\
k_1 &= q_2 - 2q_3 = -2(z_1 + \rho_1 z_2 + e\sin\vartheta_1\, x_2) \\
k_2 &= q_4 - q_1 = e\sin\vartheta_1\,(z_1 + z_2) - \rho_1(x_1 + x_2) + 2x_2 \\
k_3 &= q_2 = -2(z_1 + z_2)
\end{aligned} \tag{3.34}
$$

The cubic polynomial in equation (3.33) can be solved using algorithms provided in [187] or [188]. The solution provided in [188] is fully analytical, such that the objective to find an analytical solution to the transfer problem is satisfied. Three solutions exist, at least one of which is real. The potential for two additional real solutions is the result of the absence of the velocities in the z-direction from the equation for the transfer angle. It has been established empirically that in most cases the two additional solutions correspond to imaginary roots of the cubic polynomial, which do not produce physically meaningful solutions. If this is not the case, an operational choice can be made between the solutions, for example based on the transfer time or the required ΔV.

Note that the cubic polynomial becomes a quadratic polynomial if the z-coordinate after the transfer is equal in magnitude but opposite in sign to the z-coordinate before the transfer. The second coefficient could similarly be made to vanish. Such transfers are possible in theory, but they are unlikely to occur often in practice where the initial conditions for the algorithm are likely to be impacted by noise and dispersions.

The velocities in the z-direction at the start and end of the transfer can be found using the reduced state transition matrix from equation (3.17). The x-component of the velocity at the start and end of the transfer can be found from the non-drifting condition, equation (3.13). Solving for the z-component of the velocity at the start and end of the transfer and re-arranging the non-drifting condition gives:

$$
\begin{aligned}
\Delta V_{z,1} &= \dot{\vartheta}_1 \frac{\rho_2 x_2 - \rho_1 x_1 - (1+\rho_2)\sin\varphi\, z_1}{(1+\rho_1) - (1+\rho_2)\cos\varphi} - \dot{z}_1^- \\
\Delta V_{x,1} &= k^2\{e s_1 x_1 + (\rho_1 + \rho_1^2) z_1\} + \tan\gamma_1 \left(\dot{z}_1^- + \Delta V_{z,1}\right) - \dot{x}_1^- \\
\Delta V_{z,2} &= \dot{z}_2^+ - \dot{\vartheta}_2 \cos\varphi \frac{\rho_2 x_2 - \rho_1 x_1 - \tan\varphi\,(1+\rho_1) z_1}{(1+\rho_1) - (1+\rho_2)\cos\varphi} - \\
\Delta V_{x,2} &= \dot{x}_2^+ - k^2\{e s_2 x_2 + (\rho_2 + \rho_2^2) z_2\} - \tan\gamma_2 \left(\dot{z}_2^+ - \Delta V_{z,2}\right)
\end{aligned}
\tag{3.35}
$$

3

3.3.2 Solution of the problem in differential orbital elements formulation

The transfer angle problem is now solved in terms of the differential orbital elements. The set of equations (3.25) seems easier to solve than the set of equations (3.18). The problem to be solved is re-written in matrix form:

$$
\begin{bmatrix} \delta e_{\Delta V,1} & \delta e_{\Delta V,2} \\ \delta\omega_{\Delta V,1} & \delta\omega_{\Delta V,2} \\ \delta M_{\Delta V,1} & \delta M_{\Delta V,2} \end{bmatrix}
\begin{bmatrix} \Delta\tilde{V}_{\perp,1} \\ \Delta\tilde{V}_{\perp,2} \end{bmatrix}
= \begin{bmatrix} \Delta e \\ \Delta\omega \\ \Delta M \end{bmatrix}
\tag{3.36}
$$

The following parameters have been introduced:

$$
\begin{aligned}
&\Delta e = \delta e_2^+ - \delta e_1^+ && \Delta\omega = \delta\omega_2^+ - \delta\omega_1^+ && \Delta M = \delta\tilde{M}_2^+ - \delta\tilde{M}_1^+ \\
&\delta e_{\Delta V} = -e^2\eta^2 \sin\vartheta && \delta\omega_{\Delta V} = \rho(1+e^2) - \eta^2 && \delta M_{\Delta V} = -e\eta^2\cos\vartheta
\end{aligned}
\tag{3.37}
$$

These parameters are just shorthand notations for the differences between the (periodic) in-plane elements before and after the non-drifting transfer, and the effect of a scaled ΔV on the orbital element differences. Equation (3.36) is a system of three equations with three unknowns, although it is not a linear system. The unknown transfer angle enters the equation implicitly through the functions δe_2, $\delta\omega_2$ and δM_2. To solve the equation, start with the first of equation (3.36), and solve for the second scaled ΔV:

$$
\Delta\tilde{V}_{\perp,2} = \frac{1}{\delta e_{\Delta V,2}} \Delta e - \frac{\delta e_{\Delta V,1}}{\delta e_{\Delta V,2}} \Delta\tilde{V}_{\perp,1}
\tag{3.38}
$$

Substituting this result into the second of equation (3.36) leads to an expression for the first scaled ΔV:

$$
\Delta\tilde{V}_{\perp,1} = \frac{\delta e_{\Delta V,2}\Delta\omega - \delta\omega_{\Delta V,2}\Delta e}{\delta e_{\Delta V,2}\delta\omega_{\Delta V,1} - \delta e_{\Delta V,1}\delta\omega_{\Delta V,2}}
\tag{3.39}
$$

Substituting this expression back into equation (3.38) yields the second scaled ΔV:

$$\Delta\tilde{V}_{\perp,2} = \frac{\delta\omega_{\Delta V,1}\Delta e - \delta e_{\Delta V,1}\Delta\omega}{\delta e_{\Delta V,2}\delta\omega_{\Delta V,1} - \delta e_{\Delta V,1}\delta\omega_{\Delta V,2}} \tag{3.40}$$

Substituting equations (3.39) and (3.40) into the third of equation (3.36) leads to the following equation:

$$\begin{aligned}\left(\delta e_{\Delta V,2}\delta\omega_{\Delta V,1} - \delta e_{\Delta V,1}\delta\omega_{\Delta V,2}\right)\Delta M + \left(\delta M_{\Delta V,2}\delta e_{\Delta V,1} - \delta M_{\Delta V,1}\delta e_{\Delta V,2}\right)\Delta\omega \\ + \left(\delta M_{\Delta V,1}\delta\omega_{\Delta V,2} - \delta M_{\Delta V,2}\delta\omega_{\Delta V,1}\right)\Delta e = 0\end{aligned} \tag{3.41}$$

Re-inserting the parameters dependent on the true anomaly from equation (3.37) into equation (3.41) and simplifying the result produces the following expression:

$$\begin{aligned}&\{e\sin\vartheta_2\left(\rho_1[1+e^2]-\eta^2\right) - e\sin\vartheta_1\left(\rho_2[1+e^2]-\eta^2\right)\}\Delta M \\ &\quad + \{e^2(\sin\vartheta_1\cos\vartheta_2 - \sin\vartheta_2\cos\vartheta_1)\eta^2\}\Delta\omega \\ &\quad + \{(\rho_1[1+e^2]-\eta^2)\cos\vartheta_2 - (\rho_2[1+e^2]-\eta^2)\cos\vartheta_1\}\Delta e = 0\end{aligned} \tag{3.42}$$

This equation is re-written in terms of the transfer angle. The initial true anomaly is assumed a given, while the final true anomaly is to be determined. Under this assumption angle sum and difference identities for the sine and cosine can be used to obtain an equation in terms of the transfer angle. The result is a trigonometric equation of the following form:

$$C_1\sin\varphi + C_2\cos\varphi = C_2 \tag{3.43}$$

The parameters C_1 and C_2 are:

$$\begin{aligned}C_1 &= ([1+e^2] + 2e\cos\vartheta_1)\Delta M + \eta^2\Delta\omega + 2\sin\vartheta_1\,\Delta e \\ C_2 &= 2e\sin\vartheta_1\,\Delta M - 2\cos\vartheta_1\,\Delta e\end{aligned} \tag{3.44}$$

The structure of equation (3.43) shows that there exists a unique combination of differential elements determining the transfer. The solution of equation (3.43) is

$$\sin\varphi = \frac{2C_1C_2}{C_1^2 + C_2^2}, \qquad \cos\varphi = \frac{C_2^2 - C_1^2}{C_1^2 + C_2^2} \tag{3.45}$$

To allow a comparison with the solution in terms of the Cartesian state, equation (3.43) can also be solved by making the half-angle tangent substitution from equation (3.32), which leads to:

$$\varphi = 2\tan^{-1}\frac{C_1}{C_2} \tag{3.46}$$

The most straightforward way to obtain the impulsive ΔV's for the differential orbital elements formulation of the non-drifting transfer problem is to rewrite equation (3.35) in terms of the differential orbital elements, using equation (3.14) to obtain expressions for the Cartesian position components expressed in terms of the differential orbital elements.

$$
\begin{aligned}
\dot{z}_1^+ &= \frac{a\dot{\vartheta}_1}{(1+\rho_1)-(1+\rho_2)\cos\varphi}\left\{\begin{matrix}(1+\rho_2)\sin\vartheta_2\,\delta e_2^+\\ -([1+\rho_1]\sin\vartheta_1+[1+\rho_2]\sin\varphi\cos\vartheta_1)\delta e_1^-\\ +\eta^2(\delta\omega_2^+-\delta\omega_1^-)\\ +\rho_2^2\delta\widetilde{M}_2^+ + ([1+\rho_2]\sin\varphi\, e\sin\vartheta_1-\rho_1^2)\delta\widetilde{M}_1^-\end{matrix}\right\}\\
\dot{z}_2^- &= \frac{a\dot{\vartheta}_2\cos\varphi}{(1+\rho_1)-(1+\rho_2)\cos\varphi}\left\{\begin{matrix}(1+\rho_2)\sin\vartheta_2\,\delta e_2^+\\ -(1+\rho_1)(\sin\vartheta_1+\tan\varphi\cos\vartheta_1)\delta e_1^-\\ +\eta^2(\delta\omega_2^+-\delta\omega_1^-)\\ +\rho_2^2\delta\widetilde{M}_2^+ + (\tan\varphi\,[1+\rho_1]e\sin\vartheta_1-\rho_1^2)\delta\widetilde{M}_1^-\end{matrix}\right\}
\end{aligned}
\tag{3.47}
$$

Again using equation (3.14), the velocities in the z-direction before the first ΔV and after the second ΔV can be written as:

$$
\begin{aligned}
\dot{z}_1^- &= a\dot{\vartheta}_1\{-\sin\vartheta_1\,\delta e_1^- + (1-\rho_1)\delta\widetilde{M}_1^-\}\\
\dot{z}_2^+ &= a\dot{\vartheta}_2\{-\sin\vartheta_2\,\delta e_2^+ + (1-\rho_2)\delta\widetilde{M}_2^+\}
\end{aligned}
\tag{3.48}
$$

Subtracting the proper expressions from equations (3.47) and (3.48) leads to the impulsive velocity change required in the vertical direction.

$$
\begin{aligned}
\Delta\dot{z}_1 &= a\dot{\vartheta}_1\frac{\left(1+\rho_2\right)\sin\vartheta_2\,\Delta e+\eta^2\Delta\omega+\rho_2^2\Delta M}{\left(1+\rho_1\right)-\left(1+\rho_2\right)\cos\varphi}\\
\Delta\dot{z}_2 &= -a\dot{\vartheta}_2\frac{\left(1+\rho_1\right)\sin\vartheta_2\,\Delta e+\eta^2\cos\varphi\,\Delta\omega+\left\{\cos\varphi-\left(1+\rho_1\right)\left(1-\rho_2\right)\right\}\Delta M}{\left(1+\rho_1\right)-\left(1+\rho_2\right)\cos\varphi}
\end{aligned}
\tag{3.49}
$$

Since the position does not change when an impulsive ΔV is applied, equation (3.13) implies that to maintain a periodic trajectory, the change in the velocity in the x-direction needs to be related to the change in velocity in the z-direction as follows:

$$
\Delta\dot{x} = \tan\gamma\,\Delta\dot{z}
\tag{3.50}
$$

Because of equation (3.50), the ΔV is indeed pointed along the direction perpendicular to the reference orbit velocity vector at the point of application of the manoeuvre. The magnitude of the ΔV can thus be found from:

$$\begin{aligned} \Delta V_{\perp,1} &= \frac{aV_1}{r_1} \frac{\left(1+\rho_2\right)\sin\vartheta_2\,\Delta e + \eta^2 \Delta\omega + \rho_2^2 \Delta M}{\left(1+\rho_1\right) - \left(1+\rho_2\right)\cos\varphi} \\ \Delta V_{\perp,2} &= -\frac{aV_2}{r_2} \frac{\left(1+\rho_1\right)\sin\vartheta_2\,\Delta e + \eta^2 \cos\varphi\,\Delta\omega + \left\{\cos\varphi - \left(1+\rho_1\right)\left(1-\rho_2\right)\right\}\Delta M}{\left(1+\rho_1\right) - \left(1+\rho_2\right)\cos\varphi} \end{aligned} \tag{3.51}$$

This completes the derivation of the periodic transfer problem in differential orbital elements formulation.

3

3.4 Numerical verification

The non-drifting transfer algorithms are verified by means of computer simulations. The objective of these tests is to demonstrate that the non-drifting transfer solutions presented here are correct, and useful when implemented in an on-board rendezvous guidance system. A secondary objective is to perform a preliminary investigation on the usefulness and possible restrictions and limitations of the non-drifting algorithms when applied to a rendezvous scenario in a low orbit around Mars.

The numerical algorithm proposed by Di Sotto is referred to as algorithm NDA1, the Cartesian non-drifting transfer algorithm is referred to as algorithm NDA2 and the non-drifting algorithm based on the differential orbital elements is referred to as algorithm NDA3. Three test cases are defined to verify the non-drifting transfer algorithms developed in this paper: First, algorithm NDA2 is compared to algorithm NDA1 in terms of performance. Second, the output of algorithms NDA2 and NDA3 are used in combination with an independently developed linear propagator to verify the periodicity of the transfer solution. Third and last, the output of algorithms NDA2 and NDA3 are used in combination with a Keplerian orbit propagator in the same scenarios to evaluate the performance in a non-linear dynamics environment. The last test case is used to demonstrate how the non-drifting algorithms can be incorporated in a rendezvous strategy and to establish some guidelines for the design of such rendezvous strategies based on non-drifting hops.

3.4.1 Description of the rendezvous scenarios

Two simulation scenarios are defined for a rendezvous mission which uses trajectory elements similar to the ATV approach: a hop transfer between two hold trajectories and a transfer to some terminal approach point. Numerical values of all simulation parameters and initial conditions can be found in Table 3.1. An elliptical orbit scenario for the MSR mission is used for defining the reference orbit. The semi-major axis for orbits of a given combination of apocentre and pericentre altitudes is smaller for an orbit around Mars than for an orbit around Earth. As a consequence, the orbit curvature is higher for typical rendezvous orbits around Mars, and non-linear effects on the relative dynamics become noticeable at a shorter inter-satellite distance. This provides for a more critical test of the linear guidance algorithm than an Earth-based scenario. The selected reference orbit has a moderate eccentricity. The result is that the trajectory plots remain clear, while at the same time the capacity of the algorithm to manage elliptical orbits is demonstrated.

Table 3.1: Simulation parameters and initial conditions.

Parameter	Value
Reference orbit	
Gravitational parameter of Mars	42828.87 km^3/s^2
Semi-major axis	4647 km
Eccentricity	0.2
Inclination	15°
Right ascension of the ascending node	30°
Argument of pericentre	25°
True anomaly	-
Scenario 1 (algorithm NDA1 & NDA2)	
Initial nominal coordinates (x z)	(-5, -1) km
Terminal coordinates (x z)	(1, -0.5) km
Scenario 2 (algorithm NDA3)	
Initial hold trajectory distance	-5, -10, -20, -50 km
Terminal hold trajectory distance	-1 km
Collision-free period	1 day

The hold trajectory on V-bar is defined as a generalization of the stationary point on V-bar used for circular orbit rendezvous. Such a generalization can be realized through a differential mean anomaly, a differential argument of pericentre, or a combination of the two. The trajectory that results from a differential mean anomaly is a circle in the LVLH frame. The distance of the centre of the circle to the origin is here called the mean-anomaly hold trajectory distance, and it is related to the differential mean anomaly through the following relation:

$$d_M = a\eta^{-1}\delta M \tag{3.52}$$

An example of a hold trajectory that is a combination of the motions produced by a differential mean anomaly and a differential argument of pericentre is defined as follows:

$$\delta M = \frac{1}{2}\eta a^{-1} d_{HP}, \qquad \delta\omega = \frac{1}{2} a^{-1} d_{HP} \tag{3.53}$$

Both equations (3.52) and (3.53) provide a generalization of the stationary point on V-bar that is used in circular orbit rendezvous. The hold trajectory distance is defined here as the distance of the centre of the hold trajectory to the target, regardless of whether the hold trajectory is defined through equation (3.52) or (3.53).

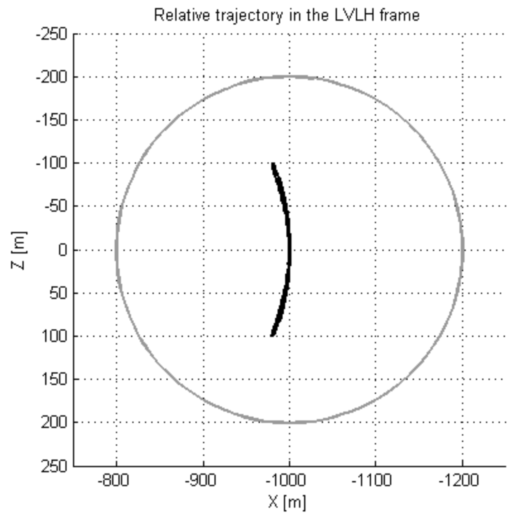

Figure 3.4: Hold trajectory alternatives, circular (grey) and mixed (black).

Figure 3.4 shows both alternatives for the hold trajectories, with the hold trajectory defined by means of equation (3.52) shown in grey and by means of equation (3.53) shown in black. The hold trajectory defined by equation (3.53) has the advantage over the trajectory defined by equation (3.52) that the trajectory is smaller, and the movement along the x-direction in particular is quite small. This can be an advantage especially for highly elliptic orbits.

The first scenario is a transfer to the terminal approach point. A typical rendezvous scenario could require that the chaser move to a certain fixed point in the LVLH frame and perform station-keeping there, before closing in on the target by means of a forced motion approach. Algorithms NDA1 and NDA2 provide such a transfer while maintaining a drift-free trajectory. This scenario is used for the comparison between NDA1 and NDA2, and for the linear and Keplerian propagation tests of NDA2. For these simulations it is convenient to define the initial and terminal state vectors as points in Cartesian space, and to set the initial and desired terminal velocity to zero. The velocity components of the initial and terminal state vectors are not important: inspection of equations (3.33), (3.34) and (3.35) shows that neither the transfer angle nor the required velocity at the start and the end of the transfer depend on the initial or terminal velocity (the required ΔV vectors obviously do). By contrast, if the initial and desired terminal velocities are set to zero, then the ΔV vectors should be tangential to the trajectory at the initial and desired terminal points.

The second scenario consists of a hop transfer between two hold trajectories on V-bar, both defined by means of equations (3.52) and (3.53). The objective of the scenario is to define a rendezvous strategy to close the distance from 50 km to 1 km. The transfer trajectory is a generalization of the radial hop transfer trajectory for circular orbit rendezvous that is used by the ATV. Such transfers are used in circular orbit rendezvous to safely approach the target by means of drift-free hops between stationary points on V-bar [184]. In elliptical orbit rendezvous, algorithm NDA3 is used to compute the hop between hold trajectories on or near V-bar. For this scenario, a range of initial distances is chosen to clearly demonstrate the non-linear effects on the trajectory when the Keplerian propagator is used. Some implications of the results of these simulations to the MSR rendezvous scenario will be discussed.

3.4.2 Description of the test cases

In the first test case, algorithm NDA1 serves as the basis for comparing the performance of algorithm NDA2. Algorithm NDA2 can be benchmarked with respect to algorithm NDA1 in terms of the output, that is, the transfer time and the ΔV's, and in terms of the execution speed, using a Monte Carlo simulation. The numerical algorithm NDA1 was implemented using a standard root-finding algorithm on equation (3.28) multiplied by the sine of the transfer angle φ.

Algorithm NDA3 cannot be directly compared to algorithm NDA1, because NDA1 does not allow the computation of transfer trajectories between two sets of differential orbital elements. In the second test case, the non-drifting nature of the transfer computed by means of algorithms NDA2 and NDA3 is verified by implementing the ΔV's provided by the manoeuvring algorithm in a linear propagator, and by using equation (3.9) to transform the Cartesian state after application of the first ΔV to differential orbital elements to determine whether the trajectory is indeed drift-free (that is, the differential semi-major axis is equal to zero). This transformation is applied again after the transfer is completed to verify that the correct set of differential orbital elements has been reached.

In the third test case, the usefulness in practice of the non-drifting algorithm is assessed by testing the linear algorithms NDA2 and NDA3 in conjunction with a (non-linear) Keplerian relative orbit propagator. Simulations are performed of the rendezvous approach scenarios featuring non-drifting transfers as defined above, and the behaviour of the non-linear error as a function of the initial true anomaly will be analysed.

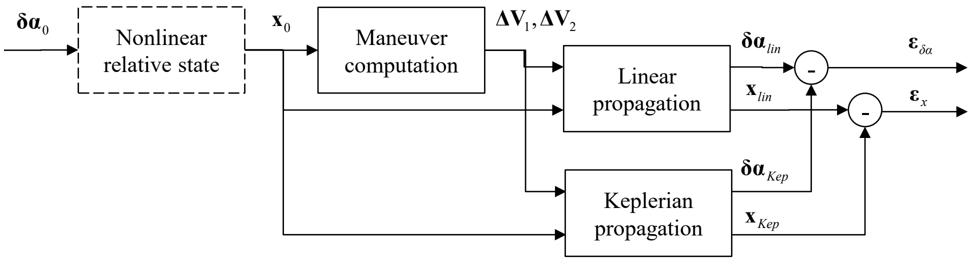

Figure 3.5: Non-linear error computation.

Figure 3.5 shows how the nonlinear errors are computed. For scenario 1, the state vector from Table 3.1 is considered to be expressed in the LVLH frame, and the Keplerian relative orbit propagator is initialized accordingly. The initial state for scenario 2 is obtained by adding the differential orbital elements (computed linearly, as described above, from the data in Table 3.1) to the reference orbit and transforming the result into a non-linear Cartesian state vector in the LVLH frame. This procedure is followed because the linearized differential orbital elements offer better accuracy than the linearized Cartesian state vector [189]. The third simulation test case represents a model of a linear guidance function on board a chaser spacecraft dealing with the non-linear effects of a Keplerian orbit. It is assumed that the state vector is perfectly known at the start of the transfer, implying that the navigation function is perfect. The cylindrical reference frame assumption is used, and the state vector is first transformed from the LVLH frame to the cylindrical reference frame [72]. The second step in the computation of the transfer is to convert the state vector (expressed in the cylindrical reference frame) to differential orbital elements using the linear transformation matrix from equation (3.9). Next, the required ΔV and the transfer angle are computed using equations (3.32) and (3.35) in case of NDA2 and (3.45) and (3.51) in case of NDA3. At the appropriate times, these ΔV vectors are added to the state vector as impulsive shots, taking into account the cylindrical reference frame assumption. This model is limited, on the one hand because it does not include perturbations such as J_2, drag or finite thrust manoeuvring, and on the other hand because it does not include the navigation and control functions. Nevertheless, this simulation scenario provides an indication of the impact of non-linear effects on the behaviour of the guidance function and follows a strategy for mitigating trajectory errors that can be used more generally. A brief parametric examination is performed on the influence of the hop distance and the hold trajectory type on the behaviour of the error due to non-linear effects. A rendezvous strategy that incorporates a series of hops based on the non-drifting transfer is defined, such that after each ΔV the trajectory remains collision-free for at least one day.

The performance metric that is used to assess the quality of the transfer solution for the first scenario is the Cartesian miss distance at the terminal point and the differential semi-major axis after the first ΔV. For the second scenario scaled differential orbital elements are used as a performance metric in addition to the Cartesian miss distance at the terminal point. The differential orbital elements are scaled such that a characteristic distance can be obtained for each differential element: the eccentricity and argument of pericentre are scaled by the semi-major axis, the differential semi-major axis is used without modification and the mean anomaly difference is scaled using equation (3.52).

3.4.3 First test: comparison of NDA2 with NDA1

The performance of algorithm NDA2 is compared to the performance of algorithm NDA1 in a set of Monte Carlo simulations involving 10,000 trials, comparing execution time and output. The initial true anomaly is randomly selected from a uniform distribution between 0 and 2π, and a 2D normally distributed random vector with a standard deviation of 100 m is added to the initial position vector. Randomly selecting the initial true anomaly and adding a random vector to the initial position while keeping the terminal position fixed allows investigating the robustness of the algorithm to changing boundary conditions while maintaining the terminal point condition required by the rendezvous scenario. In a real rendezvous mission such unpredictability in the initial conditions could be due to trajectory dispersions or navigation errors prior to the transfer.

Algorithm NDA1 requires between 8 and 18 function evaluations, with a median of 12, to reach the same accuracy as the analytical solution (double precision). The execution time of algorithm NDA2 is about 6.5 times shorter for the entire algorithm, and about 21 times shorter for just the computation of the transfer angle. Algorithm NDA2 clearly outperforms algorithm NDA1 in this respect.

A comparison of the output shows that the transfer time computed by means of NDA1 and NDA2 is the same, up to the machine precision for double precision numbers (about $1 \cdot 10^{-16}$). The computation of the ΔV is subtly different between algorithms NDA1 and NDA2. Algorithm NDA1 uses the reduced state transition matrix of equation (3.17) to obtain the ΔV, while algorithm NDA2 uses equation (3.35). Ultimately, the results of the ΔV computation are the same for both algorithms to within machine precision. Summarizing, the NDA2 algorithm produces the same result as algorithm NDA1, but the NDA2 algorithm provides the result more quickly than the NDA1 algorithm.

3.4.4 Second test: linear propagation of solutions provided by NDA2 and NDA3

The second test is to use a linear propagator based on the Yamanaka-Ankersen equations to propagate the initial state vector, and to add the impulsive ΔV vectors at the appropriate times. The periodicity of the resulting trajectories is verified by inspection of the resulting trajectory, and by conversion of the terminal state vector to differential orbital elements. Some initial remarks about the plots are in place. First, it should be noted that the directions of the x- and z-axes are reversed, following the convention established by Fehse [134]. Second, the initial true anomaly referred to in the caption of each of the figures cannot be observed directly in the depiction of the trajectories, but it is a crucial parameter that governs the evolution of the trajectory, and it is essential if the trajectory would need to be reproduced.

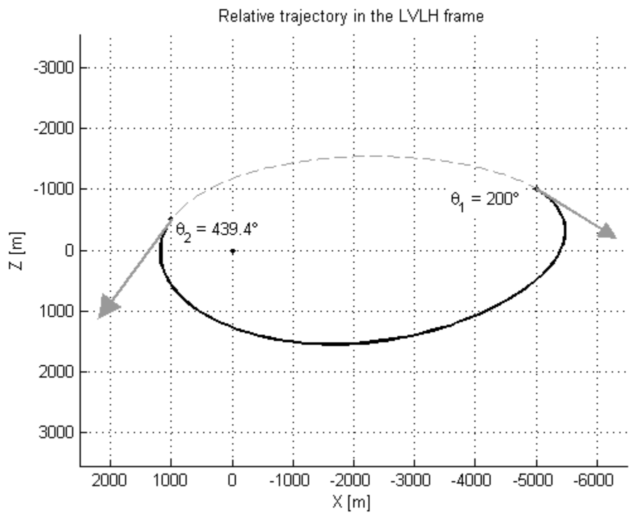

Figure 3.6: Linear propagation of nominal transfer trajectory for θ_1=200° (NDA1 & NDA2).

Figure 3.6 shows the nominal transfer trajectory for an initial true anomaly of 200°. As expected, the ΔV vectors are tangential to the transfer trajectory, because the initial relative velocity (before the first ΔV) and the desired terminal relative velocity are both set to zero. The dashed return trajectory indicates that the transfer is indeed periodic. A conversion to differential orbital elements confirms that the trajectory is indeed periodic (i.e., δa = 0). The transfer time computed by means of both NDA1 and NDA2 is 1832 (s). The first impulsive ΔV vector is [-3.269 1.782] (m/s), and the second impulsive ΔV vector is [2.528 3.835] (m/s).

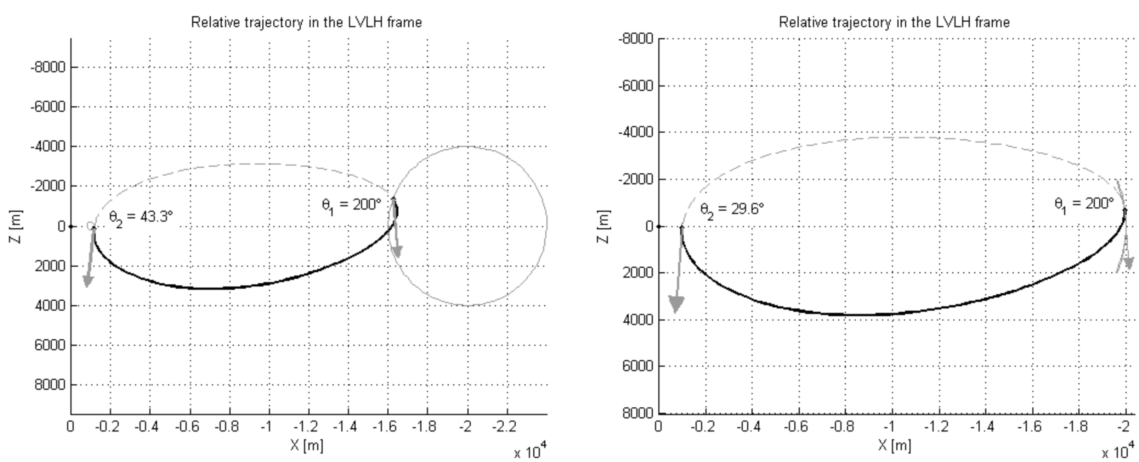

Figure 3.7: Linear propagation of hop between hold trajectories on V-bar for θ_1=200° (NDA3).

Figure 3.7 shows a hop trajectory between hold trajectories on V-bar. Initially, the chaser is moving in a circular hold trajectory at a distance of 20 km from the origin. The trajectory on the left shows a transfer between circular hold trajectories. The transfer time is 4811 (s), which is half of the orbital period. The impulsive ΔV required to initiate the transfer is [-0.254, 3.019] (m/s) and the ΔV required to end the transfer at the 1000 (m) hold trajectory is [0.359, 2.997] (m/s). The trajectory on the right shows a transfer between mixed hold trajectories. The transfer time is 4556 (s), which is about half (47%) of the orbital period. The impulsive ΔV required to initiate the transfer is [-0.217, 2.572] (m/s) and the ΔV required to end the transfer at the 1000 (m) hold trajectory is [0.313, 3.718] (m/s). By inspection of the figure, the transfer trajectories are periodic.

3.4.5 Third test: Keplerian propagation of solutions provided by NDA2 and NDA3

The last test uses a Keplerian relative orbit propagator to investigate the effects of unperturbed non-linear dynamics on the relative trajectory, and to determine to what extent the transfer trajectories remain non-drifting and therefore safe. A rendezvous strategy is defined to close the distance from 50 km down to 1 km that remains safe for at least 24 hours after the completion of a single hop.

The rendezvous strategy is examined in reverse order, in the sense that the transfer to the terminal approach point is discussed first. Note that the initial conditions for this transfer (scenario 1) have deliberately been chosen at a larger distance from the origin (see Table 3.1) than the distance of the closest hold point for the hops over V-bar (scenario 2). This has been done to demonstrate that the algorithm can manage the larger non-linear errors associated with a larger initial distance.

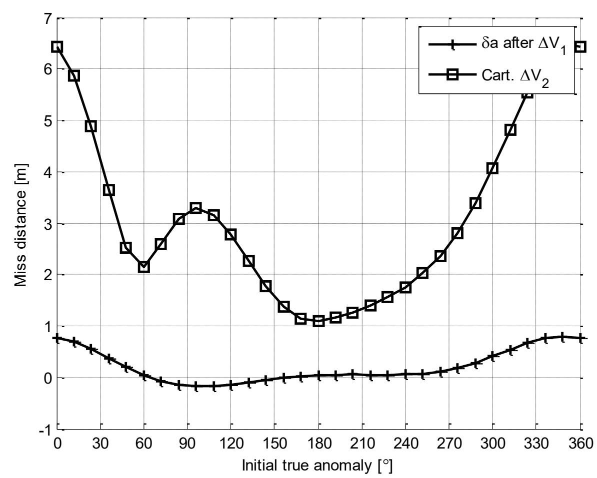

Figure 3.8: Nonlinear errors for scenario 1, transfer to terminal approach point.

Figure 3.8 shows the error due to linearization for scenario 1, which is the transfer to the terminal approach point, shown in Figure 3.6. Both the Cartesian miss distance and the differential semi-major axis remain below 1% of the distance of the terminal approach point, but there is a clear dependence on the true anomaly at which the first manoeuvre is performed. The Cartesian miss distance at the end of the transfer lies between 1 meter for transfers started near apocentre and 6.5 meters for transfers started around pericentre. The differential semi-major axis shows a similar pattern. It would make sense, from the perspective of minimizing the error due to linearization, to start the transfer around apocentre. On the other hand, based on these results, even in the worst case the chaser could remain in the transfer trajectory without applying the second ΔV for at least 12 orbits, or 32 hours, before the miss distance grows to 10% of the distance of the terminal approach point due to along-track drift. This provides sufficient margin in both time and space to communicate with the spacecraft and decide on the next steps to take. The transfer trajectory provided by algorithm NDA1 can therefore be considered as a safe element of a rendezvous strategy for MSR in this assessment.

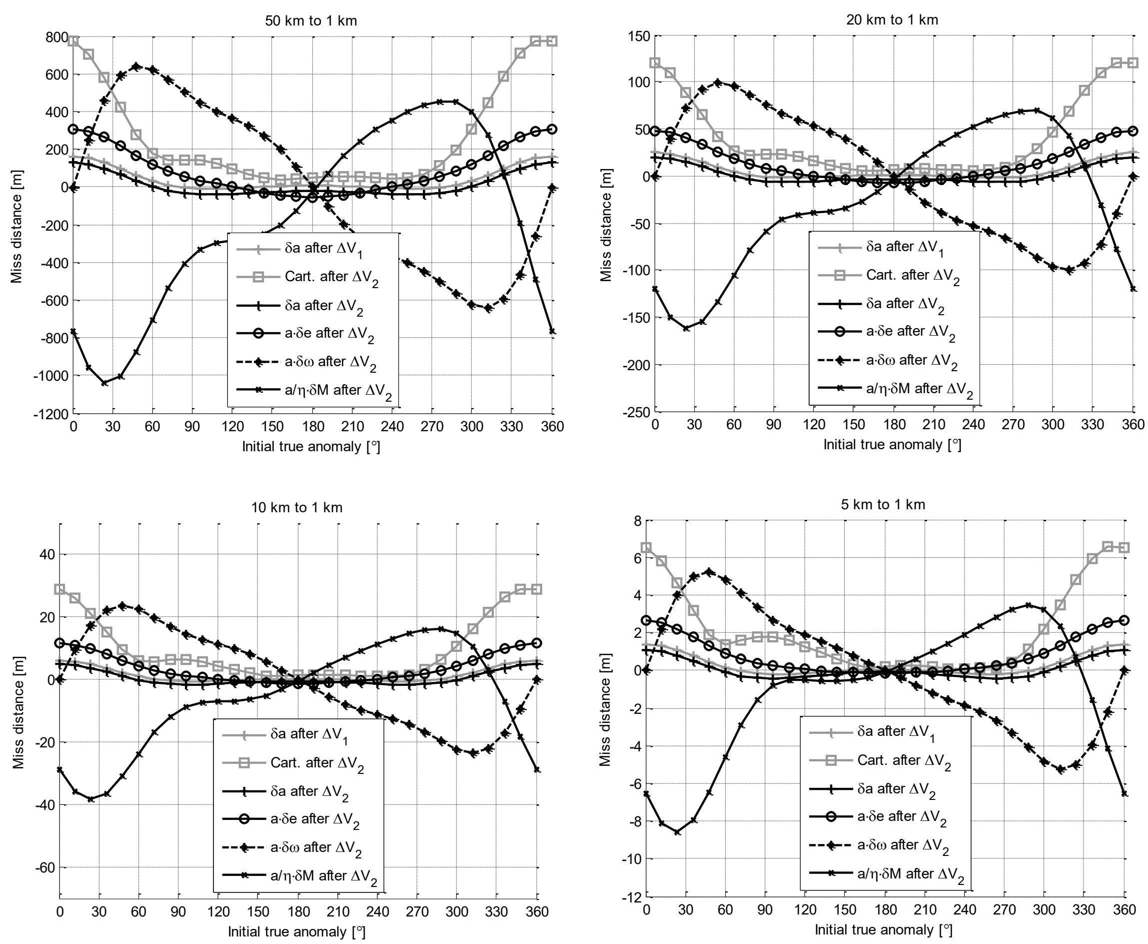

Figure 3.9: Non-linear errors for scenario 2, transfer between circular hold trajectories.

Figure 3.9 shows the error due to linearization for scenario 2, which is a hop transfer between two a circular hold trajectories (as shown on the left-hand side of Figure 3.7). The distance of the initial hold trajectory is varied between 50 km and 5 km, while the distance of the terminal hold trajectory is kept fixed at 1 km. The figure shows the error in the differential semi-major axis δa after the first and second manoeuvre, the

Cartesian miss distance after the second manoeuvre, and the errors in the differential elements δe, δω and δM after the second manoeuvre.

The error in δa gives information about the drift rate of the relative trajectory. The figure shows that a large part of the error in δa is incurred during the first ΔV. This is because the nonlinearity error is largest at this point. The error in differential semi-major axis is largest for transfers started at pericentre, and smallest for transfers started at apocentre. To achieve lowest drift due to nonlinear errors, periodic transfers should therefore be started at apocentre, if other mission constraints allow it.

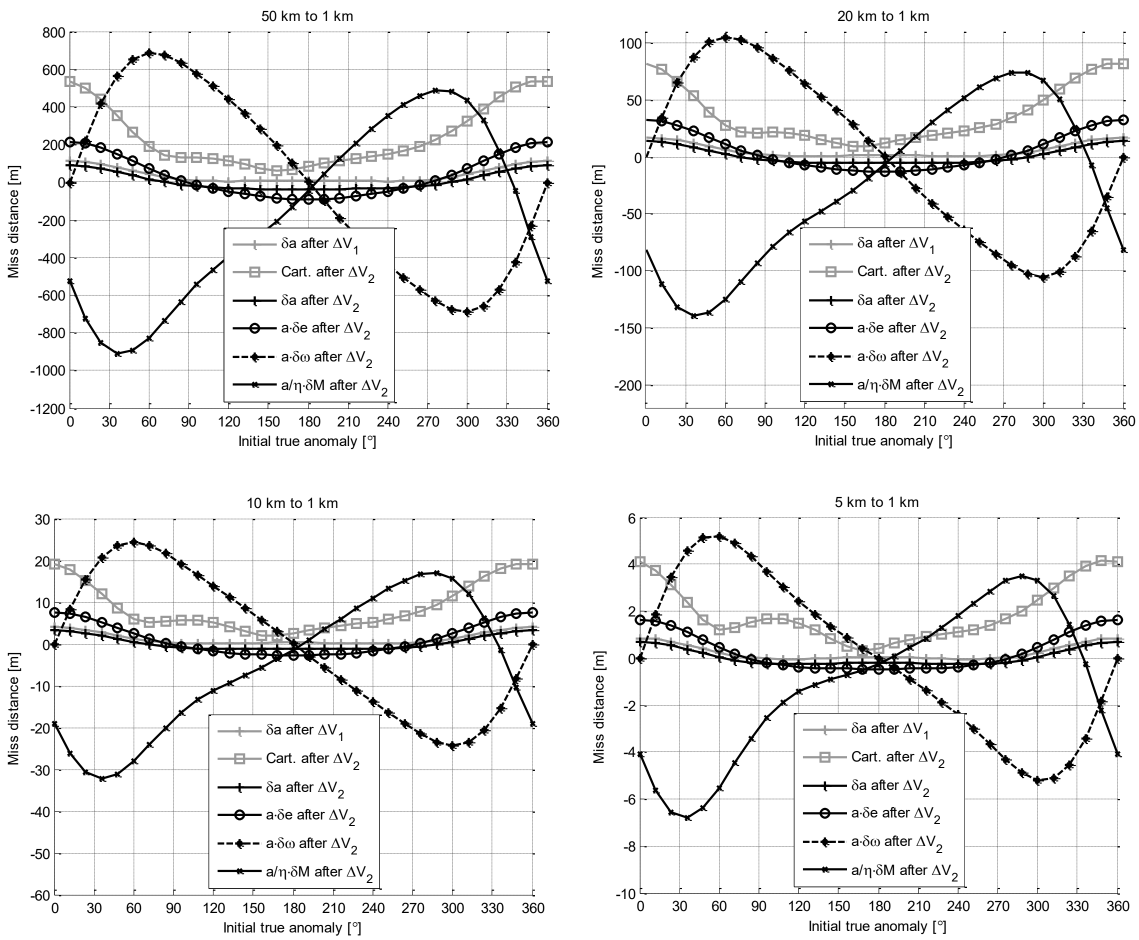

Figure 3.10: Non-linear errors for scenario 2, transfer between mixed hold trajectories.

The Cartesian miss distance is the distance between the desired terminal point and the terminal point that is actually achieved. The Cartesian miss distance shows behaviour similar to the error in δa; namely, it is largest if the transfer is started around pericentre, and smallest if it is started around apocentre. The Cartesian miss distance does not provide information on the trajectory evolution after ΔV_2. For this reason, the error in the differential elements δe, δω and δM are included. The error in the differential eccentricity shows behaviour similar to the error in δa. The differential argument of pericentre and the differential mean anomaly show the highest errors for the region between apocentre and pericentre, and these errors are opposite in sign. This indicates that the along-track error due to these differential orbital elements approximately cancels out.

Figure 3.10 shows the errors for the same scenario, with the difference that mixed hold trajectories are used (as shown on the right-hand side of Figure 3.7). A comparison between Figure 3.9 and Figure 3.10 shows that the qualitative behaviour of the error metrics is quite similar: all error metrics are largest for the largest hop distance, and for transfers started around apocentre. The mixed hold point generally shows a better performance in terms of the errors in differential semi-major axis, especially in the region around pericentre. Errors at the terminal point are generally 10% to 20% lower for the mixed hold trajectory. On the other hand, Figure 3.11 shows that the ΔV required for a hop from a 50 km hold trajectory to a 1 km hold trajectory is about 4% lower when circular hold trajectories are used.

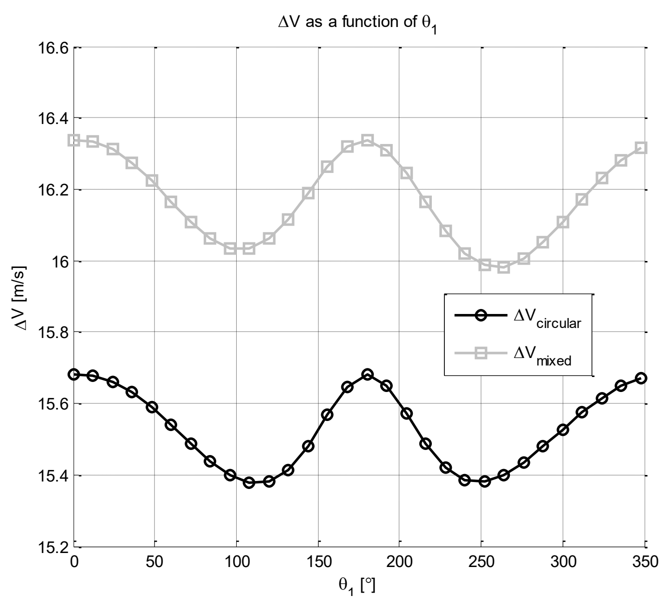

Figure 3.11: ΔV comparison between mixed and circular hold trajectories.

Figure 3.9 and Figure 3.10 and show that the error due to linearization remains below 2.1% of the initial range if the hold trajectory distance is 50 km or lower. The error in differential semi-major axis is a cause for concern because it causes a steady drift. The drift per orbit can be expressed in terms of the change in mean-anomaly hold trajectory distance as a function of the differential semi-major axis. A brief analysis of equations (3.10) and (3.52) shows that the drift per orbit is equal to $3\pi/\eta$ (or about 9.6 for the orbit under consideration) times the differential semi-major axis. The maximum error in differential semi-major axis in Figure 3.9 is 160 m, such that the maximum drift per orbit is a little over 1.5 km for the hop from 50 km to 1 km. These errors are of the same order of magnitude as the distance of the terminal hold trajectory, making a hop transfer to this distance unsafe due to nonlinear effects. Multiple smaller hops should be performed if the errors at the end of the transfer are of the same order of magnitude as the distance of the terminal hold trajectory. The error in differential semi-major axis is determined mainly by the first ΔV and depends strongly on the initial hold trajectory distance. For the hop from 50 km to 1 km, the maximum error in δa is 130 meters for the circular hold trajectory and 90 meters for the mixed hold trajectory. Figure 3.12 shows the maximum error in differential semi-major axis for a hop from a hold trajectory at 50 km distance as a function of the distance of the second hold trajectory. A hop from 50 km to 10 km would lead to a maximum Cartesian error in of 680 meters, and a drift of about 1.05 km per orbit. If this drift rate is directed towards the origin, then the trajectory would remain safe for 8.5 orbits or about 23 hours. A hop from 50 km to 20 km would lead to a maximum Cartesian error in of 550 meters, and a drift of about 850 m per orbit. The trajectory would therefore remain safe for 23 orbits or about 61 hours.

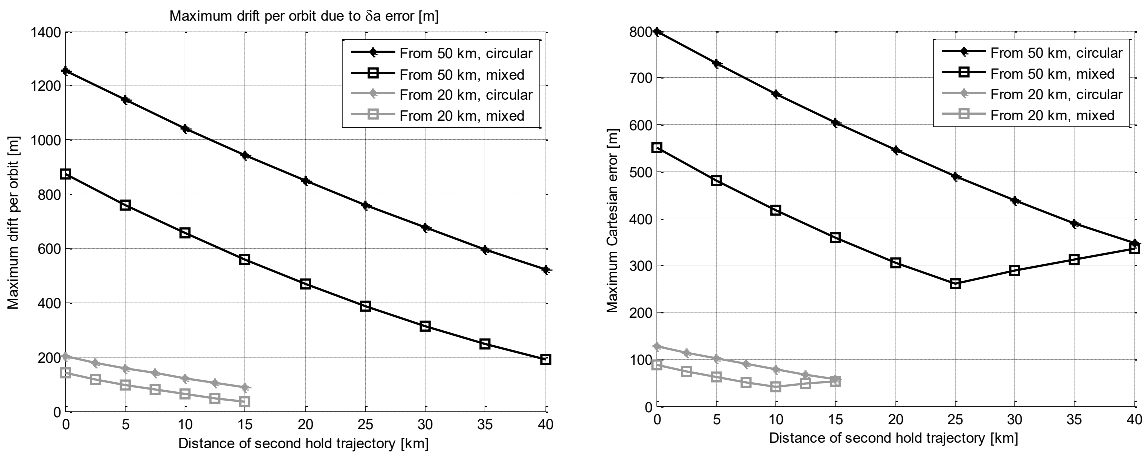

Figure 3.12: Max. Cartesian error and drift rate (absolute value) as a function of the second hold trajectory distance.

Further inspection of Figure 3.9 and Figure 3.10 shows that a single hop can be performed when the hold point distance is 10 km or smaller. In this case the maximum Cartesian error due to linearization remains below 30 m, and the drift per orbit remains below 60 m. Comparing the drift per orbit to the terminal hold trajectory distance, this means that the final trajectory remains safe for at least 16 orbits, or 42 hours. Based on this assessment, a rendezvous from 50 km to 1 km should use hold trajectories at 20 km, 10 km, and 1 km to remain safe for at least one day.

An important remark should be made with respect to the mitigation of errors after the second ΔV of all the transfer scenarios above, and the hop transfer in particular. The second ΔV could be recomputed during the transfer to reduce the effect on the terminal state of errors due to linearization, and indeed due to other causes, such as perturbations or navigation accuracy. Many of these errors show dependency on the range to the target, and the range to the target decreases when performing rendezvous. The assessment made in this section shows that the non-drifting transfer algorithms developed in this paper can provide a safe rendezvous trajectory if the hop distance is chosen such that sufficient margins remain at the terminal hold point.

3.5 Conclusions

The need for passively safe trajectories during close range elliptic orbit rendezvous has led to the investigation of the two impulse non-drifting transfer problem. The problem consists of finding the required transfer angle and the first and second velocity impulse to be applied. The work presented in this paper has improved a previously available solution in two ways. The new solution provides an analytical solution to the transfer problem, while the previous solution relied on a numerical method to solve for the transfer angle. The analytical solution is advantageous for on board computation of manoeuvres, because of improved accuracy and speed. The new solution also extends the previous solution to allow non-drifting transfers between trajectories defined in terms of differential orbital elements as well as between two points defined in the local vertical, local horizontal frame.

The non-drifting transfer algorithms can be incorporated in a generalization to eccentric orbits of a close-range circular orbit rendezvous strategy featuring non-drifting radial hops, which is used by the Automated Transfer Vehicle. This paper has shown that the advantages of the strategy are preserved in the case of eccentric orbit rendezvous. For example, the non-execution of the second burn places the chaser on a return trajectory to the point of departure. In all cases the trajectory remains passively safe, and another attempt can be made to perform the burn one revolution later. It has been demonstrated that a close-range rendezvous strategy can be designed that is safe when non-linear effects are present. The non-drifting transfer algorithms are simple, efficient, and capable of generating passively safe transfer trajectories, which makes them well suited for incorporation into an autonomous guidance function for close range rendezvous.

4
Mission analysis for Proba-3 nominal operations[4]

This paper reports the phase B mission analysis work performed for the nominal operations of the Proba-3 formation flying mission. Proba-3 will perform formation flying in HEO and perform Solar coronagraphy and formation manoeuvring demonstrations in a six-hour region around apogee. This paper addresses the nominal orbit and the initial deployment of the formation and focuses on feasibility and delta-V requirements, including trade-offs between alternatives. Challenging constraints are the absence of an omnidirectional sensor, and the requirement that the spacecraft cannot turn more than 30° away from the Sun due to thermal and power constraints.

4.1 Introduction

Proba-3 is a virtual structure formation-flying mission that will perform formation flying in a HEO. A survey of past, present and future missions utilizing formation flying was performed during an earlier phase of the project [190]. Virtual structure formation flying missions treat the formation as if it were a single rigid body, and different elements of a sensor system can be distributed over the satellites of which the formation is composed.

---

[4] This chapter was previously published in Acta Astronautica, doi: 10.1016/j.actaastro.2014.01.010. The original article did not provide details on the method used to compute the impulsive manoeuvres for the perigee pass, the statistical method used to compute the cold gas correction, or the method used to incorporate the effects of Solar radiation pressure on the evolution of the relative trajectory. This material has been included in appendices B, C and D.

This can be useful for sensor systems that require a long baseline or focal length, for example interferometers, telescopes, and coronagraph instruments. Examples of past studies are Darwin [191], TPF [192] (both interferometers), XEUS [42] and Simbol-X [193] (both X-ray telescopes). The Proba-3 mission was originally conceived as an autonomous formation flying mission in GTO [26]. Notable features that have been carried over from this initial study are the spacecraft autonomy, and the division of an orbit in apogee and perigee phases [194,195]. The Proba-3 formation consists of a coronagraph spacecraft (CSC) hosting the coronagraph instrument and an occulter spacecraft (OSC) hosting an occulter disk [196,197]. The occulter disk blocks the light of the Sun, such that only the light from the Sun's corona enters the coronagraph instrument. While in nominal formation the OSC generates a stable eclipse on the CSC that is used by the coronagraph instrument to observe the Sun's inner corona. The spacecraft are equipped with the following relative state sensors: both spacecraft are equipped with a GPS receiver and an inter-satellite link such that rGPS measurements can be made. The CSC is equipped with a Coarse Lateral Sensor (CLS) with a field of view of 5° and a Fine Lateral and Longitudinal Sensor (FLLS). For the FLLS to work, the OSC needs to be within 16.5 mm of the sensor bore sight. This works out to an effective field of view of 21 arc seconds at the nominal operating distance. Different propulsion systems are available on each spacecraft. The OSC cold-gas propulsion system (CGS) allows fine formation manoeuvres while the CSC high-performance green propellant (HPGP) thrusters are used to perform main orbital manoeuvres.

The nominal orbit consists of a forced motion apogee pass, including the formation manoeuvres around apogee, a formation break up, a free-flying perigee pass and a formation acquisition. Optional operations are a cold-gas correction of the formation break manoeuvre and a Mid-Course Manoeuvre (MCM) after perigee using the HPGP thrusters.

Deployment of the formation is the process of separating the spacecraft from their original mated configuration to the final, nominal orbit configuration. The two spacecraft are separated at apogee by means of a separation spring. Separation is followed by rendezvous operations that put the CSC and the OSC in close vicinity in a safe orbit. In this safe orbit the formation is commissioned, after which nominal operations can begin. This paper first treats the nominal operations, including the perigee pass and the apogee fine formation flying phase. It then describes the work performed on the formation deployment up to the commissioning of the nominal perigee pass and manoeuvres.

Table 4.1: Orbital parameters.

Parameter	Value
Perigee height	600 km
Apogee height	60530 km
Semi-major axis	36943 km
Eccentricity	0.8111 -
Inclination	59°
RAAN	84°
AoP	188°
Orbital period	19h38m

The reference orbit for the formation flying is a HEO. Table 4.1 presents reference orbital parameters. The nominal mission lifetime is two years.

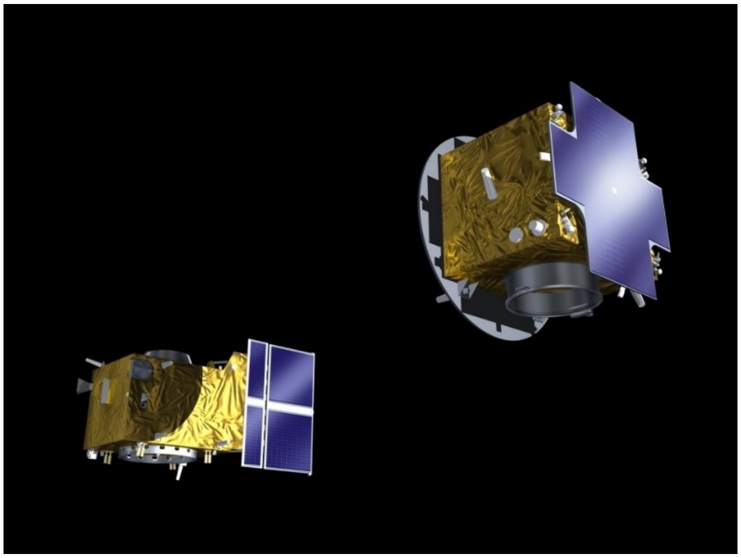

Figure 4.1: Proba-3 spacecraft ©ESA.

Figure 4.1 shows the Proba-3 spacecraft, with the CSC on the left and the OSC on the right. The Solar panels are fixed to the bodies of the spacecraft. Neither spacecraft should turn more than 30° away from the Sun direction due to thermal and power constraints. This limits the availability of the CLS and the FLLS to periods during which the angle between the CSC - OSC direction and the Sun direction is smaller than 30°.

Table 4.2 shows the characteristics of the two spacecraft. Both spacecraft are equipped with a propulsion system. The CSC is equipped with a HPGP propulsion system with a thrust of 1 N, and the OSC is equipped a 10 mN cold-gas system. Also included in the table are parameters related to Solar radiation pressure (SRP), the most important perturbation (especially in the region around apogee). The actuation errors are 5% (1σ) in magnitude and 1° (1σ) in direction for open-loop manoeuvres.

Table 4.2: Spacecraft characteristics.

Parameter	OSC	CSC
Area [m2]	1.77	3.34
Wet mass [kg]	211	339
Dry mass [kg]	190	327
SRP coefficient [-]	1.9 (1.5)	1.29
Thrust per thruster [mN]	10	1000
Specific Impulse [s]	68	235
Thruster force capacity in direction of minimum thruster force capacity [mN]	14.3	2100
Fraction of thrust allocated for control	0.2	-

For both spacecraft, the thrusters are mounted on the eight corners of the main spacecraft body. On two opposing faces of the spacecraft a group of four thrusters points along the edges of a pyramid with the face of the spacecraft as its base. Figure 4.2 shows this configuration. Because of the thruster geometry, the amount of force the spacecraft can generate is a function of the direction of the force in the spacecraft body frame. Table 4.2 provides the thruster force capacity in the direction of minimum thruster force capacity for the Proba-3 thruster configuration.

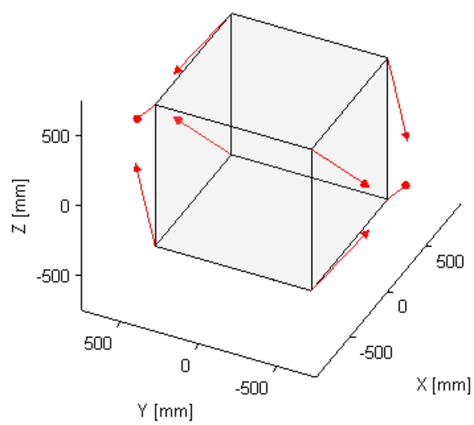

Figure 4.2: Thruster orientation.

Table 4.3 shows the accuracy of the navigation solution based on the sensors that are relevant for the formation flying mission analysis work presented here. GPS measurements are available in the region around perigee and FLLS measurements are available whenever the two spacecraft are properly aligned. In the nominal orbit alignment occurs in the region around apogee. Note that the accuracy of the rGPS solution is given for the moment the formation exits from the GPS visibility region.

Table 4.3: Navigation accuracy.

Parameter	Relative GPS	FLLS
Per-axis 1σ position error [cm]	6.12	2
Per-axis 1σ velocity error [mm/s]	0.0388	0.0017

The focus of the analyses described in this document is on the relative formation-flying of the Proba-3 mission during nominal operations. The nominal operations consist of the nominal orbit routine and the formation deployment. Off-nominal operations such as the safe orbit and the collision avoidance manoeuvre (CAM) have been presented elsewhere [198]. The relative mission analysis described in this article is an update and refinement of earlier work performed during previous phases of the project [199]. The period of the operational orbit was reduced from 24 hours to 19.7 hours. A more detailed study of the operational orbit of the formation was performed [200] and the reference operational orbit data was used to refine the relative orbit calculations. The operational orbit is left free to evolve, while the relative trajectory is controlled every orbit during nominal operations. The relative mission analysis work reported in this document updates and refines the timeline and the ΔV budget for the nominal orbit routine. It also provides a more thorough analysis of the formation analysis, including a trade-off of different alternatives.

A linearized model is used for the propagation of the relative trajectory and for manoeuvre computation. The inter-satellite distance (ISD) is small compared to the orbital radius, such that the linearization can be justified. The propagation time tends to be of the order of one orbital period between manoeuvres. During the course of the study, the effect of perturbations on the evolution of the relative trajectory has been investigated. The effect of linearization, J_2, third-body, air drag and SRP were all investigated. It was found that the effect of these perturbations over one orbital period is small compared to the effect of navigation and actuation accuracy on the trajectory evolution, except for SRP. The maximum error associated with SRP was found to be about 10 meters at the end of the perigee pass. A linear model for the SRP has therefore been included into the analysis, and an uncertainty of 20% in the knowledge of the magnitude of the SRP has been assumed. Some of the analyses in this document are reported in the Local Vertical, Local Horizontal (LVLH) reference frame and others in the VBAR reference frame. The LVLH frame and the VBAR frame are defined as follows. The z-axis of the LVLH points towards the centre of Earth, the y-axis points in the direction opposite to the orbital angular momentum vector and the x-axis completes the right-handed frame. The x-axis of the VBAR frame points along the local velocity vector, the y-axis points in the direction opposite to the orbital angular momentum vector and the z-axis completes the right-handed frame. The use of the LVLH frame has been a project decision. For certain parts of the analysis, a set of relative orbital elements was used based on the relative eccentricity vector, angular momentum vector, semi-major axis and mean anomaly [201,202].

The objective of the formation flying mission analysis study is to provide a feasible operational sequence and the ΔV required for the nominal phases of the mission. Mission analysis does not consider the attitude control of the two spacecraft. During all nominal operations except the retargeting around apogee, both spacecraft are Sun-pointing. During retargeting operations, the spacecraft are target-pointing, that is, they point at each other. The analysis of the operational orbit and the transfer strategy included a study of the ground station contact times [200]. A single ground station, Redu, is considered for the Proba-3 mission. Operational constraints (such as the ground station contacts) are considered implicitly in the sections covering the nominal orbit routine. The nominal orbit routine is performed autonomously, such that ground contacts are required only for downloading operational and scientific data. The formation deployment is performed under ground control, such that ground station contacts need to be considered.

This article is structured as follows. The first section treats the nominal orbit routine, consisting of the free-flying perigee pass and the forced motion-controlled apogee phase. The analysis of the nominal orbit provides the timeline for a single orbit. In the section on the perigee pass a trade-off is performed on three different strategies for the perigee pass, based on the ΔV, safety and the forced motion distance at the end of the perigee pass. The perigee pass trajectory is determined by the initial and terminal conditions, which in turn are dictated by the Sun-orbit geometry. The safety of the perigee pass is discussed, including the main sources of error. Finally, the three perigee pass strategies are compared in terms of ΔV. The section on the apogee phase focuses on the ΔV required for coronagraphy (essentially station-keeping along the Sun direction) and formation reconfiguration manoeuvres. The second section covers the formation deployment. Deployment strategies are traded based on their safety, and the ΔV budget for the most promising strategy is defined.

4.2 Nominal orbit

During most of the mission the Proba-3 formation will be performing the nominal orbit routine. Because of the many repetitions of this routine an investigation of the ΔV and a careful comparison of the available alternatives is crucial. In this section, the characteristics of the nominal orbital routine will be discussed. The main elements of the nominal orbit routine are a fine formation flying phase and a free-flight phase. Fine formation flying phase occurs in a 6-hour region around apogee, and a free-flight occurs in the region around perigee. A formation break or Direct Targeting Manoeuvre (DTM1) occurs at 3.5 hours after apogee, or about half an hour after the six hour apogee arc ends. A second Direct Targeting Manoeuvre (DTM2) and the start of formation acquisition occur 4.5 hours before apogee, leaving 1.5 hours to perform fine formation acquisition before the apogee arc starts. During the apogee arc coronagraphy and reconfiguration manoeuvres are performed. It is assumed that during the half hour between the end of the apogee arc and DTM1, the spacecraft continue in fine formation to maintain FLLS lock.

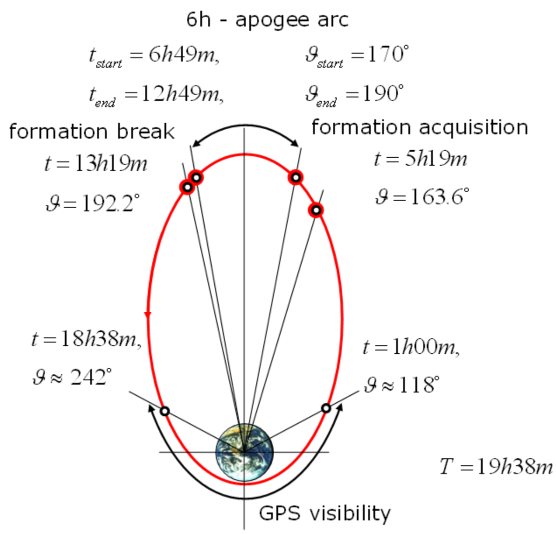

Figure 4.3: Nominal orbit routine.

Figure 4.3 shows a diagram of the consolidated orbit routine. This figure shows the time after perigee and the true anomaly of each manoeuvre, as well as the GPS visibility. It is stressed again that the navigation accuracy based on relative GPS given in table 4.3 is applicable at the end of the GPS visibility region at a true anomaly of about 180°. From that point onward a propagated navigation solution is used, and accuracy degrades over time.

The spacecraft are capable of performing adaptive mission operations on board, and as such achieve autonomy level E3 for execution of nominal mission operations according to the ECSS standards [203].

4.2.1 Perigee pass

Based on the work done during previous phases, three perigee pass strategies have been defined that are variations on the strategy selected earlier. These are:

- Direct transfer without MCM's
- Direct transfer with cold-gas correction after DTM1
- Direct transfer with 1 MCM

These direct transfer strategies have been investigated by means of linear simulations, meaning that the orbit is propagated by means of a Kepler propagator and the relative trajectory by means of a linear relative dynamics model. The direct transfer strategy uses a two-point transfer algorithm to find a trajectory between the state vectors at the time of DTM1 and DTM2. The transfer time is given by the timing of DTM1 and DTM2. The formation acquisition is computed using an algorithm that provides a straight-line approach from the initial to the terminal point. Such a straight-line approach consists of an acceleration section, followed by a constant velocity section and finally a deceleration section. The timing of the MCM (if present) is limited to a 10-hour region around apogee by a system level constraint.

The uncertainty of the terminal state vector is modelled by analytically propagating the initial covariance matrix [204] from DTM1 to the MCM, if present, or to DTM2, if not. The initial covariance matrix associated with the relative state vector at DTM1 is taken as the sum of the navigation covariance matrix and the actuation covariance matrix. The navigation covariance matrix is based on the per-axis sensor accuracy given in table 4.3, squared and placed on the diagonal. The actuation covariance matrix is based on the actuator accuracy of 5 % in magnitude and 1° in direction (1σ) and the only non-zero elements are associated with the velocity. The actuation covariance matrix is therefore composed of the covariance matrix associated with the ΔV padded with zero matrices to have the same size as the navigation covariance matrix. The uncertainty of the ΔV is computed by finding the unit vector of the ΔV and two unit vectors perpendicular to it. These three unit vectors define a frame associated with the ΔV. The covariance matrix in this frame is diagonal, and the elements along the diagonal are the square of the uncertainty in magnitude (one element) and the square of the tangent of the uncertainty in direction (two elements). The cold-gas correction is modelled as a reduction in the uncertainty of the ΔV to 5% of its original value. It is assumed that the reduction can be performed by reacquiring the FLLS and re-computing a two-point transfer to the terminal state. The strategy with one MCM is evaluated by computing the MCM ΔV statistically, based on randomly selected error state vectors from the covariance matrix at the time of the MCM. The Sun orbit geometry has a direct impact on the evolution of the perigee pass trajectory. For example, the perigee pass, the magnitude of DTM1 and the minimum ISD show an oscillation with a period of approximately half a year that correlates with the β-angle. During the apogee arc, the trajectories in the LVLH frame follow a part of the nearly circular arc. The circular arc moves over the sphere as a function of the time of the year, such that the gravity gradient to be compensated for changes. As a result, the ΔV required for station-keeping shows a seasonal variation. Precise formation flying at apogee occurs at an ISD of about 160 m.

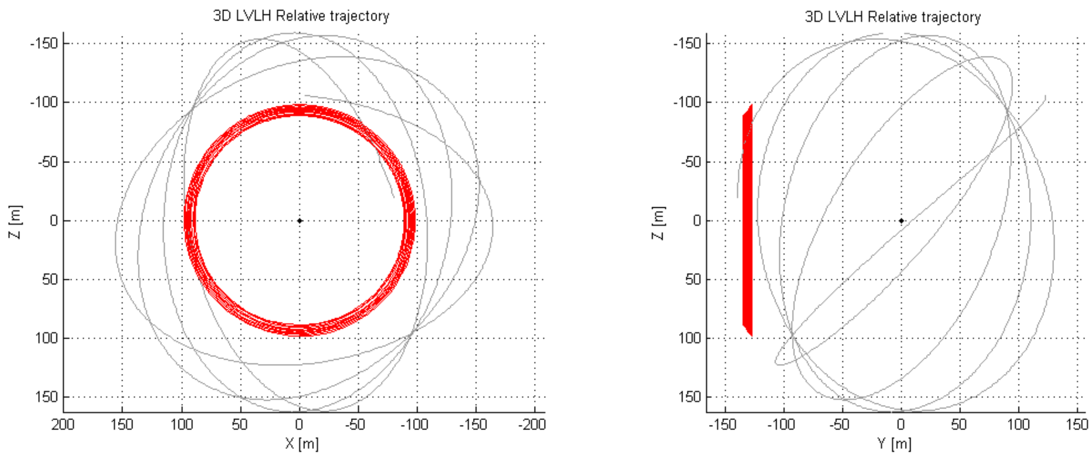

Figure 4.4: Sun direction during several orbits (red) and at apogee (grey).

Figure 4.4 shows the Sun direction during several orbits as well as the evolution of the Sun direction when the formation is at perigee. That is, the grey line connects the points where the Sun is located when the formation is exactly at apogee for every orbit during four years. If the reference orbit would be Keplerian, then the trajectory traced by the Sun direction at apogee would lie in a plane centred on the origin. In reality the plane of intersection points precesses under the influence of perturbations.

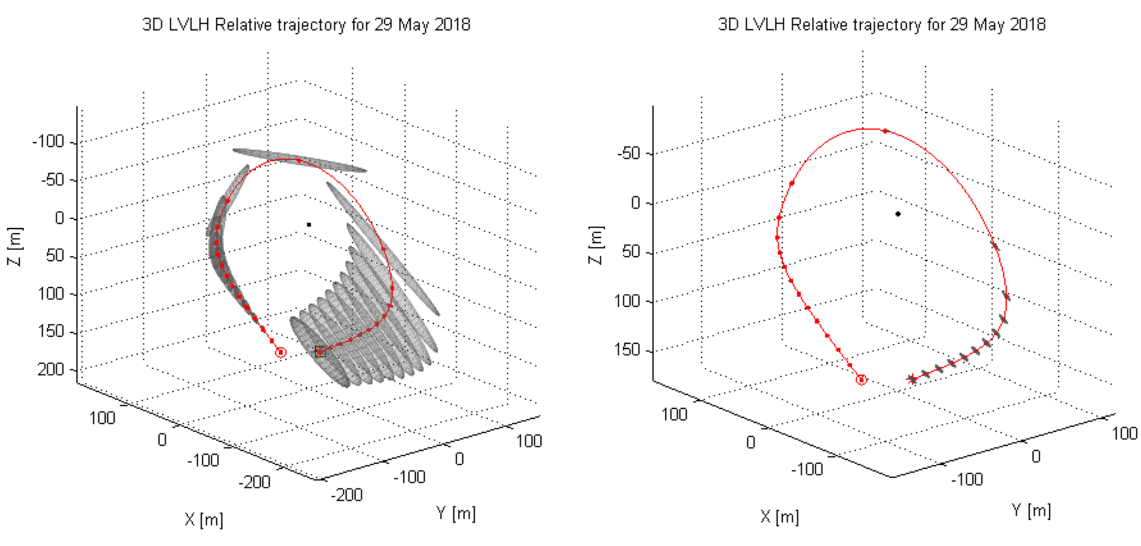

no cold-gas correction including cold-gas correction

Figure 4.5: Perigee pass trajectory including probability ellipsoid.

Figure 4.5 shows a typical perigee pass trajectory with and without a cold-gas correction manoeuvre applied after DTM1. The start of the trajectory is indicated with a red circle. Also indicated is the evolution of the probability ellipsoid. The probability ellipsoids are shown for points equally spaced in time. The physical position of the points clearly shows a fundamental aspect of the perigee pass trajectories, namely, relatively slow motion in the regions close to apogee combined with fast motion in the region around apogee. The trajectory typically has the shape of a horseshoe, where the tips are given by a point along the Sun direction at approximately 160 m distance from the target. The tips of the perigee pass trajectory lie approximately in the XZ-plane. The minimum ISD during the perigee pass never gets below 50 m.

The growth of the covariance matrix has three main causes: the navigation errors, the actuation errors, and the SRP uncertainty. The navigation errors are the same for each of the three strategies. The actuation errors associated with DTM1 are large if they are not compensated for by means of a cold-gas correction manoeuvre performed after DTM1. The rapid growth of the 3σ probability ellipsoid associated with trajectory on the left-hand side of the figure is due to actuation errors. The SRP perturbation affects all three strategies, but it can be compensated for to some extent. If SRP is not compensated, then at the end of the perigee pass the maximum error is about 12 m. This means that if up to 80% of the SRP error can be compensated for, the maximum error due to uncompensated SRP is 2.4 m, which agrees with the size of the covariance ellipsoids at the end of the perigee pass in figure 4.5. It can be concluded that the perigee pass is robust to uncertainties in the SRP.

The actuation errors can be diminished by performing a cold-gas correction manoeuvre immediately after DTM1. The procedure for performing a cold-gas correction is as follows. The CLS and the FLLS are reacquired if they were lost while performing DTM1. After navigation converges the correction manoeuvre is computed and executed by the OSC. The cold-gas correction manoeuvre corrects the errors associated with DTM1 to 5% of their original value. Figure 4.5 shows that the 3σ probability ellipsoid at the end of the transfer is large if no cold-gas correction is performed. This means that if no additional measures are taken, such as in the first strategy for the perigee pass, the fine formation acquisition needs to be performed over a larger distance, leading to an increase of the cold-gas ΔV required for the fine formation acquisition. In addition, the fine formation acquisition takes longer to accomplish. An analysis has been performed of the fine formation acquisition by randomly selecting points from the analytically propagated covariance matrix and using the straight-line approach algorithm to provide the formation acquisition. This analysis has shown that in up to 10% of the cases the fine formation acquisition cannot be performed in the time allotted for this phase. For this reason, either a cold-gas correction manoeuvre immediately after DTM1 or an MCM is required to achieve satisfactory performance, and strategy 1 needs to be discarded.

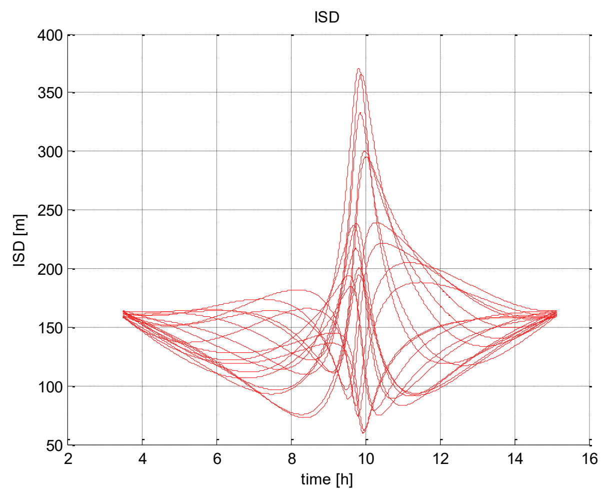

Figure 4.6: Typical ISD during perigee pass for different epochs.

Figure 4.6 show typical ISD's during the perigee pass. Perigee occurs at approximately the 10-hour point. The ISD changes relatively slowly outside the 4-hour region around perigee, while inside this region the ISD tends to change rapidly. Both the minimum and the maximum possible ISD occur around perigee. The minimum possible ISD is about 60 m, and the maximum possible ISD is about 375 m.

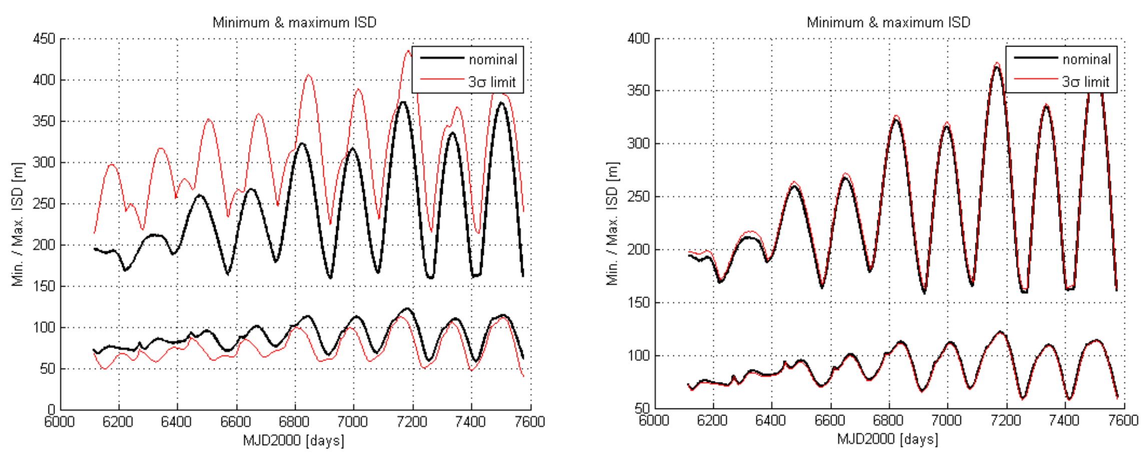

Figure 4.7: Minimum and maximum ISD during the perigee pass.

The actuation errors have a large impact on the ISD during the perigee pass. Figure 4.7 shows the evolution of the minimum and maximum ISD during the perigee pass. The figure is generated by taking the minimum and maximum ISD for each single perigee pass and plotting these points as a function of the date. The left-hand plot is representative for both the first strategy and the third strategy which features an MCM. The right-hand plot shows the results for the strategy that features a cold-gas correction. The figure shows that the nominal minimum and maximum ISD are the same for all strategies, but the 3σ bounds on the minimum and maximum ISD are wider. The minimum ISD remains above 45 meters during the entire mission if the cold-gas correction manoeuvre is not performed, such that the perigee pass trajectory is safe regardless of whether the cold-gas correction manoeuvre is performed or not.

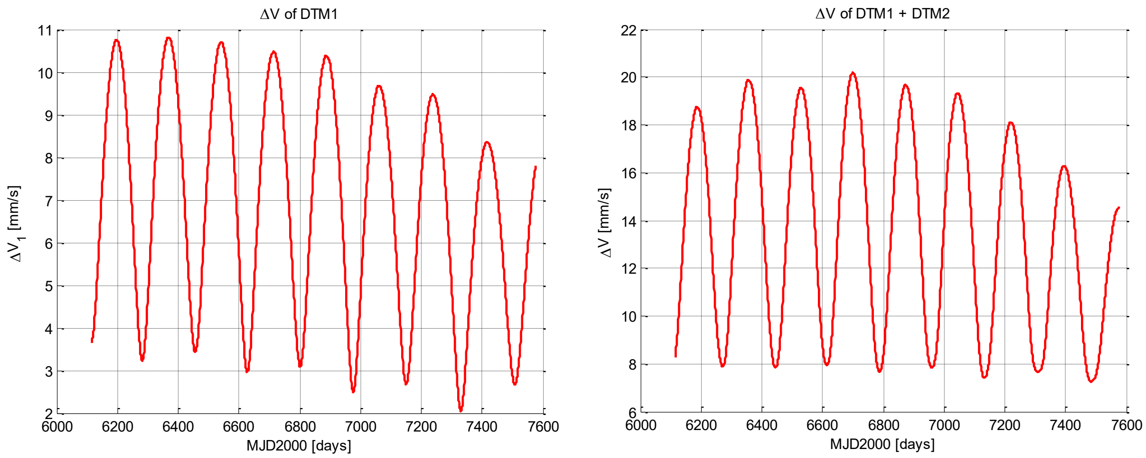

Figure 4.8: ΔV required for DTM1 (left), and DTM1 + DTM2 (right).

Figure 4.8 shows the magnitude of DTM1 as a function of the date. The magnitude of DTM1 shows an oscillation with a mean value of 6 mm/s with amplitude of about 4 mm/s. The period of the oscillation is about 182 days, and it is caused by the seasonally varying geometry of the Sun with respect to the orbital plane, and the evolution of the orbit itself. The right-hand side of the figure shows the total HPGP ΔV of the perigee pass without MCM's. The average total HPGP ΔV, averaged over the entire mission life, is 12.490 mm/s. To assess the effect of an MCM on the ΔV the timing of this manoeuvre needs to be established. Two constraints are in place: the spacecraft cannot turn more than 30° away from the Sun, and the manoeuvre needs to take place within a 10-hour region around apogee. The formation needs to be within 30° of alignment with the Sun to be able to use the relative sensors while complying with the 30° angle constraint. The Sun angle decreases below 30° about 3 hours after perigee. On the other hand, the 10-hour constraint leads to a minimum time of 4 h 49 min after perigee for the MCM.

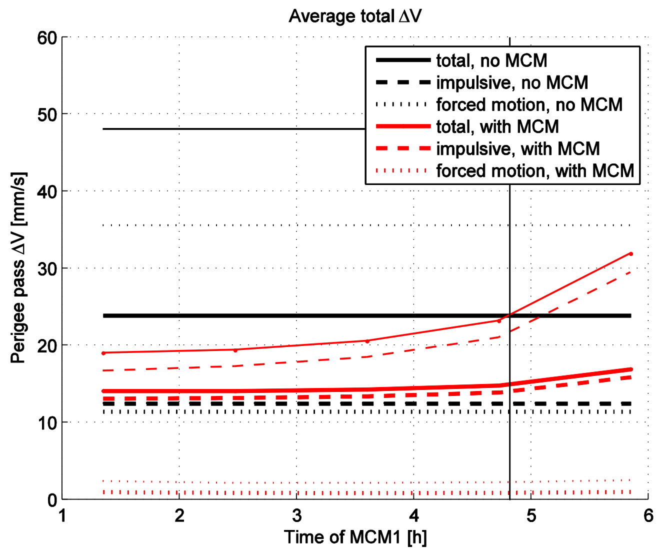

Figure 4.9: ΔV required for strategy featuring MCM.

Figure 4.9 shows the seasonally averaged ΔV of the perigee pass strategy as a function of the timing of the MCM. Time is reckoned as hours after perigee. Bold lines indicate mean values, and thin lines indicate mean values + 3σ. The vertical black line indicates the earliest time at which the MCM can be performed. The graph shows that the ΔV increases rapidly the later the MCM is performed. This indicates that the MCM should be performed as early as possible, at 4 h 49 min after perigee.

Table 4.4: Comparison of perigee pass strategies.

	Strategy 0: Basic	Strategy 1: CG correction	Strategy 2: MCM
HPGP, mean - mean + 3σ [mm/s]	12.490	12.490	15.923 - 31.99
CG, mean - mean + 3σ [mm/s]	13.28 - 37.61	3.58 - 6.93	2.64 - 4.10
Minimum Perigee pass ISD [m]	45	55	45
Forced motion distance [m]	10 - 30	1.7 – 4.7	0.75 -2
Scan for CLS	Yes	No	No

Table 4.4 compares the ΔV for each of the strategies. Performing a correction manoeuvre MCM leads to the most efficient strategy in terms of cold-gas ΔV required. Between the basic and the cold-gas correction strategy, it is more effective to perform a small correction of DTM1 using the cold-gas thrusters than to omit this correction and perform a larger formation acquisition manoeuvre. A selection is made of strategy 1. This strategy has a lower HPGP ΔV, and only a slightly larger cold-gas ΔV. The overall ΔV for this strategy is lowest. This strategy also has the highest minimum ISD during the perigee pass and is therefore safest.

During the mission lifetime of two years the formation will perform about 445 perigee pass manoeuvres, such that the total HPGP ΔV required is 11.12 m/s. The CG ΔV required for correction and for the acquisition lies between 3.19 and 6.17 m/s.

4.2.2 Apogee pass

During the apogee phase, the formation may perform coronagraphy or formation reconfiguration manoeuvres. The forced motion manoeuvres are computed on-board with parameters provided through the mission plan. For the mission analysis an estimate is provided of the ΔV based on kinematic considerations and on the magnitude of the perturbations to be rejected by the controller. This is equivalent to the ΔV required for the feed-forward component of the control. A similar procedure was followed to estimate the formation flying ΔV requirements for XEUS [205]. No feedback control function has been considered. This means that the possible effect of the control function on the ΔV has been omitted from the study.

Coronagraphy is performed during most orbits, and formation reconfiguration manoeuvres are performed on occasion to simulate the retargeting or refocusing of a formation flying space telescope. To perform Solar coronagraphy, the CSC and OSC spacecraft align with the Sun direction in such a way that the OSC shadows the CSC. Formation reconfiguration manoeuvres are intended to change the formation ISD, the direction or both. Formation reconfiguration can be performed by means of rigid manoeuvres or loose manoeuvres, depending on whether forced motion profiles or free-drift trajectories are used to link the initial and final configuration.

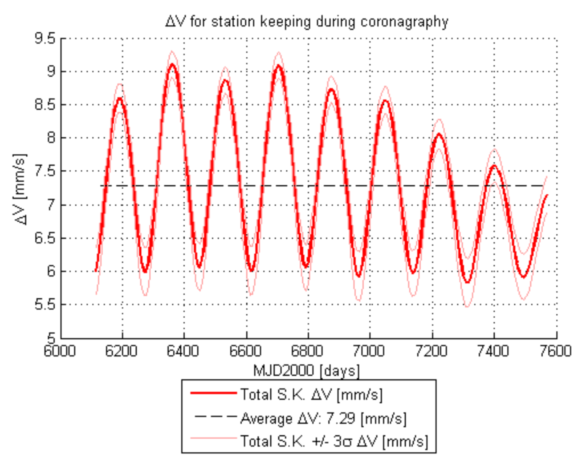

Figure 4.10: Coronagraphy ΔV.

Figure 4.10 shows the ΔV required for performing station keeping to maintain the Sun direction a distance sufficient for the OSC to cover the Sun disk during a 6 hour arc around apogee. The ΔV is estimated by integrating the feed-forward acceleration required to compensate for the gravity gradient and SRP perturbations over the duration of the formation flying arc. It has been assumed that the occulter disk partially shadows the coronagraph by subtracting the occulter disk area from the CSC area. The ΔV shows some seasonal variation, and the ΔV averaged over all seasons is equal to 7.29 mm/s. If the formation would perform station keeping during every orbit for the full two-year mission (or 890 orbits), then a CG ΔV of 6.49 m/s would be required.

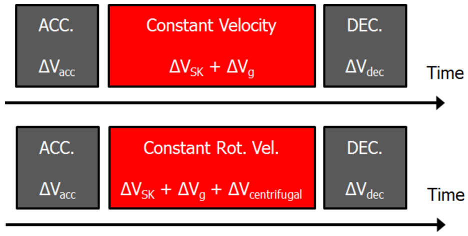

Figure 4.11: Timeline of the Rigid Resizing (top) and Rigid Retargeting (bottom).

Figure 4.11 shows the timeline for rigid resizing and retargeting manoeuvres. Both manoeuvres make use of an acceleration phase, a constant velocity or constant rotational velocity phase and a deceleration phase.

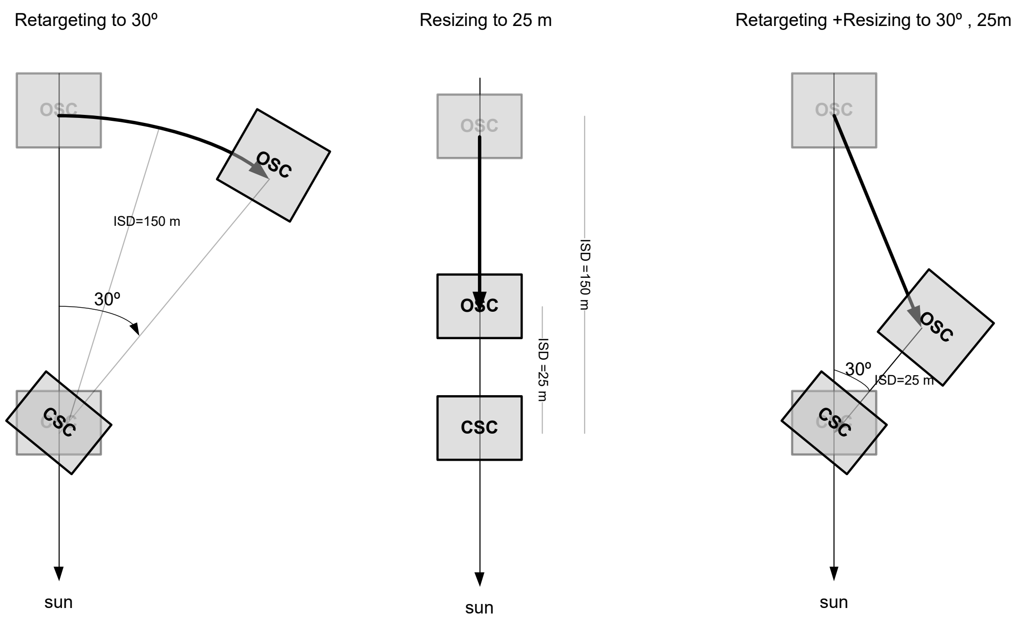

Figure 4.12: Rigid reconfiguration manoeuvres.

Figure 4.12 shows the rigid reconfiguration manoeuvres. The rigid manoeuvres consist in making the chaser/coronagraph follow a pre-determined relative trajectory with respect to the CSC. The manoeuvres are computed as follows. The final position of the OSC with respect to the CSC is computed according to the rigid reconfiguration mode final geometry. Next, maximum available acceleration to allocate to the kinematic profile is computed (taking in account a margin for control, gravity gradient and SRP compensation). The duration of the manoeuvre is the maximum allowed for the timeline, to allow a minimum ΔV and thus acceleration period. This means that two hours are allocated to arrive to the new configuration and two hours to reconfigure to original posture. The kinematic profile is built containing a phase of constant maximum acceleration in the target point direction, followed by an approach at constant velocity, followed by a deceleration to a zero relative velocity. The profile is computed by first assessing the velocity that would be necessary with an impulsive manoeuvre. From this value, together with the time to attain final position and the limit on maximum acceleration, the necessary velocity is computed, taking in account the acceleration and deceleration phases. During the transition, once the relative positions are known, it is possible to calculate the amount of ΔV necessary at each moment to counteract the effect of gravity gradient and SRP. In all the computations of these manoeuvres, the acceleration is obtained by analytical methods. In the case of retargeting, another force must be compensated, during the "free flight" phase (between acceleration and deceleration): the centrifugal force.

Table 4.5: Summary of rigid resizing.

Parameter	Value
Resizing velocity	18.5 mm/s
Acceleration phase duration	443 s
ΔV kinematic (4x)	18.5 mm/s
ΔV gravity gradient (2x)	1.7 mm/s
ΔV total	77.5 mm/s

Table 4.5 presents a summary of the analysis of the rigid resizing manoeuvre from 150 to 25 m. This rigid resizing manoeuvre is about 10 times more expensive than regular coronagraphy. The rigid resizing manoeuvre from 150 m to 25 m is the largest resizing included in the mission, so the ΔV is an upper value.

Table 4.6: Summary of rigid retargeting.

Parameter	Best case value
Retargeting velocity	11.5 mm/s
Acceleration phase duration	374 s
ΔV kinematic (4x)	11.5 mm/s
ΔV centrifugal	12.6 mm/s
ΔV gravity gradient	4 mm/s
ΔV total	62.6 mm/s

Table 4.6 presents a summary of the analysis of the rigid retargeting manoeuvre of 30°. The rigid retargeting is somewhat less expensive than the rigid resizing, but still about 9 times more than regular coronagraphy. Again, the rigid retargeting covering an angle of 30° is the largest retargeting included in the mission, such that the ΔV is an upper value.

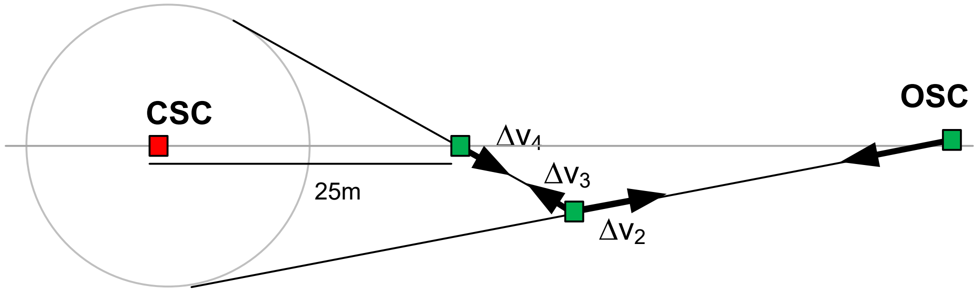

Figure 4.13: Loose resizing manoeuvre.

Figure 4.13 shows a loose resizing manoeuvre. Due to safety constraints, the manoeuvre is composed of two two-point transfers, through impulsive manoeuvres with the OSC cold-gas thrusters. The first part of the manoeuvre takes the OSC to a way point in the out-of-orbital-plane direction. From this way point the final configuration of an ISD of 25 meters in sun alignment is attained through a second two-point transfer. Never in the reconfiguration is the velocity vector directed towards a safety sphere around the CSC.

The manoeuvres are computed as follows. First, the final position of the OSC with respect to the CSC is computed according to the reconfiguration mode final geometry. The duration of the manoeuvre is the maximum allowed for the timeline, to allow a minimum ΔV and thus acceleration period. In this case, because of the errors introduced by the open-loop controlled ΔV, 0.5 hours are reserved for formation acquisition after the manoeuvre, so 1.5 hours are reserved to arrive to the new configuration, and 1.5 hours to return. For the resizing manoeuvre, the way point is computed to minimize total ΔV while keeping the trajectory pointed outside a safety sphere. The loose resizing manoeuvres are two-point transfers, which are computed as the solution to the Lambert problem. An iterative method is used to consider the non-impulsive ΔV. The time to attain that velocity using maximum acceleration is computed and the new boundary conditions (after the acceleration/deceleration phase) are computed. Using these new values, the extra velocity is computed. Iterations are repeated to a precision threshold. The two-point transfers take in account the gravity gradient and SRP to choose the magnitude and direction of the ΔV.

Table 4.7: Summary of loose resizing manoeuvre.

Parameter	Best case value
Duration of approach to waypoint	1 h 10 min
Duration of approach to terminal point	20 min
Duration of acquisition	30 sec
Duration of return	1 h 30 min
ΔV approach (4x)	28 mm/s
ΔV return (2x)	26 mm/s
ΔV station keeping (1x)	0.1 mm/s
ΔV total	164.1 mm/s

4

Table 4.7 summarizes the results of the analysis of the loose resizing manoeuvre from 150 m to 25 m. The ΔV required for safely performing loose resizing is more than twice the ΔV required for rigid resizing.

Finally, loose retargeting requires no additional safety measures in the form of waypoints. The total ΔV required for a loose retargeting over 30° is 59.2 mm/s. In general, the usefulness of loose manoeuvres could be questioned when the security constraints are considered. The only case in which the ΔV is smaller than in the rigid manoeuvres is the loose retargeting.

4.2.3 Nominal orbit ΔV

If only nominal operations are considered, then the total ΔV, without margins, for the full mission is estimated at 11.12 m/s for the high-performance green propellant system and 9.67 to 12.66 m/s for the cold-gas system. System level design has ensured that this is compatible with the masses of the spacecraft. Ultimately the mission lifetime is limited by the amount of propellant that the spacecraft can carry, such that the spacecraft carry sufficient propellant to last for two years.

4.3 Formation deployment

Formation flying starts with the formation deployment. Initially the spacecraft are mounted in a stack configuration and the separation from the stack is performed by means of a spring. At the moment of deployment neither spacecraft is fully commissioned, or more specifically, the sensors, actuators and the formation flying software still need to be switched on and commissioned. In addition, no omnidirectional sensor is present on the spacecraft. This means that the process of acquiring the formation requires ground support, and that the deployment sequence needs to be robust to large navigation and actuation errors, because the system has not been calibrated. After the initial formation deployment, the formation is placed in a safe orbit for commissioning the system. This safe orbit is a generalization to eccentric orbits of safe orbits used in formation flying in circular orbits [44]. In this section, the formation deployment is analysed first on a conceptual level, by comparing four deployment strategies and selecting the most promising alternative for further analysis. The first part of this analysis focuses on the safety of the approach and on the ΔV's required for the manoeuvres. The second part of the analysis focuses on the timeline of the deployment.

The safety of the approach trajectory is assessed by representing the trajectory in the V-bar reference frame. This is a local reference frame in which the x-axis is aligned with the velocity direction; the y-axis is opposite to the angular momentum and the z-axis completes the right-handed frame. In this reference frame the position along the z-axis is independent of the position along the x-axis, such that the projection onto the yz-plane of this reference frame is invariant even if the formation experiences along-track drift. This invariance is exact for unperturbed relative motion around a Keplerian orbit. Some variation of the trajectory projected onto this plane can be expected if perturbations are present. Margins have been defined around the trajectory that can absorb trajectory deviations due to actuation and navigation errors, and perturbations.

Figure 4.14 shows the formation deployment strategies that have been considered for Proba-3. All deployment strategies feature separation by means of springs (1) and a burn to stop the drift. Note that out-of-plane motion is not represented in these figures even though it is an element in both strategy 3 and 4. During deployment knowledge of the relative state comes from relative GPS measurements processed on ground, and manoeuvres are commanded from ground. The first strategy follows closely the rendezvous strategy of the Automated Transfer Vehicle ATV [18], using non-drifting hops (3) to advance in along-track position until the desired distance is reached. The second strategy uses a drift trajectory initiated with a single tangential burn to close the distance between the spacecraft. The drift is stopped once the proper distance is reached. The third strategy uses a cotangential transfer (2 – 3) to initiate drift and the formation is put into a safe orbit formation (4) once the spacecraft crosses R-bar. The safe orbit is subsequently shrunk (5 – 6). The fourth strategy incorporates the safe orbit at an earlier stage, at the end of the separation drift (2). The safe orbit is made to drift (3), until a safe orbit around the origin can be established (4). As in the previous strategy the safe orbit is then shrunk down (5 – 6).

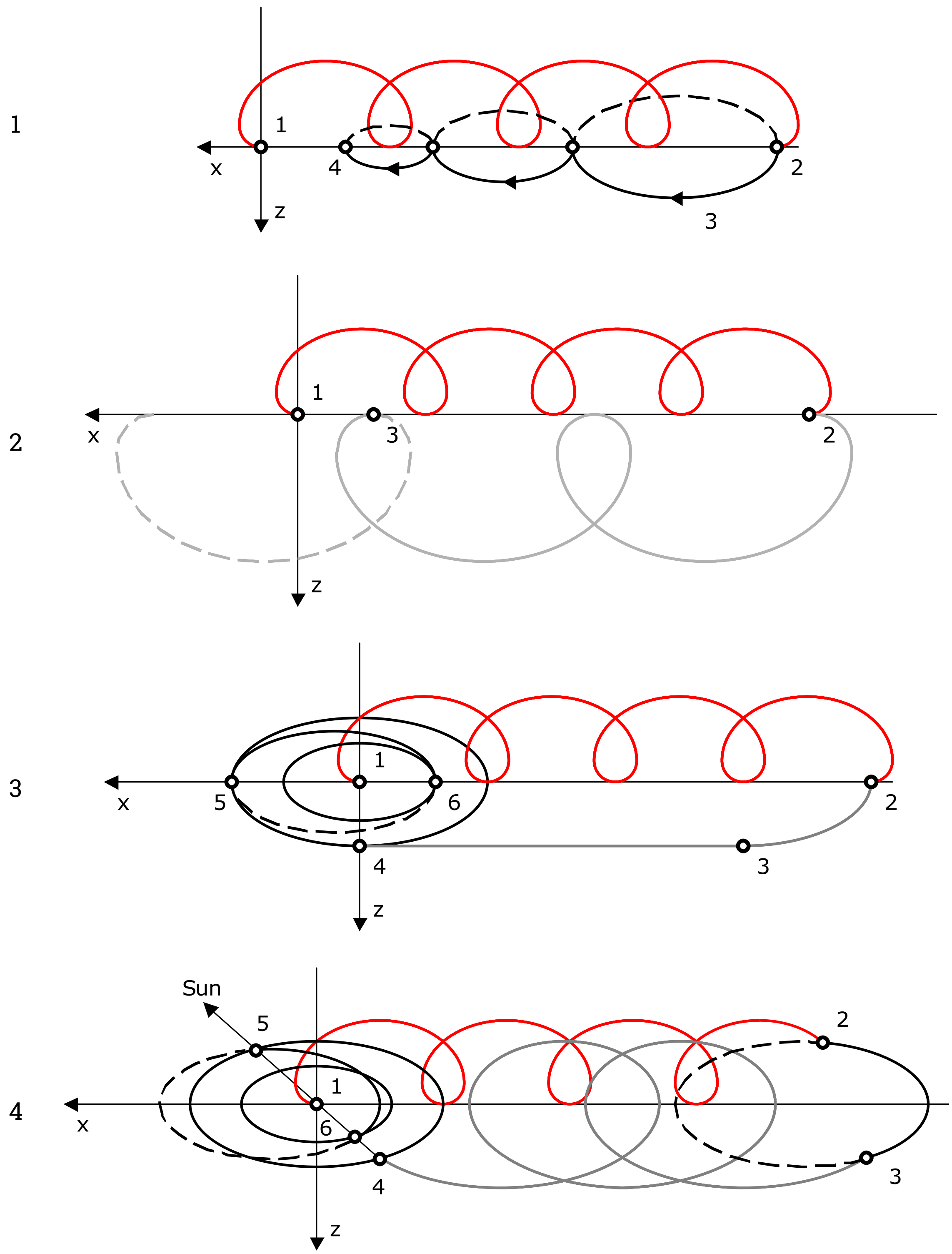

Figure 4.14: Four deployment strategy alternatives.

The first two strategies end in a hold trajectory on V-bar, while the other two end in a safe orbit around the origin. The safe orbit is the desired end point of the deployment because commissioning of the system is performed in this orbit. The criteria for the selection of the deployment strategy focus on simplicity, controllability, and robustness to measurement errors. In addition, each ΔV needs to be preceded by at least one measurement opportunity. The first strategy was discarded because measurements could not be performed before each manoeuvre, because each hop would take approximately half an orbital period. The second strategy was discarded because manoeuvres (2) and (3) do not offer sufficient control over the along-track position of the spacecraft as it arrives at point 3. In both the first and second strategy, the spacecraft is not in a safe orbit, such that collision risk exists. This is true especially if the manoeuvre close to the OSC at the origin is performed with limited accuracy. Strategy 3 was discarded because the drift trajectory (3) – (4) would need to be controlled at high precision to correctly establish the safe orbit at (4). Strategy 4 avoids the safety and precision issues associated with the other strategies by entering a safe orbit at a large along-track distance from the OSC, and then to initiate a drift back towards the OSC. During the drift backwards, the formation remains safe.

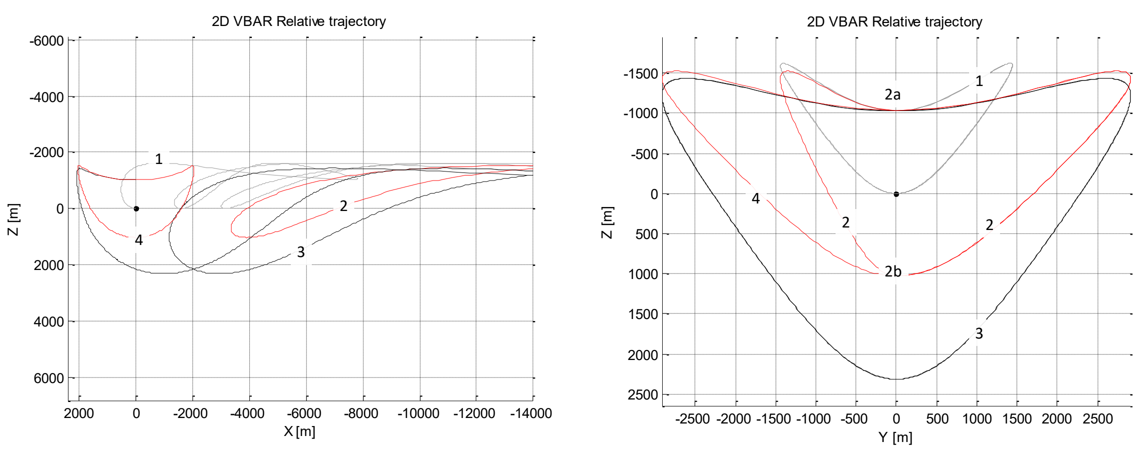

Figure 4.15: Formation deployment.

Figure 4.15 shows the formation deployment trajectory. The formation is deployed on the grey trajectory using a 10 cm/s spring separation ΔV directed 45° away from V-bar towards the out-of-plane direction. This trajectory element is labelled “1” in the figure. After drifting for two orbits, the formation is put into a safe orbit with a certain along-track distance, labelled “2” in the figure. The insertion into safe orbit is done by means of two manoeuvres. The first manoeuvre, labelled “2a”, is an along-track manoeuvre, which ensures that the drift is negated. The second manoeuvre, labelled “2b”, is an out-of-plane manoeuvre which ensures that the out-of-plane motion is adjusted according to the safe orbit dimensioning. Next, the CSC is set on a drifting trajectory, labelled “3” in the figure, in such a way that the drift trajectory is safe. This trajectory spirals around the x-axis. Finally, the CSC acquires a safe orbit around the OSC. The safe orbit is labelled “4” in the figure. The magnitude of the separation ΔV is determined by the desired size of the safe orbit.

After the safe orbit around the OSC is achieved, two transfers to smaller safe orbits are performed to achieve a small safe orbit around the target. In this safe orbit commissioning activities will take place, including calibration of the thrusters. The preliminary strategy for calibrating the thrusters is to perform a thrust with each thruster individually, with one thruster firing in a period of one orbit, and to perform orbit determination during this orbit. The ΔV that each thruster provided can be retrieved from the orbit determination.

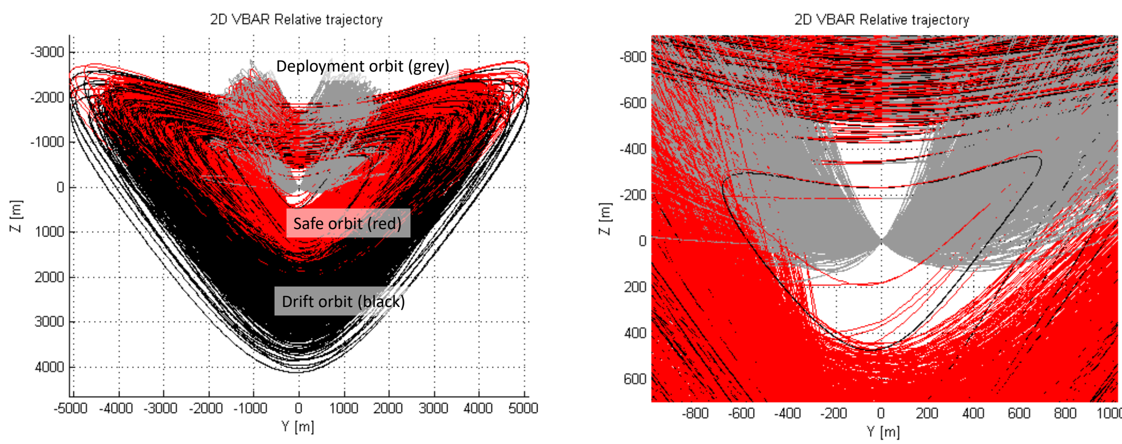

Figure 4.16: Monte Carlo simulations of deployment.

To assess the safety of the approach a Monte-Carlo simulation with 1000 shots has been performed. The Monte Carlo simulations assume a “true” state and a “measured” state. The measured state is found from the true state by adding random measurement errors. It is assumed that all manoeuvres except the initial separation are computed based on ground provided rGPS measurements. rGPS errors are assumed with a 3σ error that is the sum of the bias and noise contributions computed one orbit in advance. The thrusters are assumed to perform two times worse than during nominal operations, with a 3σ uncertainty of 10% in magnitude and 2° in direction. The deployment sequence is adjusted based on the along-track separation ΔV that is actually achieved: if the along-track separation ΔV is small, then the characteristic dimension of the safe orbit is small as well, and vice versa. Figure 4.16 shows that the dimension of the safe orbit can vary between about 400 m and 2000 m. This figure also shows that the safety features of the deployment trajectory remain intact.

Table 4.8: Deployment ΔV budget.

Event	mean ΔV [mm/s]	3σ ΔV [mm/s]
deployment	103.36	30.16
stop drift	7.43	5.32
out-of-plane	75.77	119.27
initiate drift back	9.37	6.87
establish safe orbit	9.35	7.55

Table 4.8 shows the ΔV budget for the deployment. As stated, a separation ΔV of 10 cm/s is selected, while the separation springs have a 3σ uncertainty of 30% in magnitude and 30° in direction. This is reflected in the deployment ΔV. The average deployment ΔV is 103.36 mm/s, with a 3σ variation of 30.16, as expected. The along-track manoeuvres (stop drift, initiate drift back and establish safe orbit) have a higher variability because the deployment and acquisition strategy is adjusted based on the size of the along-track ΔV provided by the separation springs: if this ΔV is low, then all other ΔV's down the line shrink. In other words, the variability of the initial separation ΔV influences the variability of all other ΔV's. The uncertainty due to navigation and thruster errors adds up to this variability.

The high variability in the out-of-plane correction manoeuvre can be explained by inspecting the deployment trajectory in figure 4.15 and figure 4.16. The variability can be explained by the uncertainty in the deployment direction. The size of the safe orbit is adjusted based on the magnitude of the separation ΔV that is applied in the along-track direction. The reason for this is that the safe orbit is established by means of a ΔV that simply stops the drift (manoeuvre 2a in figure 4.15). This manoeuvre is performed at the extremum of the z-coordinate, and the extremum of the z-coordinate is determined by the along-track component of the separation ΔV. The nominal deployment direction ensures that 50% of the deployment ΔV is in the along-track direction, and 50% in the out-of-plane direction. Consider the case in which a greater proportion of the ΔV is applied in the along-track direction. In this case the size of the terminal safe orbit grows, making a larger out-of-plane ΔV necessary to enlarge the out-of-plane dimension in accordance with the larger size of the safe orbit. At the same time, a smaller portion of the deployment ΔV is applied in the out-of-plane direction, such that the resulting out-of-plane dimension of the trajectory is smaller than intended. A larger out-of-plane ΔV is needed to compensate for the smaller deployment ΔV in the out-of-plane direction. These two effects add up, such that the variability of the deployment direction has a double impact on the variability of the required out-of-plane ΔV.

The safe orbit around the origin is used for commissioning the formation flying system. The safe orbit has been selected as the commissioning orbit due to its passive safety features. Commissioning phase will be conducted under ground control, with very limited autonomy on board. As the different elements of the system are commissioned, the level of on-board autonomy will be increased, but for the early stages of this phase, no autonomy will be present and all the required manoeuvres will have to be computed on ground.

The most restrictive requirements are associated with the FLLS sensor and with the power / thermal subsystem constraint that the spacecraft cannot rotate more than 30° from the Sun direction. The FLLS sensor requires a distance smaller than 250 m and a longitudinal velocity that is smaller than 50 mm/s. This means that the formation needs to be within 30° of an exact alignment with the Sun direction to calibrate the FLLS. The compatibility of these constraints with the safe orbit is investigated during the second and third month after launch for every launch date. One month (31 days) is taken equal to 38 full orbits. Spacecraft commissioning takes one month, and formation flying commissioning takes 2 months.

In addition, commissioning phase will be conducted under ground control, with very limited autonomy on board. As the different elements of the system are commissioned, the level of on-board autonomy will be increased, but for the early stages of this phase, no autonomy will be present and all the required manoeuvres will have to be computed on ground. This means that after each perigee pass, GPS data should be downloaded as soon as possible for ground processing (POD) and manoeuvre computations. Ideally the time between the perigee (GPS data availability) and the manoeuvre to be performed should be minimized to mitigate as much as possible the errors due to the propagation of the navigation solution. It is assumed that during the formation deployment every ground station contact with Redu can be exploited for up- and downlink. What follows below is a first assessment of the compatibility of the deployment timeline developed above and the operational constraints imposed by the ground station contacts and the Sun alignment.

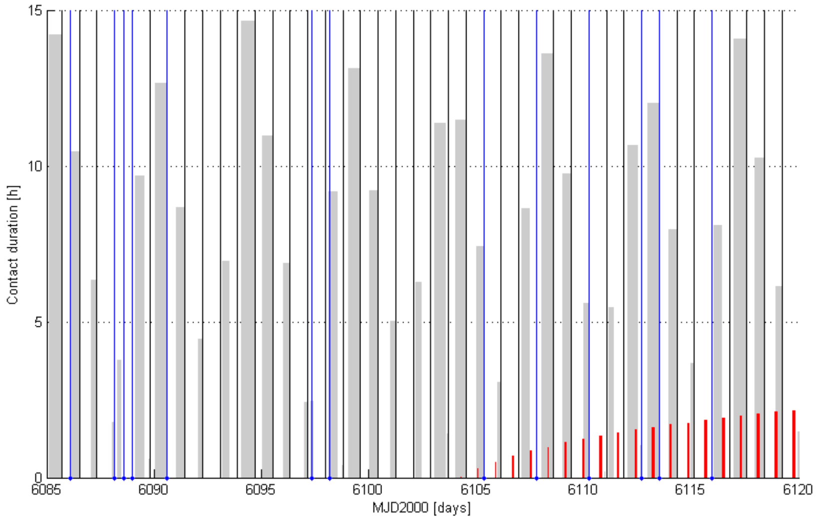

Figure 4.17: Commissioning timeline for launch on July 29th 2016.

Figure 4.17 shows a graphical representation of a typical commissioning timeline. The following elements are represented in the graphs:

- Perigee times in black vertical lines
- Manoeuvre times in dotted blue vertical lines.
- Contacts with Redu ground station in grey vertical bars
- “Sun alignment” in vertical red bars

The first manoeuvre is the spring actuation for separation, 1 month after launch. Manoeuvres 2 to 5 are the establishment of the safe orbit around the origin. Manoeuvres 6 and 7 are manoeuvres to shrink the safe orbit, and the establishment of the commissioning orbit. Manoeuvres 8 to 13 are manoeuvres required for commissioning.

Sun alignment is required for commissioning the relative metrology. Sun alignment is not always available in the safe orbit; it is dependent on the date. Figure 4.17 shows that Sun alignment becomes available after the 9th manoeuvre at epoch 6105, such that commissioning of the relative metrology needs to be performed after this date.

The timeline up to the commissioning of the perigee pass is feasible, although there are three manoeuvres that need to be prepared and performed in a short time frame. For these three manoeuvres, GPS data should be downloaded, precise orbit determination (POD) should be performed, and the manoeuvre computed and uploaded in about 1 h. This is deemed feasible, but alternatives exist: it is possible to delay the manoeuvres to 180°, which would lead to an additional margin of 2 hours. It would also be possible to include another ground station. Finally, it would be possible to postpone these manoeuvres by one or more orbits until favourable geometry occurs.

4.4 Conclusion

The mission analysis work shows that the nominal operations are feasible with the current configuration of the system. A simple and robust strategy has been selected for the perigee pass, which features a two-point transfer with a correction performed shortly after the first manoeuvre. This strategy requires a ΔV of 12.49 mm/s to be performed by the high-performance green propellant propulsion system of the coronagraph spacecraft and a ΔV of 3.58 - 6.93 mm/s to be performed by the cold-gas propulsion system of the occulter spacecraft. If the formation performs coronagraphy at apogee, then a cold-gas ΔV of on average 7.29 mm/s is required. Formation reconfiguration manoeuvres require a maximum ΔV of 77.5 mm/s in case of rigid manoeuvres and 164.1 mm/s in case of loose manoeuvres. The total ΔV for the full mission can be estimated at 11.12 m/s for the high-performance green propellant system and 9.67 to 12.66 m/s for the cold-gas system. This is compatible with the capabilities of the spacecraft for the two-year mission.

In addition, a safe deployment strategy has been defined that allows the coronagraph spacecraft to rendezvous with the occulter spacecraft and enter a safe orbit for commissioning the formation flying system. This strategy is compatible with the mission constraints. The ΔV required for the deployment is 101 and 241 mm/s.

5

Relative mission analysis for Proba-3: safe orbits and CAM[5]

This paper reports the phase B mission analysis work performed for the safe orbit and the Collision Avoidance Manoeuvres (CAM) of the Proba-3 formation flying mission, including the recovery to nominal conditions. Proba-3 will perform formation flying in HEO and perform Solar coronagraphy and formation manoeuvring demonstrations in a six-hour arc around apogee. Mission analysis in this paper addresses the safe orbit and the CAM and focuses on safety and ΔV requirements. Important constraints on the mission analysis are the absence of an omnidirectional sensor, and the requirement that the spacecraft cannot turn more than 30° away from the Sun due to thermal and power constraints. In addition, no on-board action can be taken after safe orbit entry nor after a CAM, which means that the recovery needs to be performed under ground control.

5.1 Introduction

The Proba-3 mission is designed to perform formation flying in HEO. The formation consists of a coronagraph spacecraft (CSC) and an occulter spacecraft (OSC). The spacecraft are equipped with the following relative state sensors: both spacecraft are equipped with a GPS receiver and an inter-satellite link such that rGPS measurements can be made.

[5] This chapter was previously published in International Journal of Space Science and Engineering, doi: 10.1504/IJSPACESE.2014.060599. The original article contained an error in the algorithm provided for the collision avoidance manoeuvre. The corrected algorithm and a discussion of the error is provided in appendix E.

The CSC is equipped with a Coarse Lateral Sensor (CLS) with a field of view of 5° and a Fine Lateral and Longitudinal Sensor (FLLS) with a field of view of 33 mm diameter at aperture. The spacecraft should not turn more than 30° away from the Sun direction due to thermal and power constraints. This limits the availability of the CLS and the FLLS to periods during which the angle between the CSC - OSC direction and the Sun direction is smaller than 30°. Figure 5.1 shows the Proba-3 spacecraft. The CSC is shown on the left and the OSC on the right.

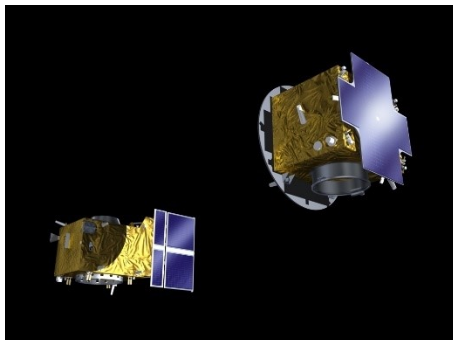

Figure 5.1: Proba-3 Spacecraft ©ESA.

Orbital parameters of the reference orbit are shown in table 5.1. For simulations of transfer manoeuvres, the orbital parameters are assumed to be fixed, and the motion is assumed to be Keplerian. For simulations to determine the stability of the safe orbit, perturbations are considered for calculation of both the reference orbit and the relative orbit.

Table 5.1: Orbital parameters.

Parameter	Value
Semi-major axis	36943 km
Eccentricity	0.8111 -
Inclination	59°
RAAN	84°
AoP	188°
Orbital period	19h38m

Table 5.2 presents the characteristics of the two spacecraft. Both spacecraft are equipped with a propulsion system. The CSC is equipped with a high-performance green propellant (HPGP) propulsion system with a thrust of 1 N, and the OSC is equipped a 10 mN cold-gas system. The table also shows the parameters used for computing the Solar radiation pressure (SRP) perturbation.

Table 5.2: Spacecraft characteristics.

Parameter	OSC	CSC
Area [m2]	1.77	3.34
Wet mass [kg]	211	339
Dry mass [kg]	190	327
SRP coefficient [-]	1.9	1.29
Thrust per thruster [mN]	10	1000
Thruster force capacity in direction of minimum thruster force capacity [mN]	14.3	2100
Fraction of thrust allocated for control	0.2	-

Table 5.3 lists the accuracy of the relative navigation. In addition to sensors listed in the table the CSC is equipped with a Coarse Lateral Sensor (CLS). This sensor is used during the process of acquisition of the FLLS, such that only the FLLS-based relative navigation is used for computing manoeuvres. For this reason, the CLS is omitted.

Table 5.3: Relative navigation accuracy.

Parameter	Relative GPS	FLLS
1σ position bias [cm]	4.07	-
1σ velocity bias [mm/s]	0.0160	-
1σ position error [cm]	2.05	0.3
1σ velocity error [mm/s]	0.0228	0.005
1σ position bias [cm]	4.07	-

GPS measurements are available in the region around perigee. The values presented in the table for the accuracy of the relative GPS solution are valid for the moment the formation exits the GPS visibility region. From that point onward, the accuracy degrades because the solution needs to be propagated. FLLS measurements are available whenever the two spacecraft are properly aligned.

This paper describes the mission analysis work performed for the off-nominal conditions, the safe orbit and the collision avoidance manoeuvres (CAM). The mission analysis work for the nominal operations is described in [48]. Both spacecraft need to be capable of transferring to the safe orbit and performing the CAM. The return to nominal is performed when both spacecraft have been restored to normal, such that the return to the nominal orbit can be performed with the CSC's more efficient HPGP propulsion system. The manoeuvres described in this article are open-loop controlled impulsive manoeuvres.

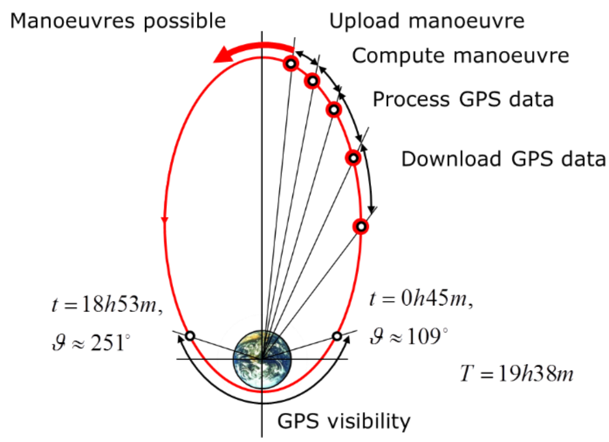

Figure 5.2: Ground control manoeuvre upload sequence.

Recovery from all off-nominal conditions is performed under ground supervision. This means that the ground needs to take the steps described in figure 5.2 before each manoeuvre is performed. First the navigation data needs to be downloaded. Next a relative navigation solution needs to be obtained. Finally, the manoeuvre needs to be computed and uploaded to the spacecraft. In investigation of the ground contacts with Redu has shown that a manoeuvre at 160° true anomaly is possible during some orbits, but not all. On the other hand, the errors associated with the GPS measurements start increasing rapidly after passing apogee. Simulations have shown that manoeuvres under ground control should be performed no later than 190° true anomaly. Under these restrictions gaps of up to two orbits exist between periods during which the ground control manoeuvre upload sequence shown in figure 5.2 can be used.

Two reference frames are used in the analysis of the relative motion. These are the LVLH frame and the VBAR frame. For both frames, the y-axis points into the direction of the negative orbital angular momentum vector. The z-axis of the LVLH frame points in the direction of the centre of Earth and the x-axis completes the right-handed frame. The VBAR frame uses a different definition. The x-axis points in the direction of the orbital velocity vector and the z-axis completes the right-handed frame. In both cases, the structure of the state vector is:

$$\mathbf{x} = [x \quad y \quad z \quad \dot{x} \quad \dot{y} \quad \dot{z}]^T \tag{5.1}$$

The structure of the paper is as follows. The safe orbit is discussed first. The safe orbit is first defined in terms of its Cartesian state. Next, the stability and the sizing of the safe orbit are discussed. Finally, all manoeuvres related to the safe orbit are investigated. These are, the entry into safe orbit, resizing of the safe orbit and return from safe orbit to nominal conditions. The CAM is discussed in the third chapter. The stop distance is discussed first, followed by a detailed description of the CAM algorithm. The behaviour over comparatively short timescales is investigated, and the return to mission is discussed. Finally, the long-term behaviour is investigated.

5.2 Safe orbit

The safe orbit is a stable non-drifting close formation flying trajectory that can be used for storing the formation during the long-eclipse season when eclipses occur around apogee for about 15 days, or after a minor malfunction has taken place and ground intervention is required. It is also used during the initial deployment and commissioning of the formation (see also [48]).

The safe orbit has been designed using the following criteria. The safe orbit should be stable for 30 days without applying control. It should be possible to recover the formation from the safe orbit quickly and with low ΔV. The ability to use the inter-satellite link and relative metrology is highly desirable.

5.2.1 Overview

The safe orbit is designed as a generalization of the eccentricity / inclination vector separation strategy that is used for formation flying in circular orbits [44]. This type of safe orbit is designed to have no difference in semi-major axis between the two spacecraft, such that in the unperturbed linearized model along-track drift is absent. The safe orbit is defined in terms of the differential eccentricity and angular momentum vectors [206], in such a way that the coronagraph spacecraft is above the occulter spacecraft at apogee and below the occulter spacecraft at perigee, or vice versa. When the spacecraft crosses V-bar (that is, the z-coordinate is zero), it has a large out-of-plane position. This means that the resulting trajectory never intersects V-bar. The safe orbit is defined with respect to the reference orbit by a change in eccentricity and a rotation around the line of apsides. All other elements of the safe orbit are the same as the reference orbit.

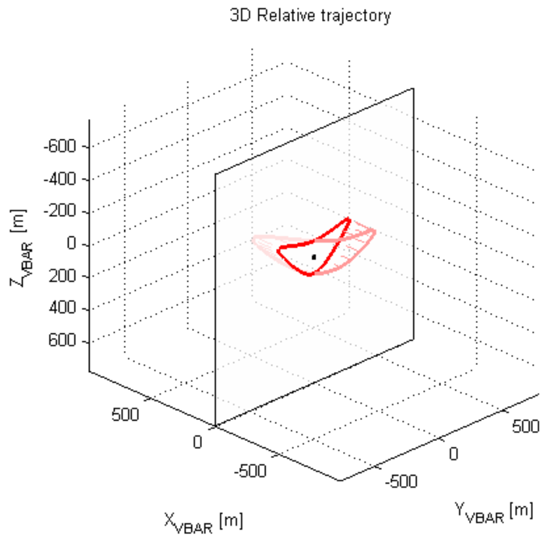

Figure 5.3: Safe Orbit.

5

Figure 5.3 shows the safe orbit trajectory. Representation of the trajectory in the V-bar aligned reference frame is advantageous because in this frame the projection of the trajectory on the YZ-plane is independent of the along-track coordinate [206]. The safety of a trajectory can be determined by inspecting the closest approach of the trajectory in the YZ-plane. The safe orbit can be defined in terms of a Cartesian state vector in the LVLH reference frame. The components of the state vector are the relative Cartesian position and velocity as defined in the introduction.

$$\begin{aligned}\mathbf{x}_{safe,\boldsymbol{ip}} &= [x \quad z \quad \dot{x} \quad \dot{z}\,]^T \\ &= \pm D\rho^{-1}[-(1+\rho)\sin\vartheta \quad -c \quad -(\rho^{-2}(e+\rho c)+c)k^2\rho^2 \quad sk^2\rho^2]^T \\ \mathbf{x}_{safe,\boldsymbol{ip}} &= [y \quad \dot{y}\,]^T = \pm D(1+e^2)\rho^{-1}[\sin\vartheta \quad \rho^{-1}(\cos\vartheta+e)k^2\rho^2]^T\end{aligned} \tag{5.2}$$

where:

D is the characteristic dimension of the formation,

a is the semi-major axis of the reference orbit,

e is the eccentricity of the reference orbit,

$k^2 = \sqrt{\mu p^{-3}},\ \rho = 1 + e\cos\vartheta\,,\ p = a(1-e^2),\ s = \rho\sin\vartheta\,,\ c = \rho\cos\vartheta,$

ϑ is the true anomaly of the reference orbit,

μ is the gravitational parameter

Note that the in-plane motion is due only to the difference in eccentricity (see [147]) and the out-of-plane motion only to the rotation around the line of apsides. The ratio of the amplitudes of the in-plane and out-of-plane motions is essentially a free parameter, but it has been fixed to limit the number of available configurations for the safe orbit. For this reason, only a single characteristic dimension is in use. The value at which the amplitude ration has been set makes the out-of-plane amplitude fairly large compared to the in-plane amplitude. The reason for selecting a large value is to ensure formation safety under the influence of perturbations for at least 30 days, see section 5.2.2.

Four configurations are possible for the safe orbit, depending on the sign of the in-plane and out-of-plane motions. The first configuration has positive sign for both in-plane and out-of-plane motion, the second has negative sign for in-plane and positive sign for out-of-plane motion, the third has positive sign for in-plane and negative sign for out-of-plane motion and the fourth has negative sign for both in-plane and out-of-plane motion.

5.2.2 Safe orbit stability

The stability of the safe orbit is analysed for various dates by propagating the orbits of the OSC and the CSC using an absolute propagator for both and subtracting the results. The reference orbit is taken as initial conditions for generating the orbit of the OSC. The initial conditions for generating the orbit of the CSC are obtained as follows. First, the Cartesian LVLH state vector is converted to differential orbital elements by means of a linear transformation [147]. Next, the linear differences in orbital elements are added to the orbital elements of the reference orbit.

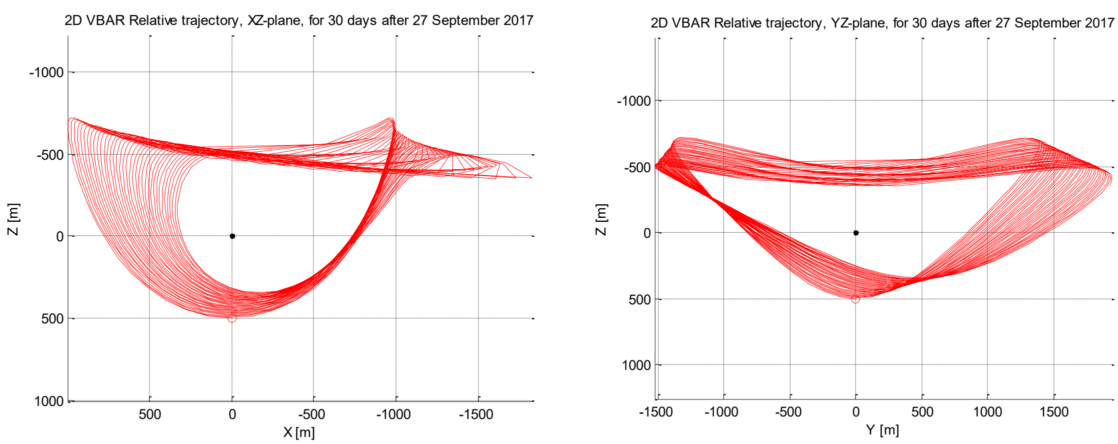

Figure 5.4. Safe orbit stability for 30 days, XZ (left) and YZ (right) projection (left).

The first year has been divided into 12 segments, and long-term simulations have been performed for each. Figure 5.4 shows the worst-case evolution of the safe orbit during a 30 day propagation period. SRP has the largest perturbative influence, followed by J_2. Figure 5.5 shows the evolution of the inter-satellite distance (ISD). The minimum

ISD decreases to 290 m after 30 days. This figure confirms that the safe orbit is indeed safe for 30 days.

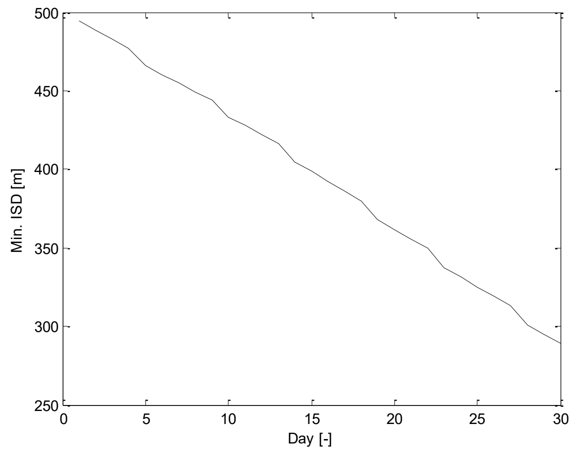

Figure 5.5. Worst case evolution of ISD.

The following observations have been made on the evolution of the relative trajectory (such as depicted in figure 5.4). Substantial along-track drift may also be present when the safe orbit is initialized. This drift has two main causes, namely, dispersions caused by navigation and actuation errors during safe orbit entry and unmodelled J_2 effect. The J_2 effect is important if transfer starts close to perigee. The cause of this phenomenon is that the J_2 perturbation causes short-period oscillations in the semi-major axis (and the other elements, but the effect is less important) which the unperturbed, linear guidance model does not consider. Both effects can lead to an along-track drift of about 13 km in 30 days, summing to a total of 26 km in 30 days.

5.2.3 Safe orbit sizing

The sizing of the safe orbit considers the stay time in the safe orbit, the insertion accuracy, and the minimum approach distance.

The characteristic dimension of the safe orbit should be set large enough to be able to cope with safe orbit insertion uncertainties and the influence of perturbations, mainly J_2 and SRP. The minimum characteristic dimension is determined as the sum of three contributions, namely, the maximum expected trajectory uncertainties at the point of closest approach, the maximum expected impact of the perturbations and the minimum ISD.

The stay time in the safe orbit determines the effect of perturbations on the trajectory; the longer the formation remains in safe orbit, the larger the effect of perturbations and the larger the safe orbit must be to accommodate perturbations. The insertion accuracy is determined by the navigation and the actuation accuracy. The actuation accuracy depends (amongst others) on the magnitude of the ΔV to be supplied, which in turn depends on the size of the safe orbit.

Table 5.4 reports the safe orbit options that lead to a safe transfer and a safe stay time for the specified period. It also shows the margins required to accommodate the perturbations and the dispersions associated with the transfer to safe orbit.

For the long eclipse season, a 15-day safety interval is required. In this case, the cumulative effect of perturbations is smaller than expected in section 5.2.2: the minimum ISD shrinks by about 100 m under the influence of J_2 and SRP. A margin of 100 m is therefore required to accommodate perturbations. The transfer itself has an insertion accuracy of 100 m. The minimum ISD has been chosen as 80 m for all safe orbit options, such that for a 15 day stay time a safe orbit with a characteristic dimension of at least 280 m is required. To make the safe orbit selection independent of the required stay time a characteristic dimension of 500 m is selected for the safe orbit regardless of the stay time. This leads to a simpler and more robust algorithm for selecting the safe orbit.

Table 5.4: Safe orbit sizing table.

Duration (days)	perturbation margin (m)	insertion accuracy margin (m)	minimum ISD (m)	characteristic dimension (m)	min entry ΔV (mm/s)	max entry ΔV (mm/s)	ΔV to resize to 150 m safe (mm/s)
10	70	90	80	240	36	70	18
15	100	100	80	280	44	78	26
20	140	130	80	350	56	93	40
25	180	160	80	420	69	108	54
30	220	200	80	500	80	125	70

5.2.4 Safe orbit entry

The safe orbit entry has been investigated by means of extensive simulations. The transfer to safe orbit needs to be available for any orbit during the mission life and for any point along the orbit. The transfer to the safe orbit is performed by means of a two-point transfer (the linearized version of Lambert's problem). The transfers have been investigated systematically, from a point along the nominal orbit sequence to each of the four configurations dividing each orbit into 20 steps of equal true anomaly during each orbit and for every date found by dividing the year in 10 steps during the first year (i.e., one transfer computed every 36 days). The transfer to a safe orbit of 500 m can always be performed safely. The maximum 3σ trajectory bounds due to insertion errors that can reasonably be expected are 190 m. The ΔV required to enter safe orbit from the nominal orbit routine lies between 80 and 125 mm/s.

Figure 5.6 shows an example of a transfer to safe orbit from nominal conditions with worst case actuation errors. Worst case trajectory uncertainties are associated with transfers to safe orbit that start in a region close to perigee. Within the set of cases that was investigated, the largest trajectory uncertainties at apogee or perigee always occurred for trajectories started within 70° of perigee.

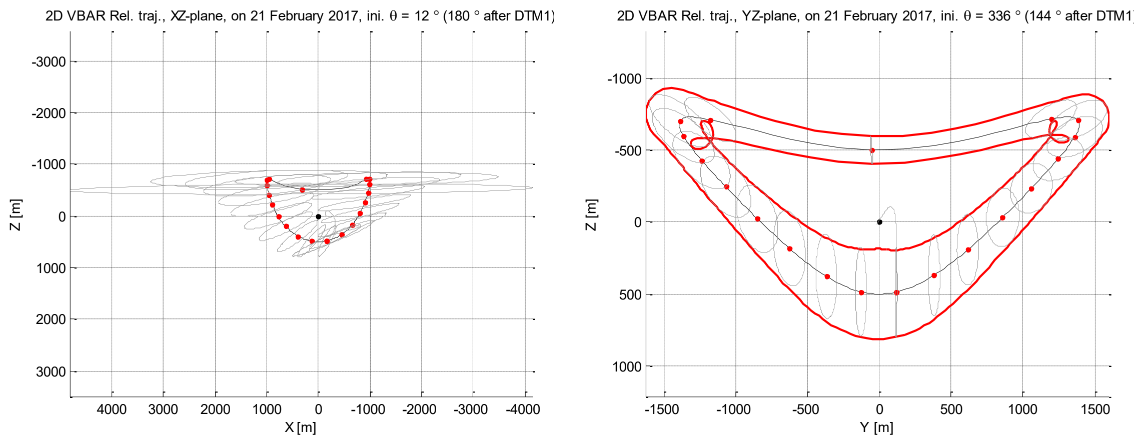

Figure 5.6: Transfer to safe orbit, worst case actuation errors.

5.2.5 Resizing the safe orbit

In certain situations, it is required to resize the safe orbit. To increase the stay time, for example, it may be required to enlarge the safe orbit. For returning from the safe orbit to nominal conditions it is required to shrink the safe orbit. Shrinking the safe orbit is the critical case because dispersions due to actuation errors may cause the trajectory to become unsafe. Resizing the safe orbit is performed using a two-point transfer from a predetermined initial true anomaly to a final true anomaly that is chosen such that the total ΔV is minimized.

Two characteristic dimensions are used for the safe orbit, namely 500 m and 1000 m. A characteristic dimension of 500 m is used for brief mission interruptions, for example during long eclipse season. A characteristic dimension of 1000 m is used during the initial deployment and during the recovery from CAM manoeuvres. Dispersions due to actuation errors prevent a direct transfer from a safe orbit to nominal conditions if the characteristic dimension of the safe orbit is larger than 200 m. This means that the safe orbit needs to be shrunk before the return to nominal conditions can be performed. Dispersions due to actuation errors limit the extent to which the safe orbit can be shrunk in a single step. The safe orbit can be safely shrunk to a characteristic dimension of 150 m from an initial characteristic dimension of 500 m. If the initial characteristic dimension is 1000 m, then the safe orbit should first be shrunk to a characteristic dimension of 250 m.

Figure 5.7 shows an example of a shrinking operation from a characteristic dimension of 1000 m down to a characteristic dimension of 250 m. The initial conditions for the shrinking operation are representative of the safe orbit at the end of formation deployment and the CAM recovery, including dispersions. The transfer takes place from a true anomaly of 160° to a true anomaly that minimizes the transfer ΔV. This true anomaly lies between 180° and 195°. Figure 5.7 shows the initial and final safe orbit during the shrinking operation. In this example, the ΔV required for shrinking the safe orbit is 145.31 mm/s, with a 3σ uncertainty of 13.75 mm/s.

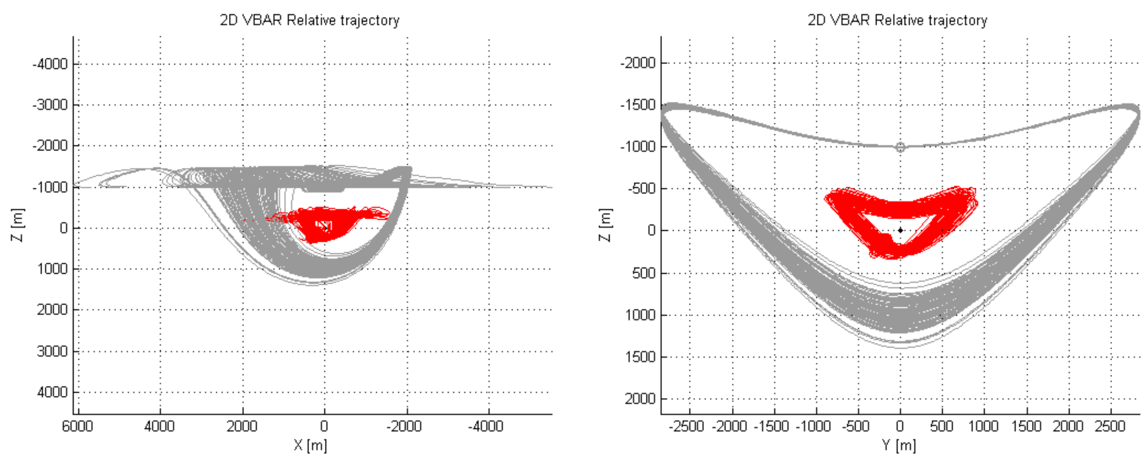

Figure 5.7: Shrinking the safe orbit from 1000 m to 250 m.

5.2.6 Return to nominal conditions

The strategy for returning to nominal operations depends on the time the spacecraft have spent in safe orbit. Safe orbit is not controlled, so, the longer the spacecraft remain in safe orbit, the longer perturbations will act on the trajectory and cause dispersions. The analysis in the previous paragraph has shown that the trajectory can drift over quite a large along-track distance, and that it can be deformed quite a lot during 30 days. It is therefore quite likely that the safe orbit trajectory will first need to be corrected. It is assumed that the process to correct the trajectory ends in a safe orbit with accuracy determined by the navigation and actuator accuracy.

The return from the safe orbit to nominal orbit conditions is examined to ensure that the OSC is in the field of view of the CLS at the end of the transfer to the nominal orbit. This condition needs to be satisfied such that the on-board formation flying software can successfully take over at that point. All manoeuvres up to this handover are performed under ground command.

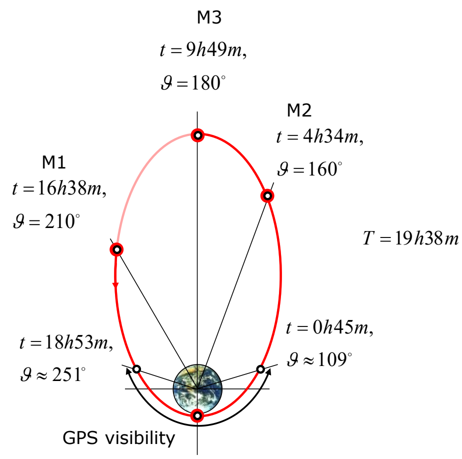

Figure 5.8: Transfer from safe orbit to nominal conditions.

Figure 5.8 shows the manoeuvring strategy for all manoeuvres up to the handover point. The transfer is initiated after a measurement arc as a two-point transfer between a true anomaly of 210° to apogee of the next orbit. GPS measurements are taken when the formation passes through perigee and a correction manoeuvre is computed and uploaded before the formation reaches a true anomaly of 160°. The correction manoeuvre is a two-point transfer between a true anomaly of 160° and apogee. The error associated with the first manoeuvre is large, because it is performed later than 190° true anomaly (see figure 5.2 and associated discussion). The large error is acceptable because the second manoeuvre can correct it. The second manoeuvre is performed at the earliest possible time according to the ground segment constraints. Manoeuvre M3 is performed without additional measurements taken after manoeuvre M2. Note that at this point the relative metrology is expected to become active.

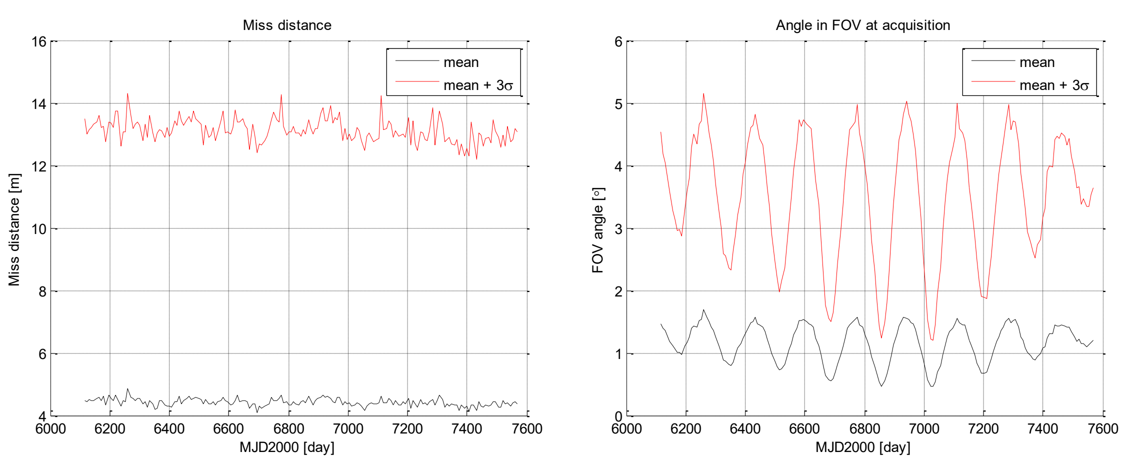

Figure 5.9: Miss distance (l); angle between CSC OSC direction and CLS bore sight (r).

Figure 5.9 shows the miss distance and the ISD at the terminal point. The mean approach distance is about 4.5 meters, while the mean + 3σ approach distance is about 13 meters. A related measure is the angle in the FOV at the terminal point. More precisely, this is the angle between the CSC-OSC direction and the CLS bore sight. It is calculated as the angle between the desired and actual terminal relative position vector: it is assumed that the CLS is pointed along the expected direction to the OSC, which is equal to the unit vector along the desired relative position vector of the OSC.

Figure 5.9 also shows the FOV angle. The mean + 3σ angle remains below 5° nearly all the time, although there are some dates (notably around 6250) at which the mean + 3σ angle is equal or slightly larger than 5°. The mean FOV angle fluctuates around 1°. The chances of finding the OSC in the CLS FOV after the transfer are quite high. The seasonally averaged, mean ΔV required for the impulsive transfer is 35 mm/s, and the mean + 3σ ΔV is 45 mm/s. On top of this a ΔV of 11.5 mm/s is required for the forced motion acquisition.

5.3 CAM

The CAM needs to provide active protection against collisions during a 10-hour arc around apogee. Both the OSC and the CSC need to be capable of providing the CAM. The CAM is designed based on considerations that cover the initial behaviour during and right after the burn (the stop and departure), the behaviour during the first few orbits and the long-term evolution. These points can be summed up as follows:

1. Ensure that the spacecraft comes to a stop safely (if required)
2. Ensure that the spacecraft moves out safely
3. Ensure that the trajectory does not return to the origin
4. Ensure that no evaporation occurs

The CAM ΔV is computed as the sum of two contributions (applied as a single ΔV), namely, the ΔV required to stop the motion, and a ΔV that is required to put the spacecraft into a drifting trajectory with a specified drift distance per orbit, meaning that the spacecraft are drifting apart after the execution of the CAM. The second contribution is computed based on the drift distance and the current in-plane relative position vector. The CAM analysis considers failures during coronagraphy operations and during formation resizing. The following scenario was considered the worst case for the stop distance analysis. During nominal operations, the ISD can be decreased from 150 m to 25 m over the course of a single apogee pass by means of a straight-line forced motion approach. This means that the two spacecraft can be in a situation where the ISD is small, and the spacecraft are moving closer together. This section discusses the CAM algorithm, the stop distance, the short-term behaviour after the CAM, the return to mission and the long-term behaviour.

5.3.1 CAM algorithm

The algorithm computes the ΔV as the sum of two components, ΔV_1 and ΔV_2.

$$\mathbf{\Delta V}_{CAM} = \mathbf{\Delta V}_1 + \mathbf{\Delta V}_2 \tag{5.3}$$

The first component nullifies the velocity. The y-component of the velocity is only nullified if it is directed towards the target.

$$\mathbf{\Delta V}_{1,ip} = -\begin{bmatrix} v_{x,LVLH} \\ v_{z,LVLH} \end{bmatrix}, \qquad \Delta V_{1,op} = \begin{cases} 0 & \operatorname{sgn}(v_{y,LVLH}) = \operatorname{sgn}(y_{LVLH}) \\ v_{y,LVLH} & \operatorname{sgn}(v_{y,LVLH}) \neq \operatorname{sgn}(y_{LVLH}) \end{cases} \tag{5.4}$$

where:

$v_{x,LVLH}, v_{y,LVLH}, v_{z,LVLH}$ Cartesian velocity vector components in the LVLH frame.

The second component of the ΔV is to be applied along V-bar. The magnitude of ΔV_2 can be computed from the current x and z components of the position vector and the desired drift rate per orbit:

$$\Delta V_2 = \frac{k^2 a \eta^4}{2\sqrt{2\rho - \eta^2}} \left(\mp \frac{\eta}{3\pi a(1-e)} D_{des} + \frac{2\rho^2}{a\eta^4} (e \sin\vartheta \, x_{LVLH} + (1+\rho) z_{LVLH} \right) \tag{5.5}$$

where:

$\rho = 1 + e\cos\vartheta\,, \qquad \eta = \sqrt{1-e^2}, \qquad k^2 = \sqrt{\mu p^{-3}}, \qquad p = a\eta^2$

a is the semi-major axis of the reference orbit,

e is the eccentricity of the reference orbit,

D_{des} is the desired drift rate per orbit.

ϑ is the true anomaly of the reference orbit,

μ is the gravitational parameter,

x_{LVLH}, z_{LVLH} are the in-plane Cartesian position vector components in the LVLH frame.

The sign of the desired drift rate depends on the direction of the in-plane ΔV. The direction is chosen such that the initial velocity after the CAM is directed away from the origin. The second component of the ΔV is given by:

$$\mathbf{\Delta V}_{2,ip} = \Delta V_2 \frac{1}{\sqrt{2\rho - \eta^2}} \begin{bmatrix} \rho \\ e \sin\vartheta \end{bmatrix} \tag{5.6}$$

5.3.2 Stop distance

This section presents an initial assessment of the safety of the formation during the execution of the CAM, based on the first component of the CAM ΔV that is aimed to stop the motion. (The second component of the ΔV ensures that the spacecraft move apart) The safety during the CAM is investigated by examining the distance travelled during the CAM. The CAM can be triggered when one spacecraft crosses the boundary of a stop sphere around the other spacecraft. This means that the size of the stop sphere should be at least large enough that during the time between the start of the application of the CAM and the end of the application of the CAM, no collision can occur. The size of the stop sphere is dependent on the maximum expected relative velocity of the formation, and on the minimum expected dimensions of the formation. The stop distance can be estimated by assuming that the spacecraft are moving in gravity-free space and that the spacecraft performing the CAM thrusts continuously in the direction opposite to the relative velocity until the motion is stopped. Under these assumptions the stop distance is given by:

$$d = \frac{1}{2}\left(\frac{m}{F}\right)V^2 \tag{5.7}$$

The OSC is equipped with cold-gas thrusters, such that the CAM performed by the OSC is the critical case for determining the stop distance. Simulations have shown [48] that the maximum velocity in the 10 hour region around apogee is 20 mm/s for the nominal orbit. This leads to a stop distance of about 3 m for the OSC. This value for the stop distance is compatible with the minimum ISD during formation flying of 25 m.

5.3.3 Short-term behaviour

The full CAM algorithm has been simulated using Monte Carlo simulations. The first component of the CAM ΔV (to stop the motion) only depends on the relative velocity, but the second component depends on the relative position also. The short-range simulations were performed primarily to investigate the safety of the CAM for a variety of operating conditions, with the secondary goal of assessing the usefulness of simple rule-of-thumb formulas such as (5.7) for establishing safe lower bounds on the approach distance and velocity. The initial position is randomly selected lying on a sphere with a radius of R. The initial velocity follows a Gaussian distribution on all components, such that the mean value takes on a particular value of 20 mm/s. The simulation uses a constant acceleration thrust arc in the VBAR reference frame to perform the CAM. An uncertainty of 5% in magnitude (1σ) and 1° in direction (1σ) is applied to the ΔV vector. After the thrust arc, the trajectory is propagated for two full revolutions and the minimum ISD during the full trajectory is stored.

Three simulations are performed: one at close range, the second at medium range, and the third at a long range. Figure 5.10 shows the results of these simulations. The initial conditions for the short-range simulation (left) lie on a sphere of radius 30 meters, with a mean velocity of 20 mm/s. The drift per orbit is set to 200 m. The initial conditions for the medium range simulation (middle) lie on a sphere of radius 75 meters, with a mean velocity of 20 mm/s. The drift per orbit is set to 500 m. The initial conditions for the long-range simulation (right) lie on a sphere of radius 160 meters, with a mean velocity of 20 mm/s. The drift per orbit is set to 800 m.

The red points represent the results of the Monte Carlo simulations. The black lines represent a theoretical evaluation of the stop distance based on equation (5.7). The short-term behaviour of the CAM algorithm corresponds well with the expectations of the minimum approach distance described in section 5.3.2.

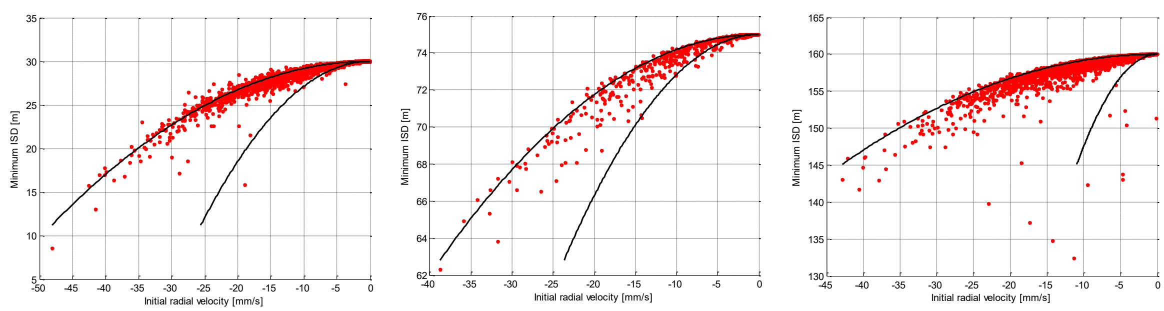

Figure 5.10: Minimum approach distance.

5.3.4 Return to mission

The recovery strategy after a CAM manoeuvre is like the deployment of the formation. The recovery after CAM should be as rapid as possible not to lose operational time. The precision with which the spacecraft returns to the safe orbit around the origin should be high so the precision with which manoeuvres are performed should be high as well. The absolute size of the error in the manoeuvre execution of the manoeuvres depends on the size of the manoeuvre, such that ΔV's should be small during the approach strategy to achieve increased accuracy.

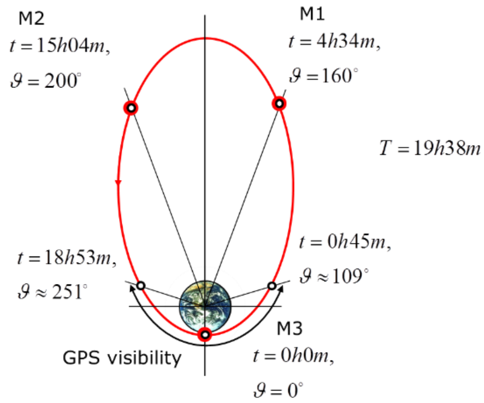

Figure 5.11: Manoeuvre location diagram for CAM recovery.

Figure 5.11 shows the locations of the manoeuvres with respect to the reference orbit. Manoeuvre 1 takes place at 160°, manoeuvre 2 takes place at 200° and manoeuvre 3 takes place at 0° true anomaly.

Figure 5.12 shows the CAM trajectory and the recovery after the CAM. The procedure followed to obtain this CAM recovery trajectory is based on ground computation of manoeuvres. The sequence of manoeuvres is the following. During the first orbit, a two-point transfer to safe orbit is computed on-ground and uploaded to the spacecraft. The manoeuvre is computed and uploaded just before 160°, such that the first ΔV is performed at 160° and the second ΔV at the true anomaly that minimizes the transfer ΔV and lies within one revolution of the first ΔV. These two manoeuvres are point 1 and 2 in the figure.

During the second orbit, a three-burn transfer to make the safe orbit drift to the origin is computed and uploaded. The manoeuvre is computed and uploaded just before 160° such that the first ΔV is performed at 160°, the second ΔV is performed at 200°, and the third ΔV is performed at perigee. These three manoeuvres are labelled 3, 4 and 5 in the figure. Note that several drifting orbits (and correction manoeuvres) can be inserted between manoeuvres 4 and 5. In this case, a single drifting orbit (orbit three) is inserted.

After manoeuvre 5 the spacecraft is in a safe orbit with characteristic dimension of 1000 m around the origin. During the fourth the safe orbit (not shown in the figure) is shrunk from 1000 m to 250 m (see section 5.2.5). During the fifth orbit (not shown in the figure) ground commands the sequence of manoeuvres to return the spacecraft to nominal conditions as described in section 5.2.6.

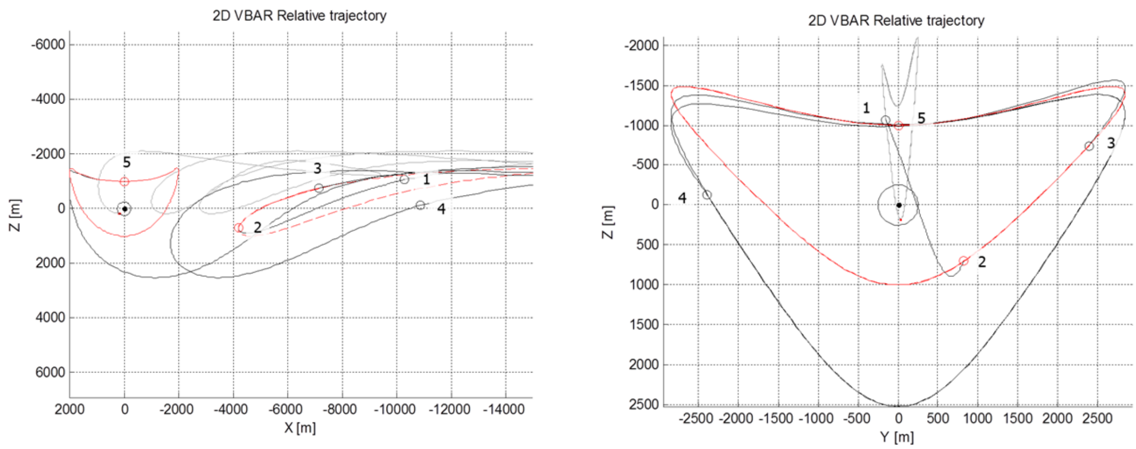

Figure 5.12: Ideal CAM recovery trajectory.

The recovery trajectory is robust to the non-execution of any of the manoeuvres, that is to say, the recovery trajectory is composed of passively safe trajectory elements [1]. The CAM and the recovery have been simulated using Monte Carlo simulations. These simulations have shown that the total impulsive ΔV required for the CAM and the recovery is 610 mm/s with a standard deviation of 73 mm/s. A ΔV of 11.5 mm/s is required for the forced motion acquisition at the end of the recovery.

5.3.5 Long-term behaviour

In case the drifting time after CAM is larger than 5 orbits, the strategy presented in section 5.3.4 will have to be complemented with a two-point transfer manoeuvre to recover most of the drifting distance in a fast way before the return to nominal conditions defined above is started. A parametric analysis has been conducted on this manoeuvre considering the type of CAM performed, the drifting time and the recovery time. Both mean and maximum ΔV has been computed through a Monte Carlo campaign of 10000 shots varying the initial position (on a sphere of radius R0) and the initial velocity (average velocity 20 mm/s).

Table 5.5 summarizes the required ΔV for the initial part of the recovery after a CAM. The ΔV has been computed in previous sections as a function of the type of CAM (short, medium, long), the drifting time after the CAM (60, 30 days) and the number of orbits in which the recovery to the intermediate point must be performed (5.7, 2.7 and 0.7 orbits). For each case, the mean ΔV and maximum ΔV is presented. As can be seen from the data, the longer the drifting time, the larger the distance to be recovered and the larger the required ΔV. On the other hand, the larger the allowed recovery time, the lower the ΔV.

Table 5.5: Recovery ΔV in m/s.

Return in # orbits		5.7		2.7		0.7	
Drifting days		60	30	60	30	60	30
Short range	max ΔV	0.770	0.449	1.407	0.659	2.428	1.049
	mean ΔV	0.295	0.149	0.511	0.257	1.041	0.523
Med. range	max ΔV	1.459	0.800	2.712	1.287	4.347	2.203
	mean ΔV	0.739	0.372	1.279	0.647	2.612	1.308
Long range	max ΔV	2.382	1.281	3.805	1.932	6.808	3.354
	mean ΔV	1.176	0.595	2.044	1.030	4.189	2.093

5.4 Conclusions

This paper has shown that the strategies developed for all manoeuvres related to the safe orbit and the collision avoidance manoeuvres for Proba-3 are feasible. All manoeuvres are safe and can be performed under ground control. Control can successfully be handed back to the spacecraft after ground commands a transfer from the safe orbit to nominal conditions.

6 Conclusions and recommendations

In this chapter the conclusions that have been drawn from this work will be summarized and recommendations for further research and developments will be given. This thesis has described a generalization of manoeuvres and relative trajectories that are used in the linearized theory of circular orbit rendezvous to elliptical orbits, and has presented the mission analysis for the Proba-3 mission in preparation of the development of a guidance function.

6.1 Research questions

This section will revisit the research questions to examine how these issues have been addressed and what results have been obtained. The first research question was the following:

1 – Can Hohmann transfers, drifting orbits and safe orbits be generalized to transfers between elliptical orbits?

Chapter 2 generalized the co-planar Hohmann transfer from circular orbits to the cotangential transfer between general co-planar elliptical orbits. The cotangential transfer is allowed to start at any point in the departure orbit. The tangentiality of the impulsive ΔV's is preserved in the generalization from circular to elliptical orbits. General co-planar elliptical orbits can have different semi-major axis, eccentricity, and argument of perigee. The cotangential transfer is more generally applicable than the Hohmann transfer in the sense that the cotangential transfer, unlike the Hohmann transfer, can accommodate departure and arrival orbits with a difference in eccentricity and argument of perigee. The increased generality with respect to the terminal conditions of the cotangential transfer does introduce singularities in the algorithm which correspond to points at which the departure trajectory and the arrival trajectory intersect.

The observation that singularities in the cotangential algorithm are due to intersecting departure and arrival trajectories leads to the development of trajectory crossing conditions and (non-tangential) impulsive manoeuvres to be applied at the crossing point. The detection of intersecting trajectories is an important check to perform before computing a cotangential transfer if the algorithm is used in an on-board autonomous guidance application. If the guidance is allowed to compute the manoeuvre at any time (or alternatively place the start of the transfer at any point in orbit), then this check needs to be performed to avoid placing the start of the transfer close to the singularity and obtaining infeasibly high ΔV's as a result.

The development of the cotangential transfer manoeuvre algorithm leads to an expression for the transverse coordinate of the relative position in the tangential frame (this is the z-coordinate; see appendix A.2 for a definition of this frame) that is used to define families of safe trajectories with simple geometric bounds. This chapter also defines drifting and non-drifting safe orbits that reach a desired relative position at a given point in the target orbit. Such trajectories are useful to achieve safe trajectories that lead to an alignment with a desired inertial direction (such as the Sun direction or the direction to a ground station) at a specific point in the target orbit.

Finally, this chapter introduces and analyses the concept of the co-elliptic orbit, which generalizes a drift orbit with no altitude variations with respect to the target orbit that is used in circular orbit rendezvous to a drift orbit with minimum altitude variations that can be used in elliptic orbit rendezvous.

The research question can be answered affirmatively, and the generalization of the Hohmann transfer demonstrates an interesting and useful connection with trajectory safety and the detection of trajectory intersections. The results presented in this chapter are valuable for defining a long-range rendezvous strategy.

2 – Can radial hop manoeuvres and V-bar hold points be generalized to transfers between elliptical orbits?

Chapter 3 provides two solutions to non-drifting transfer problems in elliptic orbits. The algorithms presented here provide generalizations of the radial hop transfer in circular orbits. The quality that is preserved is the non-drifting nature of the transfer, which is the result of the impulses being perpendicular to the orbital velocity of the reference orbit. Two different generalizations are possible, based on the assumptions that are made when generalizing the notion of hold points to elliptical orbits: the transfer can either target a point in the LVLH-frame, or a trajectory defined in terms of relative orbital elements. From the perspective of propellant consumption, it is attractive to define hold points as drift-free natural motion trajectories based on differences in either the relative mean anomaly or the relative argument of perigee. On the other hand, from the perspective of obtaining a fixed relative geometry (for example, a point on the line of sight to the target in the LVLH-frame) it may be more attractive to transfer between two points defined explicitly as Cartesian state vectors in the LVLH-frame.

The results in chapters 2 and 3 demonstrate that two-impulse transfers in the plane of the reference orbit based on impulses that are either tangential or perpendicular to the velocity vector of the reference orbit exist. The Gauss' form of Lagrange's planetary equations expressed in the orbit tangential frame show that impulses that are either tangential or perpendicular to the velocity vector of the reference orbit can only change three out of the four relative orbital elements that govern the in-plane relative motion. On the one hand, a tangential impulse can directly modify the relative semi-major axis and the two components of the relative eccentricity vector. The evolution of the relative mean anomaly is indirectly affected by the change in the relative semi-major axis. On the other hand, a perpendicular impulse can directly modify the two components of the relative eccentricity vector and the relative mean anomaly. In both cases, the relative eccentricity vector change depends on the position along the reference orbit. Two-impulse transfers based on impulses that are tangential or perpendicular to the velocity vector of the reference orbit can therefore also modify only three out of four in-plane relative orbital elements directly. Note that both transfer types solve three unknowns (namely, the magnitudes of the impulses and the transfer time) from three equations (namely, one equation for each element).

In circular orbit rendezvous, the Hohmann transfer uses tangential impulses to change the relative orbital altitude, and the radial hop transfer uses radial impulses to change the along-track distance. The along-track distance travelled during the Hohmann transfer is determined by the initial and terminal relative altitude and can therefore not be controlled directly. The radial hop transfer cannot change the relative semi-major axis. These characteristics carry over to the transfers developed for the case of elliptical orbit rendezvous, and from this preservation of characteristics it can be concluded that the cotangential transfer is the most natural generalization of the Hohmann transfer, and the non-drifting transfer is the most natural generalization of the radial hop transfer.

Furthermore, the research presented in this thesis demonstrates that the Hohmann transfer and the radial hop transfer are special cases of more general transfers. Both the Hohmann transfer and the radial hop transfer have a fixed transfer time of half an orbital period and place restrictions on the initial and terminal conditions. The research presented in this thesis has lifted the restrictions on the initial and terminal conditions and clarified the applicability of the two-impulse transfer algorithms.

The generalizations of the manoeuvres and the trajectory types from circular to elliptical reference orbits allow mission analysis and guidance design to benefit from know-how and insights gained on circular orbit rendezvous when designing and analysing manoeuvre programs and transfer trajectories for elliptic orbit rendezvous. Past studies assumed that elliptical orbit rendezvous is completely different from circular orbit rendezvous, exhibiting different geometry of the relative trajectories and requiring a completely new approach to the design of manoeuvre programs. The current research clarifies the connection between the two, and with that insight unlocks the vast amount of knowledge that has been accumulated on circular orbit rendezvous and allows it to be applied to transfers between elliptical orbits. Chapter 4 uses a circular orbit rendezvous representation of manoeuvres and relative trajectories with this new-found understanding that equivalent counterparts exist for the elliptical orbit that Proba-3 uses.

3 – How can the nominal operations be designed for the Proba-3 formation flying in a highly eccentric orbit?

Chapter 4 addresses the analysis performed for the Proba-3 mission. The design of formation flying in HEOs needs to consider the constraints that are specific to the mission at hand. The most important constraints for Proba-3 are the facts that there is no omni-directional sensor and that neither spacecraft can be oriented more than 30° away from the Sun direction. This limits the options available for the temporary formation break and re-acquisition that take place during the so-called perigee pass (see figure 4.3 for a diagram of the operations during a nominal orbit). Several options were investigated for the perigee pass: a direct transfer without a mid-course correction manoeuvre, a direct transfer with a mid-course correction manoeuvre, and a direct transfer with a cold-gas correction manoeuvre immediately after the formation break. This third strategy was found to be the most promising option, based on the ΔV required and the expected dispersion at the end of the perigee pass. The projection of the expected dispersion at the end of the perigee pass is within the field of view of the camera sensors used during the re-acquisition of the formation.

Mission analysis has shown that the inter-satellite distance during the perigee pass shows a strong seasonal variation that is dependent on the angle between the Sun direction and the orbital plane (the β angle). If this β angle is large, then the minimum inter-satellite distance is small, and vice versa. This makes sense intuitively, if one considers the extreme case in which the Sun direction is exactly perpendicular to the orbit plane. In this case, the formation needs to align along the y-axis of the LVLH-frame during the apogee arc to perform Solar coronagraphy. It follows that the starting point and the end point of the perigee pass are on the y-axis of the LVLH-frame. This in turn means that the free flying perigee pass trajectory is simply a straight line passing through the origin. Alternative solutions need to be considered for seasons with unacceptably low minimum values for the inter-satellite distance. This could either mean placing the formation in a safe configuration during seasons with a high β angle, or choosing a launch date that avoids the occurrence of large β angles throughout the mission lifetime.

The apogee phase is typical for formation flying missions that require sustained station-keeping along an inertial or quasi-inertial direction and resizing and retargeting manoeuvres are required for missions that need to investigate multiple regions of interest on the celestial sphere, and that may need to change the baseline of the instrument formed by the two spacecraft. Chapter 4 provides a high-level analysis of the ΔV required to perform such manoeuvres.

Chapter 4 also analyses the formation deployment, leveraging the theoretical foundations established in chapters 2 and 3 to define the formation deployment and acquisition at the start of the mission. Four deployment strategies were analysed, including a drift strategy to a hold point on the V-bar, radial hops between hold points on the V-bar, an approach based on a drift orbit connecting to a safe orbit, and a drifting safe orbit approach that ends in formation alignment with the Sun direction. A drifting safe orbit strategy was found to be the most attractive because this strategy is best able to manage the combination of manoeuvre execution errors, limited ground communication capability, and limited sensing opportunities. The passive safety of the safe orbit provides protection against collisions, especially at the early stages of the mission.

The mission analysis performed in chapter 4 has demonstrated that the deployment and the nominal operations of the Proba-3 formation flying mission are feasible. ΔV values have been provided for all main manoeuvres, which has allowed the Proba-3 systems engineering team to develop a reliable ΔV and propellant budget for the mission.

4 – How can the off-nominal operations be designed for the Proba-3 formation flying in a highly eccentric orbit?

The off-nominal operations are presented and discussed in chapter 5. They rely on the concepts of the safe orbit and the CAM. A theoretical development of the safe orbit was performed in section 2.4, and a practical analysis of the utilization of the safe orbit in the Proba-3 mission was performed in section 5.2. This theoretical development provides a basic justification for the passive safety of the safe orbit. The practical analysis in section 5.2.2 demonstrates the stability of the safe orbit when orbital perturbations are taken into consideration. The sizing of the safe orbit in section 5.2.3 considers margins for perturbations and insertion errors due to thruster performance. The entry into the safe orbit was further analysed in section 5.2.4. Errors in the execution of the manoeuvres can result in an along-track drift and a change in the shape of the safe orbit. Shrinking the size of the safe orbit is an essential step in returning to nominal conditions, and the thruster performance needs to be considered to ensure that this safe orbit shrinking can be performed safely. It is noted here that returning to nominal mission conditions is an essential step in the mission that is also required after the initial formation deployment. The return to nominal mission conditions was analysed in section 5.2.6. The principal constraints are due to the size of the field of view of the wide-angle camera, and to the fact that the manoeuvres are to be performed under control of operators on Earth. Performing the manoeuvres under control of the ground segment implies that the relative measurements need to be downloaded and filtered and manoeuvres need to be computed and uploaded to the spacecraft. This requires two communication steps separated by the time required to perform the calculations on Earth. However, ground contacts are limited, and this limits the options for the return strategy. The manoeuvres need to be computed and uploaded well in advance, and this degrades the accuracy with which the spacecraft can arrive at the nominal operating point as the dispersion due to manoeuvre execution uncertainties grows over time. This can lead to difficulties to ensure that the spacecraft arrives within the field of view of the camera on the other spacecraft. The strategy presented in section 5.2.6 was designed to accommodate all these constraints.

The CAM is designed for major failures and for situations where a collision is imminent. Section 5.3 analysed the CAM algorithm, both in terms of the short-term evolution, the long-term behaviour, and the steps required to return to the nominal conditions. One major concern is that while a CAM needs to drive the satellites apart, the drift rate cannot be too high as this could lead to the so-called evaporation of the formation. Evaporation occurs when the spacecraft need to spend too much propellant or too much time to return to nominal conditions. To avoid this, the CAM algorithm was designed in such a way that the drift rate per orbit is included in the algorithm as a parameter. In this way the drift rate after the CAM can be adjusted to avoid such evaporation.

The design and analysis of the off-nominal operations of Proba-3 that was performed in chapter 5 has demonstrated that safe trajectories do exist for Proba-3, and that the mission can be performed safely even if failures were to occur.

6.2 Research outlook

Enhanced autonomy

The research presented in this thesis provides a thorough theoretical background for formation flying and rendezvous manoeuvring in elliptical orbits and a practical application to the Proba-3 mission. The manoeuvres and trajectories form a set of options for formation flying and rendezvous geometry and for ways of transitioning from one geometry to another. Proba-3 features a formation flying manager function which commands and monitors the different actions of the formation flying software (such as, for example, mode switching, manoeuvre computation and execution, etc.). At present, this layer of automation only has a limited number of fixed plans. In the future a manoeuvre scheduler similar to the one proposed by Gaias, d'Amico, and Ardaens in [102] and Gaias and d'Amico in [103] could be developed that can compose trajectories and concatenate manoeuvres to fulfil higher-level objectives set by the formation flying manager.

Mission applications

Rendezvous and formation flying often form an important component of design projects that are currently active. It is expected that the techniques outlined in chapters 2 and 3 will continue to be applied to these projects, and that the rendezvous strategies will be modified based on mission needs. There is an increasing interest in On-Orbit Servicing missions and Active Debris Removal, and future research will focus on ensuring passive trajectory safety, observability, and low propellant consumption during rendezvous with an uncooperative target. It is expected that new mission applications will lead to new insights and new developments that expand the capabilities of the basic toolkit outlined in chapters 2 and 3.

Use of sophisticated relative motion models

The Yamanaka-Ankersen equations have been the method of choice for several projects, even though more sophisticated models of relative motion exist in the literature as discussed in section 1.2.3. Future projects should consider implementing and using these more accurate models for relative motion to improve the accuracy of relative navigation and potentially reduce propellant cost. The perturbation-free manoeuvre calculation algorithms presented in chapters 2 and 3 could be used in conjunction with higher-fidelity models similar to the methods proposed in [102,103,112]. The manoeuvre algorithms could also potentially be recast in terms of the more accurate theories, potentially leading to more accurate manoeuvres. The expected benefits of this approach must of course be traded against the expected effort, especially because thrusters typically introduce errors that are larger than the expected improvement in the accuracy of the calculation of the manoeuvres.

Collision and conjunction analysis

Conjunction analysis to determine the probability of on-orbit collisions makes use of three geometric filters to speed up the computational process. These filters are the apogee/perigee filter, the orbital path (or radius) filter and the time filter [208–210]. The non-linear definition of the relative elements C_1, C_2 and C_3 in chapter 2 can be used to determine whether any two orbits intersect, and the location of the intersections if they do occur. If the orbits do not intersect, then the point of closest approach can be found. The expressions for both the intersection test and the determination of the intersection points are simple and computationally efficient. This means that these tests can be used as a supplement to the existing three geometric filters for the identification of potential on-orbit collisions. A preliminary identification of the intersection points or close approaches needs to be followed up by a statistical analysis that includes the propagated orbit uncertainties. This analysis can be focused on a neighbourhood of the points that are identified rather than on the full orbit, potentially leading to a more computationally efficient algorithm.

Applications beyond rendezvous

In [70,211–216] the state transition matrix is used to compute various types of trajectory correction manoeuvres for interplanetary trajectories. It could be very interesting to study the application of the algorithms in chapters 2 and 3 to this problem. For example, non-drifting transfers could be used to change the arrival position without changing the overall transfer time, and the cotangential transfer could be used to slightly alter the semi-major axis of the transfer to change the arrival time.

7 Afterword: Proba-3 retrospective

The development time for Proba-3 is long compared to that of other missions, and especially when compared to that of the other Proba satellites. The mission analysis work presented in chapters 4 and 5 was performed almost 10 years ago. Although nothing has fundamentally changed in the overall mission concept, the mission analysis work has been updated for a new launch date and the development work on the on-board software has progressed. More details are now available on the implementation of the formation flying manoeuvres to be performed at apogee, that were only vaguely described in chapter 4, and guidance algorithms have been implemented for all phases. This section provides a brief retrospective on the development of Proba-3 and a summary of the status of the development of the guidance algorithms that flowed from the mission analysis work in chapters 4 and 5.

The phase-A study for Proba-3 started in 2006, and analysis, design and development have been ongoing since then. The work presented in this thesis roughly corresponds to the baseline in 2012 at the time of the Preliminary Design Review. Since then, many changes have occurred in the mission design, and the launch date has been pushed back repeatedly. The formation geometry is dependent on the orbit that is selected and on the Sun direction with respect to the orbital plane, and this has meant that the mission analysis work had to be repeated several times. Some of the more interesting and important changes are discussed below.

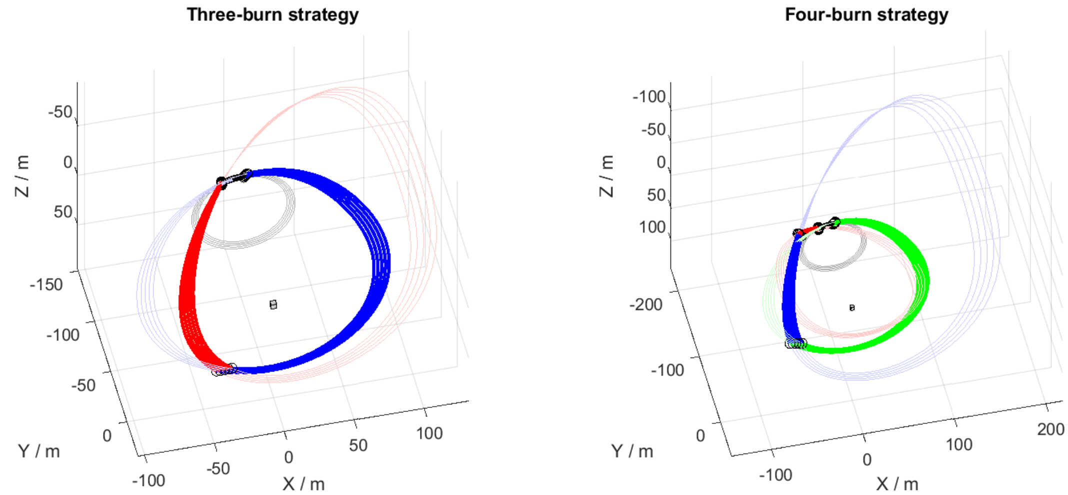

Figure 7.1: Early perigee pass trajectories featuring non-drifting transfers. Simulations run for five orbits after January 1, 2014.

Early in the design process, non-drifting transfers such as described in chapter 3 were considered for the perigee pass. The advantage of such transfers is that the drift rate is zero, such that if the mid-course correction or the formation-establishing manoeuvre cannot be performed, the chaser remains close to the target. Strategies featuring non-drifting manoeuvres were eventually discarded because of the high propellant cost compared to that of the two-point transfer strategy. Figure 7.1 shows what such perigee-pass trajectories based on non-drifting trajectories could have looked like. The plot on the left-hand side shows a three-burn-per-orbit non-drifting trajectory, and the plot on the right-hand side shows a four-burn-per-orbit non-drifting trajectory. Dark colours indicate the trajectories that are followed, while lighter colours indicate the continuation of those trajectories if no manoeuvres were performed. The circular black/grey trajectory (at the top) is the evolution of the Sun direction at the nominal inter-satellite distance of about 150 m. The red and blue (left plot), and the red, green, and blue (right plot) trajectories are segments of non-drifting trajectories that are followed during the perigee pass.

A related concept that was investigated as an option for the parking orbit (an autonomously controlled alternative to the safe orbit) was the periodic Sun-pointing trajectory. The algorithms from section 2.4.3 were used to define trajectories that align with the Sun direction at apogee, such that for a limited number of orbits the chaser would return to the vicinity of the Sun direction when the formation returns to apogee. The advantage would be that high-precision relative measurements could be taken when the formation is close to alignment, without rotating the spacecraft too far away from the Sun direction (the maximum off-pointing angle is 30°). However, the periodic Sun-pointing orbit does not lead to workable solutions for all Sun-orbit geometries, and this concept was abandoned in favour of the safe orbit concept with a simpler geometry described in section 5.2. This concept for the safe orbit has the formation align with the radial direction at apogee and perigee.

The concept of a parking orbit and an autonomous return to nominal conditions was abandoned to simplify the software development work and reduce cost. Figure 7.2 shows the initial concept for the formation reconfigurations. The nominal operations and the close safe orbit would be controlled on-board, and the far safe orbit would be a handover orbit from control by operators on Earth to autonomous control. The spacecraft would have had the capability to move from the close safe orbit to nominal operations autonomously (arrow: “start nominal operations”), and retreat safely to a safe orbit from the nominal formation orbit (arrow: “safe retreat”). The spacecraft would also have had the capabilities to compute transfers to perform CAM (arrow: “CAM”) and to shrink and control the safe orbit based on relative GPS measurements (arrows: “advance” and “retreat”). The abandonment of this concept has meant that the control of the safe orbit and the return from the safe orbit are now performed under control by operators on Earth. As such, these operations are now subject to scheduling constraints due to the need for ground communication. This makes the return from safe orbit operationally more complicated, more time-consuming, and more costly.

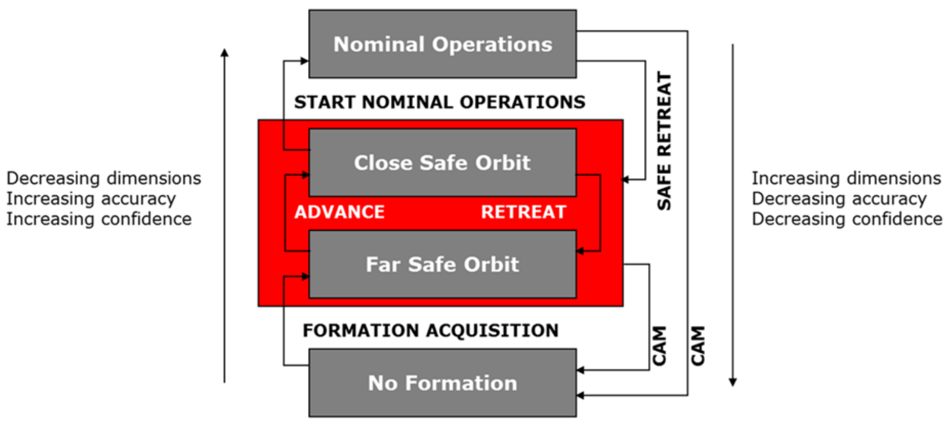

Figure 7.2: Initial concept for formation reconfigurations.

Another software mode that was removed to cut development cost is the attitude scanning manoeuvre that could be used to search for the other spacecraft with the camera sensor. Recall from section 4.2 that no relative measurements are available after the formation crosses the altitude of the GPS constellation. (This has been a design assumption; there were concerns that insufficient satellites would be visible or that the signals would be too weak to perform navigation using GPS side lobe navigation.) Acquiring camera sensor lock is essential to start the fine formation flying operations around apogee. The consequence is that all manoeuvre strategies need to consider the unknown dispersions (the knowledge error in relative position after the last relative measurement has been taken) at the end of the transfer; these dispersions cannot be larger than the field of view of the camera to ensure that the camera can detect the other spacecraft and fine formation flying operations can begin.

A quasi-omnidirectional sensor, the FFRF (Formation Flying Radio Frequency instrument) like the one flown on the PRISMA mission [207], was originally intended to be used on Proba-3. This sensor was ultimately removed because of performance and mass issues, which means that the formation needs to fly without relative sensor measurements during portions of the nominal orbit, due to sensor and attitude constraints. Recall from chapter 4 that the formation is in free flight during the perigee pass, and the spacecraft cannot turn farther away from the Sun than 30°, while the camera has a field of view of 5°. Relative GPS measurements are not available when the formation is above the altitude of the GPS constellation. The formation break manoeuvre DTM1 that initiates the perigee pass needs to be performed more accurately, and relative measurements need to be performed after that manoeuvre is performed, to ensure that the knowledge of the relative state is good enough at the time of the formation acquisition to acquire metrology. The removal of the FFRF also removes an independent chain of measurements that could be used as input to perform collision detection. Omnidirectional sensors simplify any formation flying mission design and it is recommended to consider such sensors for future missions.

7

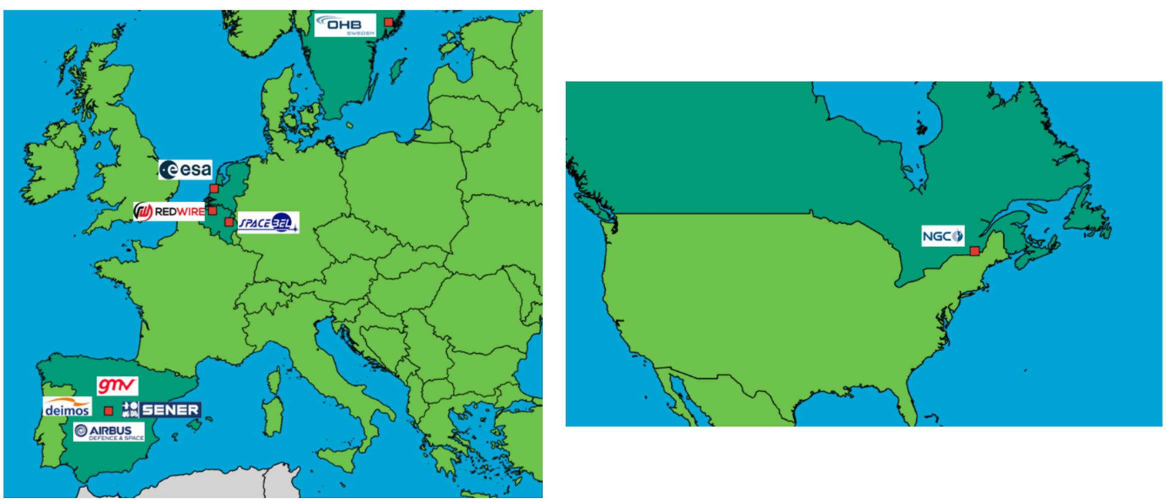

Figure 7.3: Location of customer, contractor and subcontractors involved in Proba-3.

The development of Proba-3 has taken much longer than other demonstrator missions. There are several factors that have contributed to the long development time. Firstly, the technology for high-precision formation flying did not exist yet in 2006 and had to be developed. Secondly, there are no external constraints on the launch date. Interplanetary missions typically require a specific conjunction that may occur only once every few years or even decades, and this puts a hard deadline on the mission development. Proba-3 clearly does not have any constraints on the launch date, such that studies and design changes could be performed and extended without serious consequences. The interest in Proba-3 from industry has been strong, and this has led to the formation of a large consortium. At the time of writing, the consortium is led by SENER, with the following subcontractors (in alphabetical order): Elecnor Deimos (formerly Deimos, Tres Cantos, Spain), Airbus Defence and Space (formerly EADS-CASA Espacio, Madrid, Spain), GMV (Tres Cantos, Spain), NGC Aerospace (Sherbrooke, Canada), OHB-Sweden (Stockholm, Sweden), Redwire Space (formerly QinetiQ Space NV, Kruibeke, Belgium) and Spacebel (Liège, Belgium). Figure 7.3 shows the location of the customer (ESA), the main contractor and the subcontractors. In addition to the management challenges that are inherent to a large consortium, the prime contractor has also changed. Initially it was OHB-Sweden (SSC at the time), then ESA briefly took on the role before SENER took over. Obviously, knowledge had to be transferred between different companies, and know-how was inevitably lost during this process. The duration of the project itself eventually became an obstacle as well, as many of the original engineers left the project (and sometimes their company) and others came in; know-how had to be re-acquired and project decisions that once seemed reasonable and justifiable would potentially need revisiting. Compare this to the development process of some of the CubeSat formation-flying missions: these are small, fast, and cheap, and often under the control of a single company or university. All these aspects make both project management and knowledge management much more tractable. It is interesting to again refer to the initial feasibility study for Proba-3: a small satellite mission that would be launched into GTO as a piggyback payload [26]. Seen in this light and observing the successes of small formation-flying missions, this approach could still be successfully pursued in the future.

Apart from the formation definition and the formation manoeuvres, most of the guidance algorithms have changed little from the versions presented in chapter 4. The formation definition uses the virtual structure approach. A global formation reference frame is defined for the formation, and the relative position and orientation of each of the spacecraft in this frame is defined by the required inter-satellite distance and the alignment of the relative sensors. All formation demonstration manoeuvres change the inter-satellite distance, the orientation of the global formation reference frame with respect to the inertial frame, or both. The required acceleration to be applied by the spacecraft is determined from the kinematic relations between the motion of the spacecraft and the motion of the global formation reference frame and the change in inter-satellite distance.

A

Appendices

A Review of relative motion dynamics

The theory of linearization in the context of orbital dynamics is briefly reviewed. The relative motion around circular orbits is described by the Hill-Clohessy-Wiltshire equations [149]. These equations can be recast in terms of relative orbital elements. Manoeuvres and trajectories that are useful for rendezvous and formation flying in circular orbits are reviewed, and the basic theory for linearized relative motion around eccentric orbits is described.

A.1 Orbital dynamics and linearization

This brief exposition uses the ideas and notation set out in [217]. The first paragraphs below follow the discussion of variational equations and the state transition matrix (called matrizant in the reference) in [218]. The Kepler problem is an example of an initial value problem described by an ordinary differential equation that can be written in the following form:

$$\dot{\mathbf{x}} = \boldsymbol{f}(\mathbf{x}), \qquad \mathbf{x}(t_0) = \mathbf{x}_0 \in \mathbb{R}^{2n}, n = 3 \tag{A.1}$$

The solution of the differential equation defines a mapping (or a one-parameter family of mappings) which takes the initial state to later points along the trajectory:

$$\mathbf{x} = \boldsymbol{\varphi}_t(\mathbf{x}_0), \qquad t \in \mathbb{R} \tag{A.2}$$

The map $\boldsymbol{\varphi}_t$ is the flow map of the system. The equations of motion can be linearized around a known solution of the system to form the variational equations:

$$\delta\dot{\mathbf{x}} = \mathbf{A}(t)\delta\mathbf{x} \tag{A.3}$$

where

$$\mathbf{A}(t) = \frac{\partial \boldsymbol{f}}{\partial \mathbf{x}}$$

The variational equations can be integrated to yield the state transition matrix $\boldsymbol{\Phi}_{t_0 \to t}$, which is a linear map that maps a small variation of the initial state to the state at a later moment in time. Alternatively, the state transition matrix can be viewed as the variation of the flow map with respect to the initial state:

$$\delta\mathbf{x} = \boldsymbol{\Phi}_{t_0 \to t}\delta\mathbf{x_0} \tag{A.4}$$

where

$$\boldsymbol{\Phi}_{t_0 \to t} = \left.\frac{\partial \boldsymbol{\varphi}_t}{\partial \boldsymbol{x}}\right|_{\boldsymbol{x}_0}$$

Figure A.1 summarizes the different routes to finding the solution of the variational equations in a diagram. The full nonlinear dynamical differential equations are on the top left. Integration (moving to the right) leads to the flow map $\boldsymbol{\varphi}$, while linearization (moving down) leads to the linearized differential equations of motion. The linearized equations of motion can be integrated (moving to the right) to obtain the state transition matrix $\boldsymbol{\Phi}_{t_0 \to t}$. The flow map can also be linearized to yield the state transition matrix.

$$\begin{tikzcd}
\dot{\mathbf{x}} = \boldsymbol{f}(\mathbf{x}) \arrow[r, "\int"] \arrow[d, "\delta"'] & \mathbf{x} = \boldsymbol{\varphi}_t(\mathbf{x_0}) \arrow[d, "\delta"'] \\
\boldsymbol{\delta}\dot{\mathbf{x}} = \mathbf{A}(t)\boldsymbol{\delta}\mathbf{x} \arrow[r, "\int"] & \boldsymbol{\delta}\mathbf{x} = \boldsymbol{\Phi}_{t_0 \to t}\boldsymbol{\delta}\mathbf{x}_0
\end{tikzcd}$$

Figure A.1: Diagram of dynamical equations and variational equations.

The Kepler problem is integrable, and the flow map can conveniently be written as a composition of maps as follows:

$$\boldsymbol{\varphi}_t(\mathbf{x}_0) = \boldsymbol{b} \circ \boldsymbol{k}(t) \circ \boldsymbol{b}^{-1}(\mathbf{x}_0) \tag{A.5}$$

The map $\boldsymbol{b}$ maps orbital elements $\boldsymbol{\alpha}$ to Cartesian coordinates $\mathbf{x}$:

$$\mathbf{x} = \boldsymbol{b}(\boldsymbol{\alpha}) \tag{A.6}$$

The map $\boldsymbol{k}$ maps orbital elements from the initial time to the current time and can be thought of as the flow map for the orbital elements. The map $\boldsymbol{k}$ can be interpreted as the flow map of the Kepler problem in the space defined by the orbital elements. For the two-body problem the map $\boldsymbol{k}$ is given by Kepler's equation. Equation (A.5) summarizes the procedure for (analytically) propagating a reference orbit in the two-body problem, which is as follows. First, the initial state (position and velocity) in Cartesian, inertial coordinates is transformed to orbital elements. Next, the true anomaly is propagated from the initial time to the reference time. Finally, the orbital elements are transformed back to position and velocity in Cartesian, inertial coordinates.

The state transition matrix can be found by taking the first variation of each of these transformations, as follows:

$$\mathbf{\Phi}_{t_0 \to t} = \mathbf{BKB}^{-1} = \left(\frac{\partial \boldsymbol{b}}{\partial \mathbf{x}}\right)\bigg|_t \left(\frac{\partial \boldsymbol{k}(t)}{\partial \boldsymbol{\alpha}}\right)\bigg|_{t_0} \left(\frac{\partial \boldsymbol{b}}{\partial \mathbf{x}}\right)^{-1}\bigg|_{t_0} \tag{A.7}$$

This is the approach followed in [146] to find the state transition matrix for the two-body problem in the inertial frame. The approach is based on [218], updated to modern terminology and notation. In orbital rendezvous the relative motion is customarily studied in the local vertical, local horizontal frame. The variational equations also take a simpler form in the LVLH-frame, and it appears that the simplest way to solve the equations of motion is in the LVLH-frame.

A.2 LVLH and tangential or flight-path reference frames

The LVLH-frame is a local orbital frame the origin of which is located at the centre of mass of the target spacecraft. The z-axis points towards the centre of Earth, the y-axis points in the direction opposite to the orbital angular momentum vector and the x-axis completes the right-handed frame. The advantage of the LVLH-frame in the two-body problem is that the central force is directed along the z-axis of that frame, and only changes in magnitude.

The tangential or flight-path reference frame is also a local orbital frame. The origin is located at the centre of mass of the target. The x-axis points in the direction of the orbital velocity vector of the target, the y-axis points in the direction opposite to the orbital angular momentum vector and the z-axis completes the right-handed frame. The relationship between the tangential frame and the LVLH-frame is examined in section 2.8. Figure A.2 shows the orbit in space and the LVLH- and tangential reference frames.

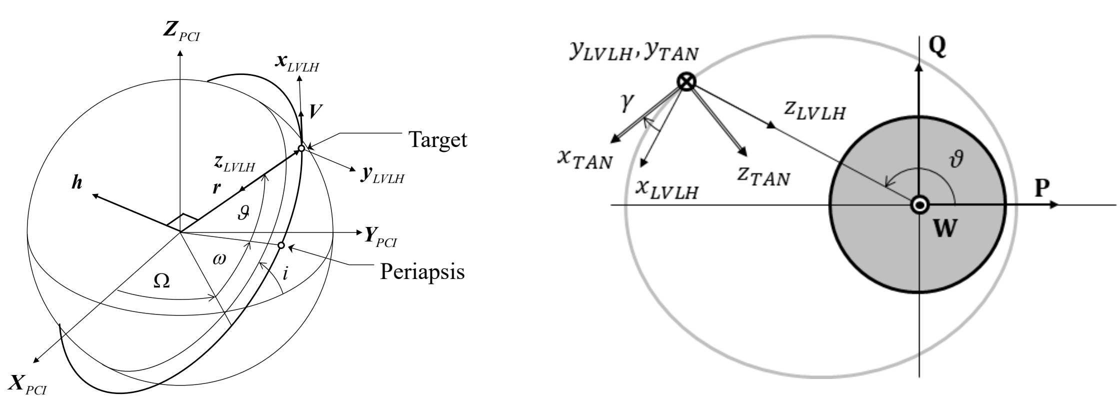

Figure A.2: Orbit in space (left) and orbital reference frames (right).

A position vector in the inertial frame is rotated to the LVLH-frame using a rotation matrix.

$$\mathbf{r}_{LVLH} = \mathbf{R}_{I \to LVLH} \mathbf{r}_I \tag{A.8}$$

Two conventions are used for rotation matrices. Compound rotations that link specific frames, such as in equation (A.8), are expressed as follows. The rotation matrix is expressed using a subscript indicating the original frame, an arrow, and the target frame. Basic rotations (rotations around one of the axes of the coordinate system) are expressed with the axis around which the rotation takes place in a subscript and with the rotation angle as a function argument. The basic rotations are as follows:

$$\begin{gathered}\mathbf{R}_x(\phi) = \begin{bmatrix} 1 & 0 & 0 \\ 0 & \cos\phi & -\sin\phi \\ 0 & \sin\phi & \cos\phi \end{bmatrix}, \qquad \mathbf{R}_y(\phi) = \begin{bmatrix} \cos\phi & 0 & \sin\phi \\ 0 & 1 & 0 \\ -\sin\phi & 0 & \cos\phi \end{bmatrix}, \\ \mathbf{R}_z(\phi) = \begin{bmatrix} \cos\phi & -\sin\phi & 0 \\ \sin\phi & \cos\phi & 0 \\ 0 & 0 & 1 \end{bmatrix}\end{gathered} \tag{A.9}$$

Note that the rotations expressed by these matrices are coordinate frame transformations, also referred to as a passive or alias transformation. For an unperturbed Kepler orbit the rotation matrix from the inertial frame to the LVLH-frame can be decomposed into a constant part and a non-constant part.

$$\mathbf{R}_{I \to LVLH} = \mathbf{R}_y(-\vartheta)\mathbf{R}_{I \to \pi} \tag{A.10}$$

where

$$\mathbf{R}_{I \to \pi} = \mathbf{R}_z\left(\frac{\pi}{2}\right)\mathbf{R}_y\left(-\frac{\pi}{2}\right)\mathbf{R}_z(\omega)\mathbf{R}_x(i)\mathbf{R}_z(\Omega)$$

A state vector consists of both position and velocity components, and the velocity in the LVLH-frame is given by:

$$\mathbf{v}_{LVLH} = -\mathbf{\Omega}_{LVLH \to I, LVLH}\mathbf{R}_{I \to LVLH}\mathbf{r}_I + \mathbf{R}_{I \to LVLH}\dot{\mathbf{r}}_I \tag{A.11}$$

where

$$\mathbf{\Omega}_{LVLH \to I, LVLH} = \left[\boldsymbol{\omega}_{LVLH \to I, LVLH}\right]_\times$$

$[\quad]_\times$ is the cross-product in matrix form

$$\boldsymbol{\omega}_{LVLH\to I,LVLH} = \dot{\vartheta}\begin{bmatrix}0\\-1\\0\end{bmatrix}$$

The case of relative motion around orbits perturbed by the oblateness of the central body (expressed as the J_2-effect) are treated in [6]. The state vector in the LVLH-frame can now be expressed as a linear transformation of the state vector in the inertial frame by assembling the transformation matrix $\mathbf{T}$.

$$\mathbf{x}_{LVLH} = \mathbf{T}_{I\to LVLH}\mathbf{x}_I \tag{A.12}$$

where

$$\mathbf{T}_{I\to LVLH} = \begin{bmatrix}\mathbf{R}_{I\to LVLH} & \mathbf{0}\\ -\boldsymbol{\Omega}_{LVLH\to I,LVLH}\mathbf{R}_{I\to LVLH} & \mathbf{R}_{I\to LVLH}\end{bmatrix}$$

$$\mathbf{T}_{I\to LVLH}^{-1} = \begin{bmatrix}\mathbf{R}_{I\to LVLH}^{-1} & \mathbf{0}\\ \mathbf{R}_{I\to LVLH}^{-1}\boldsymbol{\Omega}_{LVLH\to I,LVLH} & \mathbf{R}_{I\to LVLH}^{-1}\end{bmatrix}$$

A.3 Variational equations

The variational equations are most easily obtained in the inertial frame because relative motion in the inertial frame does not involve fictitious forces. The linearized equations of motion for relative dynamics are obtained from equation (A.3), dropping the δ that indicates the infinitesimal changes that are invoked in the linearization process.

$$\dot{\mathbf{x}}_I = \mathbf{A}_I\mathbf{x}_I \tag{A.13}$$

This equation can be written in component form as follows:

$$\frac{d}{dt}\begin{bmatrix}\mathbf{r}\\\mathbf{v}\end{bmatrix} = \begin{bmatrix}\mathbf{0} & \mathbf{I}\\ \mathbf{G}_I & \mathbf{0}\end{bmatrix}\begin{bmatrix}\mathbf{r}\\\mathbf{v}\end{bmatrix} \tag{A.14}$$

where

$$\mathbf{G}_I = \frac{\mu}{R^5}\begin{bmatrix}3X^2 - R^2 & 3XY & 3XZ\\ 3XY & 3Y^2 - R^2 & 3YZ\\ 3XZ & 3YZ & 3Z^2 - R^2\end{bmatrix}$$

The matrix $\mathbf{G}_I$ is the gravity gradient matrix for the two-body problem in inertial space. The letters X, Y, Z and R are components of the inertial position vector and the orbital radius, respectively. Capital letters are used to distinguish them from the components of the relative state vector and the magnitude of the relative position vector. The linearized equations of motion in the LVLH-frame are obtained from the equations of motion in the inertial frame by considering the first derivative of the transformation of the state vector from equation (A.12):

$$\dot{\mathbf{x}}_{LVLH} = \dot{\mathbf{T}}\mathbf{x}_I + \mathbf{T}\dot{\mathbf{x}}_I \tag{A.15}$$

Substitution of equations (A.13) and (A.12) leads to the following expression for the equations of relative motion in the LVLH-frame:

$$\dot{\mathbf{x}}_{LVLH} = \left(\dot{\mathbf{T}}\mathbf{T}^{-1} + \mathbf{T}\mathbf{A}_I\mathbf{T}^{-1}\right)\mathbf{x}_{LVLH} = \mathbf{A}_{LVLH}\mathbf{x}_{LVLH} \tag{A.16}$$

The components of the linearized relative dynamics matrix in the LVLH-frame are:

$$\mathbf{A}_{LVLH} = \begin{bmatrix} \mathbf{0} & \mathbf{I} \\ \mathbf{G}_{LVLH} - \mathbf{\Omega}^2 - \dot{\mathbf{\Omega}} & -2\mathbf{\Omega} \end{bmatrix} \tag{A.17}$$

where

$$\mathbf{\Omega} = \dot{\vartheta}\begin{bmatrix} 0 & 0 & -1 \\ 0 & 0 & 0 \\ 1 & 0 & 0 \end{bmatrix}$$

$$\mathbf{\Omega}^2 = \dot{\vartheta}^2\begin{bmatrix} -1 & 0 & 0 \\ 0 & 0 & 0 \\ 0 & 0 & -1 \end{bmatrix}$$

$$\dot{\mathbf{\Omega}} = \ddot{\vartheta}\begin{bmatrix} 0 & 0 & -1 \\ 0 & 0 & 0 \\ 1 & 0 & 0 \end{bmatrix}$$

The gravity gradient matrix in the LVLH-frame can be obtained by rotating the gravity gradient matrix in the inertial frame provided in equation (A.14) to the LVLH-frame, but one can also observe that the orbital position vector expressed in the LVLH-frame is $[0 \quad 0 \quad -R]^T$. From this observation one deduces that the gravity-gradient matrix in the LVLH-frame must be:

$$\mathbf{G}_{LVLH} = \frac{\mu}{R^3}\begin{bmatrix} -1 & 0 & 0 \\ 0 & -1 & 0 \\ 0 & 0 & 2 \end{bmatrix} \tag{A.18}$$

The linearized relative dynamics matrix in the LVLH-frame is [145]:

$$\mathbf{A}_{LVLH} = \begin{bmatrix} 0 & 0 & 0 & 1 & 0 & 0 \\ 0 & 0 & 0 & 0 & 1 & 0 \\ 0 & 0 & 0 & 0 & 0 & 1 \\ \omega^2 - k\omega^{\frac{3}{2}} & 0 & \dot{\omega} & 0 & 0 & 2\omega \\ 0 & -k\omega^{\frac{3}{2}} & 0 & 0 & 0 & 0 \\ -\dot{\omega} & 0 & 2k\omega^{\frac{3}{2}} + \omega^2 & -2\omega & 0 & 0 \end{bmatrix} \tag{A.19}$$

where

$$\frac{\mu}{R^3} = k\omega^{\frac{3}{2}}, \qquad \dot{\vartheta} = \omega = k^2\rho^2, \qquad k^2 = \sqrt{\frac{\mu}{p^3}},$$

$$\rho = 1 + e\cos\vartheta\,, \qquad \dot{\vartheta}^2 = \omega^2, \qquad \ddot{\vartheta} = \dot{\omega}$$

A.4 Solution for relative motion around a circular orbit

It is instructive to review the dynamics of circular orbit rendezvous and the manoeuvres and trajectories that apply. The relative dynamics in a circular orbit follow from the general linearized relative dynamics in equation (A.19) by letting the eccentricity tend to zero.

$$\mathbf{A}_{i.p.} = \begin{bmatrix} 0 & 0 & 1 & 0 \\ 0 & 0 & 0 & 1 \\ 0 & 0 & 0 & 2n \\ 0 & 3n^2 & -2n & 0 \end{bmatrix}, \qquad \mathbf{A}_{o.p.} = \begin{bmatrix} 0 & 1 \\ -n^2 & 0 \end{bmatrix} \tag{A.20}$$

where

$$n = \sqrt{\frac{\mu}{R^3}} = \frac{2\pi}{T}$$

Here, n is the orbital mean motion. The dynamics matrix can be placed into (real) Jordan canonical form by finding a (real) invertible matrix $\mathbf{P}$ that puts $\mathbf{J}$ into a block diagonal form, which only contains non-zero off-diagonal terms for coupled eigenvalues.

$$\mathbf{J} = \mathbf{P}^{-1}\mathbf{A}\mathbf{P} \tag{A.21}$$

The in-plane decomposition contains two pairs of eigenvalues, the first pair is a coupled eigenvalue equal to zero, with a coupling factor equal to $-\frac{3}{2}n$, and the second pair has the values $\pm ni$. The coupling factor indicates growth over time whereas the imaginary second pair indicates the presence of an oscillation. The decomposition can be written in real form as follows:

$$\mathbf{P}_{i.p.} = \begin{bmatrix} 0 & 1 & 2 & 0 \\ -1 & 0 & 0 & -1 \\ -\frac{3}{2}n & 0 & 0 & -2n \\ 0 & 0 & -n & 0 \end{bmatrix}, \quad \mathbf{P}_{i.p.}^{-1} = \begin{bmatrix} 0 & -4 & 2n^{-1} & 0 \\ 1 & 0 & 0 & 2n^{-1} \\ 0 & 0 & 0 & -n^{-1} \\ 0 & 3 & -2n^{-1} & 0 \end{bmatrix},$$
$$\mathbf{J}_{i.p.} = \begin{bmatrix} 0 & 0 & 0 & 0 \\ -\frac{3}{2}n & 0 & 0 & 0 \\ 0 & 0 & 0 & -n \\ 0 & 0 & n & 0 \end{bmatrix} \tag{A.22}$$

The out-of-plane decomposition contains a single pair of eigenvalues with values $\pm ni$. This indicates that the out-of-plane motion is governed by an oscillation.

$$\mathbf{P}_{o.p.} = \begin{bmatrix} 0 & -n \\ n & 0 \end{bmatrix}, \quad \mathbf{P}_{o.p.}^{-1} = \begin{bmatrix} 0 & n^{-1} \\ -n^{-1} & 0 \end{bmatrix}, \quad \mathbf{J}_{o.p.} = \begin{bmatrix} 0 & n \\ -n & 0 \end{bmatrix} \tag{A.23}$$

The system is solved by taking the matrix exponential, as follows:

$$e^{\mathbf{J}_{i.p.}\Delta t} = \begin{bmatrix} 1 & 0 & 0 & 0 \\ -\frac{3}{2}n\Delta t & 1 & 0 & 0 \\ 0 & 0 & \cos n\Delta t & -\sin n\Delta t \\ 0 & 0 & \sin n\Delta t & \cos n\Delta t \end{bmatrix}, \quad e^{\mathbf{J}_{o.p.}\Delta t} = \begin{bmatrix} \cos n\Delta t & \sin n\Delta t \\ -\sin n\Delta t & \cos n\Delta t \end{bmatrix} \tag{A.24}$$

The link to the relative orbital elements can be made by observing that the matrix of sines and cosines of the transfer angle can be written in terms of the initial and the terminal angle (that is to say, $\Delta t = t_1 - t_0$):

$$\begin{bmatrix} \cos n\Delta t & -\sin n\Delta t \\ \sin n\Delta t & \cos n\Delta t \end{bmatrix} = \begin{bmatrix} \cos nt_1 & -\sin nt_1 \\ \sin nt_1 & \cos nt_1 \end{bmatrix} \begin{bmatrix} \cos nt_0 & \sin nt_0 \\ -\sin nt_0 & \cos nt_0 \end{bmatrix} \tag{A.25}$$

In this way, the rotations can be absorbed into the transformation matrices. The in-plane transformation matrix $\mathbf{B}$, its inverse and the transition matrix $\mathbf{K}$ for the transformed space become:

$$\mathbf{B}_{i.p.} = \begin{bmatrix} 0 & 1 & 2\cos nt_1 & -2\sin nt_1 \\ -1 & 0 & -\sin nt_1 & -\cos nt_1 \\ -\frac{3}{2}n & 0 & -2n\sin nt_1 & -2n\cos nt_1 \\ 0 & 0 & -n\cos nt_1 & n\sin nt_1 \end{bmatrix} \tag{A.26}$$

$$\mathbf{B}_{i.p.}^{-1} = \begin{bmatrix} 0 & -4 & 2n^{-1} & 0 \\ 1 & 0 & 0 & 2n^{-1} \\ 0 & 3\sin nt_0 & -2n^{-1}\sin nt_0 & -n^{-1}\cos nt_0 \\ 0 & 3\cos nt_0 & -2n^{-1}\cos nt_0 & n^{-1}\sin nt_0 \end{bmatrix}$$

$$\mathbf{K}_{i.p.} = \begin{bmatrix} 1 & -\frac{3}{2}n(t_1 - t_0) & 0 & 0 \\ 0 & 1 & 0 & 0 \\ 0 & 0 & 1 & 0 \\ 0 & 0 & 0 & 1 \end{bmatrix}$$

Similarly, the out-of-plane transformation matrix $\mathbf{B}$, its inverse and the transition matrix $\mathbf{K}$ become:

$$\mathbf{B}_{o.p.} = \begin{bmatrix} \sin nt_1 & -\cos nt_1 \\ n\cos nt_1 & n\sin nt_1 \end{bmatrix}, \qquad \mathbf{B}_{o.p.}^{-1} = \begin{bmatrix} \sin nt_0 & n^{-1}\cos nt_0 \\ -\cos nt_0 & n^{-1}\sin nt_0 \end{bmatrix}$$
$$\mathbf{K}_{o.p.} = \begin{bmatrix} 1 & 0 \\ 0 & 1 \end{bmatrix} \tag{A.27}$$

The new coordinates can be identified as relative orbital elements, organized into a vector with the relative semi-major axis, relative mean longitude, the components of the relative eccentricity vector and the components of the relative inclination vector:

$$\boldsymbol{\delta\alpha} = [\delta a \quad \delta\lambda \quad \delta e_x \quad \delta e_z \quad \delta i_x \quad \delta i_z] \tag{A.28}$$

A.5 Relative motion around an elliptical orbit

Solving the linearized relative motion around an unperturbed Keplerian orbit has proven to be difficult, and many different approaches have been tried. Alfriend [6] provides a brief overview of conic state transition matrices. As Yamanaka and Ankersen [145] and Carter [69] point out, the main difficulty lies in obtaining a closed-form, singularity-free expression for an integral term occurring in the solution. The approach discussed by Yamanaka and Ankersen [145] and Carter [69] performs a transformation of the relative position vector, scaled by the radius of the reference orbit, and switches the independent variable from time to the true anomaly of the reference orbit. This leads to expressions for the equations of relative motion that are quite simple and succinct, but that are apparently quite difficult to solve. Interestingly, an alternative approach to find the state transition matrix is presented by Stern [70]. Stern [70] does not transform the equations of relative motion and solves the equations directly. The derivation of the solution for the state transition matrix by Stern [70] is lengthy but consists only of elementary steps. The work by Stern [70] is concerned with finding trajectory correction manoeuvres for interplanetary trajectories, and as such may have gone unnoticed in the rendezvous community.

The analyses performed in this thesis have used the state transition matrix for elliptical orbits that was found by Yamanaka and Ankersen [145]. The solution takes the following form:

$$\mathbf{x}_1 = \mathbf{\Phi}_{t_0 \to t_1} \mathbf{x}_0 = \mathbf{T}_{\vartheta}^{-1} \mathbf{\Phi}_{\vartheta_1} \mathbf{\Phi}_{\vartheta_0}^{-1} \mathbf{T}_{\vartheta_0} \mathbf{x}_0 \tag{A.29}$$

The transition matrix is composed of a scaling matrix $\mathbf{T}_{\vartheta}$, the fundamental solution matrix $\mathbf{\Phi}_{\vartheta}$ for the scaled coordinates and their respective inverse matrices. The scaling matrix $\mathbf{T}_{\vartheta}$ and its inverse are:

$$\mathbf{T}_{\vartheta}^{-1} = \begin{bmatrix} \rho^{-1}\mathbf{I} & \mathbf{0} \\ k^2 e \sin\vartheta\ \mathbf{I} & k^2 \rho\ \mathbf{I} \end{bmatrix}, \qquad \mathbf{T}_{\vartheta} = \begin{bmatrix} \rho \mathbf{I} & \mathbf{0} \\ -e\sin\vartheta\ \mathbf{I} & k^{-2}\rho^{-1}\ \mathbf{I} \end{bmatrix} \tag{A.30}$$

The fundamental solution matrix for the scaled coordinates takes a particularly simple form.

$$\begin{aligned} \mathbf{\Phi}_{\vartheta,ip} &= \begin{bmatrix} 1 & -c(1+\rho^{-1}) & s(1+\rho^{-1}) & 2\rho^2 J \\ 0 & s & c & 2-3esJ \\ 0 & 2s & 2c-e & 3(1-2esJ) \\ 0 & s' & c' & -3e(s'J + s\rho^{-2}) \end{bmatrix} \\ \mathbf{\Phi}_{\vartheta,op} &= \begin{bmatrix} \cos\vartheta & \sin\vartheta \\ -\sin\vartheta & \cos\vartheta \end{bmatrix} \end{aligned} \tag{A.31}$$

where

$$J = k^2 t, \qquad c = \rho\cos\vartheta\,, \qquad s = \rho\sin\vartheta,$$
$$c' = -(\sin\vartheta + e\sin 2\vartheta), \qquad s' = \cos\vartheta + e\cos 2\vartheta$$

The inverse of the fundamental solution matrix is:

$$\begin{aligned} \mathbf{\Phi}_{\vartheta,ip}^{-1} &= \eta^{-2} \begin{bmatrix} \eta^2 & 3e\left(\frac{s}{\rho}\right)(1+\rho^{-1}) & -es(1+\rho^{-1}) & -ec+2 \\ 0 & -3\left(\frac{s}{\rho}\right)(1+e^2\rho^{-1}) & s(1+\rho^{-1}) & c-2e \\ 0 & -3\left(\frac{c}{\rho}+e\right) & c(1+\rho^{-1})+e & -s \\ 0 & 3\rho + e^2 - 1 & -\rho^2 & es \end{bmatrix}, \\ \mathbf{\Phi}_{\vartheta,op}^{-1} &= \begin{bmatrix} \cos\vartheta & -\sin\vartheta \\ \sin\vartheta & \cos\vartheta \end{bmatrix} \end{aligned} \tag{A.32}$$

It is in fact possible to absorb the scaling matrix into the fundamental solution matrix and to factor the fundamental solution matrix into a periodic matrix that contains only functions of the true anomaly and a non-periodic matrix that is near-diagonal and that contains only functions of time. The former is the transformation matrix $\mathbf{B}$ from the Yamanaka Ankersen integration constants or Yamanaka Ankersen elements (referred to as the pseudo-initial values in [145]) and the latter is the Yamanaka Ankersen element transition matrix $\mathbf{\Phi}_y$. In this factorization the state transition matrix becomes:

$$\mathbf{x}_1 = \mathbf{\Phi}_{t_0 \to t_1} \mathbf{x}_0 = \mathbf{B}_1 \mathbf{\Phi}_{y, t_0 \to t_1} \mathbf{B}_0^{-1} \mathbf{x}_0 \tag{A.33}$$

The Yamanaka-Ankersen elements are related to the Keplerian relative orbital elements, and the transformations can be found in section 2.9. The transformation matrix from the Yamanaka-Ankersen elements to the Cartesian relative state vector is:

$$\mathbf{B} = \begin{bmatrix} \mathbf{b}_1 & \mathbf{b}_2 & \mathbf{b}_3 & \mathbf{b}_4 & \mathbf{0}_{4\times1} & \mathbf{0}_{4\times1} \\ \mathbf{0}_{2\times1} & \mathbf{0}_{2\times1} & \mathbf{0}_{2\times1} & \mathbf{0}_{2\times1} & \mathbf{b}_5 & \mathbf{b}_6 \end{bmatrix} \tag{A.34}$$

where

$$\mathbf{b}_1 = [\rho^{-1} \quad 0 \quad k^2 e \sin\vartheta \quad 0]^T$$

$$\mathbf{b}_2 = [\cos\vartheta\,(1+\rho^{-1}) \quad \sin\vartheta \quad k^2(\rho^2+1)\sin\vartheta \quad k^2\rho^2\cos\vartheta]^T$$

$$\mathbf{b}_3 = [\sin\vartheta\,(1+\rho^{-1}) \quad \cos\vartheta \quad k^2\{(\rho^2+1)\sin\vartheta + e\} \quad -k^2\rho^2\sin\vartheta]^T$$

$$\mathbf{b}_4 = [0 \quad 2\rho^{-1} \quad 3k^2\rho \quad -k^2 e\sin\vartheta]^T$$

$$\mathbf{b}_5 = [\rho^{-1}\cos\vartheta \quad k^2\sin\vartheta]^T$$

$$\mathbf{b}_6 = [\rho^{-1}\sin\vartheta \quad k^2(\cos\vartheta + e)]^T$$

The inverse transformation matrix (from the Cartesian relative state vector to the Yamanaka-Ankersen elements) is:

$$\mathbf{B}^{-1} = \begin{bmatrix} \mathbf{b}_1^{-1} & \mathbf{0}_{1\times2} \\ \mathbf{b}_2^{-1} & \mathbf{0}_{1\times2} \\ \mathbf{b}_3^{-1} & \mathbf{0}_{1\times2} \\ \mathbf{b}_4^{-1} & \mathbf{0}_{1\times2} \\ \mathbf{0}_{1\times4} & \mathbf{b}_5^{-1} \\ \mathbf{0}_{1\times4} & \mathbf{b}_6^{-1} \end{bmatrix} \tag{A.35}$$

where

$$\mathbf{b}_1^{-1} = \eta^{-2}[2\rho - \eta^2 + \rho^2(1-\rho) \quad (\rho+1)^2 e \sin\vartheta \quad -k^{-2} e \sin\vartheta\,(1+\rho^{-1}) \quad k^{-2}\rho^{-1}(2-ec)]$$

$$\mathbf{b}_2^{-1} = \eta^{-2}[-e(1+\rho) - (1-\rho^2)\cos\vartheta \quad -\{(\rho+1)^2 - \eta^2\}\sin\vartheta \quad k^{-2}\sin\vartheta\,(1+\rho^{-1}) \quad k^{-2}\rho^{-1}(c-2e)]$$

$$\mathbf{b}_3^{-1} = \eta^{-2}[(\eta^2 - \rho^2)\sin\vartheta \quad -(\rho+2)c - 2e\rho \quad k^{-2}\rho^{-1}\{(\rho+1)\cos\vartheta + e\} \quad -k^{-2}\sin\vartheta]$$

$$\mathbf{b}_4^{-1} = \eta^{-2}[\rho^2 e \sin\vartheta \quad \rho^2(1+\rho) \quad -k^{-2}\rho \quad k^{-2} e \sin\vartheta]^T$$

$$\mathbf{b}_5^{-1} = [\cos\vartheta + e \quad -k^{-2}\rho^{-1}\sin\vartheta]^T$$

$$\mathbf{b}_6^{-1} = [\sin\vartheta \quad -k^{-2}\rho^{-1}\cos\vartheta]^T$$

The Yamanaka-Ankersen element transition matrix is given by:

$$\mathbf{\Phi}_{y,ip} = \begin{bmatrix} 1 & 0 & 0 & 3J \\ 0 & 1 & 0 & -3Je \\ 0 & 0 & 1 & 0 \\ 0 & 0 & 0 & 1 \end{bmatrix}, \qquad \mathbf{\Phi}_{y,op} = \begin{bmatrix} 1 & 0 \\ 0 & 1 \end{bmatrix} \tag{A.36}$$

B Two-point transfer manoeuvres

The two-point transfer manoeuvre is used to find a transfer trajectory between an initial state vector and a terminal state vector that are given at a fixed initial and final time (which means that the transfer time is fixed). This section provides a description of the two-point transfer algorithm and discusses its applications and limitations. The core of the two-point transfer algorithm is based on the inversion of one of the partitions of the state transition matrix (specifically, the ($\mathbf{r}$, $\mathbf{v}$) block). Singularities exist in the algorithm. These singularities occur because the determinant used to compute the matrix inverse may contain zeros.

The two-point transfer algorithm is a well-known solution for computing manoeuvres [134,211,213]. Impulsive manoeuvres are defined as follows.

$$\mathbf{\Delta v} = \mathbf{v}^+ - \mathbf{v}^- \tag{B.1}$$

where

> $\mathbf{v}^-$ is the velocity immediately before the application of the impulsive manoeuvre,
>
> $\mathbf{v}^+$ is the velocity immediately after the application of the impulsive manoeuvre.

The two-point transfer solution is most easily found by examining the following partitions of the state transition matrix. The state transition matrix $\mathbf{\Phi}_{t_1 \to t_2}$ is partitioned into position and velocity components.

$$\mathbf{\Phi}_{t_1 \to t_2} = \begin{bmatrix} \mathbf{\Phi}_{rr} & \mathbf{\Phi}_{rv} \\ \mathbf{\Phi}_{vr} & \mathbf{\Phi}_{vv} \end{bmatrix} \tag{B.2}$$

Each of the partitions is a 3 by 3 matrix. The partitions of the state transition matrix establish relations between the initial position and velocity and the final position and velocity:

$$\begin{aligned} \mathbf{r}_2 &= \mathbf{\Phi}_{rr}\mathbf{r}_1 + \mathbf{\Phi}_{rv}\mathbf{v}_1^+ \\ \mathbf{v}_2^- &= \mathbf{\Phi}_{vr}\mathbf{r}_1 + \mathbf{\Phi}_{vv}\mathbf{v}_1^+ \end{aligned} \tag{B.3}$$

The velocity after the first impulsive manoeuvre is found by re-arranging the first of equations (B.3), and the velocity immediately before the second impulsive manoeuvre is found by substituting this result in the second of equations (B.3).

$$
\begin{aligned}
\mathbf{v}_1^+ &= \boldsymbol{\Phi}_{rv}^{-1}(\mathbf{r}_2 - \boldsymbol{\Phi}_{rr}\mathbf{r}_1) \\
\mathbf{v}_2^- &= (\boldsymbol{\Phi}_{vr} - \boldsymbol{\Phi}_{vv}\boldsymbol{\Phi}_{rv}^{-1}\boldsymbol{\Phi}_{rr})\mathbf{r}_1
\end{aligned} \tag{B.4}
$$

The inverse of the $(\mathbf{r}, \mathbf{v})$ block of the state transition matrix is given by:

$$
\begin{aligned}
\boldsymbol{\Phi}_{rv,ip}^{-1} &= \frac{k^2\rho_1\rho_2}{\Delta}\begin{bmatrix} \varphi_{11}^{-1} & \varphi_{12}^{-1} \\ \varphi_{21}^{-1} & \varphi_{22}^{-1} \end{bmatrix} \\
\boldsymbol{\Phi}_{rv,op}^{-1} &= \frac{k^2\rho_1\rho_2}{\sin\alpha}
\end{aligned} \tag{B.5}
$$

where

$$
\begin{aligned}
\Delta = {} & \{2(1+\mathrm{e}^2) + 3(\rho_1+\rho_2) + 2e^2\cos\alpha\}(1-\cos\alpha) \\
& + 3e(\sin\vartheta_2 - \sin\vartheta_1)\sin\alpha \\
& - 3\rho_1\rho_2\{\sin\alpha + (1+\rho_1)e\sin\vartheta_2 - (1+\rho_2)e\sin\vartheta_1\}J \\
\varphi_{11}^{-1} = {} & -3Je^2 s_1 s_2 - 2e(s_2 - s_1) + \rho_1\rho_2\sin\alpha \\
\varphi_{12}^{-1} = {} & -2\rho_2^2 + \rho_1(\rho_1 - 1) + \rho_1(\rho_2 + 1)\cos\alpha - 3e\rho_2^2 s_1 J \\
\varphi_{21}^{-1} = {} & 2\rho_1^2 - \rho_2(\rho_2 - 1) - \rho_2(\rho_1 + 1)\cos\alpha - 3e\rho_1^2 s_2 J \\
\varphi_{22}^{-1} = {} & e\sin\vartheta_2\,(\rho_2 + 1) - e\sin\vartheta_1\,(\rho_1 + 1) + (\rho_1 + 1)(\rho_2 + 1)\sin\alpha \\
& - 3\rho_1^2\rho_2^2 J \\
\alpha = {} & \vartheta_2 - \vartheta_1 \\
s = {} & \rho\sin\vartheta
\end{aligned}
$$

The in-plane and out-of-plane motions are decoupled, so separate inverses are provided for each. Both the in-plane and the out-of-plane inverse matrices contain common factors, and both feature a denominator. The denominator is a factor of the determinant of the matrix to be inverted, and division by the denominator is part of the matrix inversion. However, the denominator of both the in-plane and the out-of-plane inverse matrix can become zero. When the denominator becomes zero, a singularity occurs in the algorithm.

Figure B.1 shows the zeros in the denominator that multiplies the in-plane matrix inverse. The plot is parameterised by the true anomaly of the first manoeuvre. The eccentricity in this figure is equal to 0.1, but the qualitative picture is the same for all eccentricities. The in-plane manoeuvre becomes singular for transfer times that are integer multiples of the orbital period. In addition, there is a singularity for a transfer time between one and two revolutions whose exact location depends on the initial true anomaly.

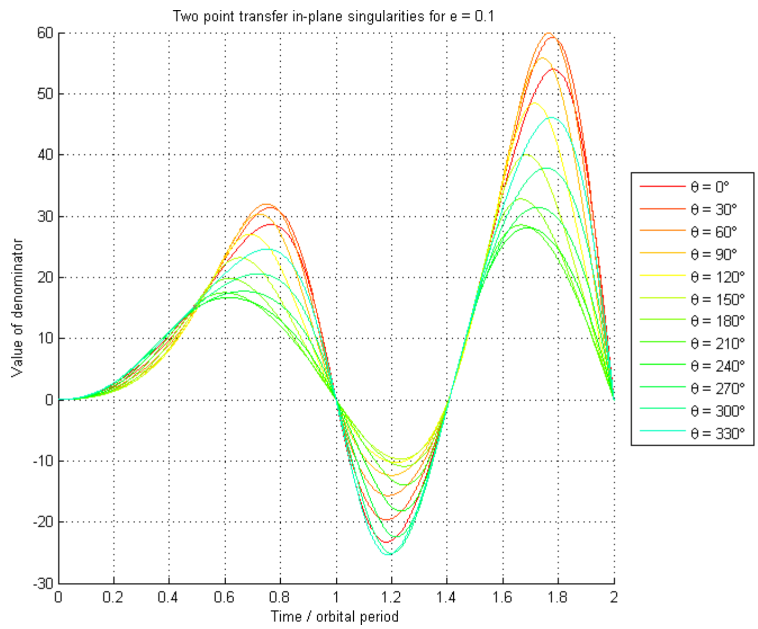

Figure B.1: Graph of in-plane denominator Δ. Zeros lead to singularities in two-point transfer algorithm.

The denominator for the out-of-plane matrix becomes zero whenever the transfer angle is equal to 180° (plus any number of full revolutions). Note that a transfer angle of 180° is not necessarily equal to a transfer time of half an orbital period; this is only the case for transfers that start and end at apogee or perigee.

Manoeuvre planning can be separated for the in-plane and the out-of-plane manoeuvres. For Proba-3 however only two-point transfers that affect both the in-plane and the out-of-plane directions are considered, such that both the in-plane and the out-of-plane singularities must be avoided.

The two-point transfer ΔV's can be re-cast in terms of a state defect expressed in terms of the Yamanaka-Ankersen elements as follows:

$$\begin{bmatrix} \boldsymbol{\Delta}\mathbf{v}_1 \\ \boldsymbol{\Delta}\mathbf{v}_2 \end{bmatrix} = \mathbf{M}_{1\to 2}\left\{\boldsymbol{\Phi}_{J,0\to 3}^{-1}\mathbf{y}_3 - \mathbf{y}_0\right\} \tag{B.6}$$

where

$$\mathbf{M}_{1\to 2} = \begin{bmatrix} \boldsymbol{\Phi}_{rv}^{-1}\mathbf{B}_{r,2} \\ \mathbf{B}_{v,2} - \boldsymbol{\Phi}_{vv}\boldsymbol{\Phi}_{rv}^{-1}\mathbf{B}_{r,2} \end{bmatrix}\boldsymbol{\Phi}_{J,0\to 2}$$

This function provides the two-point transfer manoeuvre matrix $\mathbf{M}_{1\to 2}$. The proof of equation (B.6) is obtained following the derivation of the two-point transfer algorithm in a slightly more general setting. The state vector at some time 3 after the two-point transfer can be written as a function of the state at some time 0 before the first manoeuvre and the two ΔV's:

$$\mathbf{x}_3 = \mathbf{\Phi}_{2\to3}\left(\mathbf{\Phi}_{1\to2}\left(\mathbf{\Phi}_{0\to1}\mathbf{x}_0 + \begin{bmatrix}\mathbf{0}\\ \mathbf{\Delta v}_1\end{bmatrix}\right) + \begin{bmatrix}\mathbf{0}\\ \mathbf{\Delta v}_2\end{bmatrix}\right) \tag{B.7}$$

Re-arranging terms leads to the following expression:

$$\mathbf{\Phi}_{1\to2}\begin{bmatrix}\mathbf{0}\\ \mathbf{\Delta v}_1\end{bmatrix} + \begin{bmatrix}\mathbf{0}\\ \mathbf{\Delta v}_2\end{bmatrix} = \mathbf{\Phi}_{2\to3}^{-1}\mathbf{x}_3 - \mathbf{\Phi}_{0\to2}\mathbf{x}_0 \tag{B.8}$$

The expression for the two-point transfer is now fully split into position and velocity components. Equation (B.8) can be further re-arranged into a single matrix expression:

$$\begin{bmatrix}\mathbf{\Phi}_{rv,1\to2} & \mathbf{0}\\ \mathbf{\Phi}_{vv,1\to2} & \mathbf{I}\end{bmatrix}\begin{bmatrix}\mathbf{\Delta v}_1\\ \mathbf{\Delta v}_2\end{bmatrix} = \begin{bmatrix}\mathbf{r}_2^*\\ \mathbf{v}_2^*\end{bmatrix} \tag{B.9}$$

where

$$\begin{bmatrix}\mathbf{r}_2^*\\ \mathbf{v}_2^*\end{bmatrix} = \mathbf{\Phi}_{2\to3}^{-1}\mathbf{x}_3 - \mathbf{\Phi}_{0\to2}\mathbf{x}_0 = \mathbf{\Phi}_{0\to2}(\mathbf{\Phi}_{0\to3}^{-1}\mathbf{x}_3 - \mathbf{x}_0)$$

It should be noted that the expressions for the position and velocity defects $\mathbf{r}_2$* and $\mathbf{v}_2$* depend on the time of the second manoeuvre only through the state transition matrix $\mathbf{\Phi}_{0\text{->}2}$. This expression is of the familiar form **Ax** = **b**, and the second block column is already in a very convenient form, making the inverse of the matrix extremely easy to compute using Gauss-Jordan elimination through pivoting on the augmented matrix, such that the solution of the ΔV's is:

$$\begin{bmatrix}\mathbf{\Delta v}_1\\ \mathbf{\Delta v}_2\end{bmatrix} = \begin{bmatrix}\mathbf{\Phi}_{rv,1\to2}^{-1} & \mathbf{0}\\ -\mathbf{\Phi}_{vv,1\to2}\mathbf{\Phi}_{rv,1\to2}^{-1} & \mathbf{I}\end{bmatrix}\begin{bmatrix}\mathbf{r}_2^*\\ \mathbf{v}_2^*\end{bmatrix} \tag{B.10}$$

The state defect is now re-written in terms of the pseudo-initial value vectors:

$$\begin{aligned}\begin{bmatrix}\mathbf{r}_2^*\\ \mathbf{v}_2^*\end{bmatrix} &= \mathbf{\Phi}_{0\to2}(\mathbf{\Phi}_{0\to3}^{-1}\mathbf{x}_3 - \mathbf{x}_0) = \mathbf{B}_2\mathbf{\Phi}_{J,0\to2}\mathbf{B}_0^{-1}\left(\mathbf{B}_0\mathbf{\Phi}_{J,0\to3}^{-1}\mathbf{B}_3^{-1}\mathbf{B}_3\mathbf{y}_3 - \mathbf{B}_0\mathbf{y}_0\right)\\ &= \mathbf{B}_2\mathbf{\Phi}_{J,0\to2}\left(\mathbf{\Phi}_{J,0\to3}^{-1}\mathbf{y}_3 - \mathbf{y}_0\right) = \begin{bmatrix}\mathbf{B}_{2,r}\\ \mathbf{B}_{2,v}\end{bmatrix}\mathbf{\Phi}_{J,0\to2}\left(\mathbf{\Phi}_{J,0\to3}^{-1}\mathbf{y}_3 - \mathbf{y}_0\right)\end{aligned} \tag{B.11}$$

Inserting equation (B.11) into equation (B.10) and simplifying leads to the expression for the two-point transfer manoeuvre matrix:

$$
\begin{aligned}
\begin{bmatrix} \Delta\mathbf{v}_1 \\ \Delta\mathbf{v}_2 \end{bmatrix} &= \begin{bmatrix} \boldsymbol{\Phi}^{-1}_{rv,1\to2} & \mathbf{0} \\ -\boldsymbol{\Phi}_{vv,1\to2}\boldsymbol{\Phi}^{-1}_{rv,1\to2} & \mathbf{I} \end{bmatrix} \begin{bmatrix} \mathbf{B}_{2,r} \\ \mathbf{B}_{2,v} \end{bmatrix} \boldsymbol{\Phi}_{J,0\to2}\left(\boldsymbol{\Phi}^{-1}_{J,0\to3}\mathbf{y}_3 - \mathbf{y}_0\right) \\
&= \begin{bmatrix} \boldsymbol{\Phi}^{-1}_{rv,1\to2}\mathbf{B}_{2,r} \\ \mathbf{B}_{2,v} - \boldsymbol{\Phi}_{vv,1\to2}\boldsymbol{\Phi}^{-1}_{rv,1\to2}\mathbf{B}_{2,r} \end{bmatrix} \boldsymbol{\Phi}_{J,0\to2}\left(\boldsymbol{\Phi}^{-1}_{J,0\to3}\mathbf{y}_3 - \mathbf{y}_0\right) \\
&= \mathbf{M}_{1\to2,0}\left(\boldsymbol{\Phi}^{-1}_{J,0\to3}\mathbf{y}_3 - \mathbf{y}_0\right)
\end{aligned}
\tag{B.12}
$$

The right-hand side of this equation is composed of a matrix containing the partitions of the state transition matrix, inverted or otherwise, and the state defect. The state defect at time 2 can be obtained from a state vector at some time 3 after the second manoeuvre and a state vector at some time 0 before the first manoeuvre as shown above.

The $(\mathbf{v}, \mathbf{v})$ block of the state transition matrix is given by:

$$
\begin{aligned}
\boldsymbol{\Phi}_{vv,ip} &= \frac{1}{\rho_1\eta^2}\begin{bmatrix} \varphi_{11} & \varphi_{12} \\ \varphi_{21} & \varphi_{22} \end{bmatrix} \\
\boldsymbol{\Phi}_{vv,op} &= \frac{1}{\rho_1}\{\cos\alpha + (\rho_1 - 1)\}
\end{aligned}
\tag{B.13}
$$

where

$$
\begin{aligned}
\varphi_{11} &= -\{\rho_2^2(1-\rho_2) + \eta^2 + 2\rho_1^2\rho_2\} + \cos\alpha\,(\rho_1+1)(\rho_2^2+\eta^2) \\
&\qquad + 3Je\sin\vartheta_2\,\rho_1^2\rho_2^2 \\
\varphi_{12} &= -2e\rho_2(s_2 - s_1) + \rho_1\sin\alpha\,(\rho_2^2+\eta^2) - 3Je^2 s_1 s_2 \rho_2 \\
\varphi_{21} &= 3\rho_1^2\rho_2^2(\rho_2 - 1)J + e\sin\vartheta_2\,(\rho_1^2 - \rho_2^2) - (\rho_1+1)\rho_2^2\sin\alpha \\
\varphi_{22} &= -2e\rho_2 c_2 - e^2 s_1\sin\vartheta_2 + \rho_1\rho_2^2\cos\alpha + 3Jes_1\rho_2^2(1-\rho_2) \\
\alpha &= \vartheta_2 - \vartheta_1 \\
s &= \rho\sin\vartheta \\
c &= \rho\cos\vartheta
\end{aligned}
$$

C Statistical two-point transfer manoeuvres

The two-point transfer manoeuvre can be generalized for use with the covariance matrix. Given a covariance matrix at a specific point of a transfer trajectory, the statistics of a mid-course manoeuvre can be computed. This approach is followed in chapter 4. The statistical two-point transfer manoeuvre can most easily be derived using the square root of the covariance matrix, in a manner that is similar to the unscented transformation in an unscented Kalman filter [219–223]. The covariance matrix is decomposed as follows, for example using a Cholesky decomposition [224]:

$$\mathbf{P} = \mathbf{S}\mathbf{S}^T \tag{C.1}$$

The matrix $\mathbf{S}$ can be thought of as the square root of the matrix $\mathbf{P}$. The covariance matrix can be decomposed in 3 x 3 submatrices for the position, the velocity, and cross-terms. Similarly, the matrix $\mathbf{S}$ can be partitioned into a 3 x 6 position block and a 3 x 6 velocity block.

$$\begin{bmatrix} \mathbf{P}_{rr} & \mathbf{P}_{rv} \\ \mathbf{P}_{vr} & \mathbf{P}_{vv} \end{bmatrix} = \begin{bmatrix} \mathbf{S}_r \\ \mathbf{S}_v \end{bmatrix} \begin{bmatrix} \mathbf{S}_r^T & \mathbf{S}_v^T \end{bmatrix} = \begin{bmatrix} \mathbf{S}_r\mathbf{S}_r^T & \mathbf{S}_r\mathbf{S}_v^T \\ \mathbf{S}_v\mathbf{S}_r^T & \mathbf{S}_v\mathbf{S}_v^T \end{bmatrix} \tag{C.2}$$

The matrix $\mathbf{S}$ can be propagated to a future epoch using the state transition matrix:

$$\mathbf{S}_2 = \mathbf{\Phi}_{1\to 2}\mathbf{S}_1 \tag{C.3}$$

Just as equation (B.3), this matrix equation can be partitioned into position and velocity components.

$$\begin{aligned} \mathbf{S}_{r,2} &= \mathbf{\Phi}_{rr}\mathbf{S}_{r,1} + \mathbf{\Phi}_{rv}\mathbf{S}_{v^+,1} \\ \mathbf{S}_{v^-,2} &= \mathbf{\Phi}_{vr}\mathbf{S}_{r,1} + \mathbf{\Phi}_{vv}\mathbf{S}_{v^+,1} \end{aligned} \tag{C.4}$$

The solution is the same as for equation (B.3):

$$\begin{aligned} \mathbf{S}_{v^+,1} &= -\mathbf{\Phi}_{rv}^{-1}\mathbf{\Phi}_{rr}\mathbf{S}_{r,1} \\ \mathbf{S}_{v^-,2} &= (\mathbf{\Phi}_{vr} - \mathbf{\Phi}_{vv}\mathbf{\Phi}_{rv}^{-1}\mathbf{\Phi}_{rr})\mathbf{S}_{r,1} \end{aligned} \tag{C.5}$$

This means that the matrices $\mathbf{S}$ for the first and the second ΔV can easily be found:

$$\begin{aligned} \mathbf{S}_{\Delta v,1} &= \mathbf{S}_{v^+,1} - \mathbf{S}_{v^-,1} &&= -\mathbf{\Phi}_{rv}^{-1}\mathbf{\Phi}_{rr}\mathbf{S}_{r,1} - \mathbf{S}_{v^-,1} \\ \mathbf{S}_{\Delta v,2} &= \mathbf{S}_{v^+,2} - \mathbf{S}_{v^-,2} &&= \mathbf{0} - (\mathbf{\Phi}_{vr} - \mathbf{\Phi}_{vv}\mathbf{\Phi}_{rv}^{-1}\mathbf{\Phi}_{rr})\mathbf{S}_{r,1} \end{aligned} \tag{C.6}$$

Finally, the covariance matrices of the first and second ΔV are obtained through equation (C.1).

$$\begin{aligned}\mathbf{P}_{\Delta v,1} &= \mathbf{\Phi}_{rv}^{-1}\mathbf{\Phi}_{rr}\mathbf{P}_{rr,1}\mathbf{\Phi}_{rr}^{T}\mathbf{\Phi}_{rv}^{-T} + \mathbf{P}_{v^{-}r,1}\mathbf{\Phi}_{rr}^{T}\mathbf{\Phi}_{rv}^{-T} + \mathbf{\Phi}_{rv}^{-1}\mathbf{\Phi}_{rr}\mathbf{P}_{rv^{-},1} + \mathbf{P}_{v^{-}v^{-},1} \\ \mathbf{P}_{\Delta v,2} &= (\mathbf{\Phi}_{vr} - \mathbf{\Phi}_{vv}\mathbf{\Phi}_{rv}^{-1}\mathbf{\Phi}_{rr})\mathbf{P}_{rr,1}(\mathbf{\Phi}_{vr} - \mathbf{\Phi}_{vv}\mathbf{\Phi}_{rv}^{-1}\mathbf{\Phi}_{rr})^{T}\end{aligned} \tag{C.7}$$

The elements of the covariance matrix after the application of the correction manoeuvre are given by:

$$\begin{aligned}\mathbf{P}_{\mathrm{r}v^{+}} &= \mathbf{P}_{v^{+}r}^{T} = -\mathbf{P}_{rr,1}\mathbf{\Phi}_{rr}^{T}\mathbf{\Phi}_{rv}^{-T} \\ \mathbf{P}_{v^{+}v^{+}} &= \mathbf{\Phi}_{rv}^{-1}\mathbf{\Phi}_{rr}\mathbf{P}_{rr,1}\mathbf{\Phi}_{rr}^{T}\mathbf{\Phi}_{rv}^{-T}\end{aligned} \tag{C.8}$$

D Solar radiation pressure

Solar radiation pressure is modelled as a constant acceleration in the inertial frame. The basic equations for relative motion are:

$$\dot{\mathbf{x}}(t) = \mathbf{A}(t)\mathbf{x}(t) + \mathbf{D}(t)\mathbf{u}(t), \qquad \mathbf{x}(t_0) = \mathbf{x}_0 \tag{D.1}$$

where

$\mathbf{u}(\tau)$ is the input acceleration,

$\mathbf{D}(\tau) = \begin{bmatrix} \mathbf{0} \\ \mathbf{I} \end{bmatrix}$

The solution consists of the state transition matrix multiplying the initial state, and the input response acting on the input [115]:

$$\mathbf{x}(t) = \mathbf{\Phi}(t, t_0)\mathbf{x}(t_0) + \int_{t_0}^{t} \mathbf{\Phi}(t, \tau)\mathbf{D}(\tau)\mathbf{u}(\tau)d\tau \tag{D.2}$$

The Sun direction is assumed to be constant in the inertial frame, such that the Solar radiation pressure is a constant acceleration in the inertial frame:

$$\mathbf{x}(t) = \mathbf{\Phi}(t, t_0)\mathbf{x}(t_0) + \left\{\int_{t_0}^{t} \mathbf{\Phi}(t, \tau)\mathbf{D}\mathbf{R}_{ECI\rightarrow LVLH}(\tau)d\tau\right\}\mathbf{u}_{ECI} \tag{D.3}$$

The procedure outlined in [225] is followed to perform the integration in equation (D.3). The process can be summarized as follows:

- Decompose rotation matrix $\mathbf{R}_{ECI\rightarrow LVLH}$ into $\mathbf{R}_{PQW\rightarrow LVLH}$ times $\mathbf{R}_{ECI\rightarrow PQW}$, using the perifocal frame as an intermediate frame. The second of these two is a constant matrix for a Keplerian orbit and can be taken outside of the integral on the right. The perifocal frame is shown in figure 2.1.
- Decompose matrix $\mathbf{\Phi}_{\tau\rightarrow t}$ into $\mathbf{B}_t$ times $\mathbf{\Phi}_J(\tau)$ times $\mathbf{B}_\tau^{-1}$. $\mathbf{B}_t$ does not depend on τ and can be taken outside the integral on the left.
- Perform matrix product $\mathbf{B}_\tau^{-1}$ times $\mathbf{D}$ times $\mathbf{R}_{PQW\rightarrow LVLH}(\tau)$. This leads to a 6 x 3 matrix that is analogous to the Lagrange planetary equations in Gauss form for the chosen set of trajectory constants. Examine the structure of matrix $\mathbf{\Phi}_J(\tau)$ and note that it is equal to the identity matrix plus two non-diagonal elements that depend on time (i.e., τ).
- Next, transform all instances of τ (in $\mathbf{\Phi}_J(\tau)$ and in the differential $d\tau$) first to mean anomaly and then to eccentric anomaly and transform all instances of true anomaly in matrix $\mathbf{B}_\tau^{-1} \cdot \mathbf{D} \cdot \mathbf{R}_{PQW\rightarrow LVLH}(\tau)$ to eccentric anomaly.

- Find the integrals of all elements of the matrix integrand, first of $\mathbf{B}_\tau^{-1} \cdot \mathbf{D} \cdot \mathbf{R}_{PQW\to LVLH}(\tau)$ and then of the non-zero off-diagonal elements of $\mathbf{\Phi}_J(\tau)$ multiplying $\mathbf{B}_\tau^{-1} \cdot \mathbf{D} \cdot \mathbf{R}_{PQW\to LVLH}(\tau)$. Finally, collect the integrals in matrix $\mathbf{S}_{PQW}$.

The decomposition of $\mathbf{R}_{ECI\to LVLH}$ and $\mathbf{\Phi}_{\tau\to t}$ leads to the following expression:

$$\mathbf{x}_{SRP} = \int_{t_0}^{t} \mathbf{B}_{LVLH}(t)\mathbf{\Phi}_y(t)\mathbf{\Phi}_y^{-1}(\tau)\mathbf{B}_{v,LVLH}^{-1}\big(\vartheta(\tau)\big)\mathbf{R}_{PQW\to LVLH}\big(\vartheta(\tau)\big)\mathbf{R}_{ECI\to PQW}\mathbf{u}_{ECI}\,d\tau \tag{D.4}$$

where

$$\mathbf{R}_{PQW\to LVLH} = \begin{bmatrix} -\sin\vartheta & \cos\vartheta & 0 \\ 0 & 0 & -1 \\ -\cos\vartheta & -\sin\vartheta & 0 \end{bmatrix}$$

The matrix that transforms the velocity components of the state vector in the perifocal frame is formed from the matrix that transforms the velocity components of the state vector in the LVLH-frame and the rotation matrix from the LVLH-frame to the perifocal frame.

$$\mathbf{B}_{v,PQW}^{-1} = \mathbf{B}_{v,LVLH}^{-1}\mathbf{R}_{PQW\to LVLH} \tag{D.5}$$

The in-plane transformation matrix is:

$$\mathbf{B}_{v,PQW,ip}^{-1} = n^{-1}\eta \begin{bmatrix} \rho^{-1}(2e - 2\cos\vartheta - e\cos^2\vartheta + e^2\cos\vartheta) & -\rho^{-1}(2\sin\vartheta + e\sin\vartheta\cos\vartheta) \\ \rho^{-1}(\cos^2\vartheta + e\cos\vartheta - 2) & \rho^{-1}(\sin\vartheta\cos\vartheta + 2e\sin\vartheta) \\ -\rho^{-1}(\sin\vartheta\cos\vartheta + e\sin\vartheta) & \rho^{-1}(\cos^2\vartheta + 2e\cos\vartheta + 1) \\ \sin\vartheta & -\cos\vartheta - e \end{bmatrix} \tag{D.6}$$

The out-of-plane transformation matrix is:

$$\mathbf{B}_{v,PQW,op}^{-1} = n^{-1}\eta^3 \begin{bmatrix} \rho^{-1}\sin\vartheta \\ \rho^{-1}\cos\vartheta \end{bmatrix} \tag{D.7}$$

Taking the constant matrices outside of the integral leads to:

$$\mathbf{x}_{SRP} = \mathbf{B}_{LVLH}(t)\mathbf{\Phi}_y(t,t_0)\left\{\int_{t_0}^{t} \mathbf{\Phi}_y^{-1}(\tau,t_0)\mathbf{B}_{v,PQW}^{-1}\big(\vartheta(\tau)\big)d\tau\right\}\mathbf{R}_{ECI\to PQW}\mathbf{u}_{ECI} \tag{D.8}$$

The term between curly brackets is the matrix $\mathbf{S}_{PQW}$. The effect of Solar radiation pressure can now be found using the following expression:

$$\mathbf{x}_{SRP} = \mathbf{B}_{LVLH}(t)\mathbf{\Phi}_y(t,t_0)\mathbf{S}_{\mathrm{PQW}}(t,t_0;t_0)\mathbf{R}_{ECI\rightarrow PQW}\mathbf{u}_{ECI} \tag{D.9}$$

The SRP acceleration is expressed in the inertial frame as $\mathbf{u}_{ECI}$ (that is, $\mathbf{u}_{ECI}$ contains both the direction and magnitude of the SRP acceleration). The differential of time $d\tau$ is related to the differential of the mean anomaly dM as:

$$d\tau = n^{-1}dM \tag{D.10}$$

The mean anomaly and its differential are transformed to the eccentric anomaly and its differential using:

$$M = E - e\sin E\,, \qquad dM = (1 - e\cos E)dE \tag{D.11}$$

Next, all instances of the true anomaly are transformed to the eccentric anomaly. The true anomaly occurs within cosine and sine terms, and in the term ρ. These terms can be expressed in terms of the eccentric anomaly:

$$\cos\vartheta = \frac{\cos E - e}{1 - e\cos E}, \qquad \sin\vartheta = \frac{\eta\sin E}{1 - e\cos E}, \qquad \rho = 1 + e\cos\vartheta = \frac{\eta^2}{1 - e\cos E} \tag{D.12}$$

Equations (D.13) to (D.22) demonstrate the transformations, simplifications and the integration applied to each of the non-zero elements of the matrix $\mathbf{S}_{PQW}$. The result is summarized in equation (D.23).

$$
\begin{aligned}
y_{1,P} = n^{-1}&\left\{\int_{t_0}^{t}(\rho^{-1}\eta(2e - 2\cos\vartheta - e\cos^2\vartheta + e^2\cos\vartheta) - 3\eta^{-2}n\tau\sin\vartheta)d\tau\right\}u_P \\
&= n^{-2}\left\{\int_{M_0}^{M}(\rho^{-1}\eta(2e - 2\cos\vartheta - e\cos^2\vartheta + e^2\cos\vartheta)\right. \\
&\left.- 3\eta^{-2}M\sin\vartheta)dM\right\}u_P \\
&= n^{-2}\left\{\int_{E_0}^{E}\left(\eta\eta^{-2}(1 - e\cos E)\left(2e - 2\frac{\cos E - e}{1 - e\cos E}\right.\right.\right. \\
&\left.- e\left(\frac{\cos E - e}{1 - e\cos E}\right)^2 + e^2\frac{\cos E - e}{1 - e\cos E}\right) \\
&\left.\left.- 3\eta^{-2}(E - e\sin E)\frac{\eta\sin E}{1 - e\cos E}\right)(1 - e\cos E)dE\right\}u_P \\
&= -n^{-2}\left\{\int_{E_0}^{E}\eta^{-1}(2\cos E - 7e - e^3\cos^2 E + 3E\sin E + 2e^3\right. \\
&\left.+ 2e\cos^2 E + 3e^2\cos E - e^4\cos E)dE\right\}u_P \\
&= n^{-2}\eta^{-1}\left[3E\cos E - (5 + 3e^2 - e^4)\sin E - \frac{1}{4}e(2 - e^2)\sin 2E\right. \\
&\left.+ \frac{3}{2}e(4 - e^2)E\right]_{E_0}^{E}u_P
\end{aligned}
\tag{D.13}
$$

$$
\begin{aligned}
y_{1,Q} = n^{-1}&\left\{\int_{t_0}^{t}\big(-\rho^{-1}\eta(2\sin\vartheta + e\sin\vartheta\cos\vartheta) + 3\eta^{-2}n\tau(\cos\vartheta + e)\big)d\tau\right\}u_Q \\
&= n^{-2}\left\{\int_{M_0}^{M}\big(-\rho^{-1}\eta(2\sin\vartheta + e\sin\vartheta\cos\vartheta)\right. \\
&\left.+ 3\eta^{-2}M(\cos\vartheta + e)\big)dM\right\}u_Q \\
&= n^{-2}\left\{\int_{E_0}^{E}\left(-\eta^{-1}(1 - e\cos E)\left(2\frac{\eta\sin E}{1 - e\cos E}\right.\right.\right. \\
&\left.+ e\frac{\eta\sin E}{1 - e\cos E}\frac{\cos E - e}{1 - e\cos E}\right) \\
&\left.\left.+ 3\eta^{-2}(E - e\sin E)\left(\frac{\cos E - e}{1 - e\cos E} + e\right)\right)(1 - e\cos E)dE\right\}u_Q \\
&= n^{-2}\left\{\int_{E_0}^{E}(e^2\sin E - 2e\sin E\cos E - 2\sin E + 3E\cos E)dE\right\}u_Q \\
&= n^{-2}\left[3E\sin E + \frac{1}{2}e\cos^2 E + (5 - e^2)\cos E + \frac{1}{4}e\cos 2E\right]_{E_0}^{E}u_Q
\end{aligned}
\tag{D.14}
$$

$$
\begin{aligned}
y_{2,P} = n^{-1}&\left\{\int_{t_0}^{t}(\rho^{-1}\eta(\cos^2\vartheta + e\cos\vartheta - 2) + 3e\eta^{-2}n\tau\sin\vartheta)d\tau\right\}u_P \\
&= n^{-2}\left\{\int_{M_0}^{M}(\rho^{-1}\eta(\cos^2\vartheta + e\cos\vartheta - 2) + 3e\eta^{-2}M\sin\vartheta)dM\right\}u_P \\
&= n^{-2}\left\{\int_{E_0}^{E}\left(\eta^{-1}(1-e\cos E)\left(\left(\frac{\cos E - e}{1-e\cos E}\right)^2 + e\frac{\cos E - e}{1-e\cos E} - 2\right)\right.\right. \\
&\left.\left. + 3e\eta^{-2}(E - e\sin E)\frac{\eta\sin E}{1-e\cos E}\right)(1-e\cos E)dE\right\}u_P \\
&= -n^{-2}\eta^{-1}\left\{\int_{E_0}^{E}(\cos^2 E + 3e\cos E - 3e^2 + e^3\cos E + 3e\,E\sin E\right. \\
&\left. - 2)dE\right\}u_P \\
&= n^{-2}\eta^{-1}\left[\frac{1}{4}\sin 2E - 3eE\cos E - 3\left(\frac{1}{2} + e^2\right)E\right. \\
&\left. + (6+e^2)e\sin E\right]_{E_0}^{E} u_P
\end{aligned}
\tag{D.15}
$$

$$
\begin{aligned}
y_{2,Q} = n^{-1}&\left\{\int_{t_0}^{t}\big(\eta\rho^{-1}\sin\vartheta\,(2e + \cos\vartheta) - 3\eta^{-2}n\tau e(e + \cos\vartheta)\big)d\tau\right\}u_Q \\
&= n^{-2}\left\{\int_{M_0}^{M}\big(\eta\rho^{-1}\sin\vartheta\,(2e + \cos\vartheta) - 3\eta^{-2}Me(e + \cos\vartheta)\big)dM\right\}u_Q \\
&= n^{-2}\left\{\int_{E_0}^{E}\left(\eta^{-1}(1-e\cos E)\frac{\eta\sin E}{1-e\cos E}\left(2e + \frac{\cos E - e}{1-e\cos E}\right)\right.\right. \\
&\left.\left. - 3\eta^{-2}(E - e\sin E)e\left(e + \frac{\cos E - e}{1-e\cos E}\right)\right)(1-e\cos E)dE\right\}u_Q \\
&= n^{-2}\left\{\int_{E_0}^{E}\left(\frac{1}{2}(1+e^2)\sin 2E + e\sin E - 3eE\cos E\right)dE\right\}u_Q \\
&= -n^{-2}\left[\frac{1}{4}(1+e^2)\cos 2E + 3eE\sin E + 4e\cos E\right]_{E_0}^{E} u_Q
\end{aligned}
\tag{D.16}
$$

$$
\begin{aligned}
y_{3,P} = n^{-1}&\left\{\int_{t_0}^{t}\big(-\eta\rho^{-1}\sin\vartheta\,(e + \cos\vartheta)\big)d\tau\right\}u_P \\
&= n^{-2}\left\{\int_{M_0}^{M}\big(-\eta\rho^{-1}\sin\vartheta\,(e + \cos\vartheta)\big)dM\right\}u_P \\
&= n^{-2}\left\{\int_{E_0}^{E}\left(-\eta^{-1}(1-e\cos E)\frac{\eta\sin E}{1-e\cos E}\left(e + \frac{\cos E - e}{1-e\cos E}\right)\right)(1\right. \\
&\left. - e\cos E)dE\right\}u_P \\
&= -\frac{1}{2}n^{-2}\eta^2\left\{\int_{E_0}^{E}\sin 2E\,dE\right\}u_P \\
&= \frac{1}{4}n^{-2}\eta^2[\cos 2E]_{E_0}^{E}u_P
\end{aligned}
\tag{D.17}
$$

$$
\begin{aligned}
y_{3,Q} = n^{-1}&\left\{\int_{t_0}^{t}\left(\rho^{-1}\eta(\cos^2\vartheta + 2e\cos\vartheta + 1)\right)d\tau\right\}u_Q \\
&= n^{-2}\left\{\int_{M_0}^{M}\left(\rho^{-1}\eta(\cos^2\vartheta + 2e\cos\vartheta + 1)\right)dM\right\}u_Q \\
&= n^{-2}\left\{\int_{E_0}^{E}\eta^{-1}(1 - e\cos E)\left(\left(\frac{\cos E - e}{1 - e\cos E}\right)^2 + 2e\frac{\cos E - e}{1 - e\cos E}\right.\right. \\
&\left.\left. + 1\right)(1 - e\cos E)dE\right\}u_Q \\
&= n^{-2}\left\{\int_{E_0}^{E}\eta(1 + \cos^2 E - 2e\cos E)dE\right\}u_Q \\
&= n^{-2}\eta\left[\frac{1}{4}\sin 2E - 2e\sin E + \frac{3}{2}E\right]_{E_0}^{E}u_Q
\end{aligned}
\tag{D.18}
$$

$$
\begin{aligned}
y_{4,P} = n^{-1}\eta^3\eta^{-2}&\left\{\int_{t_0}^{t}\sin\vartheta\, d\tau\right\}u_P \\
&= n^{-2}\eta^3\eta^{-2}\left\{\int_{M_0}^{M}\sin\vartheta\, dM\right\}u_P \\
&= n^{-2}\eta\left\{\int_{E_0}^{E}\frac{\eta\sin E}{1 - e\cos E}(1 - e\cos E)dE\right\}u_P \\
&= n^{-2}\eta^2\left\{\int_{E_0}^{E}\sin E\, dE\right\}u_P = n^{-2}\eta^2[-\cos E]_{E_0}^{E}u_P
\end{aligned}
\tag{D.19}
$$

$$
\begin{aligned}
y_{4,Q} = -n^{-1}\eta^3\eta^{-2}&\left\{\int_{t_0}^{t}(\cos\vartheta + e)d\tau\right\}u_Q \\
&= -n^{-2}\eta^3\eta^{-2}\left\{\int_{M_0}^{M}(\cos\vartheta + e)dM\right\}u_Q \\
&= -n^{-2}\eta\left\{\int_{E_0}^{E}\left(\frac{\cos E - e}{1 - e\cos E} + e\right)(1 - e\cos E)dE\right\}u_Q \\
&= -n^{-2}\eta^3\left\{\int_{E_0}^{E}\cos E\, dE\right\}u_Q = -n^{-2}\eta^3[\sin E]_{E_0}^{E}u_Q
\end{aligned}
\tag{D.20}
$$

$$
\begin{aligned}
y_{5,W} = n^{-1}&\left\{\int_{t_0}^{t}(\eta^3\rho^{-1}\sin\vartheta)d\tau\right\}u_W \\
&= n^{-2}\left\{\int_{M_0}^{M}(\eta^3\rho^{-1}\sin\vartheta)dM\right\}u_W \\
&= n^{-2}\left\{\int_{E_0}^{E}\left(\eta(1 - e\cos E)\frac{\eta\sin E}{1 - e\cos E}\right)(1 - e\cos E)dE\right\}u_W \\
&= n^{-2}\left\{\int_{E_0}^{E}\eta^2\left(\sin E - \frac{1}{2}e\sin 2E\right)dE\right\}u_W \\
&= n^{-2}\eta^2\left[\frac{1}{4}e\cos 2E - \cos E\right]_{E_0}^{E}u_W
\end{aligned}
\tag{D.21}
$$

$$
\begin{aligned}
y_{6,W} = n^{-1}\left\{\int_{t_0}^{t}(-\eta^3\rho^{-1}\cos\vartheta)d\tau\right\}u_W \\
&= n^{-2}\left\{\int_{M_0}^{M}(-\eta^3\rho^{-1}\cos\vartheta)dM\right\}u_W \\
&= n^{-2}\left\{\int_{E_0}^{E}\left(-\eta(1-e\cos E)\frac{\cos E-e}{1-e\cos E}\right)(1-e\cos E)dE\right\}u_W \\
&= n^{-2}\left\{\int_{E_0}^{E}\eta\left(-(1+e^2)\cos E+\frac{1}{2}e\cos 2E+\frac{3}{2}e\right)dE\right\}u_W \\
&= n^{-2}\eta\left[\frac{3}{2}eE-(1+e^2)\sin E+\frac{1}{4}e\sin 2E\right]_{E_0}^{E}u_W
\end{aligned}
\tag{D.22}
$$

Collect the anti-derivatives in matrix $\mathbf{S}_{PQW}$

$$
\mathbf{S}_{PQW} = \begin{bmatrix}
\mathbf{S}_{PQW}(1,1) & \mathbf{S}_{PQW}(1,2) & 0 \\
\mathbf{S}_{PQW}(2,1) & \mathbf{S}_{PQW}(2,2) & 0 \\
\mathbf{S}_{PQW}(3,1) & \mathbf{S}_{PQW}(3,2) & 0 \\
\mathbf{S}_{PQW}(4,1) & \mathbf{S}_{PQW}(4,2) & 0 \\
0 & 0 & \mathbf{S}_{PQW}(5,3) \\
0 & 0 & \mathbf{S}_{PQW}(6,3)
\end{bmatrix}
\tag{D.23}
$$

where

$$
\begin{aligned}
\mathbf{S}_{PQW}(1,1) = n^{-2}\eta^{-1}\Big(3E\cos E-(5+3e^2-e^4)\sin E-\frac{1}{4}e(2-e^2)\sin 2E \\
&+\frac{3}{2}e(4-e^2)E\Big)
\end{aligned}
$$

$$
\mathbf{S}_{PQW}(2,1) = n^{-2}\eta^{-1}\left(\frac{1}{4}\sin 2E-3eE\cos E-3\left(\frac{1}{2}+e^2\right)E+(6+e^2)e\sin E\right)
$$

$$
\mathbf{S}_{PQW}(3,1) = \frac{1}{4}n^{-2}\eta^2(\cos 2E)
$$

$$
\mathbf{S}_{PQW}(4,1) = -n^{-2}\eta^2(\cos E)
$$

$$
\mathbf{S}_{PQW}(1,2) = n^{-2}\left(3E\sin E+\frac{1}{2}e\cos^2 E+(5-e^2)\cos E+\frac{1}{4}e\cos 2E\right)
$$

$$
\mathbf{S}_{PQW}(2,2) = -n^{-2}\left(\frac{1}{4}(1+e^2)\cos 2E+3eE\sin E+4e\cos E\right)
$$

$$
\mathbf{S}_{PQW}(3,2) = n^{-2}\eta\left(\frac{1}{4}\sin 2E-2e\sin E+\frac{3}{2}E\right)
$$

$$
\mathbf{S}_{PQW}(4,2) = -n^{-2}\eta^3(\sin E)
$$

$$
\mathbf{S}_{PQW}(5,3) = n^{-2}\eta^2\left(\frac{1}{4}e\cos 2E-\cos E\right)
$$

$$\mathbf{S}_{PQW}(6,3) = n^{-2}\eta\left(\frac{3}{2}eE - (1+e^2)\sin E + \frac{1}{4}e\sin 2E\right)$$

E Corrected CAM algorithm

The original CAM algorithm was developed to operate on a given state vector in the tangential frame, and this original formulation was used to derive the results in chapter 5. The original algorithm required a transformation of the state vector from the LVLH-frame to the tangential frame. The basic idea of the original algorithm is to first find the initial velocity required to establish a non-drifting trajectory for the given initial position in the tangential frame, and then to add a tangential ΔV to achieve the specified drift per orbit. A non-drifting trajectory is found by calculating the tangential velocity required for the given initial position to achieve a relative semi-major axis equal to zero, and setting the transverse velocity (that is, in the z-direction of the tangential frame) to zero. The CAM ΔV consists of the ΔV required to establish the non-drifting trajectory (which is the initial velocity required to establish the non-drifting trajectory minus the given initial velocity) plus the ΔV required to establish the specified drift rate.

Before publication of the article on which chapter 5 is based, the algorithm was modified to operate on a state vector expressed in the LVLH-frame, and this modified algorithm was included in the article. After publication it was found that the modification contained a mistake. The modification did not consider the angular velocity of the tangential frame with respect to the LVLH-frame. The original algorithm defined a ΔV to stop the velocity in the tangential frame, and the modified algorithm defined a ΔV to stop the velocity in the LVLH-frame (equation (5.4)), but a state vector with zero velocity in the tangential frame has a non-zero velocity in the LVLH-frame due to the angular velocity of the tangential frame with respect to the LVLH-frame. This can readily be seen from equations (2.71) and (2.72): the velocity in the LVLH-frame is the sum of a rotation matrix multiplying the velocity in the tangential frame and an angular velocity matrix multiplying the position in the tangential frame. The correction to the algorithm adds a term that corrects for the angular velocity of the tangential frame with respect to the LVLH-frame. The correction is the ΔV computed in equation (E.3). Equation (5.5) is the sum of equations (E.4) (multiplied by a constant) and (E.5), and equation (5.4) has been corrected to include the contribution of equation (E.3).

The corrected CAM algorithm computes the CAM ΔV as the sum of three components: ΔV_{stop}, ΔV_{drift} and $\Delta V_{correction}$. Note that although the ΔV is computed as the sum of three contributions, the ΔV is performed as a **single** manoeuvre.

$$\mathbf{\Delta V}_{CAM} = \mathbf{\Delta V}_{stop} + \mathbf{\Delta V}_{drift} + \mathbf{\Delta V}_{correction} \tag{E.1}$$

The in-plane and out-of-plane components of the stop ΔV are computed as:

$$\begin{aligned}\mathbf{\Delta V}_{stop,ip} &= -\begin{bmatrix} v_{x,LVLH} \\ v_{z,LVLH} \end{bmatrix} + \mathbf{\Delta V}_{stop,VBAR}, \\ \Delta V_{stop,op} &= \begin{cases} 0 & \operatorname{sgn}(v_{y,LVLH}) = \operatorname{sgn}(v_{y,LVLH}) \\ -v_{y,LVLH} & \operatorname{sgn}(v_{y,LVLH}) \neq \operatorname{sgn}(v_{y,LVLH}) \end{cases}\end{aligned} \tag{E.2}$$

The in-plane components of the ΔV required to stop the motion with respect to the tangential frame instead of the LVLH-frame are computed as:

$$\mathbf{\Delta V}_{stop,VBAR} = -\dot{\gamma}\theta^{-2}(\rho x_{LVLH} - e \sin\vartheta \, z_{LVLH}) \begin{bmatrix} e \sin\vartheta \\ \rho \end{bmatrix} \tag{E.3}$$

where

$$\dot{\gamma} = k^2\rho^2\theta^{-2}(\rho - \eta^2), \qquad k^2 = \sqrt{\frac{\mu}{p^3}}, \qquad \eta^2 = 1 - e^2$$

$$\theta^2 = 2\rho - \eta^2, \qquad \rho = 1 + e\cos\vartheta$$

The drift ΔV is computed as:

$$\begin{aligned}\mathbf{\Delta V}_{drift,ip} &= \mp\frac{\eta^5 k^2}{6\pi\theta^2} D \begin{bmatrix} \rho \\ -e\sin\vartheta \end{bmatrix} \\ \mathbf{\Delta V}_{drift,op} &= 0\end{aligned} \tag{E.4}$$

where

$\mp = \operatorname{sgn}(\rho x_{LVLH} - e\sin\vartheta \, z_{LVLH})$

D is the drift rate per orbit

The correction ΔV is computed as:

$$\begin{aligned}\mathbf{\Delta V}_{correction,ip} &= \frac{k^2\rho^2}{\theta^2}(e\sin\vartheta \, x_{LVLH} + (1+\rho) z_{LVLH}) \begin{bmatrix} \rho \\ -e\sin\vartheta \end{bmatrix} \\ \mathbf{\Delta V}_{correction,op} &= 0\end{aligned} \tag{E.5}$$

F Survey of formation flying and rendezvous missions

Table F.1 presents a survey of automated formation flying and rendezvous missions. Most missions typically associated with crewed spaceflight (such as e.g., the Space Shuttle and the Soyuz) except for the ATV have been excluded. The following abbreviations have been used for the mission type classification:

- AA: astronomy and astrophysics
- TD: technology demonstrator
- TC: telecommunications
- OOS: On-Orbit Servicing
- ADR: Active Debris Removal
- HP: heliophysics
- EO: Earth observation
- PS: planetary science

Additional information on these missions can be found in the references and on the following websites:

https://directory.eoportal.org

https://www.nanosats.eu/

Table F.1: Formation flying and rendezvous missions.

mission	type	size class	orbit type	relative formation	# sats	launch date	reference
AAReST	AA TD	nano	LEO	N/A	3	2022-12-28	[226–228]
Aerocube-10	TD	nano	LEO	e / i separation	2	2019-04-17	[53]
Aerocube-4	TD	nano	LEO	along-track separation	3	2012-09-13	[229]
Aerocube-OCSD	TD	nano	LEO	e / i separation	2	2017-11-12	[230–234]
ASTRA	TC	large	GEO	e / i separation	6	1996-04-08	[9,31,235]
ASTRO / NextSat	OOS TD		LEO	rendezvous	2	2007-03-09	[236,237]
Astrobee	TD	nanosat	LEO	rendezvous	3	2019-07-25	[238–240]
A-train	EO	various	LEO	along-track separation	7	2014-07-02	[23]
ATV	CT	large	LEO	rendezvous based on Hohmann transfer and radial hop	2	2014-07-29	[17,18,241,242]
BEESAT-14/15	TD	nano	LEO	e / i separation	2	2022-12-28	[243]
BIROS/AVANTI	TD	mini	LEO	e / i separation	2	2016-06-22	[49,61,62,244,245]
BROS	EO	nano	LEO	along-track separation	2	2022-06-30	[246]
CanX-4/5	TD	nano	LEO	along-track separation	2	2014-06-30	[52,111,247–249]

mission	type	size class	orbit type	relative formation	# sats	launch date	reference
				projected circular orbit			
Canyval-C	TD	nano	LEO	e / i separation inertial alignment	2	2021-03-22	[65,250]
Canyval-X	TD	nano	LEO	e / i separation inertial alignment	2	2018-01-12	[64,251]
CIRCE	EO	nano	LEO	along-track separation	2	2022-12-28	[252–254]
ClearSpace-1	ADR TD	N/A	LEO	rendezvous	2	2025-06-30	[255]
Cluster 1	HP	medium	HEO	tetrahedron	4	1996-06-04	[28]
Cluster 2	HP	medium	HEO	tetrahedron	4	2000-07-16	[29,30]
CPOD	TD	nano	LEO	e / i separation forced motion	2	2022-12-28	[55,256,257]
Darwin	AA	medium	L2	planar array	3 to 5	2015-06-30	[38,258–262]
DELFFI-1/2	EO TD	nano	LEO	N/A	2	2015-06-30	[263]
eDeorbit	ADR TD	large	LEO	e/i separation-based rendezvous forced motion along V-bar motion synchronization	2	2025-06-30	[46,264,265]
ELSA-d	TD	mini	LEO	e/i separation-based rendezvous forced motion along V-bar	2	2021-03-22	[266–269]
ETS-VII	TD	large	LEO	in-plane tangential hop forced motion along V-bar	2	1997-11-28	[270–276]
FAST	EO TD	micro mini	LEO	along-track separation	2	2011-12-31	[277–279]
GomX4	EO TD	nano	LEO	along-track separation	2	2018-02-02	[280–282]
Grace	EO	mini	LEO	along-track separation e / i separation during switch	2	2002-03-17	[11,37,81]
Grace FO	EO	medium	LEO	along-track separation	2	2018-05-22	[81]
Grail	PS	mini	LLO	along-track separation	2	2011-09-10	[33,283,284]
GSSAP	EO	medium	GEO	N/A	2	2014-07-28	[285,286]
Hawkeye 360 - 4, 5, 6	EO	micro	LEO	pendulum projected circular orbit along-track separation	3	2022-06-30	[54]
HawkEye 360 - 2	EO	micro	LEO	pendulum projected circular orbit along-track separation	3	2021-01-24	[54]
HawkEye 360 - 3	EO	micro	LEO	pendulum projected circular orbit	3	2021-06-30	[54]

mission	type	size class	orbit type	relative formation	# sats	launch date	reference
				along-track separation			
HawkEye pathfinder (Hawk A, B, C)	EO	micro	LEO	pendulum projected circular orbit along-track separation	3	2018-12-03	[54]
HummerSat	TD	mini micro	LEO		2	2012-11-18	[287,288]
IPERDRONE	TD	nano	LEO	N/A	2	2022-12-28	[289]
IRASSI	AA	large	L2	3D swarm	5	2030-06-30	[41,290,291]
JC2Sat-FF	TD	micro	LEO	along-track separation	2	2013-06-30	[292]
Kosmos 186/188	TD	large	LEO	rendezvous and docking	2	1967-10-27	[120]
LIFE	AA	N/A	L2	x-array	3 to 5	N/A	[40,293–296]
LISA observatory	AA	large	helio	triangular	3	2034-06-30	[35,297]
MAGNARO	TD	nano	LEO	along-track separation	2	2023-01-31	[298]
mDot	AA	mini nano	LEO	e / i separation (RAAN separation)	2	2025-12-31	[56]
MEV-1	OOS	large	GEO	rendezvous and docking	2	2019-10-09	[32]
MEV-2	OOS	large	GEO	rendezvous and docking	2	2020-08-15	[32]
MMS	HP	medium	HEO	tetrahedron	4	2015-03-13	[27,299–301]
Morning constellation	EO TD	mini	LEO	along-track separation	4 (2)	2000-11-21	[36]
NanoACE	TD	nano	LEO	N/A	1	2017-07-14	[302]
Netsat	TD	nano	LEO	eccentricity separation pendulum	4	2020-09-28	[50,303,304]
New Worlds Mission / Starshade	AA	large	L2	inertial alignment along Sun direction	2	2030-06-30	[305,306]
PAN	TD	nano	LEO	rendezvous	2	2022-01-13	[307,308]
PRISMA	TD	mini micro	LEO	e / i separation rendezvous trajectories inspection trajectories	2	2010-06-15	[3,45,162,309–311]
PRISMA: IRIDES & COBRA-IRIDES experiment	TD	mini micro	LEO	e / i separation	2	2010-06-15	[312,313]
PRISMA: NEAT pathfinder experiment	TD	mini micro	LEO	inertial alignment along Sun direction	2	2010-06-15	[314]
PROBA 3	TD HP	mini	HEO	inertial	2	2023-06-30	[26,315,316]
RACE	TD	nano	LEO	e / i separation rendezvous	2	2024-12-31	[317–319]
Range-A/B	TD	nano	LEO	along-track separation	2	2018-12-03	[320,321]
RemoveDebris	TD	mini nano	LEO	various	3	2018-04-02	[322–324]
OSAM-1 / RestoreL	TD	large	LEO	rendezvous based on coelliptic orbits and Hohman	2	2024-06-30	[325,326]

mission	type	size class	orbit type	relative formation	# sats	launch date	reference
				transfers e / i separation			
SAMSON	TD	nano	LEO	N/A	3	2021-03-22	[327]
SATURN	TD	nano	LEO	N/A	3	2025-12-31	[328]
Seeker 1.0	TD	nano	LEO	forced motion linear trajectories	2	2019-04-17	[329,330]
SEIRIOS	AA TD	micro nano	LEO	pendulum	3	2025-12-31	[68]
SERPENT	TD	nanosat	LEO	N/A	2	2022-12-31	[331]
Simbol-X	AA	medium large	HEO	continuous forced motion	2	2014-06-30	[43,332–334]
SNAP-1 & Tsinghua 1	TD	nano	LEO	rendezvous with Tsinghua 1	2	2000-06-28	[335]
SNIPE	EO	nano	LEO	e / i separation projected circular orbit	4	2022-12-28	[336]
SPHERES	TD	nano	LEO	various	3	2006-05-18	[337,338]
Starlight	TD	mini	helio	virtual paraboloid	2	2006-06-30	[339,340]
Starling1	TD	nano	LEO	along-track separation projected circular orbit	4	2022-07-31	[59]
STRaND-2A/2B	TD	nano	LEO	rendezvous	2	N/A	[341]
SULIS	TD HP	nano	LEO helio	inertial alignment along Sun direction	3 x 2	2025-12-31	[34]
SWARM-EX		nano	LEO	along-track separation projected circular orbit	6 to 12	2024-06-30	[58]
Tandem-L	EO	N/A	LEO	e / i separation	2	2024-06-30	[342]
TerraSAR-X / Tandem-X	EO	medium	LEO	e / i separation	2	2010-06-21	[24,163,343,344]
TPF	AA	N/A	L2	x-array fixed inertial	5	2015-06-30	[25,39,192,345,346]
Tianwang 1	TD	nano	LEO	N/A	3	2015-09-25	[347,348]
TOM	EO	nano	LEO	pendulum + along-track separation	3	2023-12-31	[51,349]
Ukko	TD	nano	LEO	rendezvous	2	2023-01-01	[350]
VISORS	HP	nano	LEO	inertial along Sun direction e / i separation	2	2023-12-31	[57,351]
VTXO	AA	nano mini	HEO	inertial along Sun direction	2	2024-12-31	[67]
XSS-10	TD	micro	LEO	forced motion fly-around	1 + 1	2003-01-29	[352]
XSS-11	TD	mini	LEO	natural motion fly-around at 500 m	1 + 1	2005-03-11	[353]

References

[1] Fehse, W. *Automated Rendezvous and Docking of Spacecraft*. Cambridge University Press, Cambridge, UK, 2003. ISBN 978-0-521-82492-7

[2] Woffinden, D. C., and Geller, D. K. "Navigating the Road to Autonomous Orbital Rendezvous." *AIAA Journal of Spacecraft and Rockets*, Vol. 44, No. 4, 2007, pp. 898–909. https://doi.org/10.2514/1.30734.

[3] Bodin, P., Larsson, R., Nilsson, F., Chasset, C., Noteborn, R., and Nylund, M. "PRISMA: An In-Orbit Test Bed for Guidance, Navigation, and Control Experiments." *Journal of Spacecraft and Rockets*, Vol. 46, No. 3, 2009, pp. 615–623. https://doi.org/10.2514/1.40161.

[4] CleanSpace, Safe Close Proximity Operations, ESA-TECSYE-TN-010228, ESA, Sep 30, 2018.

[5] Swiatek, P., Innocenti, L., Wolahan, A., Capogna, F., Caiazzo, A., and Vakaet, C. Design Principles for Sustainable Close Proximity Operations. Paper #6177 Proceedings of the First International Orbital Debris Conference, Sugar Land, Texas, USA, 2019.

[6] Alfriend, K. T., Ed. *Spacecraft Formation Flying: Dynamics, Control and Navigation*. Butterworth-Heinemann, Oxford, 2010. https://doi.org/10.1016/C2009-0-17485-8

[7] Sherwood, R., Chien, S., Castano, R., and Rabideau, G. Spacecraft Autonomy Using Onboard Processing for a SAR Constellation Mission. Proceedings of the ISPRS Commission I Mid-Term Symposium in conjunction with Pecora 15/Land Satellite Information IV Conference Integrated Remote Sensing at the Global, Regional and Local Scale, Denver, Colorado, USA, 2002.

[8] Breger, L., Inalhan, G., Tillerson, M., and How, J. P. Cooperative Spacecraft Formation Flying: Model Predictive Control with Open- and Closed-Loop Robustness. In *Modern Astrodynamics*, Elsevier, 2006, pp. 237–277. https://doi.org/10.1016/S1874-9305(07)80010-0

[9] Chao, C.-C. G. *Applied Orbit Perturbation and Maintenance*. American Institute of Aeronautics and Astronautics, Inc., Washington, DC, USA, 2005. ISBN 978-1-884989-17-9. https://doi.org/10.2514/4.989179

[10] Ren, W., and Beard, R. Virtual Structure Based Spacecraft Formation Control with Formation Feedback. Proceedings of the AIAA Guidance, Navigation, and Control

Conference and Exhibit, Monterey, California, USA, 2002. https://doi.org/10.2514/6.2002-4963

[11] Kirschner, M., Montenbruck, O., and Bettadpur, S. Flight Dynamics Aspects of the GRACE Formation Flying. Proceedings of the 16th International Symposium on Spaceflight Dynamics, Pasadena, California, USA, 2001.

[12] Walker, J. G. “Satellite Constellations.” *Journal of the British Interplanetary Society*, Vol. 37, 1984, p. 559.

[13] Hadaegh, F. Y., Chung, S.-J., and Manohara, H. M. “On Development of 100-Gram-Class Spacecraft for Swarm Applications.” *IEEE Systems Journal*, Vol. 10, No. 2, 2016, pp. 673–684. https://doi.org/10.1109/JSYST.2014.2327972.

[14] Bandyopadhyay, S., Foust, R., Subramanian, G. P., Chung, S.-J., and Hadaegh, F. Y. “Review of Formation Flying and Constellation Missions Using Nanosatellites.” *Journal of Spacecraft and Rockets*, Vol. 53, No. 3, 2016, pp. 567–578. https://doi.org/10.2514/1.A33291.

[15] Bandyopadhyay, S., Subramanian, G. P., Foust, R., Morgan, D., Chung, S.-J., and Hadaegh, F. A Review of Impending Small Satellite Formation Flying Missions. Proceedings of the 53rd AIAA Aerospace Sciences Meeting, Kissimmee, Florida, USA, 2015. https://doi.org/10.2514/6.2015-1623

[16] Di Mauro, G., Lawn, M., and Bevilacqua, R. “Survey on Guidance Navigation and Control Requirements for Spacecraft Formation-Flying Missions.” *Journal of Guidance, Control, and Dynamics*, Vol. 41, No. 3, 2018, pp. 581–602. https://doi.org/10.2514/1.G002868.

[17] De Pasquale, E. ATV Jules Verne: A Step by Step Approach for In-Orbit Demonstration of New Rendezvous Technologies. Proceedings of the SpaceOps 2012, Stockholm, Sweden, 2012. https://doi.org/10.2514/6.2012-13

[18] Fabrega, J., Frezet, M., and Gonnaud, J.-L. ATV GNC During Rendezvous. In *3rd ESA International Conference on Spacecraft Guidance, Navigation and Control Systems*, No. ESA SP-381, 1997, pp. 85–93.

[19] Labourdette, P., Julien, E., Chemama, F., and Carbonne, D. ATV Jules Verne Mission Manoeuvre Plan. Proceedings of the International Symposium on Space Flight Dynamics, Toulouse, France, 2008.

[20] Skrobot, G. L., and Coelho, R. ELaNa - Educational Launch of Nanosatellite. Proceedings of the 26th Annual AIAA/USU Conference on Small Satellites, Logan, Utah, USA, 2012. https://digitalcommons.usu.edu/smallsat/2011/all2011/14/

[21] Roberts, J., and Hadaller, A. Behind the US's Largest Rideshare Launch: Spaceflight's SSO-A. Proceedings of the AIAA/USU Conference on Small Satellites, Logan, Utah, USA, 2019. https://digitalcommons.usu.edu/smallsat/2019/144/

[22] Schoneman, S., Roberts, J., Hadaller, A., Frego, T., Smithson, K., and Lund, E. SSO-A: The First Large Commercial Dedicated Rideshare Mission. Proceedings of the AIAA/USU Conference on Small Satellites, Logan, Utah, USA, 2018. https://digitalcommons.usu.edu/smallsat/2018/all2018/261/

[23] Kidder, S. Q., Kankiewicz, J. A., and Haar, T. H. V. The A-Train: How Formation Flying Is Transforming Remote Sensing. Proceedings of the Joint 2007 EUMETSAT Meteorological Satellite Conference and the 15th American Meteorological Society Satellite Meteorology and Oceanography Conference, Amsterdam, The Netherlands, 2007.

[24] Krieger, G., Moreira, A., Fiedler, H., Hajnsek, I., Werner, M., Younis, M., and Zink, M. "TanDEM-X: A Satellite Formation for High-Resolution SAR Interferometry." *IEEE Transactions on Geoscience and Remote Sensing*, Vol. 45, No. 11, 2007, pp. 3317–3341. https://doi.org/10.1109/TGRS.2007.900693.

[25] Gómez, G., Lo, M., Masdemont, J., and Museth, K. Simulation of Formation Flight Near L2 for the TPF Mission. Proceedings of the Space Flight and Mechanics Meeting, Santa Barbara, California, USA, 2001. https://hdl.handle.net/2014/16137

[26] Borde, J., Teston, F., Santandrea, S., and Boulade, S. Feasibility of the Proba 3 Formation Flying Demonstration Mission as a Pair of Microsats in GTO. In *4S Symposium: Small Satellites, Systems and Services*, No. ESA SP-571, La Rochelle, France, 2004.

[27] Fuselier, S. A., Lewis, W. S., Schiff, C., Ergun, R., Burch, J. L., Petrinec, S. M., and Trattner, K. J. "Magnetospheric Multiscale Science Mission Profile and Operations." *Space Science Reviews*, Vol. 199, Nos. 1–4, 2016, pp. 77–103. https://doi.org/10.1007/s11214-014-0087-x.

[28] Escoubet, C. P., Fehringer, M., and Goldstein, M. "The Cluster Mission." *Annales Geophysicae*, Vol. 19, No. 10/12, 2001, pp. 1197–1200. https://doi.org/10.5194/angeo-19-1197-2001.

[29] Warhaut, M., Matussi, S., and Ferri, P. "Cluster-II: Evolution of the Operations Concept." *ESA Bulletin*, Vol. 102, 2000, pp. 61–67.

[30] Escoubet, C. P. "Cluster-II: Scientific Objectives and Data Dissemination." *ESA Bulletin*, Vol. 102, 2000, pp. 54–60.

[31] Wauthier, P., Francken, P., and Laroche, H. Co-Location of Six ASTRA Satellites: Assessment after One Year of Operations. In *12th International Symposium on Space Flight Dynamics*, No. ESA SP-403, Darmstadt, Germany, 1997.

[32] Pyrak, M., and Anderson, J. Performance of Northrop Grumman's Mission Extension Vehicle (MEV) RPO Imagers at GEO. Proceedings of the Advanced Maui Optical and Space Surveillance Technologies Conference (AMOS), Maui, Hawaii, USA, 2021.

[33] Zuber, M. T., Smith, D. E., Asmar, S. W., Konopliv, A. S., Lemoine, F. G., Melosh, H. J., Neumann, G. A., Phillips, R. J., Solomon, S. C., Watkins, M. M., Wieczorek, M. A., Williams, J. G., Andrews-Hanna, J. C., Head, J. W., Kiefer, W. S., Matsuyama, I., McGovern, P. J., Nimmo, F., Taylor, G. J., Weber, R. C., Goossens, S. J., Kruizinga, G. L., Mazarico, E., Park, R. S., and Yuan, D.-N. Gravity Recovery and Interior Laboratory (GRAIL): Extended Mission and Endgame Status. Proceedings of the 44th Lunar and Planetary Science Conference, The Woodlands, Texas, USA, 2013.

[34] Scullion, E., Morton, R., Morgan, H., and Lin, H. Coronal Magnetism Explorer: ESA Solar Physics Mission White Paper. 2019.

[35] Larson, S. L. LISA: A Modern Astrophysical Observatory. Proceedings of the 33rd SLAC Summer Institute on Particle Physics: Gravity in the Quantum World and the Cosmos, Menlo Park, California, USA, 2005.

[36] Kelly, A. C., and Case, W. F. Constellation Operations - Lessons Learned for Future Exploration. Proceedings of the SpaceOps 2006 Conference, Rome, Italy, 2006. https://doi.org/10.2514/6.2006-5809

[37] Kirschner, M., Montenbruck, O., and D'Amico, S. Safe Switching of the Grace Formation Using an Eccentricity/Inclination Vector Separation. Proceedings of the 18th International Symposium on Space Flight Dynamics, Munich, Germany, 2004.

[38] Fridlund, C. V. M. "Darwin – The Infrared Space Interferometry Mission." *ESA Bulletin*, Vol. 103, 2000, pp. 20–25.

[39] Beichman, C., Gómez, G., Lo, M., Masdemont, J., and Romans, L. "Searching for Life with the Terrestrial Planet Finder: Lagrange Point Options for a Formation Flying Interferometer." *Advances in Space Research*, Vol. 34, No. 3, 2004, pp. 637–644. https://doi.org/10.1016/j.asr.2003.05.032.

[40] Quanz, S. P., Ottiger, M., Fontanet, E., Kammerer, J., Menti, F., Dannert, F., Gheorghe, A., Absil, O., Airapetian, V. S., Alei, E., Allart, R., Angerhausen, D., Blumenthal, S., Buchhave, L. A., Cabrera, J., Carrión-González, Ó., Chauvin, G., Danchi, W. C., Dandumont, C., Defrère, D., Dorn, C., Ehrenreich, D., Ertel, S., Fridlund, M., Muñoz, A. G., Gascón, C., Girard, J. H., Glauser, A., Grenfell, J. L., Guidi, G., Hagelberg, J., Helled, R.,

Ireland, M. J., Janson, M., Kopparapu, R. K., Korth, J., Kozakis, T., Kraus, S., Léger, A., Leedjärv, L., Lichtenberg, T., Lillo-Box, J., Linz, H., Liseau, R., Loicq, J., Mahendra, V., Malbet, F., Mathew, J., Mennesson, B., Meyer, M. R., Mishra, L., Molaverdikhani, K., Noack, L., Oza, A. V., Pallé, E., Parviainen, H., Quirrenbach, A., Rauer, H., Ribas, I., Rice, M., Romagnolo, A., Rugheimer, S., Schwieterman, E. W., Serabyn, E., Sharma, S., Stassun, K. G., Szulágyi, J., Wang, H. S., Wunderlich, F., Wyatt, M. C., and collaboration, the L. "Large Interferometer For Exoplanets (LIFE): I. Improved Exoplanet Detection Yield Estimates for a Large Mid-Infrared Space-Interferometer Mission." *arXiv:2101.07500 [astro-ph]*, 2022.

[41] Buinhas, L., Ferrer-Gil, E., and Forstner, R. IRASSI: InfraRed Astronomy Satellite Swarm Interferometry — Mission Concept and Description. Proceedings of the 2016 IEEE Aerospace Conference, Big Sky, MT, USA, 2016. https://doi.org/10.1109/AERO.2016.7500633

[42] Parmar, A. N., Arnaud, M., Barcons, X., Bleeker, J., Hasinger, G., Kunieda, H., Palumbo, G., Takahashi, T., Turner, M. J. L., de Korte, P., Willingale, R., Rando, N., Lyngvi, A., Gondoin, P., Lumb, D., Bavdaz, M., and Verhoeve, P. XEUS - The X-Ray Evolving Universe Spectroscopy Mission. In *SPIE Astronomical Telescopes + Instrumentation*, No. 6266, Orlando, Florida, USA, 2006. https://doi.org/10.1117/12.674336

[43] Ferrando, P., Arnaud, M., Briel, U., Citterio, O., Clédassou, R., Duchon, P., Fiore, F., Giommi, P., Goldwurm, A., Hasinger, G., Kendziorra, E., Laurent, P., Lebrun, F., Limousin, O., Malaguti, G., Mereghetti, S., Micela, G., Pareschi, G., Rio, Y., Roques, J. P., Strüder, L., and Tagliaferri, G. Simbol-X: Mission Overview. Proceedings of the SPIE Astronomical Telescopes + Instrumentation, Orlando, Florida, USA, 2006. https://doi.org/10.1117/12.673266

[44] D'Amico, S., and Montenbruck, O. "Proximity Operations of Formation-Flying Spacecraft Using an Eccentricity/Inclination Vector Separation." *Journal of Guidance, Control, and Dynamics*, Vol. 29, No. 3, 2006, pp. 554–563. https://doi.org/10.2514/1.15114.

[45] Berge, S., Jakobsson, B., Bodin, P., Edfors, A., and Persson, S. Rendezvous and Formation Flying Experiments Within the PRISMA In-Orbit Testbed. In *6th International ESA Conference on Guidance, Navigation and Control Systems*, No. ESA SP-606, Loutraki, Greece.

[46] Telaar, J., Ahrns, I., Estable, S., Rackl, W., De Stefano, M., Lampariello, R., Santos, N., Serra, P., Canetri, M., Ankersen, F., and Gil Fernandez, J. GNC Architecture for the e.Deorbit Mission. Proceedings of the 7th European Conference for Aeronautics and Space Sciences (EUCASS), Milan, Italy, 2017. https://doi.org/10.13009/EUCASS2017-317

[47] Sharifi, M. A., Sneeuw, N., and Keller, W. "Gravity Recovery Capability of Four Generic Satellite Formations." *Gravity Field of the Earth. General Command of Mapping*, No. special issue 18, pp. 211–216.

[48] Peters, T. V., Branco, J., Escorial, D., Tarabini Castellani, L., and Cropp, A. Mission Analysis for Proba-3 Nominal Operations. Proceedings of the 7th International Workshop on Satellite Constellations and Formation Flying, Lisbon, Portugal, 2013.

[49] Gaias, G., Ardaens, J.-S., and Schultz, C. The AVANTI Experiment: Flight Results. Proceedings of the 10th International ESA Conference on Guidance, Navigation & Control Systems, Salzburg, Austria, 2017.

[50] Nogueira, T., Scharnagl, J., Kotsiaros, S., and Schilling, K. NetSat-4G A Four Nano-Satellite Formation for Global Geomagnetic Gradiometry. Proceedings of the 10th IAA Symposium on Small Satellites for Earth Observation, Berlin, Germany, 2015.

[51] Schilling, K. TIM: A Small Satellite Formation for Joint 3D Earth Observation. Proceedings of the 9th International Workshop on Satellite Constellations and Formation Flying, Boulder, Colorado, USA, 2017.

[52] Roth, N. H., Risi, B., Grant, C. C., and Zee, R. E. Flight Results from the CanX-4 and CanX-5 Formation Flying Mission. In *Small Satellites, Systems & Services Symposium (4S)*, No. 30, Valetta, Malta, 2016.

[53] Gangestad, J. W., Venturini, C. C., Hinkley, D. A., and Kinum, G. A Sat-to-Sat Inspection Demonstration with the AeroCube-10 1.5U CubeSats. Proceedings of the Small Satellite Conference, Logan, Utah, USA, 2021. https://digitalcommons.usu.edu/smallsat/2021/all2021/134/

[54] Sarda, K., CaJacob, D., Orr, N., and Zee, R. Making the Invisible Visible: Precision RF-Emitter Geolocation from Space by the HawkEye 360 Pathfinder Mission. Proceedings of the Small Satellite Conference, Logan, Utah, USA, 2018. https://digitalcommons.usu.edu/smallsat/2018/all2018/263/

[55] Roscoe, C. W. T., Westphal, J. J., and Mosleh, E. "Overview and GNC Design of the CubeSat Proximity Operations Demonstration (CPOD) Mission." *Acta Astronautica*, Vol. 153, 2018, pp. 410–421. https://doi.org/10.1016/j.actaastro.2018.03.033.

[56] D'Amico, S., Koenig, A., Macintosh, B., and Mall, S. System Design of the Miniaturized Distributed Occulter/Telescope (MDOT) Science Mission. Proceedings of the Small Satellites Conference, Logan, Utah, USA, 2019. https://digitalcommons.usu.edu/smallsat/2019/all2019/81/

[57] Koenig, A. W., D'Amico, S., and Lightsey, E. G. Formation Flying Orbit and Control Concept for the VISORS Mission. Virtual Event. Proceedings of the AIAA Scitech 2021 Forum, 2021. https://doi.org/10.2514/6.2021-0423

[58] Agarwal, R., Oh, B., Fitzpatrick, D., Buynovskiy, A., Lowe, S., Lisy, C., Kriezis, A., Lan, B., Lee, Z., Thomas, A., Wallace, B., Costantino, E., Miner, G., Thayer, J., D'Amico, S., Lemmer, K., Lohmeyer, W., and Palo, S. Coordinating Development of the SWARM-EX CubeSat Swarm Across Multiple Institutions. Proceedings of the Small Satellite Conference, Logan, Utah, USA, 2021. https://digitalcommons.usu.edu/smallsat/2021/all2021/230/

[59] Sanchez, H., Mcintosh, D., Cannon, H., Pires, C., Sullivan, J., D'Amico, S., O'Connor, B., Starling1: Swarm Technology Demonstration. Proceedings of the Small Satellites Conference, Logan, Utah, USA, 2018. https://digitalcommons.usu.edu/smallsat/2018/all2018/299/

[60] Gaias, G., Ardaens, J.-S., and Montenbruck, O. "Model of J2 Perturbed Satellite Relative Motion with Time-Varying Differential Drag." *Celestial Mechanics and Dynamical Astronomy*, Vol. 123, No. 4, 2015, pp. 411–433. https://doi.org/10.1007/s10569-015-9643-2.

[61] Ardaens, J.-S., and Gaias, G. Angles-Only Relative Orbit Determination during the AVANTI Experiment. Proceedings of the 26th International Symposium on Space Flight Dynamics (ISSFD), Matsuyama, Japan, 2017.

[62] Gaias, G., and Ardaens, J.-S. "In-Orbit Experience and Lessons Learned from the AVANTI Experiment." *Acta Astronautica*, Vol. 153, 2018, pp. 383–393. https://doi.org/10.1016/j.actaastro.2018.01.042.

[63] Koenig, A. W., Guffanti, T., and D'Amico, S. "New State Transition Matrices for Spacecraft Relative Motion in Perturbed Orbits." *Journal of Guidance, Control, and Dynamics*, Vol. 40, No. 7, 2017, pp. 1749–1768. https://doi.org/10.2514/1.G002409.

[64] Park, J.-P., Park, S., Lee, K., Oh, H. J., Choi, K. Y., Song, Y. B., Yim, J.-C., Lee, E., Hwang, S.-H., Kim, S., Kang, S. J., Kim, M.-S., Jin, S., Lee, S. H., Kwon, S. H., Lee, D. S., Cho, W.-H., Park, J.-H., Yeo, S.-W., Seo, J.-W., Lee, K. B., Lee, S., Yang, J.-H., Kim, G. nam, Lee, J., Kim, Y. W., and Kim, T.-H. Mission Analysis and CubeSat Design for CANYVAL-X Mission. Proceedings of the SpaceOps 2016 Conference, Daejeon, Korea, 2016. https://doi.org/10.2514/6.2016-2493

[65] Kim, G.-N., Park, S.-Y., Lee, T., Kang, D.-E., Jeon, S., Son, J., Kim, N., Park, Y.-K., and Song, Y. "Development of CubeSat Systems in Formation Flying for the Solar Science Demonstration: The CANYVAL-C Mission." *Advances in Space Research*, Vol. 68, No. 11, 2021, pp. 4434–4455. https://doi.org/10.1016/j.asr.2021.09.021.

[66] Tacconi, L. J. (chair). *Voyage 2050 Final Recommendations from the Voyage 2050 Senior Committee*. European Space Agency, 2021.

[67] Krizmanic, J., Shah, N., Calhoun, P. C., Harding, A. K., Purves, L. R., Webster, C. M., Corcoran, M. F., Schrader, C. R., Stochaj, S. J., Rankin, K. A., Smith, D. T., Kota, K., Park, H., Boucheron, L. E., and Nasari, A. VTXO: The Virtual Telescope for x-Ray Observations. Virtual Event. Proceedings of the Space Telescopes and Instrumentation 2020: Ultraviolet to Gamma Ray, United States, 2020. https://doi.org/10.1117/12.2562714

[68] Ikari, S., Kondo, H., Nakasuka, S., and Matsuo, T. SEIRIOS: A Demonstration of Space Infrared Interferometer by Formation Flying of Micro-Satellites. Proceedings of the Small Satellite Conference, Logan, Utah, USA, 2021. https://digitalcommons.usu.edu/smallsat/2021/all2021/252/

[69] Carter, T. E. "State Transition Matrices for Terminal Rendezvous Studies: Brief Survey and New Example." *Journal of Guidance, Control, and Dynamics*, Vol. 21, No. 1, 1998, pp. 148–155. https://doi.org/10.2514/2.4211.

[70] Stern, R. G. *Interplanetary Midcourse Guidance Analysis*. Sc. D. Thesis. Massachusetts Institute of Technology, Cambridge, Massachusetts, USA, 1963.

[71] Alfriend, K. T., and Yan, H. "Evaluation and Comparison of Relative Motion Theories." *Journal of Guidance, Control, and Dynamics*, Vol. 28, No. 2, 2005, pp. 254–261. https://doi.org/10.2514/1.6691.

[72] Gim, D.-W., and Alfriend, K. T. "State Transition Matrix of Relative Motion for the Perturbed Noncircular Reference Orbit." *AIAA Journal of Guidance, Control and Dynamics*, Vol. 26, No. 6, 2003, pp. 956–971. https://doi.org/10.2514/2.6924.

[73] Brouwer, D. "Solution of the Problem of Artificial Satellite Theory Without Drag." *Astronomical Journal*, Vol. 64, 1959, pp. 378–397. https://doi.org/10.1086/107958

[74] Brouwer, D., and Clemence, G. M. *Methods of Celestial Mechanics*. Academic Press, New York, NY, USA, 1961. ISBN 978-1-4832-0075-0

[75] Sullivan, J., Grimberg, S., and D'Amico, S. "Comprehensive Survey and Assessment of Spacecraft Relative Motion Dynamics Models." *Journal of Guidance, Control, and Dynamics*, Vol. 40, No. 8, 2017, pp. 1837–1859. https://doi.org/10.2514/1.G002309.

[76] Gaias, G., and Colombo, C. Semi-Analytical Framework for Precise Relative Motion in Low Earth Orbits. Proceedings of the 7th International Conference on Astrodynamics Tools and Techniques (ICATT), Oberpfaffenhofen, Germany, 2018.

[77] Gaias, G., Lara, M., and Colombo, C. Accurate Osculating/Mean Orbital Elements Conversions for Spaceborne Formation Flying. Proceedings of the 27th International Symposium on Space Flight Dynamics (ISSFD), Melbourne, Australia, 2018.

[78] Gaias, G., Ardaens, J.-S., and Colombo, C. "Precise Line-of-Sight Modelling for Angles-Only Relative Navigation." *Advances in Space Research*, Vol. 67, No. 11, 2021, pp. 3515–3526. https://doi.org/10.1016/j.asr.2020.05.048.

[79] Chihabi, Y., and Ulrich, S. "Analytical Spacecraft Relative Dynamics with Gravitational, Drag and Third-Body Perturbations." *Acta Astronautica*, Vol. 185, 2021, pp. 42–57. https://doi.org/10.1016/j.actaastro.2021.04.043.

[80] Chihabi, Y., and Ulrich, S. Spacecraft Formation Guidance Law Using a State Transition Matrix with Gravitational, Drag and Third-Body Perturbations. Proceedings of the AIAA Scitech 2020 Forum, Orlando, FL, USA, 2020. https://doi.org/10.2514/6.2020-1460

[81] D'Amico, S., and Carpenter, J. R. Satellite Formation Flying and Rendezvous. In *Position, Navigation, and Timing Technologies in the 21st Century* (Y. T. J. Morton, F. Diggelen, J. J. Spilker, B. W. Parkinson, S. Lo, and G. Gao, eds.), Wiley, 2020, pp. 1921–1946. https://doi.org/10.1002/9781119458555.ch63

[82] Woffinden, D. C., and Geller, D. K. "Observability Criteria for Angles-Only Navigation." *IEEE Transactions on Aerospace and Electronic Systems*, Vol. 45, No. 3, 2009, pp. 1194–1208. https://doi.org/10.1109/TAES.2009.5259193.

[83] Grzymisch, J., and Fichter, W. "Analytic Optimal Observability Maneuvers for In-Orbit Bearings-Only Rendezvous." *Journal of Guidance, Control, and Dynamics*, Vol. 37, No. 5, 2014, pp. 1658–1664. https://doi.org/10.2514/1.G000612.

[84] Geller, D. K., and Klein, I. "Angles-Only Navigation State Observability During Orbital Proximity Operations." *Journal of Guidance, Control, and Dynamics*, Vol. 37, No. 6, 2014, pp. 1976–1983. https://doi.org/10.2514/1.G000133.

[85] Sullivan, J., Koenig, A. W., and D'Amico, S. Improved Maneuver-Free Approach to Angles-Only Navigation for Space Rendezvous. AAS 16-530. Proceedings of the 26th AAS/AIAA Space Flight Mechanics Meeting, Napa, CA, USA, 2016.

[86] Kruger, J., and D'Amico, S. "Autonomous Angles-Only Multi-Target Tracking for Spacecraft Swarms." *Acta Astronautica*, Vol. 189, 2021, pp. 514–529. https://doi.org/10.1016/j.actaastro.2021.08.049.

[87] Kruger, J., Wallace, K., Koenig, A. W., and D'Amico, S. Autonomous Multi-Observer Angles-Only Navigation for Spacecraft Swarms around Planetary Bodies. Proceedings of the 2021 IEEE Aerospace Conference (50100), Big Sky, MT, USA, 2021. https://doi.org/AERO50100.2021.9438363

[88] Koenig, A. W., Kruger, J., Sullivan, J., and D'Amico, S. ARTMS: Enabling Autonomous Distributed Angles-Only Orbit Estimation for Spacecraft Swarms.

Proceedings of the 2021 American Control Conference (ACC), New Orleans, LA, USA, 2021. https://doi.org/10.23919/ACC50511.2021.9483242

[89] Roscoe, C. W. T., Westphal, J. J., Griesbach, J. D., and Schaub, H. "Formation Establishment and Reconfiguration Using Differential Elements in J2-Perturbed Orbits." *Journal of Guidance, Control, and Dynamics*, Vol. 38, No. 9, 2015, pp. 1725–1740. https://doi.org/10.2514/1.G000999.

[90] Sengupta, P., and Vadali, S. R. "Analytical Solution for Power-Limited Optimal Rendezvous near an Elliptic Orbit." *Journal of Optimization Theory and Applications*, Vol. 138, No. 1, 2008, pp. 115–137. https://doi.org/10.1007/s10957-008-9369-3.

[91] Cho, H.-C., and Park, S.-Y. "Analytic Solution for Fuel-Optimal Reconfiguration in Relative Motion." *Journal of Optimization Theory and Applications*, Vol. 141, No. 3, 2009, pp. 495–512. https://doi.org/10.1007/s10957-008-9482-3.

[92] Cho, H.-C., Park, S.-Y., and Choi, K.-H. "Application of Analytic Solution in Relative Motion to Spacecraft Formation Flying in Elliptic Orbit." *Journal of Astronomy and Space Sciences*, Vol. 25, No. 3, 2008, pp. 255–266. https://doi.org/10.5140/JASS.2008.25.3.255.

[93] Lawden, D. F. *Optimal Trajectories for Space Navigation*. Butterworth and Co, 1963.

[94] Prussing, J. E. "Optimal Two- and Three-Impulse Fixed-Time Rendezvous in the Vicinity of a Circular Orbit." *Journal of Spacecraft and Rockets*, Vol. 40, No. 6, 1970, pp. 952–959. https://doi.org/10.2514/2.7041.

[95] Prussing, J. E. "Optimal Four-Impulse Fixed-Time Rendezvous in the Vicinity of a Circular Orbit." *AIAA Journal*, Vol. 7, No. 5, 1969, pp. 928–935. https://doi.org/10.2514/3.5246.

[96] Prussing, J. E., and Chiu, J.-H. "Optimal Multiple-Impulse Time-Fixed Rendezvous between Circular Orbits." *Journal of Guidance, Control, and Dynamics*, Vol. 9, No. 1, 1986, pp. 17–22. https://doi.org/10.2514/3.20060.

[97] Jezewski, D. J., and Rozendaal, H. L. "An Efficient Method for Calculating Optimal Free-Space n-Impulse Trajectories." *AIAA Journal*, Vol. 6, No. 11, 1968, pp. 2160–2165. https://doi.org/10.2514/3.4949.

[98] Lion, P. M., and Handelsman, M. "Primer Vector on Fixed-Time Impulsive Trajectories." *AIAA Journal*, Vol. 6, No. 1, 1968, pp. 127–132. https://doi.org/10.2514/3.4452.

[99] Betts, J. T. *Practical Methods for Optimal Control and Estimation Using Nonlinear Programming*. Society for Industrial and Applied Mathematics, 2010. https://doi.org/10.1137/1.9780898718577

[100] Conway, B. *Spacecraft Trajectory Optimization*. Cambridge University Press, 2014. https://doi.org/10.1017/CBO9780511778025

[101] Anderson, P. V., and Schaub, H. "N-Impulse Formation Flying Feedback Control Using Nonsingular Element Description." *Journal of Guidance, Control, and Dynamics*, Vol. 37, No. 2, 2014, pp. 540–548. https://doi.org/10.2514/1.60766.

[102] Gaias, G., D'Amico, S., and Ardaens, J. S. "Generalised Multi-Impulsive Manoeuvres for Optimum Spacecraft Rendezvous in near-Circular Orbit." *International Journal of Space Science and Engineering*, Vol. 3, No. 1, 2015, p. 68. https://doi.org/10.1504/IJSPACESE.2015.069361.

[103] Gaias, G., and D'Amico, S. "Impulsive Maneuvers for Formation Reconfiguration Using Relative Orbital Elements." *Journal of Guidance, Control, and Dynamics*, Vol. 38, No. 6, 2015, pp. 1036–1049. https://doi.org/10.2514/1.G000189.

[104] Koenig, A. W., and D'Amico, S. "Fast Algorithm for Fuel-Optimal Impulsive Control of Linear Systems with Time-Varying Cost." *IEEE Transactions on Automatic Control*, Vol. 66, No. 9, 2021, pp. 4029–4042. https://doi.org/10.1109/TAC.2020.3027804.

[105] Neustadt, L. W. "Optimization, a Moment Problem, and Nonlinear Programming." *Journal of the Society for Industrial and Applied Mathematics Series A Control*, Vol. 2, No. 1, 1964, pp. 33–53. https://doi.org/10.1137/0302004.

[106] Neustadt, L. W. "A General Theory of Minimum-Fuel Space Trajectories." *Journal of the Society for Industrial and Applied Mathematics Series A Control*, Vol. 3, No. 2, 1965, pp. 317–356. https://doi.org/10.1137/0303023.

[107] Barr, R., and Gilbert, E. "Some Efficient Algorithms for a Class of Abstract Optimization Problems Arising in Optimal Control." *IEEE Transactions on Automatic Control*, Vol. 14, No. 6, 1969, pp. 640–652. https://doi.org/10.1109/TAC.1969.1099299.

[108] Gilbert, E., and Harasty, G. "A Class of Fixed-Time Fuel-Optimal Impulsive Control Problems and an Efficient Algorithm for Their Solution." *IEEE Transactions on Automatic Control*, Vol. 16, No. 1, 1971, pp. 1–11. https://doi.org/10.1109/TAC.1971.1099656.

[109] Arzelier, D., Bréhard, F., Deak, N., Joldes, M., Louembet, C., Rondepierre, A., and Serra, R. "Linearized Impulsive Fixed-Time Fuel-Optimal Space Rendezvous: A New Numerical Approach." *IFAC-PapersOnLine*, Vol. 49, No. 17, 2016, pp. 373–378. https://doi.org/10.1016/j.ifacol.2016.09.064.

[110] Eyer, J. K. *A Dynamics and Control Algorithm for Low Earth Orbit Precision Formation Flying Satellites*. University of Toronto, Toronto, Canada, 2009. https//hdl.handle.net/1807/19186

[111] Newman, J. Z. *Drift Recovery and Station Keeping for the CanX-4 & CanX-5 Nanosatellite Formation Flying Mission*. University of Toronto, Toronto, Canada, 2015.

[112] Chernick, M., and D'Amico, S. "New Closed-Form Solutions for Optimal Impulsive Control of Spacecraft Relative Motion." *Journal of Guidance, Control, and Dynamics*, Vol. 41, No. 2, pp. 301–319. https://doi.org/10.2514/1.G002848.

[113] Chernick, M., and D'Amico, S. Closed-Form Optimal Impulsive Control of Spacecraft Formations Using Reachable Set Theory. Proceedings of the 2018 AAS/AIAA Astrodynamics Specialist Conference, Snowbird, UT, USA, 2018. https://doi.org/10.2514/1.G005218

[114] D'Amico, S. *Relative Orbital Elements as Integration Constants of Hill's Equations*. Publication DLR TN 05-08. Deutsches Zentrum für Luft- und Raumfahrt, Oberpfaffenhofen, Germany, 2005.

[115] Danby, J. M. A. Perturbations. In *Fundamentals of Celestial Mechanics*, Willmann-Bell, Richmond, VA, USA, 1988, pp. 315–369. ISBN: 978-0943396200

[116] Breger, L., and How, J. P. "Gauss's Variational Equation-Based Dynamics and Control for Formation Flying Spacecraft." *Journal of Guidance, Control, and Dynamics*, Vol. 30, No. 2, 2007, pp. 437–448. https://doi.org/10.2514/1.22649.

[117] Carril, P. PROBA-3 Formation-Flying. ESA, 2013. https://www.esa.int/ESA_Multimedia/Images/2011/04/Proba-3_formation-flying

[118] PROBA-3 Takes Important Step in the Integration of Its Satellites. SENER, Jan, 2022. https://www.group.sener/noticias/proba-3-program-takes-important-step-integration-two-satellites

[119] Banks, M., and Mestreau-Garreau, A. Millimetric Precision for Flying Satellites. Horizon Magazine, Jun, 2013. https://ec.europa.eu/research-and-innovation/en/horizon-magazine/millimetric-precision-flying-satellites

[120] Dyson, M. J. *Space and Astronomy*. Facts on File, New York, 2007. ISBN 978-0816055364

[121] Lyons, D. Elliptical Parking Orbits for Mars Sample Return. Proceedings of the AIAA / AAS Astrodynamics Specialist Conference and Exhibit, Honolulu, HI, USA, 2008. https://doi.org/10.2514/6.2008-6423

[122] Peters, T. V., and Strippoli, L. Guidance for Elliptic Orbit Rendezvous, AAS 10-175. Proceedings of the 20th AAS/AIAA Spaceflight Mechanics Meeting, San Diego, CA, USA, 2010.

[123] Pons, A. P. *GTO Debris Mitigation Using Natural Perturbations*. Delft University of Technology, Delft, The Netherlands, 2017. http://resolver.tudelft.nl/uuid:f550d59a-7d15-46dd-a084-025ace46e643

[124] Pinardell Pons, A., and Noomen, R. "Ariane 5 GTO Debris Mitigation Using Natural Perturbations." *Advances in Space Research*, Vol. 63, No. 7, 2019, pp. 1992–2002. https://doi.org/10.1016/j.asr.2018.12.001.

[125] Montenbruck, O., Kirschner, M., D'Amico, S., and Bettadpur, S. "E/I-Vector Separation for Safe Switching of the GRACE Formation." *Aerospace Science and Technology*, Vol. 10, No. 7, 2006, pp. 628–635. https://doi.org/10.1016/j.ast.2006.04.001.

[126] Woffinden, D. C., and Geller, D. K. "Relative Angles-Only Navigation and Pose Estimation for Autonomous Orbital Rendezvous." *Journal of Guidance, Control, and Dynamics*, Vol. 30, No. 5, 2007, pp. 1455–1469. https://doi.org/10.2514/1.28216.

[127] Gaias, G., and D'Amico, S. "Angles-Only Navigation to a Noncooperative Satellite Using Relative Orbital Elements." *Journal of Guidance, Control, and Dynamics*, Vol. 37, No. 2, 2014, pp. 439–451. https://doi.org/10.2514/1.61494.

[128] Lovell, T. A. and Lee, T. Nonlinear Observability for Relative Satellite Orbits with Angles-Only Measurements. Proceedings of the 24th International Symposium on Space Flight Dynamics, Laurel, Maryland, USA, 2014.

[129] Montenbruck, O., and Gill, E. Introductory Astrodynamics. In *Satellite Orbits – Models, Methods, and Applications*, Springer-Verlag, Berlin Heidelberg, Germany, 2000, pp. 15–51. https://doi.org/10.1007/978-3-642-58351-3

[130] Bate, R. R., Mueller, D. D., and White, J. E. Orbit Determination from Observation. In *Fundamentals of Astrodynamics*, Dover Publications, 1971, pp. 51–150. ISBN: 978-0486600611

[131] Legendre, P., Deguine, B., Garmier, R., and Revelin, B. Two Line Element Accuracy Assessment Based on a Mixture of Gaussian Laws. Proceedings of the AIAA/AAS Astrodynamics Specialist Conference and Exhibit, Guidance, Navigation, and Control and Co-located Conferences, Keystone, Colorado, USA, 2006. https://doi.org/10.2514/6.2006-6518

[132] D'Amico, S., Ardaens, J.-S., Gaias, G., Benninghoff, H., Schlepp, B., and Jørgensen, J. L. "Noncooperative Rendezvous Using Angles-Only Optical Navigation: System Design and Flight Results." *Journal of Guidance, Control, and Dynamics*, Vol. 36, No. 6, 2013, pp. 1576–1595. https://doi.org/10.2514/1.59236.

[133] Peters, T. V., and Escorial Olmos, D. "Relative Mission Analysis for Proba-3: Safe Orbits and CAM." *Int. J. of Space Science and Engineering*, Vol. 2, No. 2, 2014, pp. 135–156. https://doi.org/10.1504/IJSPACESE.2014.060599.

[134] Fehse, W. Orbit Dynamics and Trajectory Elements. In *Automated Rendezvous and Docking of Spacecraft*, Cambridge University Press, Cambridge, UK, 2003, pp. 29–75. ISBN 978-0-521-82492-7

[135] Gaias, G., and Ardaens, J.-S. "Flight Demonstration of Autonomous Noncooperative Rendezvous in Low Earth Orbit." *Journal of Guidance, Control, and Dynamics*, Vol. 41, No. 6, 2018, pp. 1337–1354. https://doi.org/10.2514/1.G003239.

[136] Wen, W. L.-S. "A Study of Cotangential, Elliptical Transfer Orbits in Space Flight." *Journal of the Aerospace Sciences*, Vol. 28, No. 5, 1961, pp. 411–417. https://doi.org/10.2514/8.9010.

[137] Zhang, G., Zhou, D., Mortari, D., and Henderson, T. A. "Analytical Study of Tangent Orbit and Conditions for Its Solution Existence" *AIAA Journal of Guidance, Control, and Dynamics*, Vol. 35, No. 1, 2012, pp. 186–194. https://doi.org/10.2514/1.53396.

[138] Doll, J. R., and Gobetz, F. W. "A Survey of Impulsive Trajectories." *AIAA Journal*, Vol. 7, No. 5, 1969, pp. 801–834. https://doi.org/10.2514/3.5231.

[139] Moyer, H. G. "An Analytic Treatment of Cotangential Transfer." *AIAA Journal*, Vol. 5, No. 6, 1967, pp. 1197–1198. https://doi.org/10.2514/3.4164.

[140] Bender, D. F. "Optimum coplanar two-impulse transfers between elliptic orbits." *Aerospace Engineering*, Vol. 21, 1962, pp. 44–52.

[141] Burns, R. E. "Forbidden tangential orbit transfers between intersecting Keplerian orbits." *Acta Astronautica*, Vol. 19, No. 8, 1989, pp. 649-656,. https://doi.org/10.1016/0094-5765(89)90133-1.

[142] Zhang, G., Wang, D., Cao, X., and Sun, Z. "Tangent Orbital Rendezvous Using Linear Relative Motion with J2 Perturbations." *Mathematical Problems in Engineering*, Vol. 2013, 2013. https://doi.org/10.1155/2013/531672.

[143] Peters, T. V., and Strippoli, L. Innovative Guidance Techniques for Rendezvous on Elliptic Orbits. In *4th International Conference on Astrodynamics Tools and Techniques*, No. 3–6, ESAC, Madrid, Spain, 2010.

[144] Yin, J., and Han, C. "Elliptical formation control based on relative orbit elements." *Chinese Journal of Aeronautics*, Vol. 26, No. 6, 2013, pp. 1554–1567. https://doi.org/10.1016/j.cja.2013.07.014.

[145] Yamanaka, K., and Ankersen, F. “New State Transition Matrix for Relative Motion on an Arbitrary Elliptical Orbit.” *Journal of Guidance, Control, and Dynamics*, Vol. 25, No. 1, 2002, pp. 60–66. https://doi.org/10.2514/2.4875.

[146] Montenbruck, O., and Gill, E. Linearization. In *Satellite Orbits – Models, Methods, and Applications*, Springer-Verlag, Berlin Heidelberg, Germany, 2000, pp. 233–256. https://doi.org/10.1007/978-3-642-58351-3

[147] Schaub, H., and Junkins, J. L. Spacecraft Formation Flying. In *Analytical Mechanics of Space Systems*, AIAA, Reston VA, USA, 2003, pp. 593–674. https://doi.org/10.2514/4.861550

[148] Sullivan, J., and D’Amico, S. “Nonlinear Kalman Filtering for Improved Angles-Only Navigation Using Relative Orbital Elements.” *Journal of Guidance, Control, and Dynamics*, Vol. 40, No. 9, 2017, pp. 2183–2200. https://doi.org/10.2514/1.G002719.

[149] Clohessy, W. H., and Wiltshire, R. S. “Terminal Guidance System for Satellite Rendezvous.” *Journal of Aerospace Sciences*, Vol. 27, 1960, pp. 653–658. https://doi.org/10.2514/8.8704.

[150] Arsenault, J. L., Ford, K. C., and Koskela, P. E. “Orbit Determination Using Analytic Partial Derivatives of Perturbed Motion.” *AIAA Journal*, Vol. 8, No. 1, 1970, pp. 4–12. https://doi.org/10.2514/3.5597.

[151] Alfriend, K. T., Vadali, S. R., Gurfil, P., How, J. P., and Breger, L. Linear Equations of Relative Motion. In *Spacecraft Formation Flying: Dynamics, Control and Navigation*, Elsevier, Oxford, 2010, pp. 83–121. https://doi.org/10.1016/C2009-0-17485-8

[152] Lara, M., and Gurfil, P. “Integrable Approximation of J2-Perturbed Relative Orbits.” *Celestial Mechanics and Dynamical Astronomy*, Vol. 114, No. 3, 2012, pp. 229–254. https://doi.org/10.1007/s10569-012-9437-8.

[153] Ben-Yaacov, O., and Gurfil, P. “Long-Term Cluster Flight of Multiple Satellites Using Differential Drag.” *Journal of Guidance Control Dynamics*, Vol. 36, No. 6, 2013, pp. 1731–1740. https://doi.org/10.2514/1.61496.

[154] Fehse, W. Approach Safety and Collision Avoidance. In *Automated Rendezvous and Docking of Spacecraft*, Cambridge University Press, Cambridge, UK, 2003, pp. 76–107. ISBN 978-0-521-82492-7

[155] Peters, T. V., Noomen, R., and Colmenarejo, P. “Analytical Solutions to Two-Impulse Nondrifting Transfer Problems for Rendezvous in Elliptical Orbits.” *Journal of Guidance, Control, and Dynamics*, Vol. 37, No. 3, 2014, pp. 775–788. https://doi.org/10.2514/1.61885.

[156] Battin, R. H. Variation of Parameters. In *An Introduction to the Mathematics and Methods of Astrodynamics*, AIAA, 1999, pp. 471–514. https://doi.org/10.2514/4.861543

[157] Riggi, L., and D'Amico, S. Optimal Impulsive Closed-Form Control for Spacecraft Formation Flying and Rendezvous. Proceedings of the 2016 American Control Conference, Boston, MA, USA, 2016. https://doi.org/10.1109/ACC.2016.7526587

[158] Zhang, G., Zhou, D., Sun, Z., and Cao, X. "Optimal Two-Impulse Cotangent Rendezvous Between Coplanar Elliptical Orbits." *Journal of Guidance, Control, and Dynamics*, Vol. 36, No. 3, 2013, pp. 677–685. https://doi.org/10.2514/1.59191.

[159] Battin, R. H. Two-Body Orbital Boundary-Value Problem. In *An Introduction to the Mathematics and Methods of Astrodynamics*, AIAA, 1999, pp. 237–294. https://doi.org/10.2514/4.861543

[160] Strippoli, L., Novelli, G., Gil Fernandez, J., Colmenarejo, P., Le Peuvedic, C., Lanza, P., and Ankersen, F. "Integrated Vision-Based GNC for Autonomous Rendezvous and Capture around Mars." *CEAS Space Journal*, Vol. 7, 2015, pp. 143–157. https://doi.org/10.1007/s12567-015-0090-4.

[161] Chao, C.-C. Advanced Concepts of Orbit Control. In *Applied Orbit Perturbation and Maintenance*, American Institute of Aeronautics and Astronautics, Inc., 2005. https://doi.org/10.2514/4.989179

[162] De Florio, S., D'Amico, S., and Radice, G. "Flight Results of Precise Autonomous Orbit Keeping Experiment on PRISMA Mission." *Journal of Spacecraft and Rockets*, Vol. 50, No. 3, 2013, pp. 662–674. https://doi.org/10.2514/1.A32347.

[163] Montenbruck, O., Kahle, R., D'Amico, S., and Ardaens, J.-S. "Navigation and Control of the TanDEM-X Formation." *Journal of the Astronautical Sciences*, Vol. 56, No. 3, 2008, pp. 341–357. https://doi.org/10.1007/BF03256557.

[164] Jiang, F., Li, J., Baoyin, H., and Gao, Y. "Study on Relative Orbit Geometry of Spacecraft Formations in Elliptical Reference Orbits." *AIAA Journal of Guidance, Control, and Dynamics*, Vol. 31, No. 1, 2008, pp. 123–134. https://doi.org/10.2514/1.30394.

[165] Dang, Z., Wang, Z., and Zhang, Y. "Modeling and Analysis of the Bounds of Periodical Satellite Relative Motion." *Journal of Guidance, Control, and Dynamics*, Vol. 37, No. 6, 2014, pp. 1984–1998. https://doi.org/10.2514/1.G000259.

[166] Dang, Z., Li, T., Wang, Z., and Zhang, Y. "Bounds on Maximal and Minimal Distances for Coplanar Satellite Relative Motion under given Initial Conditions." *Aerospace Science and Technology*, No. 46, 2015, pp. 204–209. https://doi.org/10.1016/j.ast.2015.07.012.

[167] Whipple, P. H. Some Characteristics of Coelliptic Orbits – Case 610. NASA-CR-109655, Bellcom Inc, NASA, Washington, D.C., USA 1970.

[168] Fehse, W. Appendix A: Motion Dynamics. In *Automated Rendezvous and Docking of Spacecraft*, Cambridge University Press, Cambridge, UK, 2003, pp. 424–440. ISBN 978-0-521-82492-7

[169] Sotto, E., Bastante, J. C., and Drai, R. Guidance Algorithms for Non-Drifting Trajectory Generation and Control in RendezVous Missions into Elliptical Orbits. Proceedings of the 20th International Symposium on Space Flight Dynamics, Annapolis, MD, USA, 2007.

[170] Kaiser, C., Rank, P., Krenn, R., and Landzettel, K. Simulation of the Docking Phase for the SMART-OLEV Satellite Servicing Mission. Proceedings of the 9th International Symposium on Artificial Intelligence, Robotics and Automation for Space (iSAIRAS), Pasadena, CA, USA, 2008.

[171] Mattingly, R. L. The Many Faces of the Mars Sample Return Mission Architecture. Proceedings of the 28th Annual AAS Guidance and Control Conference, Breckenridge, CO, USA, 2005. https://hdl.handle.net/2014/37530

[172] Wingo, D. R. Orbital Recovery's Responsive Commercial Space Tug for Life Extension Missions. Proceedings of the Space 2004 Conference and Exhibit, San Diego, CA, USA, 2004. https://doi.org/10.2514/6.2004-6118

[173] Sullivan, B. R. Introduction. In *Technical and Economic Feasibility of Telerobotic On-Orbit Satellite Servicing*, University of Maryland, College Park, MD, USA, 2005, pp. 1–9. https://ssl.umd.edu/node/86

[174] Wolfsberger, W., Weiß, J., and Rangnitt, D. "Strategies and Schemes for Rendezvous on Geostationary Transfer Orbit." *Acta Astronautica*, Vol. 10, No. 8, 1983, pp. 527–538. https://doi.org/10.1016/0094-5765(83)90051-6.

[175] Kimura, S., Nagai, Y., Yamamoto, H., Kozawa, H., Sugimoto, S., Nakamura, S., Masuda, K., and Abe, N. Rendezvous Experiments on SmartSat-1. Proceedings of the 2nd IEEE International Conference on Space Mission Challenges for Information Technology, Pasadena, CA, USA, 2006. https://doi.org/10.1109/SMC-IT.2006.65

[176] Sjoberg, F., Jakobsson, B., Negueruela, C., Karlsson, A., Pokrupa, N., Sallander, E., Crowe, B., Burger, F., Tarabini-Castellani, L., Teston, F., and Llorente-Martınez, S. High Precision Formation Flying Guidance, Navigation and Control for the Proba-3 Mission. Proceedings of the 59th International Astronautical Congress 2008, Glasgow, UK, 2008.

[177] Bernard, D., Dorais, G., Gamble, E., Kanefsky, B., Kurien, J., Man, G. K., Millar, W., Muscettola, N., Nayak, P., Rajan, K., Rouquette, N., Smith, B., Taylor, W., and Tung, Y. Spacecraft Autonomy Flight Experience: The DS1 Remote Agent Experiment.

Proceedings of the AIAA Space Technology Conference and Exhibition, AIAA, Albuquerque, New Mexico, USA, 1999. https://doi.org/10.2514/6.1999-4512

[178] Wertz, J. R. Autonomous Navigation and Autonomous Orbit Control in Planetary Orbits as a Means of Reducing Operations Cost. Proceedings of the 5th International Symposium on Reducing the Cost of Spacecraft Ground Systems and Operations, Pasadena, CA, USA, 2002.

[179] LaVallee, D., Jacobsohn, J., Olsen, C., and Reilly, J. Intelligent Control for Spacecraft Autonomy - an Industry Survey. Proceedings of Space 2006 (AIAA SPACE Forum), San Jose, CA, USA, 2006. https://doi.org/10.2514/6.2006-7384

[180] Silva, N., Ganet, M., Gogibus, E., Delpy, P., and Augros, P. Autonomous Rendezvous: Guidance and Control in Elliptical Orbit. Proceedings of the AIAA Guidance, Navigation and Control Conference and Exhibit, Hilton Head, SC, USA, 2007. https://doi.org/10.2514/6.2007-6355

[181] Schaub, H., and Alfriend, K. T. "J2 Invariant Relative Orbits for Spacecraft Formations." *Celestial Mechanics and Dynamical Astronomy*, Vol. 79, No. 2, 2001, pp. 77–95. https://doi.org/10.1023/A:1011161811472.

[182] Sabatini, M., Izzo, D., and Bevilacqua, R. "Special Inclinations Allowing Minimal Drift Orbits for Formation Flying Satellites." *AIAA Journal of Guidance, Control, and Dynamics*, Vol. 31, No. 1, 2008, pp. 94–100. https://doi.org/10.2514/1.30314.

[183] Broucke, R. A. "Solution of the Elliptic Rendezvous Problem with the Time as Independent Variable." *Journal of Guidance, Control, and Dynamics*, Vol. 26, No. 4, 2003, pp. 615–621. https://doi.org/10.2514/2.5089.

[184] Fehse, W. The Drivers for the Approach Strategy. In *Automated Rendezvous and Docking of Spacecraft*, Cambridge University Press, Cambridge, UK, 2003, pp. 112–164. ISBN 978-0-521-82492-7

[185] Alfriend, K. T., Vadali, S. R., Gurfil, P., How, J. P., and Breger, L. Perturbation Mitigation. In *Spacecraft Formation Flying: Dynamics, Control and Navigation*, Elsevier, Oxford, 2010, pp. 185–225. https://doi.org/10.1016/C2009-0-17485-8

[186] Tschauner, J. "Elliptic Orbit Rendezvous." *AIAA Journal*, Vol. 5, No. 6, 1967, pp. 1110–1113. https://doi.org/10.2514/3.4145.

[187] Battin, R. H. Hypergeometric Functions and Elliptic Integrals. In *An Introduction to the Mathematics and Methods of Astrodynamics, Revised Edition*, AIAA, 1999, pp. 33–78. https://doi.org/10.2514/4.861543

[188] Weisstein, E. W. Cubic Equation. In *CRC Concise Encyclopedia of Mathematics*, Chapman & Hall / CRC, Boca Raton, FL, USA, 2002, pp. 610–614.

[189] Junkins, J. L., Akella, M. R., and Alfriend, K. T. "Non-Gaussian Error Propagation in Orbital Mechanics." *Journal of the Astronautical Sciences*, Vol. 44, 1996, p. 541–563.

[190] Neguerela, C., Carrascosa, C., and Llorente, S. European Formation Flying GNC Development for Small Missions. In *59th International Astronautical Congress*, No. 3, Glasgow, UK, 2008.

[191] European Space Agency, "DARWIN Mission Summary Status." *ESA Document SCI/AM/DARWIN-SUMSTAT/06*, No. 2.2, 2007.

[192] Scharf, D. P., and Lawson, P. R. *Terrestrial Planet Finder Interferometer: TPF-I Technology Milestone #2 Report: Formation Control Performance Demonstration, Jet Propulsion Laboratory*. National Aeronautics and Space Administration, Pasadena, CA, USA, 2008.

[193] Ferrando, P. Simbol–X: A New Generation Hard X-Ray Telescope. In *SPIE's 48th Annual Meeting*, No. 5168, San Diego, CA, USA, 2003. https://doi.org/10.1117/12.521998

[194] Mestreau-Garreau, A., Gantois, K., Santovincenzo, A., Cropp, A., Evans, D., François, M., Kerhousse, P., and Teston, F. Proba 3 High Precision Formation Flying Mission. Proceedings of the 4th International Conference on Spacecraft Formation Flying Missions & Technologies, Saint-Hubert, Québec, Canada, 2011.

[195] Tarabini Castellani, L. PROBA-3 Formation Flying Mission. Proceedings of the 7th International Workshop on Satellite Constellations and Formation Flying, Lisbon, Portugal, 2013.

[196] Turck-Chièze, S., *et. al.*, Scientific Objectives of the Novel Formation Flying Mission Aspiics. In *SOHO-17 - 10 Years of SOHO and Beyond*, No. 617, 2006.

[197] Plesseria, J.-Y., *et. al.*, Design and Development of Aspiics, an Externally Occulted Solar Coronagraph for Proba-3 Mission. Proceedings of the 5th International Conference on Spacecraft Formation Flying Missions and Technologies, Munich, Germany, 2013.

[198] Peters, T. V., and Escorial, D. Relative Mission Analysis for Proba 3: Safe Orbits and CAM. Proceedings of the 5th International Conference on Spacecraft Formation Flying Missions and Technologies, Munich, Germany, 2013.

[199] Peters, T. V., Tarabini Castellani, L., Negueruela, C., Llorente, S., and Jakobsson, B. Proba-3 Formation Flying Mission Analysis. In *3rd International Symposium on Formation Flying, Missions and Technology*, No. ESA SP-654, ESA/ESTEC, Noordwijk, The Netherlands, 2008.

[200] Bellei, G., and Bastante, F. Mission Analysis for Operational Orbit and Transfer Strategy of ESA PROBA-3 Mission. Proceedings of the 1st International Academy of

Astronautics Conference on Dynamics and Control of Space Systems (DyCoSS), Porto, Portugal, 2012.

[201] Peters, T. V., Peyrard, J., and Carrascosa, C. Safe Orbits for Proba-3. Proceedings of the 4th International Conference on Spacecraft Formation Flying Missions and Technologies, Saint-Hubert, Québec, Canada, 2011.

[202] Kristiansen, K. U., Palmer, P. L., and Roberts, M. "Relative Motion of Satellites Exploiting the Super-Integrability of Kepler's Problem." *Celestial Mechanics and Dynamical Astronomy*, Vol. 106, No. 4, 2010, pp. 371–390. https://doi.org/10.1007/s10569-009-9253-y.

[203] European Cooperation for Space Standardization, Space Segment Operability. In *ECSS-E-ST-70-11C,* ESA, The Netherlands, 2008.

[204] Schiff, C. Adapting Covariance Propagation to Account for the Presence of Modeled and Unmodeled Maneuvers. Proceedings of the AIAA/AAS astrodynamics specialist conference and exhibit, Keystone, Colorado, USA; 2006. https://doi.org/10.2514/6.2006-6294

[205] Mitsuda, K., Inoue, H., Kunieda, H., Yamakawa, H., Kuninaka, H., and Hashimoto, T. Study of Formation Flying for the XEUS Mission and the ISAS Design of the ISAS Design of the Detector Spacecraft. Proceedings of the Astronomical Telescopes and Instrumentation, Waikoloa, Hawai'i, USA, 2003. https://doi.org/10.1117/12.461292

[206] Peters, T. V., Peyrard, J., and Carrascosa, C. Safe Trajectories for Proba-3. Proceedings of the 4th International Conference on Spacecraft Formation Flying Missions & Technologies, Saint-Hubert, Québec, Canada, 2011.

[207] Montenbruck, O., and Delpech, M. Cross-Validation of GPS and FFRF-Based Relative Navigation for the PRISMA Mission. Proceedings of the 4th ESA Workshop on Satellite Navigation User Equipment Technologies NAVITEC'2008, Noordwijk, The Netherlands, 2008.

[208] Woodburn, J., Coppola, V., and Stoner, F. "A Description of Filters for Minimizing the Time Required for Orbital Conjunction Computations." *Advances in the Astronautical Sciences*, Vol. 135, No. 2, 2009, pp. 1157–1173.

[209] Hoots, F. R., Crawford, L. L., and Roehrich, R. L. "An Analytic Method to Determine Future Close Approaches between Satellites." *Celestial Mechanics*, Vol. 33, No. 2, 1984, pp. 143–158. https://doi.org/10.1007/BF01234152.

[210] Kerr, E., and Ortiz, N. S. State of the Art and Future Needs in Conjunction Analysis Methods, Processes and Software. Proceedings of the 8th European Conference on Space Debris, Darmstadt, Germany, 2021

[211] Battin, R. H. *An Introduction to the Mathematics and Methods of Astrodynamics, Revised Edition*. American Institute of Aeronautics and Astronautics, Reston, VA, 1999. https://doi.org/10.2514/4.861543

[212] Stern, R. G., and Potter, J. E. “Optimization of Midcourse Velocity Corrections.” *IFAC Proceedings Volumes*, Vol. 2, No. 1, 1965, pp. 70–83. https://doi.org/10.1016/S1474-6670(17)69070-0.

[213] Tempelman, W. “Linear Guidance Laws for Space Missions.” *Journal of Guidance, Control, and Dynamics*, Vol. 9, No. 4, 1986, pp. 495–502. https://doi.org/10.2514/3.20137.

[214] Tempelman, W. “Linearized Impulsive Guidance Laws.” *AIAA Journal*, Vol. 3, No. 11, 1965, pp. 2148–2149. https://doi.org/10.2514/3.3328.

[215] Chuang, C.-H., Goodson, T. D., Ledsinger, L. A., and Hanson, J. “Optimality and Guidance for Planar Multiple-Burn Orbit Transfers.” *Journal of Guidance, Control, and Dynamics*, Vol. 19, No. 6, 1996, pp. 1310–1316. https://doi.org/10.2514/3.21787.

[216] Tempelman, W. Properties of Conic State Transition Matrices and Associated Time Partials. Proceedings of the 21st Aerospace Sciences Meeting, Reno, Nevada, USA, 1983. https://doi.org/10.2514/6.1983-14

[217] Leimkuhler, B., and Reich, S. *Simulating Hamiltonian Dynamics*. Cambridge University Press, Cambridge, UK, 2004. https://doi.org/10.1017/CBO9780511614118

[218] Broucke, R. A. “On the Matrizant of the Two-Body Problem.” *Astronomy and Astrophysics*, Vol. 6, 1970, pp. 173–182.

[219] Julier, S. J., and Uhlmann, J. K. A New Extension of the Kalman Filter to Nonlinear Systems. In *AeroSense ’97*, No. 3068, Orlando, Florida, USA, 1997. https://doi.org/10.1117/12.280797

[220] Julier, S. J., and Uhlmann, J. K. A New Approach for Filtering Nonlinear Systems. Proceedings of the 1995 American Control Conference - ACC’95, Seattle, Washington, United States, 1995. https://doi.org/10.1109/ACC.1995.529783

[221] Menegaz, H. M. T., Ishihara, J. Y., Borges, G. A., and Vargas, A. N. “A Systematization of the Unscented Kalman Filter Theory.” *IEEE Transactions on Automatic Control*, Vol. 60, No. 10, 2015, pp. 2583–2598. https://doi.org/10.1109/TAC.2015.2404511.

[222] Van der Merwe, R., and Wan, E. A. The Square-Root Unscented Kalman Filter for State and Parameter-Estimation. In *2001 IEEE International Conference on Acoustics, Speech, and Signal Processing. Proceedings*, No. 6, Salt Lake City, UT, USA, 2001, pp. 3461–3464. https://doi.org/10.1109/ICASSP.2001.940586

[223] Wan, E. A., and Van der Merwe, R. The Unscented Kalman Filter for Nonlinear Estimation. Proceedings of the IEEE 2000 Adaptive Systems for Signal Processing, Communications, and Control Symposium, Lake Louise, AB, Canada, 2000. https://doi.org/10.1109/ASSPCC.2000.882463

[224] Press, W. H., Ed. *Numerical Recipes in C: The Art of Scientific Computing*. Cambridge University Press, Cambridge, Massachusetts, 1992. ISBN: 0-521-43108-5

[225] Kozai, Y. "Effects of Solar Radiation Pressure on the Motion of an Artificial Satellite." *Smithsonian Contributions to Astrophysics*, Vol. 6, 1963, pp. 109–112.

[226] Underwood, C., Pellegrino, S., Lappas, V., Bridges, C., Taylor, B., Chhaniyara, S., Theodorou, T., Shaw, P., Arya, M., Breckinridge, J., Hogstrom, K., Patterson, K. D., Steeves, J., Wilson, L., and Horri, N. Autonomous Assembly of a Reconfigurable Space Telescope (AAReST) – A CubeSat/Microsatellite Based Technology Demonstrator. Proceedings of the Small Satellite Conference, Logan, Utah, USA, 2013. https://digitalcommons.usu.edu/smallsat/2013/all2013/87/

[227] Underwood, C., Pellegrino, S., Lappas, V. J., Bridges, C. P., and Baker, J. "Using CubeSat/Micro-Satellite Technology to Demonstrate the Autonomous Assembly of a Reconfigurable Space Telescope (AAReST)." *Acta Astronautica*, Vol. 114, 2015, pp. 112–122. https://doi.org/10.1016/j.actaastro.2015.04.008.

[228] Underwood, C., Pellegrino, S., Priyadarshan, H., Simha, H., Bridges, C., Goel, A., Talon, T., Pedivellano, A., Leclerc, C., Wei, Y., Royer, F., Sakovsky, M., Marshall, M., Jackson, K., Sommer, C., Nair, S. V. S., and Baker, J. "AAReST Autonomous Assembly Reconfigurable Space Telescope Flight Demonstrator." Proceedings of the 69th International Astronautical Congress, Bremen, Germany, 2018.

[229] Gangestad, J. W., Hardy, B. S., and Hinkley, D. A. Operations, Orbit Determination, and Formation Control of the AeroCube-4 CubeSats. Proceedings of the Small Satellite Conference, Logan, Utah, USA, 2013. https://digitalcommons.usu.edu/smallsat/2013/all2013/116/

[230] Rose, T. S., Rowen, D. W., LaLumondiere, S., Werner, N. I., Linares, R., Faler, A., Wicker, J., Coffman, C. M., Maul, G. A., Chien, D. H., Utter, A., Welle, R. P., and Janson, S. W. Optical Communications Downlink from a 1.5U Cubesat: OCSD Program. Proceedings of the International Conference on Space Optics - ICSO 2018, Chania, Greece, 2019. https://doi.org/10.1117/12.2535938

[231] Janson, S. W., and Welle, R. P. The NASA Optical Communication and Sensor Demonstration Program. Proceedings of the Small Satellite Conference, Logan, Utah, USA, 2013. https://digitalcommons.usu.edu/smallsat/2013/all2013/53/

[232] Janson, S. W., and Welle, R. P. The NASA Optical Communication and Sensor Demonstration Program: An Update. Proceedings of the Small Satellite Conference, Logan, Utah, USA, 2014. https://digitalcommons.usu.edu/smallsat/2014/NextPad/1/

[233] Janson, S. W., Welle, R. P., Rose, T. S., Rowen, D. W., Hinkley, D. A., and Hardy, B. S. The NASA Optical Communication and Sensors Demonstration Program: Preflight Update. Proceedings of the Small Satellite Conference, Logan, Utah, USA, 2015. https://digitalcommons.usu.edu/smallsat/2015/all2015/14/

[234] Janson, S., Welle, R., Rose, T., Rowen, D., Hardy, B., Dolphus, R., Doyle, P., Faler, A., Chien, D., Chin, A., Maul, G., Coffman, C., Lumondiere, S. D. L., and Hinkley, D. The NASA Optical Communications and Sensor Demonstration Program: Initial Flight Results. Proceedings of the Small Satellite Conference, Logan, Utah, USA, 2016. https://digitalcommons.usu.edu/smallsat/2016/TS3YearInReview/2/

[235] Lee, B.-S., Lee, J.-S., and Choi, K.-H. "Analysis of a Station-Keeping Maneuver Strategy for Three Geostationary Satellites Collocation." *IFAC Proceedings Volumes*, Vol. 31, No. 21, Seoul, Korea, 1998, pp. 295–300. https://doi.org/10.1016/S1474-6670(17)41093-7.

[236] Evans, J. W., Piñon, E. I., and Mulder, T. A. Autonomous Rendezvous Guidance and Navigation for Orbital Express and Beyond. AAS 06-194. Proceedings of the 16th AAS/AIAA Space Flight Mechanics Conference, Tampa, Florida, USA, 2006.

[237] Knight, R., Chouinard, C., Jones, G., and Tran, D. Planning and Scheduling Challenges for Orbital Express. Proceedings of the 6th International Workshop on Planning and Scheduling for Space, Pasadena, California, USA, 2009.

[238] Bualat, M. G., Smith, T., Smith, E. E., Fong, T., and Wheeler, D. Astrobee: A New Tool for ISS Operations. Proceedings of the 2018 SpaceOps Conference, Marseille, France, 2018. https://doi.org/10.2514/6.2018-2517

[239] Bualat, M., Barlow, J., Fong, T., Provencher, C., and Smith, T. Astrobee: Developing a Free-Flying Robot for the International Space Station. Proceedings of the AIAA Space 2015 Conference and Exposition, Pasadena, California, USA, 2015.

[240] Smith, T., Barlow, J., Bualat, M., Fong, T., Provencher, C., Sanchez, H., and Smith, E. Astrobee: A New Platform for Free-Flying Robotics on the International Space Station. Proceedings of the International Symposium on Artificial Intelligence, Robotics, and Automation in Space (i-SAIRAS), Beijing, China, 2016.

[241] Ganet, M., Quinquis, I., Bourdon, J., and Delpy, P. ATV GNC during Rendezvous with ISS. Proceedings of the 5th Cranfield DCSSS Conference, Cambridge, UK, 2002.

[242] Gonnaud, J. L., and Pascal, V. ATV Guidance, Navigation and Control for Rendezvous with ISS. In *4th ESA International Conference on Spacecraft Guidance, Navigation and Control Systems*, No. ESA SP-425, Paris, France, 2000, pp. 501.

[243] Kulu, E. Beesat 14-15 @ Nanosats Database. Nanosats Database, Dec, 2021. https://www.nanosats.eu/sat/beesat-14-15

[244] Gaias, G., Ardaens, J.-S., and Terzibaschian, T. Paving the Way for Future On-Orbit Servicing Missions: The Avanti Experiment. Proceedings of the 25th International Symposium on Space Flight Dynamics (ISSFD), Munich, Germany, 2015.

[245] Gaias, G., Ardaens, J.-S., and D'Amico, S. The Autonomous Vision Approach Navigation and Target Identification (Avanti) Experiment: Objectives and Design. Proceedings of the GNC 2014: 9th International ESA Conference on Guidance, Navigation & Control Systems, Porto, Portugal, 2014.

[246] Krebs, G. D. Bros 1, 2 (Birkeland, Huygens). Gunter's Space Page, Jan, 2021. https://space.skyrocket.de/doc_sdat/bros-1.htm

[247] Bonin, G., Orr, N., Armitage, S., Roth, N., Risi, B., and Zee, R. E. The CanX-4&5 Mission: Achieving Precise Formation Flight at the Nanosatellite Scale. Proceedings of the 64th International Astronautical Congress, Beijing, China, 2013.

[248] Bonin, G., Roth, N., Armitage, S., Newman, J., Risi, B., and Zee, R. E. CanX−4 and CanX−5 Precision Formation Flight: Mission Accomplished! Proceedings of the Small Satellite Conference, Logan, Utah, USA, 2015. https://digitalcommons.usu.edu/smallsat/2015/all2015/3/

[249] Newman, J. Drift Recovery and Station Keeping Results for the Historic CanX-4 CanX-5 Formation Flying Mission. Proceedings of the Small Satellite Conference, Logan, Utah, USA, 2015. https://digitalcommons.usu.edu/smallsat/2015/all2015/54/

[250] Kim, G.-N., Park, S.-Y., Lee, T., Kang, D.-E., Kim, N., Jeon, S., Lee, E., and Song, Y. Development of Formation Flying CubeSats and Operation Systems for the CANYVAL-C Mission: Launch and Lessons Learned. Proceedings of the Small Satellite Conference, Logan, Utah, USA, 2021. https://digitalcommons.usu.edu/smallsat/2021/all2021/237/

[251] Lee, Y., Park, S.-Y., Park, J.-P., and Song, Y. "Numerical Analysis of Relative Orbit Control Strategy for CANYVAL-X Mission." *Journal of Astronomy and Space Sciences*, Vol. 36, No. 4, 2019, pp. 235–248. https://doi.org/10.5140/JASS.2019.36.4.235.

[252] Agathanggelou, A. P., Attrill, G. D. R., Nicholas, A. C., Routledge, G. J., Kataria, D. O., Mitchell, C. N., Watson, R. J., Williams, J., Carman, T., Budzien, S. A., and Dymond, K. F. CIRCE: Coordinated Ionospheric Reconstruction Cubesat Experiment.

Proceedings of the Small Satellite Conference, Logan, Utah, USA, 2020. https://digitalcommons.usu.edu/smallsat/2020/all2020/117/

[253] Attrill, G. D. R., Nicholas, A. C., Routledge, G., Miah, J. A., Kataria, D. O., Mitchell, C. N., Watson, R. J., Williams, J., Agathanggelou, A., Brown, C. M., Budzien, S. A., Carman, T., Chaudery, R., Dymond, K. F., Finne, T. T., Fortnam, A., Fritz, B., Hands, A., Marquis, P. J., Murphy, S., Pinto-Jayawardena, T., Rust, D., Ryden, K. A., Schofield, D., Stephan, A. W., Wiggins, K., and Underwood, C. "Coordinated Ionospheric Reconstruction CubeSat Experiment (CIRCE), *In Situ* and Remote Ionospheric Sensing (IRIS) Suite." *Journal of Space Weather and Space Climate*, Vol. 11, 2021. https://doi.org/10.1051/swsc/2020066.

[254] Nicholas, A. C., Attrill, G. D., Dymond, K. F., Budzien, S. A., Stephan, A. W., Fritz, B. A., Routledge, G. J., Miah, J. A., Brown, C. M., Marquis, P. J., Finne, T. T., Mitchell, C. N., Watson, R. J., Kataria, D. O., and Williams, J. Coordinated Ionospheric Reconstruction CubeSat Experiment (CIRCE) Mission Overview. Proceedings of the CubeSats and SmallSats for Remote Sensing III, San Diego, USA, 2019. https://doi.org/10.1117/12.2528767

[255] Viertl, J. *Removal of VESPA upper part - Executive Summary Report*. Publication CS-ESA-SOR-TD-005. Clearspace, 2020. https://nebula.esa.int/content/removal-vespa-upper-part

[256] Williams, A. CubeSat Proximity Operations Demonstration (CPOD) Overview. Proceedings of the In-Space Inspection Workshop 2014, Houston, Texas, USA, 2014.

[257] Bowen, J., Tsuda, A., Abel, J., and Villa, M. CubeSat Proximity Operations Demonstration (CPOD) Mission Update. Proceedings of the 2015 IEEE Aerospace Conference, Big Sky, MT, USA, 2015. https://doi.org/10.1109/AERO.2015.7119124

[258] Cockell, C. S., Léger, A., Fridlund, M., Herbst, T. M., Kaltenegger, L., Absil, O., Beichman, C., Benz, W., Blanc, M., Brack, A., Chelli, A., Colangeli, L., Cottin, H., Foresto, F. C. du, Danchi, W. C., Defrère, D., Herder, J.-W. den, Eiroa, C., Greaves, J., Henning, T., Johnston, K. J., Jones, H., Labadie, L., Lammer, H., Launhardt, R., Lawson, P., Lay, O. P., LeDuigou, J.-M., Liseau, R., Malbet, F., Martin, S. R., Mawet, D., Mourard, D., Moutou, C., Mugnier, L. M., Ollivier, M., Paresce, F., Quirrenbach, A., Rabbia, Y. D., Raven, J. A., Rottgering, H. J. A., Rouan, D., Santos, N. C., Selsis, F., Serabyn, E., Shibai, H., Tamura, M., Thiébaut, E., Westall, F., and White, G. J. "*Darwin*—A Mission to Detect and Search for Life on Extrasolar Planets." *Astrobiology*, Vol. 9, No. 1, 2009, pp. 1–22. https://doi.org/10.1089/ast.2007.0227.

[259] d'Arcio, L., Karlsson, A., Bavdaz, M., and Jagemann, T. Search for Extraterrestrial Planets: The DARWIN Mission. Proceedings of the International

Conference on Space Optics 2006, Noordwijk, The Netherlands, 2017. https://doi.org/10.1117/12.2308153

[260] Fridlund, C. V. M. "The Darwin Mission." *Advances in Space Research*, Vol. 34, No. 3, 2004, pp. 613–617. https://doi.org/10.1016/j.asr.2003.05.031.

[261] Kaltenegger, L., Karlsson, A., Fridlund, M., and Absil, O. Overview of the Darwin Mission. In *Conference on Towards Other Earths: DARWIN/TPF and the Search for Extrasolar Terrestrial Planets*, No. ESA SP-539, Noordwijk, The Netherlands, 2003, pp. 459–464.

[262] Leger, A., and Herbst, T. "DARWIN Mission Proposal to ESA." *arXiv:0707.3385 [astro-ph]*, 2007.

[263] Guo, J., Bouwmeester, J., and Gill, E. From Single to Formation Flying CubeSats: An Update of the Delfi Programme. Proceedings of the Small Satellite Conference, Logan, Utah, USA, 2013. https://digitalcommons.usu.edu/smallsat/2013/all2013/38/

[264] Estable, S., Pruvost, C., Ferreira, E., Telaar, J., Fruhnert, M., Imhof, C., Rybus, T., Peckover, G., Lucas, R., Ahmed, R., Oki, T., Wygachiewicz, M., Kicman, P., Lukasik, A., Santos, N., Milhano, T., Arroz, P., Biesbroek, R., and Wolahan, A. "Capturing and Deorbiting Envisat with an Airbus Spacetug. Results from the ESA e.Deorbit Consolidation Phase Study." *Journal of Space Safety Engineering*, Vol. 7, No. 1, 2020, pp. 52–66. https://doi.org/10.1016/j.jsse.2020.01.003.

[265] Estable, S., Telaar, J., Lange, M., Ahrns, I., Pegg, K., Jacobsen, D., Gerrits, D., Theybers, M., Dayers, L., Bussche, S. V., Ilsen, S., Lampariello, R., Wygachiewicz, M., Santos, N., Canetri, M., Serra, P., Santiago, L. S., Łukasik, A., Ratti, J., Puddephatt, D., Brito, L. E., Bondy, M., Biesbroek, R., and Wolahan, A. Definition of an Automated Vehicle with Autonomous Fail-Safe Reaction Behavior to Capture and Deorbit Envisat. In *7th European Conference on Space Debris*, No. 7, Darmstadt, Germany, 2017.

[266] Blackerby, C., Okamoto, A., Fujimoto, K., Okada, N., Forshaw, J. L., and Auburn, J. ELSA-D: An in-Orbit End-of-Life Demonstration Mission. Proceedings of the 69th International Astronautical Congress, Bremen, Germany, 2018.

[267] Forshaw, J., Iizuka, S., Blackerby, C., and Okada, N. ELSA-d – A Novel End-of-Life Debris Removal Mission: Mission Overview, CONOPS, and Launch Preparations. Proceedings of the First International Orbital Debris Conference, Sugar Land, Texas, USA, 2019.

[268] Forshaw, J., Lopez, R., Okamoto, A., Blackerby, C., and Okada, N. The ELSA-d End-of-Life Debris Removal Mission: Mission Design, In-Flight Safety, and Preparations for Launch. Proceedings of the Advanced Maui Optical and Space Surveillance Technologies Conference, Maui, Hawaii, USA, 2019.

[269] Wokes, D. S. ELSA-d: Mission Design and Performance to Date. Proceedings of the 2021 ESA Clean Space Industrial Days, online only, 2021.

[270] Kawano, I., Mokuno, M., Kasai, T., and Suzuki, T. “First Autonomous Rendezvous Using Relative GPS Navigation by ETS-VII.” *Navigation*, Vol. 48, No. 1, 2001, pp. 49–56. https://doi.org/10.1002/j.2161-4296.2001.tb00227.x.

[271] Kawano, I., Mokuno, M., Suzuki, T., Koyama, H., and Kunugi, M. “Approach Trajectory Design for Autonomous Rendezvous of ETS-VII.” *Japan Society of Aeronautical Space Sciences*, Vol. 49, 2002, pp. 432–437. https://doi.org/10.2322/jjsass.49.432.

[272] Kawano, I., Mokuno, M., Horiguchi, H., and Kibe, K. In-Orbit Demonstration of an Unmanned Automatic Rendezvous and Docking System by the Japanese Engineering Test Satellite ETS-VII. Proceedings of the Guidance, Navigation, and Control Conference, Scottsdale, Arizona, USA, 1994. https://doi.org/10.2514/6.1994-3648

[273] Kawano, I., Mokuno, M., and Kasai, T. Result and Evaluation of Autonomous Rendezvous Docking Experiment of ETS-VII. Proceedings of the Guidance, Navigation, and Control Conference and Exhibit, Portland, Oregon, USA, 1999. https://doi.org/10.2514/6.1999-4073

[274] Kawano, I., Mokuno, M., Yamanaka, K., Suzuki, T., Koyama, H., and Kunugi, M. “Replanning of Rendezvous Docking Experiment of ETS-VII, and Its Result.” *Transactions of the Japan Society of Mechanical Engineers Series C*, Vol. 68, No. 671, 2002, pp. 2059–2066. https://doi.org/10.1299/kikaic.68.2059.

[275] Kawano, I., Mokuno, M., Kasai, T., Suzuki, T., Koyama, H., and Kunugi, M. “Result of Remote Pilot Rendezvous Experiment by ETS-VII.” *Transactions of the Japan Society of Mechanical Engineers Series C*, Vol. 68, No. 672, 2002, pp. 2354–2362. https://doi.org/10.1299/kikaic.68.2354.

[276] Mokuno, M., Kawano, I., Horiguchi, H., and Kibe, K. Development of ETS-VII RVD System - Preliminary Design and EM Development Phase (Engineering Test Satellite and RendezVous Docking). Proceedings of the Guidance, Navigation, and Control Conference, Baltimore, Maryland, USA, 1995. https://doi.org/10.2514/6.1995-3357

[277] Maessen, D., Guo, J., Gill, E., Gunter, B., Chu, Q. P., Bakker, G., Laan, E., Moon, S., Kruijff, M., and Zheng, G. T. Conceptual Design of the FAST-D Formation Flying Spacecraft. In *Small Satellite Missions for Earth Observation: New Developments and Trends*, Springer, Heidelberg, 2010, pp. 155–163.

[278] Maessen, D., Guo, J., Gill, E., Laan, E., Moon, S., and Zheng, G. T. Mission Design of the Dutch-Chinese FAST Micro-Satellite Mission. In *Small Satellite Missions for*

Earth Observation: New Developments and Trends, Springer, Heidelberg, Germany, 2010, pp. 187–194.

[279] Guo, J., Maessen, D. C., Gill, E., Moon, S. G., and Zheng, G. Status of the Fast Mission: Micro-Satellite Formation Flying for Technology, Science and Education. Proceedings of the 60th International Astronautical Congress, Daejeon, Korea, 2009.

[280] Alminde, L. K., Bisgaard, M., Portillo, I. A., Smith, D., and Perez, L. L. GOMX-4: Demonstrating the Building Blocks of Constellations. Proceedings of the Small Satellite Conference, Logan, Utah, USA, 2017. https://digitalcommons.usu.edu/smallsat/2017/all2017/81/

[281] Holst, R., Nielsen, J., Gerhardt, D., and Ahumada, J. A. G. Attitude and Orbit Control Results of the GOMX-4 Tandem CubeSat Mission. Proceedings of the 69th International Astronautical Congress, Bremen, Germany, 2018.

[282] León Perez, L., Koch, P., and Walker, R. GOMX-4 - The Twin European Mission for IOD Purposes. Proceedings of the Small Satellite Conference, Long Beach, California, USA, 2018. https://digitalcommons.usu.edu/smallsat/2018/all2018/296/

[283] Antreasian, P. G., Bhat, R. S., Broschart, S. B., Chung, M. K., Criddle, K. E., Goodson, T. D., Jefferson, D. C., Lau, E. L., Mohan, S., Parker, J. S., Roncoli, R. B., Ryne, M. S., You, T. H., Young, B. T., and Antreasian, P. G. Navigation of the Twin Grail Spacecraft into Science Formation at the Moon. Proceedings of the 23rd International Symposium on Space Flight Dynamics, Pasadena, California, USA, 2012. https://hdl.handle.net/2014/42998

[284] Spath, S. R. Small Spacecraft Design for the GRAIL Mission. Proceedings of the Small Satellite Conference, Logan, Utah, USA, 2012. https://digitalcommons.usu.edu/smallsat/2012/all2012/21/

[285] Jie, G., Jinggang, G., Zuowei, W., and Nan, L. Research on the Technological Development of GSO Small Satellite. In *5th Asia Conference on Mechanical Engineering and Aerospace Engineering (MEAE 2019)*, No. 288, L. H. Ky, Y. Xia, C. H. Su, C. W. Tong, A. Y. Bani Hashim, and M. Islam, eds., 2019. https://doi.org/10.1051/matecconf/201928802003

[286] Welsch, C. P., Armand, B., Garber, D., Repp, M., and Robinson, A. The Case for Commercially Hosted Space Situational Awareness Payloads. Proceedings of the Advanced Maui Optical and Space Surveillance Technologies Conference, Maui, Hawaii, USA, 2014.

[287] Zhang, X., Xie, B., Dai, S., Zhang, W., Hu, G., and Lan, D. First Micro-Satellite and New Enhanced Small Satellite Series in DFH Satellite Co. Ltd. Proceedings of the 57th International Astronautical Congress, Valencia, Spain, 2006.

[288] Zhang, X., Xie, B., Dai, S., Zhang, W., Hu, G., and Lan, D. "First Micro-Satellite and New Enhanced Small Satellite Series in DFH Satellite Co. Ltd." *Acta Astronautica*, Vol. 61, Nos. 1–6, 2007, pp. 234–242. https://doi.org/10.1016/j.actaastro.2007.01.044.

[289] Brunello, A., Valmorbida, A., Lorenzini, E. C., Cantoni, S., De Stefano Fumo, M., Fedele, A., Gardi, R., and Votta, R. "Deorbiting Small Satellites from the ISS Using a Tether System." *CEAS Space Journal*, Vol. 13, 2021, pp. 217–230. https://doi.org/10.1007/s12567-020-00337-1.

[290] Buinhas, L., Frankl, K., Linz, H., and Förstner, R. "IRASSI Infrared Space Interferometer: Formation Geometry and Relative Dynamics Analysis." *Acta Astronautica*, Vol. 153, 2018, pp. 394–409. https://doi.org/10.1016/j.actaastro.2018.02.005.

[291] Linz, H., Bhatia, D., Buinhas, L., Lezius, M., Ferrer, E., Förstner, R., Frankl, K., Philips-Blum, M., Steen, M., Bestmann, U., Hänsel, W., Holzwarth, R., Krause, O., and Pany, T. "InfraRed Astronomy Satellite Swarm Interferometry (IRASSI): Overview and Study Results." *Advances in Space Research*, Vol. 65, No. 2, 2020, pp. 831–849. https://doi.org/10.1016/j.asr.2019.06.022.

[292] Yoshihara, K., van Mierlo, M., Ng, A., Kumar, B. S., Ruiter, A. D., Horiguchi, H., and Hashimoto, H. JC2Sat-FF: An International Collaboration Nano-Sat Project Overview of the System Analyses and Design. In *IAA Symposium Small Satellites Systems and Services (4S)*, No. ESA SP-660, Rhodes, Greece, 2008.

[293] Konrad, B. S., Alei, E., Angerhausen, D., Carrión-González, Ó., Fortney, J. J., Grenfell, J. L., Kitzmann, D., Mollière, P., Rugheimer, S., Wunderlich, F., and Quanz, S. P. "Large Interferometer For Exoplanets (LIFE): III. Spectral Resolution, Wavelength Range and Sensitivity Requirements Based on Atmospheric Retrieval Analyses of an Exo-Earth." *Astronomy & Astrophysics*, 2022. https://doi.org/10.1051/0004-6361/202141964.

[294] Hansen, J. T., and Ireland, M. J. "Large Interferometer For Exoplanets (LIFE): VI. Ideal Kernel-Nulling Array Architectures for a Space-Based Mid-Infrared Nulling Interferometer." *Astronomy & Astrophysics*, 2022. https://doi.org/10.48550/arXiv.2201.04891.

[295] Defrère, D., Léger, A., Absil, O., Beichman, C., Biller, B., Danchi, W. C., Ergenzinger, K., Eiroa, C., Ertel, S., Fridlund, M., Muñoz, A. G., Gillon, M., Glasse, A., Godolt, M., Grenfell, J. L., Kraus, S., Labadie, L., Lacour, S., Liseau, R., Martin, G., Mennesson, B., Micela, G., Minardi, S., Quanz, S. P., Rauer, H., Rinehart, S., Santos, N. C., Selsis, F., Surdej, J., Tian, F., Villaver, E., Wheatley, P. J., and Wyatt, M. "Space-Based Infrared Interferometry to Study Exoplanetary Atmospheres." *Experimental Astronomy*, Vol. 46, No. 3, 2018, pp. 543–560. https://doi.org/10.1007/s10686-018-9613-2.

[296] Quanz, S. P., Absil, O., Benz, W., Bonfils, X., Berger, J.-P., Defrère, D., van Dishoeck, E., Ehrenreich, D., Fortney, J., Glauser, A., Grenfell, J. L., Janson, M., Kraus, S., Krause, O., Labadie, L., Lacour, S., Line, M., Linz, H., Loicq, J., Miguel, Y., Pallé, E., Queloz, D., Rauer, H., Ribas, I., Rugheimer, S., Selsis, F., Snellen, I., Sozzetti, A., Stapelfeldt, K. R., Udry, S., and Wyatt, M. "Atmospheric Characterization of Terrestrial Exoplanets in the Mid-Infrared: Biosignatures, Habitability, and Diversity." *Experimental Astronomy*, 2021. https://doi.org/10.1007/s10686-021-09791-z.

[297] Danzmann, K. "LISA - an ESA Cornerstone Mission for a Gravitational Wave Observatory." *Classical and Quantum Gravity*, Vol. 14, No. 6, 1997, pp. 1399–1404. https://doi.org/10.1088/0264-9381/14/6/002.

[298] Kulu, E. Magnaro @ Nanosats Database. Nanosats Database, Aug, 2021. https://www.nanosats.eu/sat/magnaro

[299] Farahmand, M., Long, A., Hollister, J., and Rose, J. Magnetospheric Multiscale Mission Navigation Performance During Apogee-Raising and Beyond. Proceedings of the 2017 AAS/AIAA Astrodynamics Specialist Conference, Stevenson, Washington, USA, 2017.

[300] Hughes, S. Formation Design and Sensitivity Analysis for the Magnetospheric Multiscale Mission (MMS). Proceedings of the AIAA/AAS Astrodynamics Specialist Conference and Exhibit, Honolulu, Hawaii, USA, 2008. https://doi.org/10.2514/6.2008-7357

[301] Roscoe, C. W. T., Vadali, S. R., Alfriend, K. T., and Desai, U. P. "Optimal Formation Design for Magnetospheric Multiscale Mission Using Differential Orbital Elements." *Journal of Guidance, Control, and Dynamics*, Vol. 34, No. 4, 2011, pp. 1070–1080. https://doi.org/10.2514/1.52484.

[302] Krebs, G. D. NanoACE. Gunter's Space Page, Aug, 2021. https://space.skyrocket.de/doc_sdat/nanoace.htm

[303] Schilling, K. NetSat - Four Cooperating Networked CubeSats Flying as Formation. Proceedings of the 4th CubeSat Industry Days, ESA/ESTEC, Noordwijk, The Netherlands, 2017.

[304] Schilling, K., Bangert, P., Busch, S., Dombrovski, S., Freimann, A., Kramer, A., Nogueira, T., Ris, D., Scharnagl, J., Tzschichholz, T., Islas, G., and Zhou, L. NetSat: A Four Pico/Nano-Satellite Mission for Demonstration of Autonomous Formation Flying. Proceedings of the 66th International Astronautical Congress, Jerusalem, Israel, 2015.

[305] Arenberg, J. W., and Cash, W. "New Worlds Observer: A Novel Mission Concept for Exoplanetary Studies." *Proceedings of the International Astronomical Union*, Vol. 1, No. C200, 2005, pp. 199–204. https://doi.org/10.1017/S174392130600932X.

[306] Cash, W. and New Worlds Study Team. The New Worlds Observer: The Astrophysics Strategic Mission Concept Study. In *Pathways Towards Habitable Planets*, No. 430, Barcelona, Spain, 2009, pp. 353–360.

[307] Elandt, R., Aslan, S., and Peck, M. A. Six-Axis Thruster Characterization Technique for Small Satellites. Proceedings of the 55th AIAA Aerospace Sciences Meeting, Grapevine, Texas, USA, 2017. https://doi.org/10.2514/6.2017-0482

[308] Arestie, S., Lightsey, E. G., and Hudson, B. "Development of A Modular, Cold Gas Propulsion System for Small Satellite Applications." *Journal of Small Satellites,* Vol. 1, No. 2, 2012, pp. 63-74

[309] De Florio, S., and D'Amico, S. "The Precise Autonomous Orbit Keeping Experiment on the Prisma Mission." *The Journal of the Astronautical Sciences*, Vol. 56, No. 4, 2008, pp. 477–494. https://doi.org/10.1007/BF03256562.

[310] Gill, E., D'Amico, S., and Montenbruck, O. "Autonomous Formation Flying for the PRISMA Mission." *Journal of Spacecraft and Rockets*, Vol. 44, No. 3, 2007, pp. 671–681. https://doi.org/10.2514/1.23015.

[311] Larsson, R., Berge, S., Bodin, P., and Jönsson, U. Fuel Efficient Relative Orbit Control Strategies for Formation Flying and Rendezvous within PRISMA. In *Rocky Mountain Guidance and Control Conference*, No. 125, Breckenridge, Colorado, USA, 2006, pp. 25–40.

[312] Escorial Olmos, D. *COBRA Executive Summary*. Publication GMV 22484/14 V1/14. 2014. https://nebula.esa.int/sites/default/files/neb_study/1188/C4000110632ExS.pdf

[313] Peters, T. V. The COBRA IRIDES Experiment. Proceedings of the 65th International Astronautical Congress, Toronto, Canada, 2014.

[314] Delpech, M., Malbet, F., Karlsson, T., Larsson, R., Léger, A., and Jorgensen, J. "Flight Demonstration of Formation Flying Capabilities for Future Missions (NEAT Pathfinder)." *Acta Astronautica*, Vol. 105, No. 1, 2014, pp. 82–94. https://doi.org/10.1016/j.actaastro.2014.05.027.

[315] Peñin, L. F., Scoarnec, Y., Fernández-Ibarz, J. M., Cazorla, C., Villa, J. R., Kassel, R., Benito, F. J., de Aragón, A., Baudoux, D., and Strippoli, L. Proba-3: ESA's Small Satellites Precise Formation Flying Mission to Study the Sun's Inner Corona as Never before. Proceedings of the Small Satellite Conference, Logan, Utah, USA, 2020. https://digitalcommons.usu.edu/smallsat/2020/all2020/105/

[316] Tiraplegui, S., Serrano, D., Peñin, L. F., Contreras, R., and Rodriguez, G. Proba-3: Challenges and Needs for Sub-Millimetre Autonomous Formation Flying. Proceedings

of the 8th European Conference for Aeronautics and Aerospace Sciences (EUCASS), Madrid, Spain, 2019. https://doi.org/10.13009/EUCASS2019-764

[317] Walker, R. CubeSats: An ESA Perspective. Proceedings of the 7th Industry Space Days, ESA/ESTEC, Noordwijk, The Netherlands, 2018.

[318] Pirat, C. S. *Guidance, Navigation and Control for Autonomous Rendezvous and Docking of Nano-Satellites*. École Polytechnique Fédérale De Lausanne, 2018.

[319] Pirat, C. "Vision Based Navigation for Autonomous Cooperative Docking of CubeSats." *Acta Astronautica*, Vol. 146, 2018, pp. 418–434. https://doi.org/10.1016/j.actaastro.2018.01.059.

[320] Hart, K. A., Gunter, B. C., and Braun, R. D. Aerodynamics of the RANGE Nanosatellites from Direct Flowfield Simulation. Proceedings of the AIAA SPACE 2016, Long Beach, California, USA, 2016. https://doi.org/10.2514/6.2016-5520

[321] Groesbeck, D. S., Hart, K. A., and Gunter, B. C. "Simulated Formation Flight of Nanosatellites Using Differential Drag with High-Fidelity Rarefied Aerodynamics." *Journal of Guidance, Control, and Dynamics*, Vol. 42, No. 5, 2019, pp. 1175–1184. https://doi.org/10.2514/1.G003871.

[322] Aglietti, G. S., Taylor, B., Fellowes, S., Ainley, S., Tye, D., Cox, C., Zarkesh, A., Mafficini, A., Vinkoff, N., Bashford, K., Salmon, T., Retat, I., Burgess, C., Hall, A., Chabot, T., Kanani, K., Pisseloup, A., Bernal, C., Chaumette, F., Pollini, A., and Steyn, W. H. "RemoveDEBRIS: An in-Orbit Demonstration of Technologies for the Removal of Space Debris." *The Aeronautical Journal*, Vol. 124, No. 1271, 2020, pp. 1–23. https://doi.org/10.1017/aer.2019.136.

[323] Forshaw, J., Aglietti, G., Fellowes, S., Salmon, T., Retat, I., Hall, A., Chabot, T., Pisseloup, A., Tye, D., Bernal, C., Chaumette, F., Pollini, A., and Steyn, W. "The Active Space Debris Removal Mission RemoveDebris. Part 1: From Concept to Launch." Vol. 168, 2020, pp. 293–309. https://doi.org/10.1016/j.actaastro.2019.09.002.

[324] Aglietti, G. S., Taylor, B., Fellowes, S., Salmon, T., Retat, I., Hall, A., Chabot, T., Pisseloup, A., Cox, C., Zarkesh, A., Mafficini, A., Vinkoff, N., Bashford, K., Bernal, C., Chaumette, F., Pollini, A., and Steyn, W. H. "The Active Space Debris Removal Mission RemoveDebris. Part 2: In Orbit Operations." *Acta Astronautica*, Vol. 168, 2020, pp. 310–322. https://doi.org/10.1016/j.actaastro.2019.09.001.

[325] Shoemaker, M. A., Vavrina, M., Gaylor, D. E., Mcintosh, R., Volle, M., and Jacobsohn, J. OSAM-1 Decommissioning Orbit Design. Proceedings of the AAS/AIAA Astrodynamics Specialist Conference, South Lake Tahoe, California, USA, 2020

[326] Physorg. NASA's On-Orbit Servicing, Assembly, and Manufacturing 1 (OSAM-1) Mission Ready for Spacecraft Build. May 06, 2021. https://phys.org/news/2021-05-nasa-on-orbit-osam-mission-ready.html

[327] Gurfil, P., Herscovitz, J., and Pariente, M. The SAMSON Project – Cluster Flight and Geolocation with Three Autonomous Nano-Satellites. Proceedings of the Small Satellite Conference, Logan, Utah, USA, 2012. https://digitalcommons.usu.edu/smallsat/2012/all2012/56/

[328] Kulu, E. Saturn @ Nanosats Database. Nanosats Database, Aug, 2021. https://www.nanosats.eu/sat/saturn

[329] Banker, B., and Askew, S. Seeker 1.0: Prototype Robotic Free Flying Inspector Mission Overview. Proceedings of the Small Satellite Conference, Logan, Utah, USA, 2019. https://digitalcommons.usu.edu/smallsat/2019/all2019/151/

[330] Sullivan, J., Gambone, E., Kirven, T., Pedrotty, S., and Wood, B. Rapid Development of the Seeker Free-Flying Inspector Guidance, Navigation, and Control System. Proceedings of the 42nd Annual AAS Guidance, Navigation, and Control Conference, Breckenridge, Colorado, USA, 2019.

[331] Dhamani, N., Martin, G. C., Schubert, C. D., Singh, P., Hatten, N., and Akella, M. Applications of Machine Learning and Monocular Vision for Autonomous On-Orbit Proximity Operations. Proceedings of the AIAA Scitech 2020 Forum, Orlando, Florida, USA, 2020. https://doi.org/10.2514/6.2020-1376

[332] Ferrando, P., Arnaud, M., Briel, U., Cavazzuti, E., Clédassou, R., Counil, J. L., Fiore, F., Giommi, P., Goldwurm, A., Lamarle, O., Laurent, P., Lebrun, F., Malaguti, G., Mereghetti, S., Micela, G., Pareschi, G., Piermaria, M., Roques, J. P., Santangelo, A., Tagliaferri, G., Rodriguez, J., and Ferrando, P. The Simbol-X Mission. In *Simbol-X: Focusing on the Hard X-Ray Universe: Proceedings of the 2nd International Simbol-X Symposium*, No. 1126, Paris, France, 2009, pp. 3–8. https://doi.org/10.1063/1.3149459

[333] Guidotti, P. Y., Delpech, M., Djalal, S., Gaudel-Vacaresse, A., Berges, J. C., Gamet, P., and Marle, O. L. GNC Challenges for Simbol-X Formation Flying Mission. In *Trudy MAI*, 2009, pp. 139–149.

[334] Pareschi, G., and Ferrando, P. "The Simbol-X Hard X-Ray Mission." *Experimental Astronomy*, Vol. 20, 2006, pp. 139–149. https://doi.org/10.1007/s10686-006-9062-1.

[335] Richardson, D. G., and Savignol, J. SNAP-1: A Low Cost Modular COTS-Based Nano-Satellite – Design, Construction, Launch and Early Operations Phase. Proceedings of the Small Satellite Conference, Logan, Utah, USA, 2001. https://digitalcommons.usu.edu/smallsat/2001/all2001/39/

[336] Kang, S., Song, Y., and Park, S.-Y. "Nanosat Formation Flying Design for SNIPE Mission." *Journal of Astronomy and Space Sciences*, Vol. 37, No. 1, 2020, pp. 51–60. https://doi.org/10.5140/JASS.2020.37.1.51.

[337] LeVasseur, D. SPHERES and Astrobee Space Station Robotic Free Flyers. Proceedings of the 3rd In-Space Inspection Workshop 2017, Houston, Texas, USA, 2017.

[338] Otero, A. S. *The SPHERES Satellite Formation Flight Testbed: Design and Initial Control*. Massachusetts Institute of Technology, Cambridge, Massachusetts, USA, 2000.

[339] Blackwood, G., Lay, O., Deininger, W., Ahmed, A., Duren, R., Noecker, C., and Barden, B. The StarLight Mission: A Formation-Flying Stellar Interferometer. In *Astronomical Telescopes and Instrumentation*, No. 4852, Waikoloa, Hawai'i, USA, 2002. https://doi.org/10.1117/12.460942

[340] Deininger, W. D., Weiss, M. A., Wiemer, D. J., Hoffman, C. N., Cleven, G. C., Patel, K. C., Linfield, R. P., and Livesay, L. L. Description of the StarLight Mission and Spacecraft Concept. In *2001 IEEE Aerospace Conference Proceedings*, No. 1, Big Sky, MT, USA, 2001. https://doi.org/10.1109/AERO.2001.931709

[341] Bridges, C. P., Taylor, B., Horri, N., Underwood, C. I., Kenyon, S., Barrera-Ars, J., Pryce, L., and Bird, R. STRaND-2: Visual Inspection, Proximity Operations & Nanosatellite Docking. Proceedings of the 2013 IEEE Aerospace Conference, Big Sky, MT, USA, 2013. https://doi.org/10.1109/AERO.2013.6497348

[342] Zink, M., Krieger, G., and Amiot, T. Interferometric Performance of a Cartwheel Constellation for TerraSAR-L. In *FRINGE 2003 Workshop*, No. ESA SP-550, Frascati, Italy, 2003.

[343] Krieger, G., Zink, M., Bachmann, M., Bräutigam, B., Schulze, D., Martone, M., Rizzoli, P., Steinbrecher, U., Walter Antony, J., De Zan, F., Hajnsek, I., Papathanassiou, K., Kugler, F., Rodriguez Cassola, M., Younis, M., Baumgartner, S., López-Dekker, P., Prats, P., and Moreira, A. "TanDEM-X: A Radar Interferometer with Two Formation-Flying Satellites." *Acta Astronautica*, Vol. 89, 2013, pp. 83–98. https://doi.org/10.1016/j.actaastro.2013.03.008.

[344] Snopek, K., Grunwaldt, L., and Koenig, R. Challenges of the TerraSAR/TanDEM-X Formation. Proceedings of the 16th International Workshop on Laser Ranging, Poznan, Poland, 2008.

[345] Lawson, P. R., Lay, O. P., Peters, R. D., Ksendzov, A., Gappinger, R. O., Martin, S. R., and Scharf, D. P. Technology Challenges for Exoplanet Detection with Mid-IR Interferometry. Proceedings of the International Conference on Space Optics 2008, Toulouse, France, 2017. https://doi.org/10.1117/12.2308239

[346] Lawson, P. R., Lay, O. P., Johnston, K. J., and Beichman, C. A. *Terrestrial Planet Finder Interferometer Science Working Group Report*. Publication JPL Publication 07-1. Jet Propulsion Laboratory / California Institute of Technology, Pasadena, California, USA, 2007

[347] Wu, S., Mu, Z., and Chen, W. TW-1: A Cubesat Constellation for Space Networking Experiments. Proceedings of the 6th European CubeSat Symposium, Estavayer-le-Lac, Switzerland, 2016.

[348] Wu, S., Chen, W., Cao, C., Zhang, C., and Mu, Z. "A Multiple-CubeSat Constellation for Integrated Earth Observation and Marine/Air Traffic Monitoring." *Advances in Space Research*, Vol. 67, No. 11, 2021, pp. 3712–3724. https://doi.org/10.1016/j.asr.2020.04.025.

[349] Zakšek, K., James, M. R., Hort, M., Nogueira, T., and Schilling, K. "Using Picosatellites for 4-D Imaging of Volcanic Clouds: Proof of Concept Using ISS Photography of the 2009 Sarychev Peak Eruption." *Remote Sensing of Environment*, Vol. 210, 2018, pp. 519–530. https://doi.org/10.1016/j.rse.2018.02.061.

[350] Kulu, E. Ukko @ Nanosats Database. Nanosats Database, Jan, 2022. https://www.nanosats.eu/sat/ukko

[351] Lightsey, E. G., Arunkumar, E., Kimmel, E., Paletta, A., Rawson, W., Selvamurugan, S., Sample, J., Guffanti, T., Bell, T., Koenig, A., Park, H., Rabin, D., Daw, A., and Kamalabadi, F. Concept of Operations for the Visors Mission: A Two Satellite Cubesat Formation Flying Telescope. Proceedings of the 2022 AAS Guidance, Navigation and Control Conference, Breckenridge, Colorado, USA, 2022.

[352] Davis, T., Baker, M. T., Belchak, T., and Larsen, W. XSS-10 Micro-Satellite Flight Demonstration Program. Proceedings of the Small Satellite Conference, Logan, Utah, USA, 2003. https://digitalcommons.usu.edu/smallsat/2003/all2003/25/

[353] Kornfeld, R. P., Bunker, R. L., Cucullu, G. C., Essmiller, J. C., Hadaegh, F. Y., Liebe, C. C., Padgett, C. W., Wong, E. C., and Grove, O. New Millennium ST6 Autonomous Rendezvous Experiment (ARX). Proceedings of the 2003 IEEE Aerospace Conference, Big Sky, MT, USA, 2003. https://doi.org/10.1109/AERO.2003.1235067

Curriculum Vitae

Thomas Vincent Peters was born on the 25th of December 1979 in Emmen, the Netherlands. He is an experienced project manager and GNC engineer with proven track record of solving challenging GNC design problems.

Experience

Jan 2023 – present	OHB	AOCS & GNC Architect
May 2006 – Nov 2022	GMV	Project Manager and GNC Engineer
Jun – Nov 2005	CNES/CSG	Internship, treatment of Ariane 5 radar tracking data
Jan – Jun 2004	Dutch Space	MSc thesis project, ConeXpress rendezvous mission analysis
Oct – Dec 2003	Dutch Space	Internship, design of robotic system for tele-testing and remote observation for ESTEC's Large Space Simulator
Jan – Mar 2003	TU Delft	Student assistant, supervision 2nd year student design project

Education

2021 – 2024	TU Delft	Candidate Doctor of Philosophy (PhD) at Astrodynamics and Space Missions as fully external student. Dissertation: Guidance for rendezvous and formation flying in elliptical orbits
Oct 2004 – Nov 2005	ISU	MSc, Space Studies, with honours Was awarded a half grant to participate
Summer 2004	ISU	Summer Session Program in Adelaide, Australia Was awarded a full grant to participate
1998 – 2005	TU Delft	MSc at Astrodynamics and Satellite Systems, Faculty of Aerospace Engineering, with honours Thesis: Analysis, design and simulation of ConeXpress rendezvous strategies Participated in DARE – Delft Aerospace Rocket Engineering Was awarded one of 25 grants "sterbeurs" in first year of study
1992 – 1998	Stedelijk Gymnasium Leeuwarden	Secondary school; subjects: Dutch, English, Latin, Math A, Math B, Physics, Chemistry, Biology, Philosophy Average grade 9 out of 10 Participated in Biology Olympiad in 1997 and 1998, achieved best 20 of The Netherlands in both years. Participated in Chemistry Olympiad 1998, achieved best 20 of The Netherlands Participated in Physics Olympiad 1998, achieved best 50 of The Netherlands

Personal Interests

Sailing, martial arts, yoga, ice skating, hobby craft, cooking, general science, astrodynamics

Publications

This thesis

Peters, T. V., Noomen, R., 2020 , "Linear cotangential transfers and safe orbits for elliptic orbit rendezvous," AIAA Journal of Guidance, Control, and Dynamics, doi: 10.2514/1.G005152

Peters, T. V. et. al., 2014, "Mission analysis for PROBA-3 nominal operations," Acta Astronautica, Volume 102, September–October 2014, Pages 296–310, doi: 10.1016/j.actaastro.2014.01.010

Peters, T. V., Escorial Olmos, D., 2014, "Relative mission analysis for PROBA-3: safe orbits and CAM," Int. J. of Space Science and Engineering, 2014 Vol.2, No.2, pp.135 – 156. doi: 10.1504/IJSPACESE.2014.060599

Peters, T. V., Noomen, R., Colmenarejo, P., 2014, "Analytical Solutions to Two-Impulse Nondrifting Transfer Problems for Rendezvous in Elliptical Orbits," AIAA Journal of Guidance, Control, and Dynamics, Vol. 37, No. 3 (2014), pp. 775-788. doi: 10.2514/1.61885

Other peer-reviewed papers

Peters, T. V., et. al., 2018, "Attitude control analysis of tethered de-orbiting," Acta Astronautica, Volume 146, May 2018, Pages 316-331. doi: 10.1016/j.actaastro.2018.03.016

Peters, T. V., Escorial Olmos, D., 2016, "COBRA Contactless De-Tumbling," CEAS Space Journal, doi: 10.1007/s12567-016-0116-6

Book chapter

Peters, T., Silvestrini, S., Colagrossi, A., Pesce, V., Guidance. In *Modern Spacecraft Guidance, Navigation, and Control – From System Modeling to AI and Innovative Applications* (Pesce, V., Andrea Colagrossi, A., Silvestrini, S., eds.), Elsevier, Amsterdam, the Netherlands, 2022, pp. 381 – 440, ISBN: 9780323909167, doi: 10.1016/B978-0-323-90916-7.00008-1

Conference papers

Peters, T. V., Briz Valero, J. F., Perez Gonzalez, J. A., Cuffolo, A., Cropp, A., 2019, “GNC for Lunar ascent, orbit transfer and rendezvous in near-rectilinear halo orbits,” IAC-19-C1,7,9, Proceedings of the 70th International Astronautical Congress, 21–25 October 2019, Washington, D.C., USA

Peters, T. V., Escorial Olmos, D., 2016, “Applicability of COBRA concept to de-tumbling space debris objects,” Proceedings of the 6th International Conference on Astrodynamics Tools and Techniques, March 14 – 17 2016, Darmstadt, Germany

Peters, T.V., 2016, Formation Flying Guidance for Space Debris Observation, Manipulation and Capture. In *Astrodynamics Network AstroNet-II. Astrophysics and Space Science Proceedings, vol 44.*, (Gómez, G., Masdemont, J. eds.), Springer, Cham, Germany, ISBN: 978-3-319-79564-5, doi: 10.1007/978-3-319-23986-6_16

Peters, T. V., Escorial Olmos, D., 2015 “COBRA contactless detumbling,” in Proceedings of the 5th CEAS Air & Space Conference, 7-11 September 2015, Delft University of Technology (The Netherlands)

Peters, T. V., Escorial Olmos, D., Pellacani, A., Avilés Rodrigálvarez, M., Lavagna, M., Ferrari, F., Attina, P., Parissenti, G., Cropp, A., 2014, “The COBRA IRIDES experiment,” IAC-14-A6.6.9, Proceedings of the 65th International Astronautical Congress, 29 September – 3 October 2014, Toronto, Canada

Peters, T. V., Pellacani, A., Attina, P., Lavagna, M., Benvenuto, R., Luraschi, E., 2013, “Cobra Active Debris Removal Concept”, IAC-13-A6,6,6, Proceedings of the 64th International Astronautical Congress, 23-27 September 2013, Beijing, China

Peters, T. V., Escorial Olmos, D., 2013, “Relative mission analysis for PROBA-3: safe orbits and CAM,” Proceedings of the 5th International Conference on Spacecraft Formation Flying Missions and Technologies, 29-31 May 2013, Munich, Germany

Peters, T. V., Pellacani, A., Attina, P., Lavagna, M., Benvenuto, R., Luraschi, E., 2013, “Space Debris Orbit Modification Using Chemical Propulsion Shepherding,” Proceedings of the 6th European Conference on Space Debris, 22-25 April 2013, Darmstadt, Germany

Peters, T. V., Branco, J., Escorial Olmos, D., Tarabini-Castellani, L., Cropp, A., 2013, “Mission Analysis for PROBA-3 Nominal Operations,” IWSCFF-2013-07-06, Proceedings of the 7th International Workshop on Satellite Constellations and Formation Flying, 13 – 15 March 2013, Lisbon, Portugal

Peters, T. V., Peyrard, J., Carrascosa, C., Escorial Olmos, D., 2011, "Detailed design of the PROBA-3 formation flying guidance," IAC-11,C1,7,6, Proceedings of the 62nd International Astronautical Congress, 3-7 October 2011, Cape Town, South Africa

Peters, T. V., Carrascosa, C., Peyrard, J., 2011, "Safe Trajectories for PROBA-3," Proceedings of the 4th International Conference on Spacecraft Formation Flying Missions and Technologies, 18-20 May 2011, St. Hubert, Canada

Peters, T. V., 2010, "Formation acquisition and control strategies for formations in highly elliptic orbits," IAC-10.C1.5.4, Proceedings of the 61st International Astronautical Congress, 27 September - 1 October 2010, Prague, Czech Republic

Peters, T. V., Strippoli, L., 2010, "Innovative Guidance Techniques for Rendezvous on Elliptic Orbits", Proceedings of the 4th International Conference on Astrodynamics Tools and Techniques, 3 - 6 May 2010, ESAC, Madrid, Spain

Peters, T. V., Strippoli, L., 2010, "Guidance for Elliptic Orbit Rendezvous," AAS 10-175, Proceedings of the AAS/AIAA Space Flight Mechanics Meeting held February 14-17, 2010, San Diego, California, USA

Peters, T. V., Cadenas, R., Graziano, M., Modenini, D., Tortora, P., Kervendal, E., Kohler, J., 2009, "ARMADA: Autorotation, feasible alternative to traditional martian entry, descent and landing," Paper IAC-09.D1.1.10, Proceedings of the 59th International Astronautical Congress, 12-16 October 2009, Daejeon, Korea

Peters, T. V., Tarabini-Castellani, L., de Negueruela, C., Llorente, S., Jakobsson, B., 2008, "PROBA-3 Formation Flying Mission Analysis," Proceedings of the 3rd International Symposium on Formation Flying, Missions and Technologies, 23-25 April 2008, ESTEC, Noordwijk, The Netherlands